

0000823



# SCIENCE & ENGINEERING SYMPOSIUM PROCEEDINGS 16-19 OCTOBER



THEME: "Advanced Technologies — Key to  
Capabilities at Affordable Costs"

**DISTRIBUTION STATEMENT A**  
Approved for Public Release  
Distribution Unlimited

**VOL. IV. BASIC RESEARCH**

**CO-SPONSORED BY  
NAVAL MATERIAL COMMAND  
AIR FORCE SYSTEMS COMMAND**



- Avionics
- Propulsion
- Flight Dynamics
- Basic Research

- Material
- Armament
- Human Resources

~~Guenther~~  
TL  
505  
.S45  
1978  
v.4

19991214 083

TECH LIBRARY KAFB, NM



0000823

PROCEEDINGS  
OF THE  
1978 SCIENCE AND ENGINEERING SYMPOSIUM

16 - 19 OCTOBER 1978

NAVAL AMPHIBIOUS BASE  
CORONADO, CALIFORNIA

VOLUME IV

APPROVED FOR PUBLIC RELEASE,  
DISTRIBUTION UNLIMITED

U.S. Air Force  
Air Force Weapons Laboratory  
Technical Library



## SYMPOSIUM OFFICIALS

### CO-SPONSORS

NAVAL MATERIAL  
COMMAND

AIR FORCE SYSTEMS  
COMMAND

### HOSTS

NAVAL OCEAN SYSTEMS  
CENTER  
WEST COAST COORDINATOR

NAVAL AMPHIBIOUS BASE  
FACILITIES

### CO-CHAIRMEN

WILLIAM KOVEN  
Associate Technical Director  
Naval Air Research and  
Technology  
Naval Air Systems Command

DR. BERNARD KULP  
Chief Scientist  
Director of Science and  
Technology  
Air Force Systems Command

### DEPUTY CO-CHAIRMEN

JAMES MULQUIN  
Advanced Systems Technology  
Planning  
Naval Air Research and  
Technology  
Naval Air Systems Command

MAJOR LARRY FEHRENBACHER  
Assistant to Chief Scientist  
Director of Science and  
Technology  
Air Force Systems Command

TL  
505  
.545  
1978  
v. 4

## PREFACE

The initial co-sponsored Air Force Systems Command/Naval Material Command Science and Engineering Symposium was held at the Naval Amphibious Base, Coronado on 16 - 19 October 1978. The theme of the 1978 Symposium was "Advanced Technologies - Key to Capabilities at Affordable Cost."

The objectives of this first joint Navy/Air Force Science and Engineering Symposium were to:

- . Provide a forum for military and civilian laboratory scientific and technical researchers to demonstrate the spectrum and nature of 1978 achievements by their services in the areas of
  - . Armament
  - . Avionics
  - . Basic Research
  - . Flight Dynamics
  - . Human Resources
  - . Materials
  - . Propulsion
- . Recognize outstanding technical achievement in each of these areas and select the outstanding technical paper within the Navy and the Air Force for 1978
- . Assist in placing the future Air Research and Development of both services in correct perspective and to promote the exchange of ideas between the Navy and Air Force Laboratories
- . Stress the need for imagination, vision and overall excellence within the technology community, assuring that the air systems of the future will not only be effective but affordable.

Based upon the success of the initial joint symposium (which was heretofore an Air Force event), future symposia are planned with joint Navy/Air Force participation.

## TABLE OF CONTENTS

### VOLUME I

#### AVIONICS

R. S. VAUGHN, NADC

COL R. LOPINA, AFAL

#### CO-CHAIRMEN

|  |     |
|--|-----|
| The Airborne Electronic Terrain Map System (AETMS)<br>Capt F. Barney, USAF and Dr. L. Tamburino, AFAL  | 1   |
| The Assessment of GaAs Passivation and Its Applications<br>Dr. F. Schuermeyer, J. Blassingame, AFAL and Dr. H. Hartnagel,<br>Univ. of New Castle-Upon-Thames, England                          | 17  |
| Identification of Impurity Complexes in Gallium Arsenide Device<br>Material by High Resolution Magneto-Photoluminescence<br>G. McCoy, Maj R. Almassy, USAF, D. Reynolds and C. Litton,<br>AFAL | 50  |
| Microcircuit Analysis Techniques Using Field-Effect Liquid<br>Crystals<br>D. J. Burns, RADC  | 69  |
| Surface Acoustic Wave Frequency Synthesizer for JTIDS<br>P. H. Carr, A. J. Budreau and A. J. Slovodnik, RADC   | 85  |
| Enhanced Measurement Capability Using a Background Suppression<br>Scheme<br>G. A. Vanasse and E. R. Huppi, AFGL  | 110 |
| Spectrum Estimation and Adaptive Controller for Long-Range<br>Complex Scattering Targets<br>R. F. Ogrodnik, RADC   | 122 |
| Spatial and Temporal Coding of GaAs Lasers for a Laser Line<br>Scan Sensor<br>Capt R. S. Shinkle, USAF, ASD  | 149 |

### VOLUME II

#### PROPULSION

#### AERO-PROPULSION

A. A. MARTINO, NAPC

COL G. STRAND, AFAPL

#### CO-CHAIRMEN

## ROCKET PROPULSION

B. W. HAYES, NWC

COL W. F. MORRIS, AFRPL

CO-CHAIRMEN

|   |     |
|---|-----|
| Airbreathing Propulsion Functional Area Review<br>Col G. E. Strand, USAF, AFAPL                                       | 164 |
| Rocket Propulsion Overview<br>Col W. F. Morris, USAF, AFRPL   | 196 |
| Role of Turbine Engine Technology on Life Cycle Cost<br>R. F. Panella and R. G. McNally, AFAPL                        | 212 |
| VORBIX Augmentation - An Improved Performance Afterburner for Turbo Fan Engines<br>W. W. Wagner, NAPC                 | 247 |
| A Retirement for Cause Study of an Engine Turbine Disk<br>R. Hill, AFAPL, R. Reimann, AFML and L. Ogg, ASD            | 265 |
| Payoffs of Variable Cycle Engines for Supersonic VSTOL Aircraft<br>R. T. Lazarick and P. F. Piscopo, NAPC             | 296 |
| The Coanda/Refraction Concept for Gasturbine Engine Exhaust Noise Suppression During Ground Testing<br>D. Croce, NAEC | 322 |
| Expendable Design Concept<br>Lt D. C. Hall, USAF, AFAPL and H. F. Due, Teledyne CAE                                   | 349 |
| The Supersonic Expendable Turbine Engine Development Program<br>T. E. Elsasser, NAPC                                  | 363 |
| Unique Approach for Reducing Two Phase Flow Losses in Solid Rocket Motors<br>Lt D. C. Ferguson, USAF, AFRPL           | 383 |
| Missile System Propulsion Cook-Off<br>R. F. Vetter, NWC   | 414 |
| A Powerful New Tool for Solid Rocket Motor Design<br>W. S. Woltoz, AFRPL  | 428 |
| Quantification of the Thermal Environment for Air-Launched Weapons<br>H. C. Schafer, NWC                              | 453 |

A Study of Rocket-Propelled Stand-Off Missiles 470  
Lt L. K. Slimak, USAF, AFRPL

Prediction of Rocket Motor Exhaust Plume Effects on Missile Effectiveness 496  
A. C. Victor, NWC

### VOLUME III

#### FLIGHT DYNAMICS

C. A. DeCRESCENTE, NADC COL G. CUDAHY, USAF, AFFDL  
CO-CHAIRMEN

Air Force Flight Dynamics Functional Area Review 521  
Col G. F. Cudahy, USAF, AFFDL

A Functional Area Review (FAR) of Navy Flight Dynamics 592  
C. A. DeCrescente, NADC

Aircraft Aft-Fuselage Sonic Damping 615  
G. Pigman, E. Roeser and M. Devine, NADC

Active Control Applications to Wing/Store Flutter Suppression 626  
L. J. Hutsell, T. E. Noll and D. E. Cooley, AFFDL

Maximum Performance Escape System (MPES) 657  
J. J. Tyburski, NADC and W. J. Stone, NWC

Status of Circulation Control Rotor and X-Wing VTOL Advanced Development Program 673  
T. M. Cbancy, D. G. Kirkpatrick and R. M. Williams, DTNSRDC

AFFTC Parameter Identification Experience 697  
Lt D. P. Maunder, USAF, AFFTC

Developments in Flight Dynamics Technology for Navy V/STOL Aircraft 719  
J. W. Clark, Jr., and C. Henderson, NADC

Cost Effective Thrust Drag Accounting 750  
R. B. Sorrells, III, AEDC

Drag Prediction for Wing-Body-Nacelle Configurations 766  
T. C. Tai, DTNSRDC

Numerical Solution of the Supersonic and Hypersonic Viscous Flow Around Thin Delta Wings 793  
Maj G. S. Bluford, USAF and Dr. W. L. Hankey, AFFDL

|   |     |
|---|-----|
| Optimization of Airframe Structures: A Review and Some Recommendations<br>V. B. Venkayya, AFFDL | 828 |
| Use of Full Mission Simulation for Aircraft Systems Evaluation<br>K. A. Adams, AFFDL            | 870 |

## VOLUME IV

### BASIC RESEARCH

|   |                       |  |
|---|-----------------------|--|
| DR. E. H. WEINBERG, NAL   | DR. L. KRAVITZ, AFOSR |  |
| CO-CHAIRMEN   |                       |  |
| The Electronic and Electro-Optic Future of III-V Semiconductor Compounds<br>H. L. Lessoff, NRL and J. K. Kennedy, RADC  | 885                   |  |
| Collective Ion Acceleration and Intense Electron Beam Propagation Within an Evacuated Dielectric Tube<br>Capt R. L. Gullickson, USAF, AFOSR, R. K. Parker and J. A. Pasour, NRL | 912                   |  |
| High Spatial Resolution Optical Observations Through the Earth's Atmosphere<br>Capt S. P. Worden, USAF, AFGL  | 939                   |  |
| High Burnout Schottky Barrier Mixer Diodes for X-Band and Millimeter Frequencies<br>A. Christou, NRL  | 954                   |  |
| New Energetic Plasticizers: Synthesis, Characterization and Potential Applications<br>Lt R. A. Hildreth, USAF, Lt S. L. Clift, USAF and Lt J. P. Smith, FJSRL                   | 968                   |  |
| Improved Corrosion and Mechanical Behavior of Alloys by Means of Ion Implantation<br>J. K. Hirvonen and J. Butler, NRL  | 981                   |  |
| Symmetric Body Vortex Wake Characteristics in Supersonic Flow<br>Dr. W. L. Oberkampf, Univ of Texas at Austin and Dr. D. C. Daniel, AFATL                                       | 1000                  |  |
| Materials Effects in High Reflectance Coatings<br>H. E. Bennett, NWC  | 1033                  |  |

|  |      |
|--|------|
| Improved Substrate Materials for Surface Acoustic Wave (SAW) Devices<br>Capt R. M. O'Connell, USAF, RADC   | 1058 |
| A Simple Prediction Method for Viscous Drag and Heating Rates<br>T. F. Zien, NSWC  | 1075 |
| Assessing the Impact of Air Force Operations on the Stratosphere Composition<br>C. C. Gallagher and Capt R. V. Pieri, USAF, AFGL   | 1110 |
| On the Modelling of Turbulence Near a Solid Wall<br>K. Y. Chien, NSWC  | 1131 |
| Atmospheric Electric Hazards to Aircraft<br>L. H. Ruhnke, NRL  | 1146 |
| Efficient Operation of a 100 Watt Transverse Flow Oxygen-Iodine Chemical Laser<br>Maj W. E. McDermott, USAF, Capt N. R. Pchelkin, USAF,<br>Dr. J. Bernard and Maj R. R. Bousek, USAF, AFWL | 1161 |

## VOLUME V

### MATERIALS

|  |                                |  |
|--|--------------------------------|--|
| F. S. WILLIAMS, NADC   | COL P. O. BOUCHARD, USAF, AFML |  |
| CO-CHAIRMEN  |                                |  |
| Advanced Materials Technologies - The Key to New Capabilities at Affordable Costs<br>Col P. O. Bouchard, USAF, AFML                          | 1173                           |  |
| Ceramics in Rolling Element Bearings<br>C. F. Bersch, NAVAIR   | 1182                           |  |
| Group Technology Key to Manufacturing Process Integration<br>Capt D. Shunk, USAF, AFML   | 1198                           |  |
| An Attempt to Predict the Effect of Moisture on Carbon Fiber Composites<br>J. M. Augl, NSWC  | 1213                           |  |
| Evaluation of Spectrometric Oil Analysis Techniques for Jet Engine Condition Monitoring<br>Lt T. J. Thomson, USAF and K. J. Eisentraut, AFML | 1252                           |  |

|  |      |
|--|------|
| Characterization of Structural Polymers, Using Nuclear Magnetic Resonance Techniques<br>W. B. Moniz, C. F. Poranski, Jr., A. N. Garroway and H. A. Resing, NRL | 1287 |
| On the Variation of Fatigue Crack Opening Load with Measurement Location<br>D. E. Macha, D. M. Corbly, J. W. Jones, AFML                                       | 1308 |
| Environmentally Induced Catastrophic Damage Phenomena and Control<br>Dr. J. L. DeLuccia, NADC  | 1335 |
| Improved High Temperature Capability of Titanium Alloys by Ion Implantation/Plating<br>S. Fujishiro, AFML and E. Eylon, Univ of Cincinnati                     | 1366 |
| Measurement of the Physical Properties and Recombination Process in Bulk Silicon Materials<br>Lt T. C. Chandler, USAF, AFML                                    | 1384 |
| Deuterated Synthetic Hydrocarbon Lubricant<br>A. A. Corte, NADC  | 1396 |
| The Cordell Plot: Key to a Better Understanding of the Behavior of Fiber-Reinforced Composites<br>T. M. Cordell, AFML  | 1410 |

## VOLUME VI

### ARMAMENT

DR. J. MAYERSAK, AFATL                      R. M. HILLYER, NWC  
CO-CHAIRMEN

|  |      |
|--|------|
| Armament Technology - Functional Overview<br>Dr. J. R. Mayersak, AFATL   | 1434 |
| • The Digital Integrating Subsystem-Modularity, Flexibility and Standardization of Hardware and Software<br>D. L. Gardner, AFATL | 1449 |
| Bank-To-Turn (BTT) Technology<br>R. M. McGehee, AFATL  | 1490 |
| Advances in Microwave Striplines with Applications<br>J. A. Mosko, NWC   | 1507 |



|  |      |
|--|------|
| Considerations for the Design of Microwave Solid-State Transmitters<br>M. Afendykiew, Jon Bumgardner and Darry Kinman, NWC | 1543 |
| Strapdown Seeker Guidance for Air-to-Surface Tactical Weapons<br>Capt T. R. Callen, USAF, AFATL                            | 1590 |
| Optimizing the Performance of Antennas Mounted on Complex Airframes<br>Dr. C. L. Yu, NWC                                   | 1614 |

## VOLUME VII

### HUMAN RESOURCES

|  |                     |      |
|--|---------------------|------|
| H. J. CLARK, AFHRL   | DR. J. HARVEY, NTEC |      |
| CO-CHAIRMEN  |                     |      |
| Human Resources Research and Development<br>H. J. Clark, AFHRL   |                     | 1640 |
| Human Resources in Naval Aviation<br>Dr. J. Harvey, NTEC   |                     | 1649 |
| LCCIM: A Model for Analyzing the Impact of Design on Weapon System Support Requirements and LCC<br>H. A. Baran, AFHRL, A. J. Czuchry and J. C. Goclowski, Dynamics Research Corp |                     | 1683 |
| Pacts: Use of Individualized Automated Training Technology<br>Dr. R. Breaux, NTEC  |                     | 1703 |
| Increasing the Affordability of I-Level Maintenance Training Through Simulation<br>G. G. Miller, D. R. Baum and D. I. Downing, AFHRL   |                     | 1711 |
| Psychomotor/Perceptual Measures for the Selection of Pilot Trainees<br>D. R. Hunter, AFHRL   |                     | 1741 |
| Modern Maintenance Training Technology and Our National Defense Posture<br>Dr. W. J. King and Dr. P. E. Van Hemel, NTEC  |                     | 1758 |
| Prediction of System Performance and Cost Effectiveness Using Human Operator Modelling<br>LCDR N. E. Lane, USN, W. Leyland, NADC and H. I. Strieb (Analytics)                    |                     | 1781 |

|  |      |
|--|------|
| An Inflight Physiological Data Acquisition and Analysis System<br>Capt J. T. Merrifield, USAF, T. P. Waddell, D. G. Powell,<br>USAF/SAM and E. B. Croson, PMTC                                 | 1804 |
| Synthetic Selection of Naval Aviators: A Novel Approach<br>D. E. Norman, D. Wightman, NTEC and CDR L. Waldeisen, NAMRL   | 1821 |
| Modeling: The Air Force Manpower and Personnel System for<br>Policy Analysis<br>Capt S. B. Polk, USAF, AFHRL   | 1831 |
| Evoked Brain Potentials as Predictors of Performance: The<br>Hemispheric Assymetry as Related to Pilot and Radar Intercept<br>Officer Performance<br>Dr. B. Rimland and Dr. G. W. Lewis, NPRDC | 1841 |
| Launch Opportunity for Air-to-Ground Visually Delivered Weapons<br>R. A. Erickson and C. J. Burge, NWC   | 1863 |

## VOLUME VIII

### AVIONICS, PROPULSION, AND FLIGHT DYNAMICS (CLASSIFIED)

|  |     |
|--|-----|
| Functional Area Review of Avionics<br>Col R. F. Lopina, USAF, AFAL   | 1   |
| The MADAIR System<br>J. A. Titus, NCSC   | 27  |
| Electronically Agile Array for Long-Range Airborne<br>Surveillance Radar<br>Dr. J. K. Smith, NADC                                | 89  |
| Automatic Ship Classification System<br>W. G. Hueber and Dr. L. A. Wilson, NWC   | 118 |
| Reduction of False Alarm Rates in Aircraft Attack Warning<br>Systems<br>H. L. Jaeger, NWC  | 144 |
| Impact of Focal Plane Array Technology on Airborne Forward<br>Looking Infrared Sensors<br>M. Hess and S. Campana, NADC           | 179 |
| Advanced Sonobuoy Technology - ERAPS (Expendable Reliable<br>Acoustic Path Sonobuoy)<br>J. J. Stephenosky, NADC                  | 200 |
| NAVSTAR Global Positioning System Field Test Results Aboard<br>Air Force and Navy Test Vehicles<br>LCDR J. A. Strada, USN, SAMSO | 220 |
| An Overview of Soviet Propulsion Capabilities<br>W. A. Zwart, FTD  | 240 |
| Reduced Observables - An Approach for Providing More<br>Effective and Affordable Combat Weapon Systems<br>D. E. Fraga, AFFDL     | 273 |
| Soviet Method of Calculating the Aerodynamic Characteristics<br>of Wings Flying in Ground Effect<br>Lt C. R. Gallaway, USAF, FTD | 330 |

## VOLUME IX

### MATERIALS, ARMAMENT, AND HUMAN RESOURCES (CLASSIFIED)

|  |     |
|--|-----|
| Soviet Materials for Aircraft Engines<br>R. F. Frontani, FTD   | 362 |
| CCD Camera/Tracker Seeker Technology<br>G. F. Teate, NWC   | 390 |
| Warhead Designs for Wide Area Antiarmor Cluster Munitions<br>Dr. J. C. Foster and Capt E. M. Cutler, USAF, AFATL | 404 |
| Active Moving Target Tracking Seeker Captive Flight Test<br>A. N. DiSalvio, AFATL                                | 427 |
| Inter-Laboratory Air-to-Air Missile Technology - An Innovative<br>Approach<br>T. C. Aden, AFATL                  | 449 |
| Aimable Ordnance for Tactical Anti-Air and Anti-Surface Missiles<br>T. R. Zulkoski and P. H. Amundson, NWC       | 485 |
| Manned Threat Quantification<br>Capt G. J. Valentino, USAF and Lt R. B. Kaplan, USAF, AMRL                       | 549 |

THE ELECTRONIC AND ELECTRO-OPTIC FUTURE OF  
III-V SEMICONDUCTOR COMPOUNDS

BY

H. Lessoff, Naval Research Laboratory  
Washington, DC 20375

J. K. Kennedy, Rome Air Development Center  
L. G. Hanscom Field, Bedford, MA 01731

# The Electronic and Electro-Optic Future of III-V Semiconductor Compounds

## ABSTRACT

This paper will assess activities directed toward the material development of a III-V compound semiconductor based microwave, millimeter wave and electro-optic technology. The background and status of the materials and device work on III-V compounds will be reviewed. Questions concerning the materials aspects, band structure, transport and chemical properties and device status, as well as other pertinent areas, will be discussed to help resolve the primary question - what is the future of III-V compounds, binary, ternary and quaternary. The various current activities will be reviewed and projections of the device potential will be made based on materials progress. With any device technology, no matter how fine the arguments for improved device performance, nor how good the actual proven performance of prototype devices, the fact remains that no device is viable until the materials technology is well developed. Conversely, device or system needs are required to push the materials technology. The implications of this problem of which comes first, the material or the device will be explored.

## Introduction

This report will present the rationale for the extensive materials efforts being expended by the DoD in III-V materials. The background and the current status will be summarized, however, there are a number of extensive review articles and conference proceedings available for this information (1,2,3,).

Questions concerning the materials properties, electro-optic physics, chemical properties and device potential will be presented to help resolve the more fundamental questions: why work on the III-V materials which are inherently more costly than silicon? and, do the III-V alloys have any advantage over other semiconductors? In order to fully evaluate these alloys the potential of the materials for devices must be discussed. At the outset, it must be stated that the major effort in the microwave and millimeter wave properties of the III-V alloys is being funded by the Department of Defense; however, in the fiber optic communication area there is considerable commercial potential and private industry is supporting a significant effort.

## Microwave and Millimeter Wave Materials

The motivating drives within the semiconductor device industry are higher efficiency, speed and power and lower cost, noise and size. The development of silicon for solid state electronics resulted in a major change in communications, computations, and other technologies. Indeed, today it is difficult to find an area of modern civilization untouched by the silicon revolution. Certainly the military has undergone an evolution in its basic strategy due in no small measure to the electronic capability available with silicon based semiconducting devices.

This change in the electronic capability has occurred in less than 30 years with the introduction of, initially, the silicon transistor and then the integrated circuit. Silicon was not the first semiconducting material in spite of its overwhelming dominance. Initially, transistors were, and are still to a limited extent, made from germanium. However the energy gap of germanium, 0.65 eV, is too low, and intrinsic conduction

occurs below  $100^{\circ}\text{C}$  thus limiting the operating characteristics of germanium semiconducting devices.

Silicon has an energy gap of 1.11 eV and intrinsic conduction does not occur below  $250^{\circ}\text{C}$ ; thus the useful operating range of silicon devices is improved compared to germanium. Other advantages of silicon are seen in Table 1 where in terms of utilization the ability for a diffusion based technology was and is a prime consideration for integrated circuit devices and systems. It is not necessary to point out the impact the silicon integrated circuit has made on the military system applications as devices as automotive ignition systems to advanced missiles and satellites. The silicon integrated circuit has made significant changes in the everyday life styles of each person in the civilized world from toys to modern communications.

Indeed, if one considers the tremendous range of current and potential applications of silicon in electronics it is quite logical to ask: why spend large amounts of resources to develop other semiconductor material technologies which do not have many of the obvious advantages of silicon. Among the disadvantages of the III-V compounds: they are relatively difficult to prepare, the elements are quite costly, they do not appear suitable for a diffusion based technology, and, at least to date, they are difficult to passify.

These disadvantages notwithstanding, in the area of microwave and millimeter wave technology the devices based on III-V materials can perform functions which cannot be readily achieved using silicon. As seen in Table 2 the band gaps of GaAs and InP are higher than silicon; therefore higher operating temperatures are possible. At the charge carrier velocities, necessary for high speed operation, gallium arsenide (GaAs) and indium phosphide have distinct advantages over silicon. Figure 1 shows that the low field mobility of GaAs ( $8600\text{ cm}^2/\text{v-sec}$ ) is greater than InP ( $4000\text{ cm}^2/\text{v-sec}$ ) which in turn is significantly greater than Si; at higher fields the velocity of the carriers in InP is significantly higher than in the others which projects a higher frequency of operation for devices based on InP. It is also evident that in contrast with Si, InP and GaAs



possess a region of negative differential mobility which is used to advantage in transferred electron devices, TED. Already microwave tubes are being displaced by the III-V semiconductors for low power applications. Today, 5 W devices at 8 GHz have been prepared (4) and there are projections for 5 W devices at 20 GHz (5). Higher speed computers will require devices based on the III-V technology since silicon, even with submicron technology, is velocity limited. Signal processing in the millimeter or microwave range frequencies requires devices and material properties not available in silicon. NRL is currently doing in-house III-V material preparation activity in bulk single crystals and both liquid epitaxial growth in thin single crystals and device research for microwave and millimeter wave devices. Other DoD laboratories having significant in-house microwave materials and devices efforts include Naval Ocean Systems Center, Air Force Wright Patterson AFSC, and the Army laboratories in the Electronics Command.

### Fiber Optics

While the present primary commercial application of fiber optics is as either decorative or functional light guides, it has long been recognized that the enormous commercial potential of fiber optics lies in its use for short and long range communications. Recent advances in fiber optics component technology have paved the way for moving optical communications systems out of the laboratory and into commercial use. This fact was dramatically demonstrated in the summer of 1977 when both the Bell System (in its Chicago experiment) and ITT (at a location north of London) announced that they were installing commercial telephone service over optical links.

The advantages enjoyed by fiber optics systems compared to their conventional coaxial cable or twisted wire communications systems counterparts are shown in Table 3.

All of these advantages are reflected in urgent Naval and Air Force Communications Systems requirements for point-to-point, distributive network, and intrusion resistant and radiation hardened systems.

The basic building blocks of a fiber optic data transmission system are: 1) a transmitter (a solid state light source), 2) a transmission path (an optical fiber), and 3) a receiver (a solid state detector). The major technical breakthrough in long distance data transmission occurred in 1970 when Corning Glass Works announced the development of low loss, high quality fused silica fibers. These fibers had attenuation losses as low as 20 dB/Km. Since then, fiber attenuation has dropped steadily. Presently, attenuations of 0.5 dB/Km or less have been achieved in the 1.1 to 1.3  $\mu\text{m}$  region.

An optimum light source is one which can couple maximum power with adequate bandwidth into the optical fiber. Its wavelength should suffer only minimum attenuation in the fiber and should match the maximum responsivity of the photodetector. Materials selection for such solid state light sources reduces very rapidly to the III-V materials. The indirect band gap of the elemental semiconductors and the stoichiometric variations of II-VI materials eliminate these two classes of materials from consideration. If, when we consider the III-V materials, we eliminate from consideration those compounds formed with B or N (since the preparation of these materials is difficult and insufficiently advanced to make P-N junction devices practical), then nine binary compounds and their 18 ternary alloys remain. Figure 2 shows: 1) six of these binary compounds and the distinct wavelengths they provide and 2) several of the more widely investigated ternary alloys and the wavelength ranges to which they correspond.

The most widely used fiber optics light sources are LED or laser structures based on the GaAs-AlGaAs system. This system yields the most efficient room temperature LEDs and CW lasers, because even without close control of alloy composition, this alloy system can provide almost perfectly lattice matched heterojunction optoelectronic devices over the entire alloy compositional range. The lattice matching inherent in this system effectively eliminates the misfit dislocations common at heterojunction interfaces of other alloy systems with poor lattice fit. The presence of such dislocations causes minority carrier recombination, morphology and surface recombination problems which degrade or prevent device operation.

The function of the receiver or solid state light detector in a fiber optic system is to convert light signals to electrons which can be handled by traditional circuitry. For the 0.8 to 0.9 wavelength range of the GaAs-AlGaAs emitters, silicon avalanche or P-I-N photo-diodes are the most commonly used detectors because of their high efficiency, low noise, uniform response and high reliability.

For long range optical communications one disadvantage of GaAs-AlGaAs sources is that their 0.8 to 0.9  $\mu\text{m}$  output is not optimally matched to the characteristics of the best available optical fibers. State-of-the-art fused silica fibers exhibit minimum absorption and dispersion in the 1.1 to 1.3  $\mu\text{m}$  region. To take advantage of this inherent property of low loss fibers, so crucial to the successful solution of pressing Naval and Air Force long range optical communications problems, several in-house laboratories are actively engaged in the development of III-V quaternary alloy systems. Quaternary alloys have one more degree of freedom than ternary alloys. This additional degree of freedom permits the independent variation of the energy bandgap and the lattice constant over wide ranges. Of the possible quaternary alloy systems covering this wavelength range the GaInAsP-InP system appears to be the most promising because:

(1) Well controlled thin films have been grown via LPE, (2) Room temperature DH lasers emitting at wavelengths between 1.0 and 1.3  $\mu\text{m}$  have been fabricated successfully, (3) Operating lifetimes in excess of 5000 hours have been achieved. Thus it appears, that the necessary exploratory research for adequate source development in this alloy system is well underway. Rome Air Development Command is doing growth of bulk InP single crystals and vapor phase epitaxial growth of binary and quaternary alloys. Other DoD laboratories are doing vapor phase and liquid phase growth of III-V compounds for electro-optic applications.

#### Current Efforts and Results

The in-house activities on III-V materials at the Naval Research Laboratory and at Rome Air Development Command, L. G. Hanscom Field were undertaken to meet some of the critical needs for better substrates of GaAs and InP as well as to prepare epitaxial layers for electronic

and electro-optic applications. The programs were so divided that semi-insulating substrates and liquid phase epitaxial growth of GaAs and InP was performed at NRL and "n" and "p" substrates of InP and vapor phase epitaxial growth of GaAs was performed at RADC. Samples and information exchange were performed between the two laboratories as well as with other laboratories working in the III-V area.

It was found quite early that the commercially available compounded InP and GaAs was not of sufficient purity to prepare reproducible substrate material. A compounding apparatus developed by E. Swiggard et.al. (6) that uses a pyrolytic boron nitride (PBN) boat and protective liners (Fig. 3) has resulted in the ability to prepare high purity GaAs and InP with no detectable Si impurities. The impurity level of the GaAs is so low the material becomes semi-insulating due to residual oxygen.

The high purity GaAs and InP is grown in single crystal form using the liquid encapsulated Czochralski method (Fig. 4) and a PBN crucible to hold the melt (7). Typical properties of the grown single crystals are shown in Table 4. The GaAs can be prepared in semi-insulating form with residual oxygen doping for ion implantation applications and Cr/Te doped for liquid and vapor phase epitaxial growth. The semi-insulating InP is Fe doped with the dopant concentration an order of magnitude lower than that previously necessary. The single crystals have been used in in-house laboratories and in industry for physical and device evaluation; and results to date are so promising that industry is adopting the methods developed. A manufacturing technology program is scheduled for funding this fiscal year. GaAs FET's have been prepared by direct ion implantation into the non-intentionally doped substrate. Results to date indicate state-of-the-art device performance with potentially major cost savings. The ability to prepare GaAs and InP devices by ion implantation directly into the substrate holds the promise of eliminating a major disadvantage of the III-V's when compared to Si, namely III-V technology could be a diffusion like technology.

For the first time InP FET's have been prepared by ion implantation (8) as a result of the availability of

high purity semi-insulating InP substrates. InP MISFET's have also been prepared and may open the potential of an MOS technology for the III-V's.

The liquid phase epitaxial growth is performed in an apparatus shown in Figure 5. The introduction of a second well in the sliding seal boat has allowed the growth substrates to be etched just prior to growth. The etch back removes any damaged layer which may develop by heating and processing before growth (10). The epitaxial layers grown in this manner have resulted in the ability to make GaAs microwave devices having no extra buffer layers to protect the active layer from the substrate. V.L. Wrick et. al. (11) have used the etch back process to grow epitaxial InP layers of extremely high purity which previously was not attainable. The processes developed are being used to prepare both microwave and electro-optic devices and can result in significant savings by having better epitaxial layer uniformity and reproducibility as well as by reducing the cost and increasing yield by removing the extra step of growing a buffer layer.

As already mentioned for long range fiber optics communication systems, available quartz fibers show minimum absorption and dispersion in the 1.1 to 1.3 micron range and InP-GaInAsP sources are developing nicely. Detector development however has not proceeded as smoothly. GaInAsP-InP photodetectors have been developed which have demonstrated greater responsivity at 1.05  $\mu\text{m}$  than the best Si photodiodes operating at 0.85  $\mu\text{m}$ . However development of quaternary avalanche and P-I-N diodes has not proceeded quite as smoothly due to the higher purity requirements necessary for efficient operation. LPE systems have thus far not successfully demonstrated the ability to reduce the as grown carrier concentrations to much below  $1 \times 10^{16}$  carriers/cm<sup>3</sup> without resorting to prolonged baking cycles.

In the case of GaAs, VPE systems have been used very successfully to achieve high purity layers ever since the mole fraction effect was first described by Cairns and Fairman (12). Clarke (13) in England and Fairman (14) et. al. in the U.S.A. have successfully shown that the mole fraction effect can also be used to prepare very high purity InP. In order to successfully fabricate high efficiency detector structures for the 1.1 to 1.3  $\mu\text{m}$

range by VPE, a vapor phase system must be developed which can successfully deposit high purity GaInAsP. The hydride system originally described by Tiejten and Armick (15) appears to be ideally suited to handle the growth of GaInAsP when modified as shown in Figure 9. Kennedy et. al. (16,17) have successfully shown that the mole fraction effect also applied to the hydride system (Fig. 6) and have also determined the effect of the Ga/As ratio (Fig. 6), deposition temperature (Fig. 7), and HCl concentration (Fig. 8) on mobility of the deposited GaAs layers. A double tube hydride system designed to study the effect of various growth parameters on the purity of GaInAsP layers is currently under construction at RADC/ES (Fig. 9).

### Conclusion

The promise of the III-V technology for military applications is just beginning to be realized. Those areas of electronics which can use the inherent cost advantages of silicon will continue to do so. However, use of the III-V's will result in the development of new technologies in high speed logic and data processing, in compact and reliable microwave and millimeter wave systems, and in a revolutionary use of electro-optics for communications and control functions. An example of the potential of the electro-optics is that in the first year of full service of a fiber optic link in Chicago by Bell Telephone an average outage rate of 0.02% or less for a conventional trunking system went down to a projected rate of 0.0001% for the optical link. Projected lifetimes for III-V lasers at room temperature are over one million hours.

Thus, the cooperative in-house materials efforts are and will continue to aid the development of these new technologies in areas where the prime user is the military. Future work will be done in these military laboratories having the unique capabilities for materials development. Already significant advances have taken place in programs at NRL and RADC on a cooperative basis and industry is voluntarily making tests and devices using the in-house materials.

### Acknowledgements

The work reported on is a summary of the activities of a number of scientists at the Naval Research

Laboratory and Rome Air Development Command including  
E. Swiggard, R. Henry, S. Lee. P. Nordquist, W. Potter,  
and D. Davies.

## References

1. J. W. Harrson, Technical Rept. AFAL-TR-72, 312, (Jan. 1973).
2. J. K. Kennedy, H. Lessoff and D. L. Lile, Technical Rept. RADC-TR-77-398, (Nov. 1977).
3. E. M. Swiggard and H. Lessoff, NRL Memo Report 3845 (1978).
4. E. Cohen, NRL, Private communication, (1978).
5. T. Irie, Microwave J., 24, (Feb. 19, 1978).
6. E. M. Swiggard, S. H. Lee and F. W. Von Batchelder, "Gallium Arsenide and Related Compounds, Inst. Phys. Conf., 33b, 23 (1976).
7. R. L. Henry and E. M. Swiggard, J. Electron Mater. 7, 647 (1978).
8. K. R. Gleason et. al., Appl. Phys. Lett. 32, 578 (1978).
9. L. Messick, D. L. Lile, and A. R. Clawson, Appl. Phys. Lett. 32, 494 (1978).
10. P.E.R. Nordquist, Jr., H. Lessoff and E. M. Swiggard, Mater. Res. Bull., 10, 939 (1976).
11. V. L. Wrick, et. al., Electron. Lett. 12, 394 (1976).
12. B. Cairns and R. Fairman, J. Electrochem. Soc., 115, 327c (1968).
13. R. C. Clark, B. D. Joyce and W. H. E. Wilgors, Solid St. Commun. 8, 1125 (1970).
14. R. D. Fairman, M. O. Mori and F. B. Frank, Gallium Arsenide and Related Compounds, Inst. Phys. Conf. Ser. 33b, 45 (1976).
15. J. J. Tiejten and J. A. Armick, J. Electrochem. Soc. 113, 724 (1966).



16. J. K. Kennedy and W. D. Potter, J. Crystal Growth 19, 85 (1973).
17. J. K. Kennedy, W. D. Potter and D. E. Davies, ibid 24/25, 233 (1974).

Table 1

Advantages of Semiconducting Silicon

1. Elemental semiconductor.
2. Relative ease to purify and grow single crystal.
3. Diffusion based technology.
4. Native oxide passification.
5. Inexpensive and plentiful element.
6. Large base in commercial technology.

Table 2

## Physical Properties of Si, GaAs and InP

|   | <u>Si</u> | <u>GaAs</u> | <u>InP</u> |
|---|-----------|-------------|------------|
| Molecular weight  | 28.06     | 144.64      | 145.79     |
| Density (gm/cc)   | 2.328     | 5.316       | 4.787      |
| Thermo cond (w/cm <sup>0</sup> C)                         | 1.41      | 0.54        | 0.68       |
| Melting point ( <sup>0</sup> C)                           | 1415      | 1,238       | 1.070      |
| Mobility<br>(cm <sup>2</sup> /v-sec) (300 <sup>0</sup> C) | 1900      | 8,600       | 4,000      |
| Eg (eV)   | 1.11 I    | 1.43D       | 1.35D      |

Table 3

Advantages of Fiber Optics Systems over  
Traditional Communications Systems

- o Increased immunity to EMI and EMP.
- o Dielectric isolation between transmitter and receiver.
- o For greater intrusion resistance and security.
- o Wide signal bandwidths.
- o No spark, fire or short circuit hazards.
- o Smaller, lighter, and lower loss cables.
- o Ultimately lower cost.

Table 4

## Properties of LEC Grown GaAs and InP Crystals

| <u>Material</u> | <u>Dopant</u>              | <u>Mobility</u><br><u>(cm<sup>2</sup>/v-sec)</u> | <u>Resistivity</u><br><u>(ohm-cm)</u> | <u>Etch Pit</u><br><u>Density</u><br><u>cm<sup>-2</sup></u> |
|-----------------|----------------------------|--|---------------------------------------|---|
| GaAs            | residual<br>O <sub>2</sub> | 4000 (RT)  | 10 <sup>8</sup>                       | 1-5x10 <sup>3</sup>   |
| GaAs            | Cr:Te                      | 1200 (RT)  | 10 <sup>8</sup>                       | "   |
| InP             | -                          | 25,000 (77°)                                     | -                                     | 1-5x10 <sup>4</sup>   |
| InP             | Cr                         | -  | 10 <sup>3-4</sup>                     | "   |
| InP             | Fe                         | -  | 10 <sup>7</sup>                       | "   |

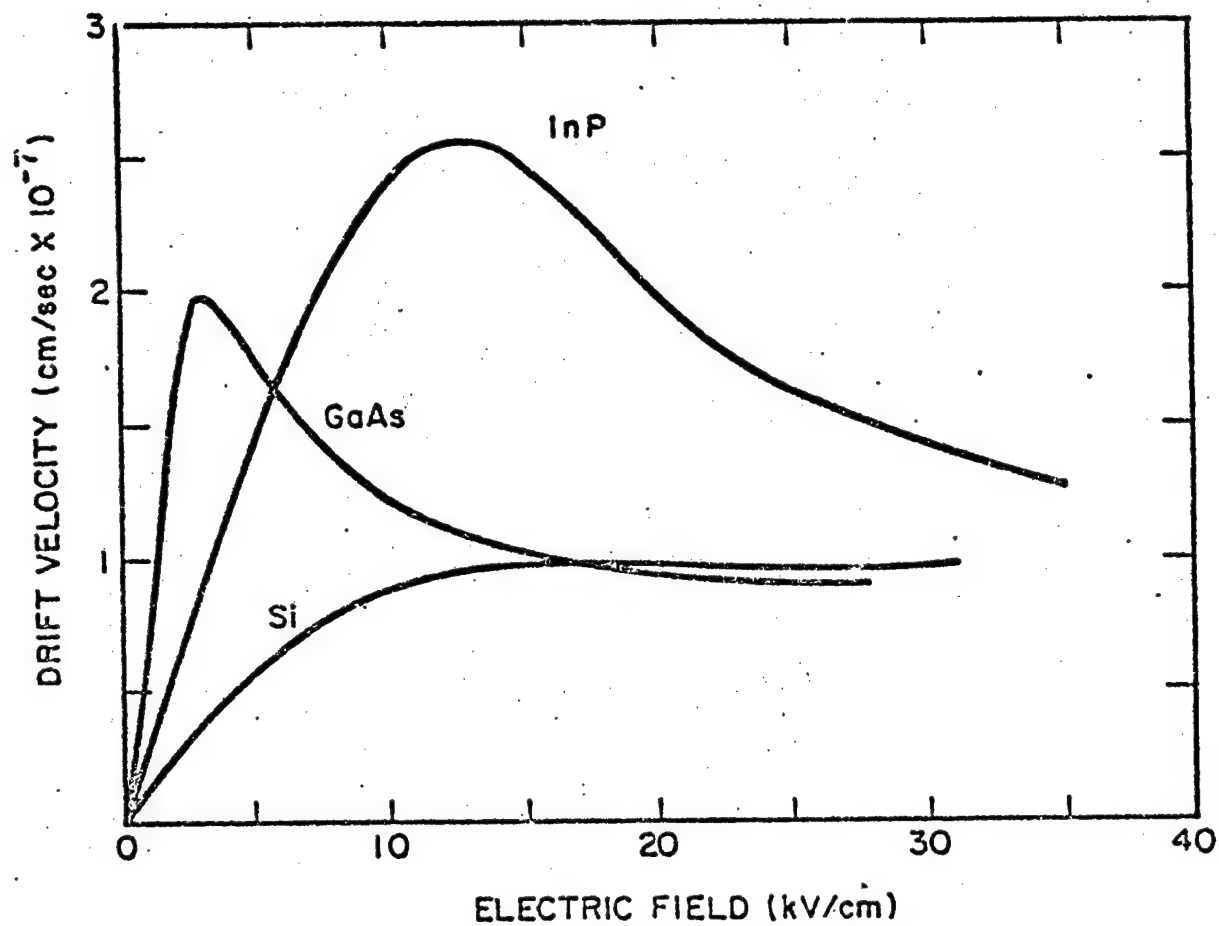


Fig. 1 Drift velocity versus electric field for GaAs, Si and InP.

### III-V TERNARY ALLOYS (I8)

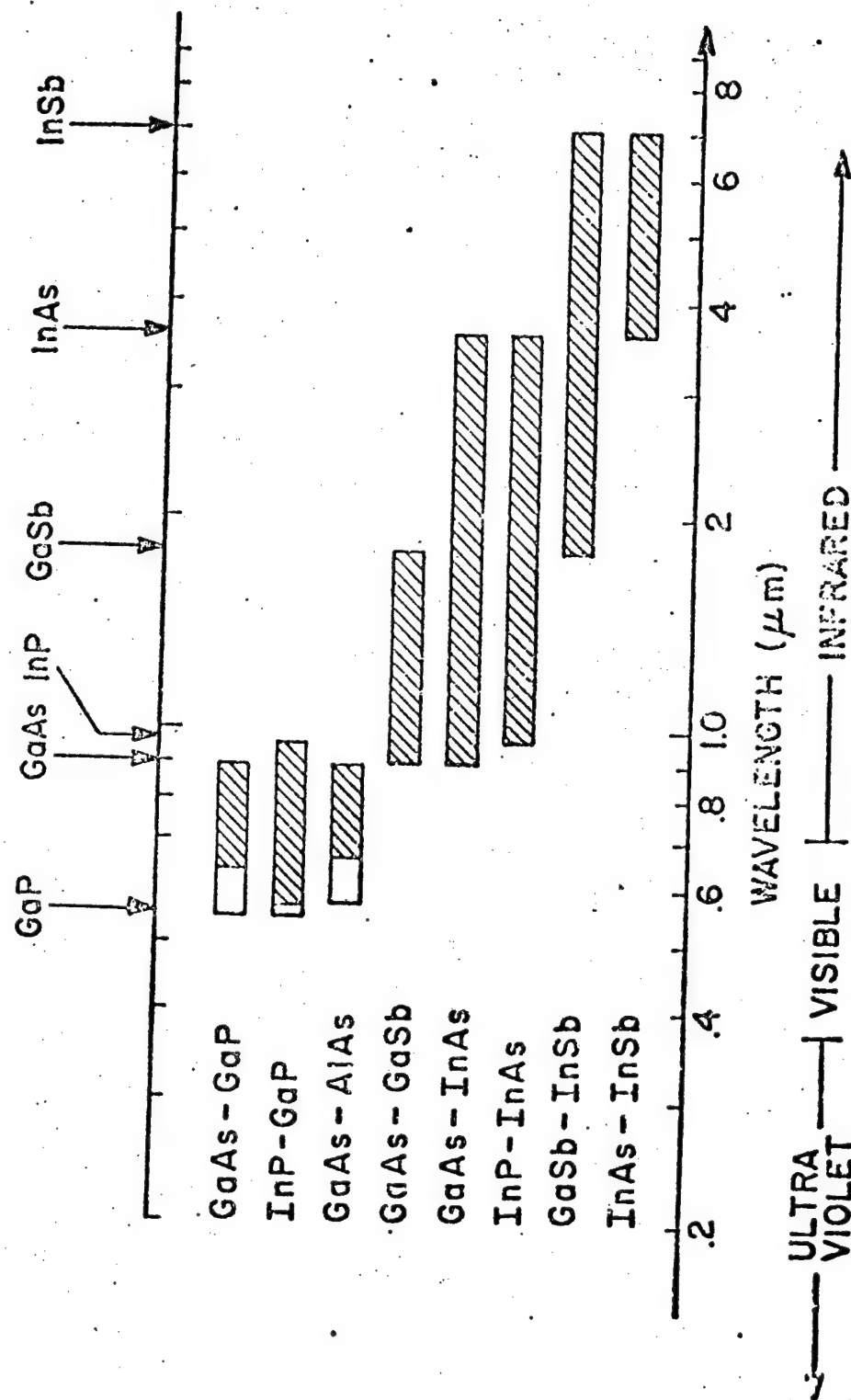
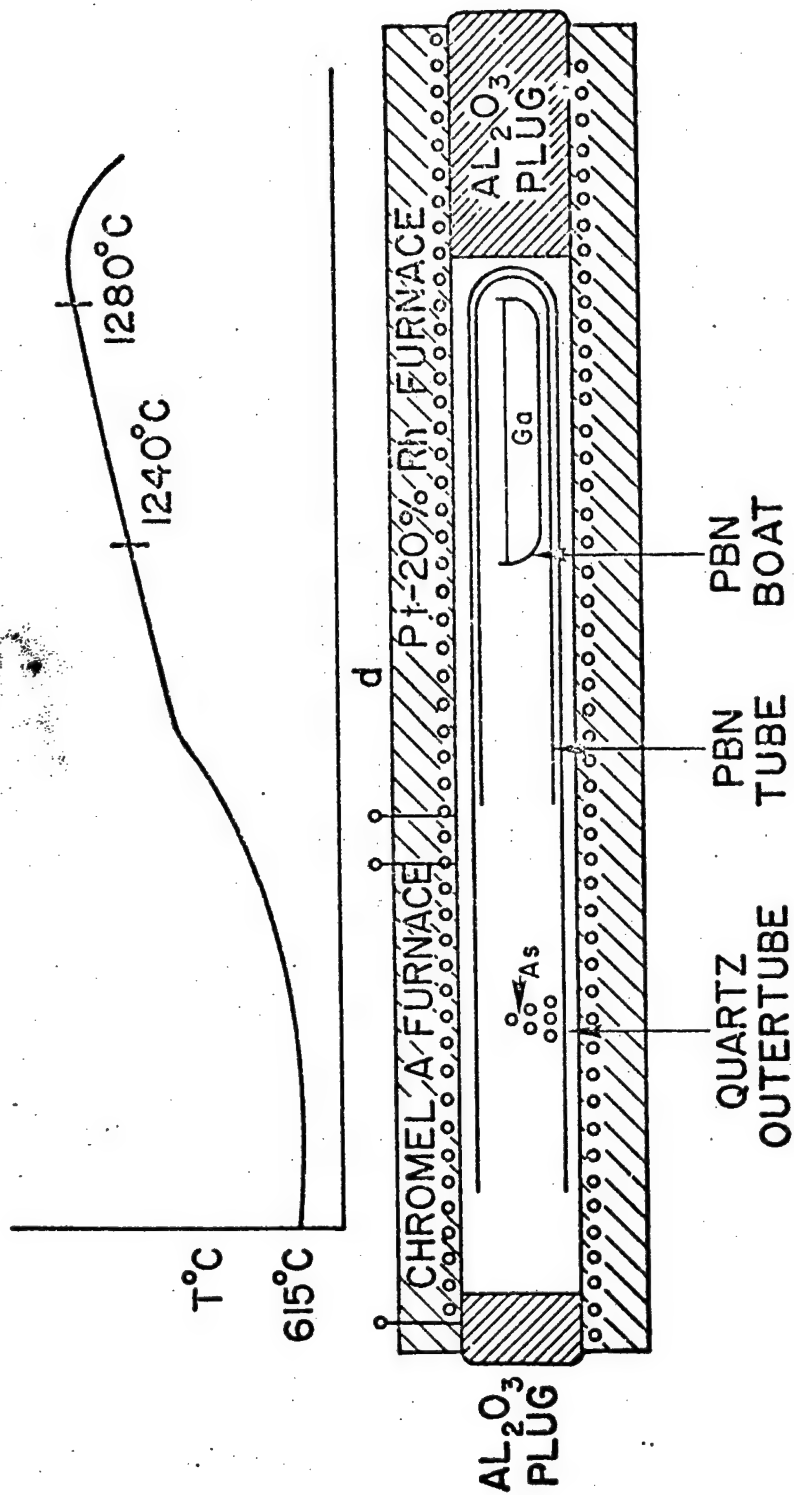


Fig. 2. III-V alloys and the wavelength ranges.



### GRADIENT FREEZE FURNACE

Fig. 3 Furnace and typical profile for compounding GaAs



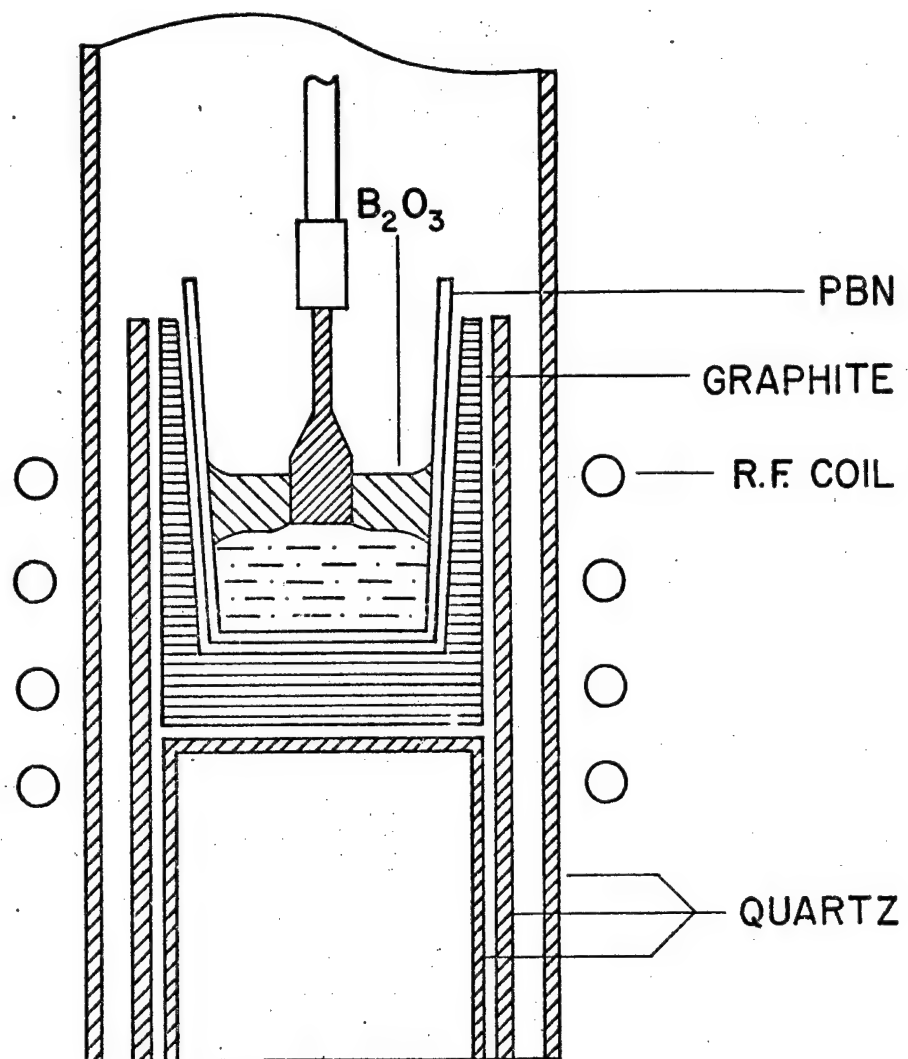


Fig. 4 LEC furnace for single crystal growth

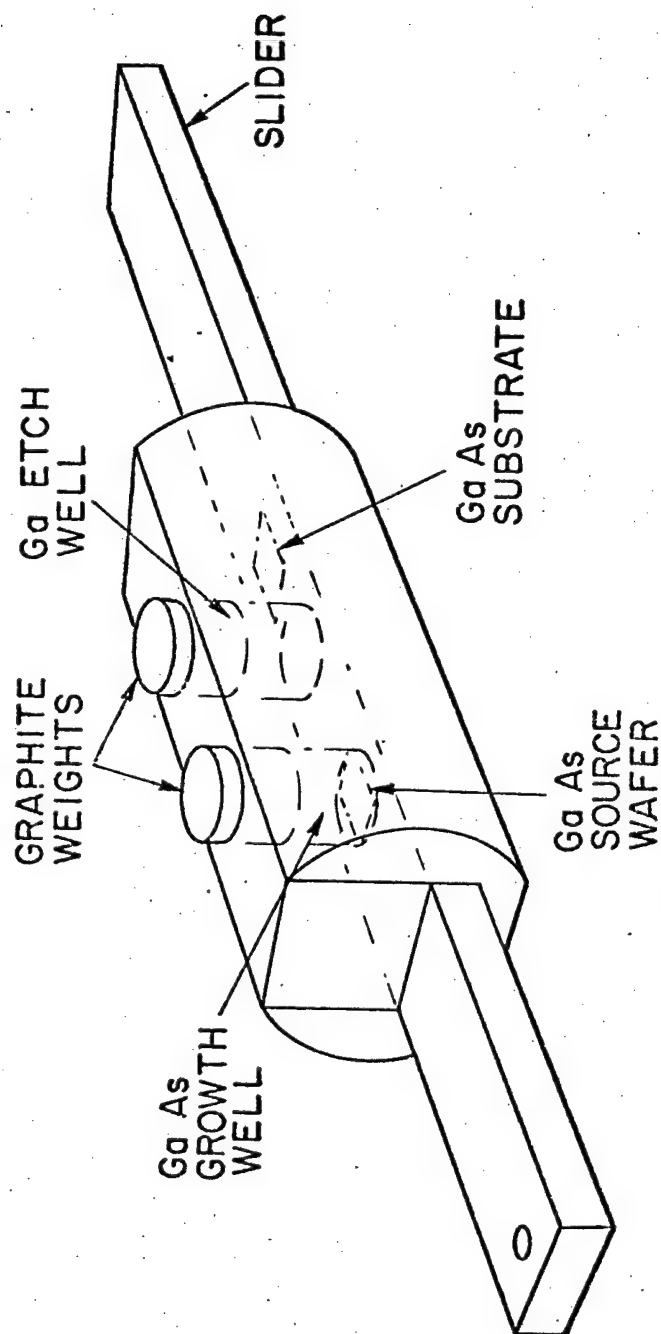


Fig. 5— Epitaxial growth reactor

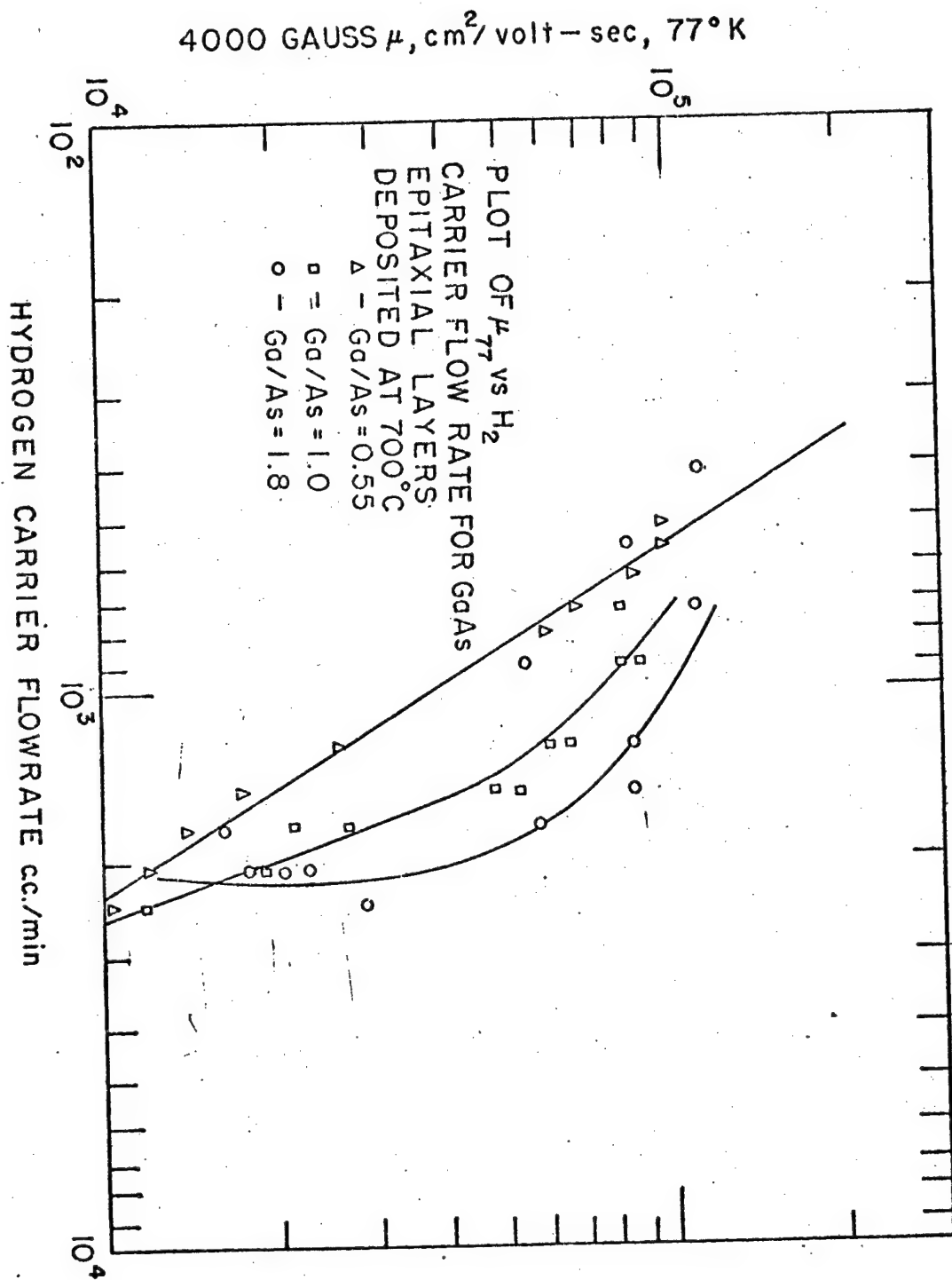


Fig. 6 4000 Gauss mobility versus the hydrogen flow rate.

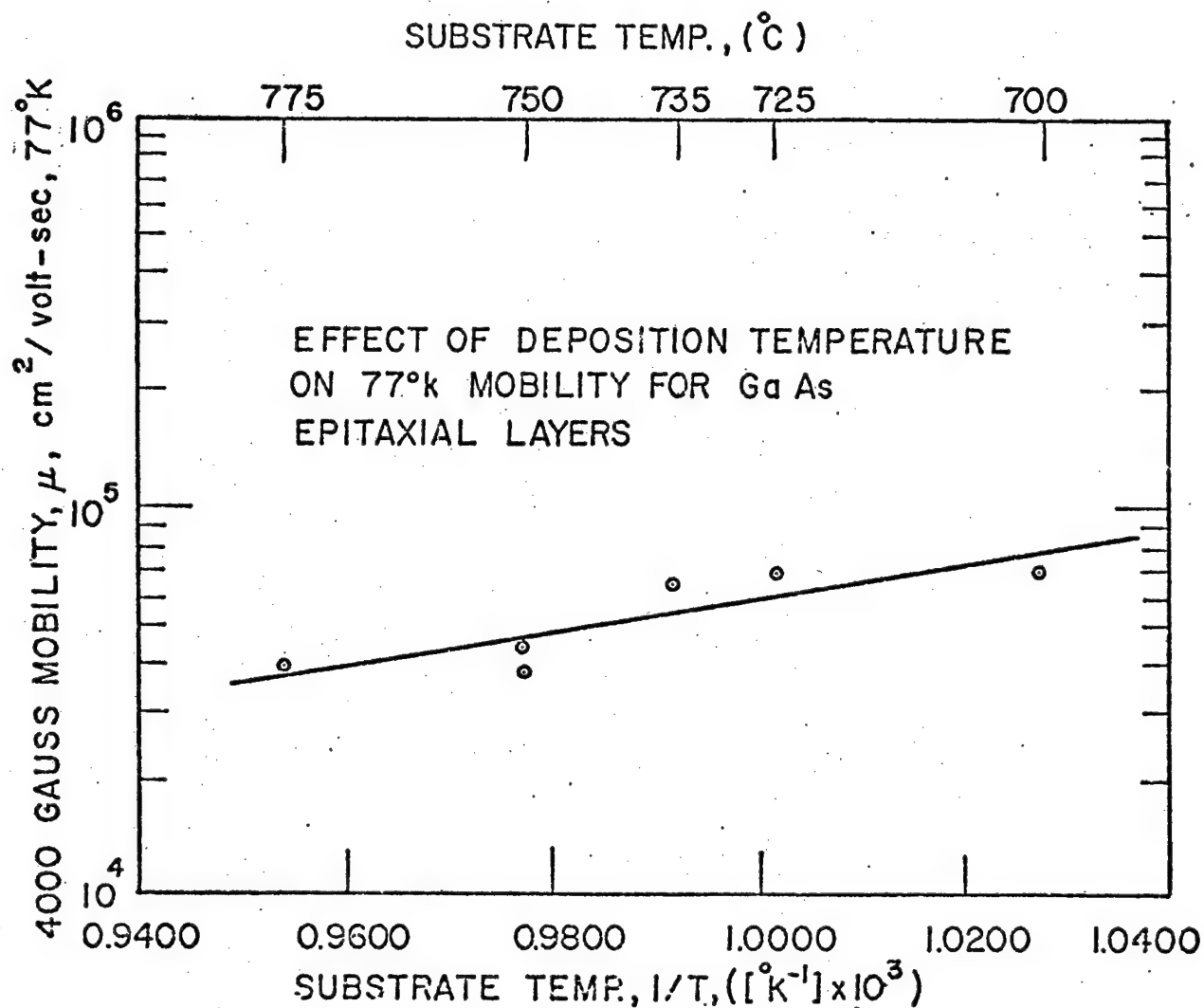


Fig. 7 4000 Gauss mobility versus deposition temperature.

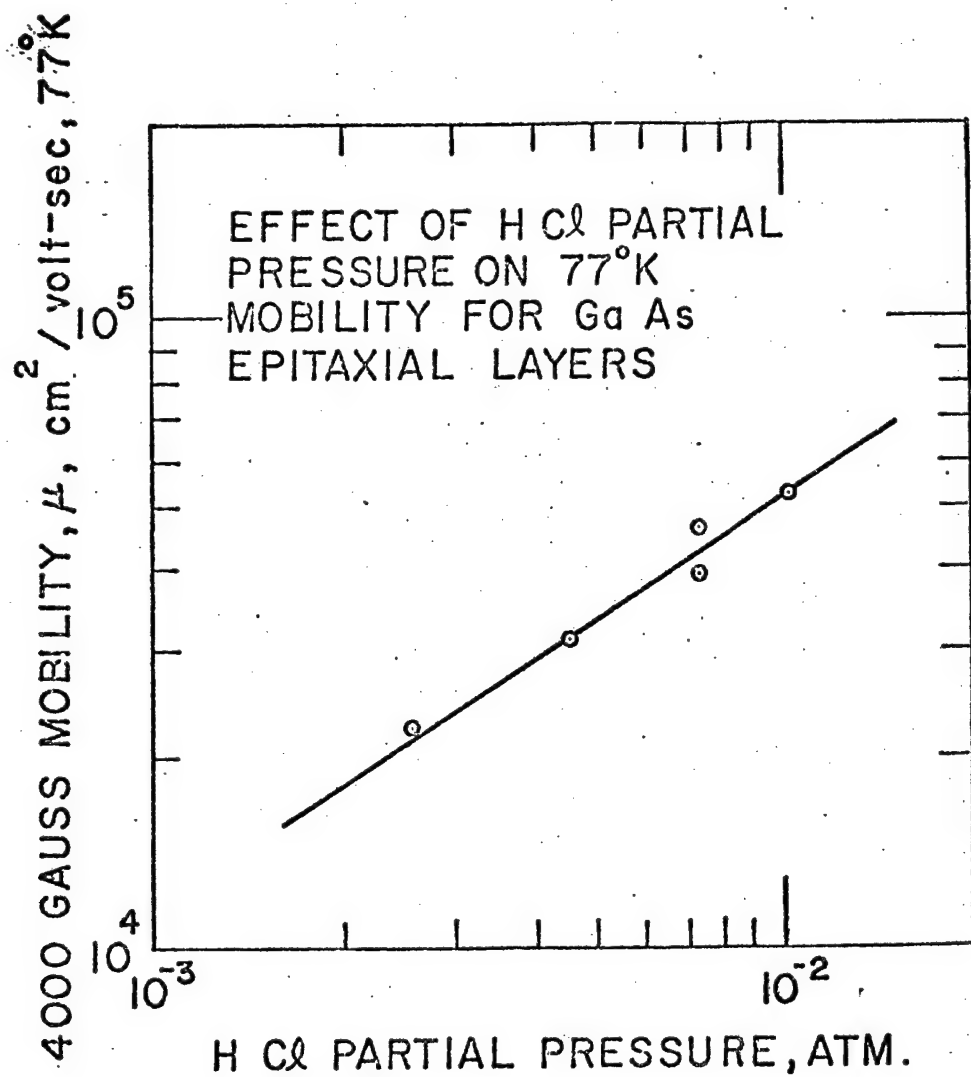


Fig. 8 4000 Gauss mobility versus HCl concentration

# DOUBLE TUBE III - V SYSTEM

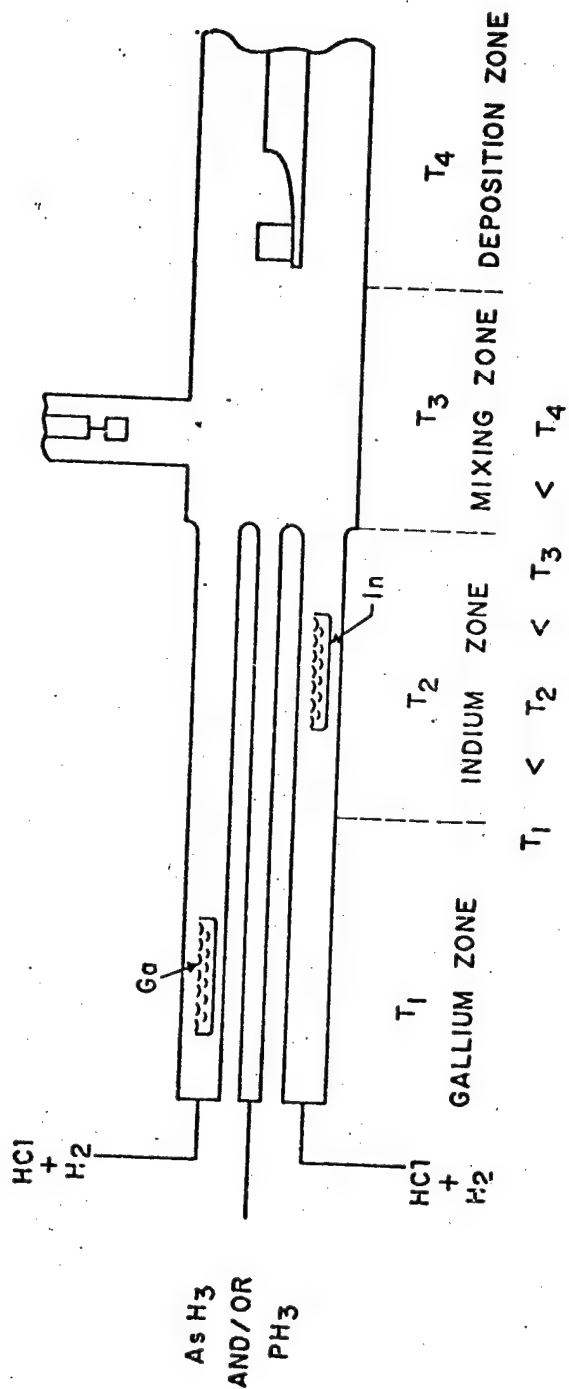


Fig. 9 Epitaxial reactor for the growth of III-V quaternary alloys

### Biographical Sketch

Howard Lessoff was born in Boston, Massachusetts on September 23, 1930. He graduated from Northeastern University in 1953 receiving a B.S. degree in chemistry. He was a member of Quartermaster Petroleum Inspection Laboratory in Charleston, South Carolina from 1953 to 1955. After military service he did graduate work as a fellow in chemistry at Northeastern University from 1955 to 1957 and received his M.S. degree.

Prior to joining the government, Mr. Lessoff was employed by RCA and Bell Telephone Laboratories as a senior scientist engaged in computer memory core development. He joined NASA Electronic Research Center in 1964 as Head, Magnetic Research Section, then transferred to the Naval Research Laboratory in 1970 where he is currently Head of the Electronic Materials Technology Branch. Mr. Lessoff has over 40 publications and patents on electronic material research, he has served on many national and international committees dealing with electronic materials. He is a member of the American Association for the Advancement of Science, Institute of Electrical and Electronic Engineers, American Assoc. of Crystal Growth, Fellow of the Washington Academy of Sciences and President of the NRL Chapter of Sigma-Xi.

John K. Kennedy was born September 10, 1931 in Boston, Massachusetts. He graduated from Boston College in 1952 with a B.S. in chemistry and from Tufts University in 1953 with a M.S. in chemistry. Mr. Kennedy was at the U.S. Army Chemical Center at Edgewater, Maryland from 1954 to 1956 doing work in radio chemistry.

Since 1956, he has been employed at Air Force Cambridge Research Laboratory, currently Rome Air Development Center in Bedford, Massachusetts. He has been involved in diffusion studies, zone refining, and presently is Research Area Leader in the Electromagnetic Materials Technology Branch. He is working on epitaxial and bulk growth of III-V semiconductors for electro-optic applications. Mr. Kennedy has over 30 technical publications and 5 patents in electronic materials. He is a member of the American Association for Crystal Growth.

COLLECTIVE ION ACCELERATION AND INTENSE ELECTRON BEAM  
PROPAGATION WITHIN AN EVACUATED DIELECTRIC TUBE

BY

R. L. Gullickson, Capt USAF

Air Force Office of Scientific Research, Bolling AFB, DC 20332

R. K. Parker and J. A. Pasour

Naval Research Laboratory, Washington, DC 20375



Collective Ion Acceleration and Intense Electron Beam  
Propagation Within an Evacuated Dielectric Tube

Abstract

Collective ion acceleration is the acceleration of ions to high energy by the electric field generated by electrons in an intense beam. Collective ion acceleration can produce accelerating fields a hundred times higher than conventional accelerators, offering the promise of very compact accelerators. However, these high fields have only been demonstrated in the laboratory over distances of a few cm. The primary goal of collective ion acceleration research is to produce these high average fields over longer distances (meters) by control of the beam front velocity or beam plasma wave velocity. We report here the results of an experiment to evaluate a new collective ion acceleration method,<sup>17</sup> which offers the promise of a passive technique for beam front velocity control. An intense, relativistic electron beam (1.5 MV, 65kA) is injected into an evacuated dielectric tube inside a metal cylinder. When the beam current exceeds the space charge limiting current, propagation of the beam stops and most of the electrons are lost to the inside wall of the tube, liberating ions. These ions provide partial space charge neutralization, allowing the beam to propagate. Some of the ions are trapped by the potential well at the head of the beam and are accelerated to the beam front velocity. We performed these experiments primarily to see if this technique, which was first demonstrated in a low voltage (83kV) machine, scales on higher voltage accelerators. We demonstrated that this method does work at higher energies. Peak ion to electron energy ratio was about 10, with proton energies up to 15 Mev. Using nuclear activation techniques, about  $10^{14}$  protons with energies greater than the electron energy were measured. Both radially and axially accelerated ions were observed. We also investigated the electron beam transport properties of the dielectric guide. The dielectric guide has promise for transporting long pulse electron beams because currents in excess of the space charge limiting value can be propagated. We found that the propagation characteristics depend strongly on the cathode geometry and that propagated energy decreases linearly with tube length. The predicted increase of ion energy with tube length was not observed because only a small part of the current reached the end of the longer tubes in the most efficient ion acceleration geometry.

## Introduction to Collective Ion Acceleration

What is It? Collective ion acceleration (CIA) is the acceleration of ions by the space charge forces generated by a collection of electrons. The ions travel in the same direction as the electrons -- opposite to the applied voltage -- and have higher energy. Conventional accelerators -- for example, proton linear accelerators in which the ions are accelerated by being dragged along in phase with a radio-frequency (rf) wave -- are limited in their average accelerating field to values of about  $10^5$  V/cm. This limitation is determined by the rate at which rf energy can be supplied to the drift tube and by the maximum voltage which can be maintained between electrodes without electrical breakdown. Collective acceleration -- in which the high electric fields are maintained by clusters of electrons instead of electrodes -- has already demonstrated accelerating fields up to 100 times greater:  $10^7$  V/cm. Therefore, collective ion acceleration offers the promise of very compact accelerators. A one GeV ( $10^9$  eV) accelerator with these field strengths could be only one meter long. To date, collective ion acceleration research has been able to produce  $10^7$  V/cm over only a few cm. The goal of current research is to produce these high fields over distances of meters.

Applications of Collective Ion Acceleration. CIA has the potential benefits of high accelerating fields, high current capability, and the ability to accelerate both light and heavy ions. Although ion currents are high, the output consists of single short pulses in present devices. Future devices may produce high average currents by operating at high repetition rates. Some CIA methods (for example, plasma wave accelerators) could operate continuously in principle but are limited in practice by intense electron beam technology which currently can provide only short (submicrosecond) pulses.

Applications of CIA are listed in Table 1.

TABLE I. Applications of Collective Ion Acceleration

- 0 Advanced Concepts in Directed Energy Weapons
  - 0 Heavy Ion Acceleration for Inertial Confinement Fusion
  - 0 Production of Transuranic Elements
  - 0 Electronuclear Breeder for Power and Fissionable  
Material Production
  - 0 High Intensity Neutron Source
  - 0 Injector for Other Accelerators
- 

Intense Relativistic Electron Beams. Collective ion acceleration requires intense relativistic electron beams (IREB). Such beams are not merely collections of individual particles; they are dominated by collective effects. Typical parameters for IREB technology are electron energy from 1 to 10 MeV, current from a few to hundreds of kiloamperes, and pulse lengths less than 100 nanoseconds. For these high current beams propagating in vacuum the electrostatic repulsive forces are almost balanced by the magnetic pinching force. If a small number of ions are introduced, partial electrostatic neutralization can occur and the two forces may be balanced.

In the most common form of IREB technology, high voltage is generated by charging a series of capacitors in parallel and discharging them in series, the "Marx generator." The Marx generator charges a pulse forming line on a time scale of microseconds. The pulse forming line provides a pulse tens of nanoseconds long to a field emission diode where the electrons are generated. These electrons enter the experimental chamber through a thin foil window, or for experiments in vacuum, a foilless diode configuration may be used.

Collective Ion Acceleration in Gas Filled Drift Tubes.

CIA was first observed in this country when a relativistic electron beam was injected into a gas filled drift tube.<sup>1</sup>

In these experiments, Graybill and Uglum observed protons moving in the same direction as the electron beam and having a kinetic energy up to three times greater than the electrons. Heavy ions were also accelerated and had energies proportional to their charge state. Subsequent experiments increased the proton to electron energy ratio as high as 20.<sup>2</sup>

A number of theories to explain the accelerated ions were suggested,<sup>3</sup> but subsequent experiments supported those theories involving the formation of a space charge potential well at the front of the beam. As a relativistic electron beam enters an evacuated conducting tube, the beam blows up to the walls of the tube because of the electrostatic repulsive forces. Electrons remain in the vicinity of the anode forming a "virtual cathode." When the work done by an electron emerging from the anode on the electric field of the virtual cathode just equals the electron voltage, the beam stops. This is referred to as "space charge limited current flow," and its value depends upon the geometry of the drift tube and upon the electron energy. The space-charge limited current can be approximated by

$$I_1 = \frac{17.8}{1+2 \ln (R/r)} \quad (\text{for } I \text{ in kiloamps})$$

This is the simplest form of the expression and assumes that  $\gamma \gg 1$  and an infinitely long tube.  $R$  is the radius of the cylindrical vacuum chamber,  $r_b$  is the beam radius, and  $\gamma$  is the relativistic electron energy factor

$$\gamma = 1/(1-v^2/c^2)^{1/2} = 1 + E(\text{MeV}) / .511$$

Current flow is limited to this maximum value until ions from the background gas or tube walls can neutralize the beam.

Olson proposed<sup>4</sup> that a deep potential well forms at the beam front; the depth of the well can be two to three times the electron voltage leaving the anode. No acceleration can occur unless the injected current exceeds the limiting current, the condition for the formation of the deep well. The acceleration depends upon the pressure of the gas in the tube because it affects the ionization time. Acceleration can occur in the deep well phase (and gives an ion energy two to three times the electron energy) or in the propagation of the beam front phase (ion energy greater than three times the electron energy).

Miller and Straw verified the predictions of the Olson theory by carefully varying the injected current just above

and below the limiting current by modifying the drift tube geometry.<sup>5</sup> Acceleration was only observed when  $I > I_1$ .

CIA With Plasma Waves. A second category of linear collective ion acceleration methods is the plasma wave accelerator. In this method, the density of an electron beam propagating in vacuum with an external magnetic field is modulated with a plasma wave. Ions are trapped in the troughs of the wave at low phase velocity; then the phase velocity of the wave is increased, accelerating the ions to high energy. The key feature of these schemes is that the phase velocity must be controllable over a wide range by modifying one of the experimental parameters. There are two types of plasma waves: the cyclotron wave and the space charge wave. The phase velocity of the cyclotron wave is controlled by changing the magnetic field (the "autoresonant accelerator"<sup>6</sup> is an example of this). The phase velocity of the space charge wave is varied by changing the electron density through variations of the current. Plasma wave accelerators are potentially the most promising of the various CIA schemes because they offer the possibility of continuous acceleration throughout the electron beam pulse; not just at the beam front. However, no one has yet been able to accelerate any ions by this method.

Vacuum Diode and Drift Tube Experiments. The third major type of linear collective ion acceleration geometry is the vacuum diode (also called the "Luce diode") geometry. In this geometry, a pointed cathode is used with a dielectric anode with a hole in it. Ions for neutralization and acceleration are generated from the anode by electron impact. This geometry has the distinction of having produced the best performance of any CIA method: ion to electron energy ratio greater than 22, heavy ions accelerated to more than 6 MeV per nucleon (80 MeV  $^{12}\text{C}$  ions),<sup>7</sup> and proton energies up to 50 MeV.<sup>8</sup> The mechanism for CIA in the vacuum diode geometry has not been conclusively determined. Both the net spacecharge theory<sup>9</sup> and a plasma wave mechanism<sup>10</sup> have been suggested to account for ion acceleration in this geometry.

Control of Beam Front or Wave Velocity. The key issue in all of these schemes is the control of the velocity of the moving electron beam front or plasma wave. For gas filled drift tubes, 5 MeV ions have already been produced by transversely sweeping a laser ionization wave in cesium gas.<sup>11</sup> Plasma wave accelerators using varying magnetic fields<sup>12</sup> or varying the ratio of current to limiting current<sup>13</sup> for phase velocity control are now being tested. In the vacuum diode

geometry, the controlled breakdown of a helical slow wave structure has been used to increase proton energies from 5 MeV without the helix to 8 MeV with it.<sup>9</sup>

Table 2 compares the best experimental results in each of these three acceleration methods with those from the evacuated dielectric tube experiments described in the next section.

TABLE 2. Comparison of Collective Ion Acceleration Experiments

| Geometry              | Velocity Control          | Lab     | $E_p/E_e$ | $E_{pmax}$ | $N_p$              | Referer |
|-----------------------|---------------------------|---------|-----------|------------|--------------------|---------|
| Gas Filled Drift Tube | Laser Ionization Wave     | PI      | 20        | 14 MeV     | $2 \times 10^{12}$ | 2,11    |
| Plasma Wave           | Magnetic Field<br>Current | ARA     | *         | *          | *                  | 12      |
|                       |                           | Cornell | *         | *          | *                  | 13      |
| Vacuum Diode          | Helix Slow Wave Structure | LLL     | 22        | 45         | $10^{14}$          | 7,9     |
| Dielectric Tube       | Ribbed Tube               | NRL     | 10        | 15         | $10^{14}$          | 14      |
|                       |                           | SPIRE   | 6         | 0.5        | $2 \times 10^{11}$ | 15      |
|                       |                           | LPI     | 5         | 3          | $10^{11}$          | 16      |

This table compares the best experimental values for each geometry. The velocity control column lists the most promising method of controlling beams front or phase velocity for this geometry; however, this method was not necessarily used to obtain the experimental results listed in the other columns. The lab names correspond to the experimental results -- not necessarily to the method of velocity control.  $E_p/E_e$  is the maximum proton energy divided by the electron energy.  $N_p$  is the total number of protons with energy greater than the electron energy. For the full name of the labs and for more detail on the experiments, consult the references. An \* means that no experimental results are available for this geometry.

## Dielectric Tube Experiment

### Discussion of the Concept

An alternative approach to collective ion acceleration has been proposed<sup>17</sup> which offers the advantage of having a simple method of beam front velocity control. When a relativistic electron beam is injected into an evacuated dielectric (typically acrylic plastic) tube with the beam current in excess of the space charge limiting current, the beam is stopped by the formation of a virtual cathode. (A concentration of electrons on the other side of the anode foil which acts like a second cathode.) The beam then blows out radially, striking the dielectric wall and liberating ions. These ions provide sufficient charge neutralization for the beam to propagate a bit further, so that the potential well at the beam front travels down the guide at a velocity determined by the rate of ion release from the walls. Some of these ions are trapped in the potential well and carried along with the electron beam.

The goal of collective ion acceleration experiments in many different geometries is to control the velocity of the beam front or of a beam plasma wave so as to produce very high accelerating fields over long distances (meters). In the dielectric tube geometry, the velocity of propagation depends on the charge deposited per unit area.<sup>17</sup> Therefore the beam front velocity is linearly proportional to the current and inversely proportional to the tube area. A linearly increasing current pulse can provide a constant acceleration, resulting in increasing ion energy with tube length. Thus the dielectric tube geometry offers the promise of a passive method for controlling the beam front velocity without the complexity associated with externally swept ionization methods.

The dielectric tube also provides enhanced electron beam propagation over conducting metal tubes. Currents in excess of the space charge limited current can be propagated without the use of an external magnetic field. These transport properties are desirable for a variety of applications including the transport of electron beams to the converter in radiation generators for nuclear weapons effects simulation and for the transport of electron beams to the target chamber in inertial confinement fusion.

Experiments at Other Labs. Two other groups have reported experimental results on CIA with dielectric tubes: SPIRE Corporation<sup>15</sup> and the Lebedev Physical Institute in



Moscow.<sup>16</sup> SPIRE initiated this concept and performed the first experiments on a low energy electron accelerator (83 kV peak diode voltage, 9 kA peak electron current, 0.3 kJ beam energy). The key results of their experiments were (1) average accelerating fields greater than  $10^6$  V/cm, (2) peak ion to electron energy ratio greater than six, (3) the beam front velocity could be controlled with guide geometry, (4) a threshold current density had to be exceeded before ion acceleration was observed, (5) ion energy increases with beam current, and (6) ion energy increases with tube length.

The Lebedev experiments were conducted with a moderate energy electron accelerator (660 kV peak diode voltage, 11 kA peak electron current, 1 kJ beam energy). The most important Lebedev results were (1) peak ion to electron energy ratio greater than five, (2) beam front velocity did not depend on the diameter of the guide, (3) proton energy corresponds to the velocity of the beam front, and (4) the proton energy did not increase with guide length.

The results reported in this paper are compared with the SPIRE and Lebedev results and with other CIA experiments in Table 2.

Goals of this Experiment. The main purpose of this experiment was to verify that the preliminary results obtained on the low voltage accelerator<sup>17</sup> scaled to higher energies when performed on a high voltage, high current electron beam machine. This goal, and others, can be summarized as follows:

- (1) energy scaling: does it work on a big machine?
- (2) length scaling: does the proton energy increase with tube length?
- (3) can the velocity of the beam front be controlled?
- (4) how are the propagation characteristics affected by the increased voltage and current?

#### Experimental Technique

The experimental configuration for the ion acceleration work, which was performed on NRL's VEBA facility,<sup>18</sup> is shown in Fig. 1. The beam was emitted from a pulsed cathode (A) and was injected into Lucite tubes (C) of various diameters (5 to 9 cm ID) and lengths (15 to 90 cm), each with a 6 mm wall thickness. Experiments were performed both with and without an anode foil (B). Attached to the 11-cm-diameter

stainless steel outer cylinder (D) was a Faraday cup (F), whose 12-mm-thick graphite current collector (E) was located  $\sim 1$  cm beyond the end of the Lucite tube. The diode voltage was monitored with a capacitive divider and the diode current was deduced from a B loop. Typically, the peak diode voltage was  $\sim 1.5$  MV and the diode current  $\sim 65$  kA. The pulse width (FWHM) was  $\sim 60$  nsec.

Electron beam propagation was studied using the Faraday cup calorimeter. The current striking the graphite collector was deduced from the voltage across a low-inductance,  $2.3\text{-m}\Omega$  shunt connecting the collector to ground. A thermocouple connected to the collector was used with a digital voltmeter to measure the total energy delivered to the calorimeter.

Two types of nuclear diagnostics were used to determine the number and energy of accelerated protons (and deuterons on a few shots). A rhodium activation detector,<sup>19</sup> located  $\sim 35$  cm above a target attached to the front of the Faraday cup, was used to measure neutron yields from p,n and d,n reactions which resulted from bombardment of both the target and the Lucite tube. The most detailed information was obtained by measuring the activation induced in the target.<sup>20</sup> To accurately determine the number of accelerated protons using this method, the proton energy and the interaction cross section at that energy must be known. Discrimination of ion energies was achieved in two ways: (1) by the use of targets with different reaction thresholds, and (2) by using stacked foil targets and relating the depth of activation to ion energy through range-energy relations. Following a shot, the target was removed from the vacuum chamber and counted using a 3" x 3" sodium iodide detector and a 512-channel pulse height analyzer.

### Electron Beam Transport

Studies of electron beam propagation in the dielectric guide were performed to check the validity of the model discussed above. First, the variation of transported current with an external, axial magnetic field was determined using a 4.1-cm-diam cathode and a 7.6-cm-diam x 45-cm-long Lucite tube. The results are shown in Fig. 2. With no magnetic field, the transported current rises rapidly to  $\sim 80\%$  of the injected current. There is a delay of  $\sim 10$  nsec relative to the diode current during which time the beam front electrons are lost to the wall, and consequently the transported current pulse is shortened. As the magnetic field is increased, there is a longer delay before the peak current is transported until, at a field of  $\sim 4$  kG, current in

excess of the space-charge limit cannot propagate. This result demonstrates that when electrons are prevented from striking the wall and liberating ions to neutralize the remainder of the beam, transport is hindered. With sufficient neutralization, however, most of the injected current can propagate.

Energy transport as a function of guide length was measured with the calorimeter using 6.4-cm-diam guides of various lengths and three cathode diameters. The results plotted in Fig. 3 show that the transported energy decreases almost linearly with guide length and that best transport is obtained with the largest diameter cathode. The energy determined by integrating the product of the Faraday cup current and diode voltage waveforms agrees to within  $\sim 10\%$  of the calorimetric value, indicating that most of the transported electrons have essentially their injected kinetic energy. Since the peak current delivered is generally of the same order as the diode current but with a decreased duration, most of the energy loss evidently results from beam-front erosion. Thus, propagation over longer distances might be possible with a longer diode pulse duration.

A measure of the beam-front velocity was obtained by noting the electrons' arrival time at the Faraday cup with different guide lengths. Results obtained with the 4.1-cm-diam cathode and 7.6-cm-diam guide are plotted in Fig. 4. These results imply a nearly constant beam-front velocity of  $\sim 2 \times 10^9$  cm/sec over the first 50 cm from the diode. Although protons traveling with this velocity would have an energy of only  $\sim 2.1$  MeV, it is doubtful that much trapping could occur with such a high initial beam front velocity. With smaller diameter cathodes, the arrival time of the electrons varied a great deal from shot to shot, so that no meaningful beam-front velocity could be deduced.

Finally, a ribbed guide was fabricated with 5-mm-wide grooves cut azimuthally at 1-cm intervals in the inner wall of a 6.4-cm-diam, 15-cm-long Lucite tube. The arrival time of the beam at the Faraday cup was delayed by 20 nsec compared to the smooth tube, presumably because the increased dielectric surface area impeded the release of ions from the wall.

Ion Acceleration. Thick graphite and copper targets were used to study ion acceleration, and from the reaction thresholds (3.2 MeV for  $^{13}\text{C}(\text{p},\text{n})$   $^{13}\text{N}$  and 4.2 MeV for  $^{63}\text{Cu}(\text{p},\text{n})$   $^{63}\text{Zn}$ ) a minimum proton energy was determined. As might

be expected from the preceding discussion, no significant acceleration of protons to energies in excess of 3.2 MeV was observed with the 4.1-cm-diam cathode, nor with cathodes of 5.7 and 6.7 cm diam. However, use of smaller diameter cathodes (12.7 mm and 3.2 mm diam) did produce significant acceleration. Best results were obtained using the configuration shown in Fig. 1b with a 6.4-cm-diam, 15-cm-long guide. Evidently the larger injection current densities obtained with the smaller cathodes together with their lower limiting currents produced more favorable proton trapping and potential well formation. Unfortunately, the low beam transport obtained with the small cathode (Fig. 3) prevented a study of scaling with guide length.

Stacked foil targets, consisting of 50-cm-thick Cu and 25- $\mu$ m-thick Ti foils were used with both smooth and ribbed guides in the optimum acceleration configuration to provide proton energy spectra. Accelerated proton yields were generally smaller with the ribbed guide, probably because of impeded ion liberation and the low beam-front velocity. Typical histograms are shown in Fig. 5. Each energy interval corresponds to a single foil, and the ordinate represents the number of protons in each interval divided by the width of that interval. The highest energy obtained on a given shot falls somewhere inside the energy range corresponding to the deepest activated foil in the stack.

Generally, it was possible to fit the data with an exponential of the form  $I_p(E) = I_0 \exp(-aE)$ , with  $a = 1.0 \pm 0.1 \text{ MeV}^{-1}$ . On several shots, there was an additional component to the spectrum, as is evident in the high-energy tail of Fig. 5a. One possible explanation for this behavior is that the lower-energy component (with a peak  $\sim 3$  times the electron energy) is associated with the break-up of the potential well as the virtual cathode is neutralized by ions from the guide wall.<sup>22</sup> The high-energy component might be comprised of ions that are actually trapped and pulled along for some distance by the propagating beam front.

To increase above background the level of any activation arising from higher-energy protons, a series of seven shots was taken in rapid succession using a target stack consisting of a 1.3-mm-thick carbon foil backed by a series of 50- $\mu$ m-thick copper foils. Activity was detected on the first copper foil, indicating protons of energy between 14.4 and 15.3 MeV. The highest peak electron energy on any of the seven shots was 1.6 MeV, so that an ion to electron energy ratio of at least 9 was achieved.

By comparing the results of the neutron activation detector with the target activation, we observed that more protons were accelerated into the guide wall than onto the target. While the maximum number of protons with energy above 3.8 MeV reaching the target on any shot was  $\sim 10^{13}$ , a total yield of  $10^{14}$  protons with energy above 3.2 MeV was inferred from the rhodium activation detector (assuming all neutrons were produced from p,n reactions and the thick target yield for the  $^{13}\text{C}(p,n)^{13}\text{N}$  reaction in Lucite was the same as in graphite).

To study the spatial distribution of ion release and acceleration, 75- $\mu\text{m}$ -thick mylar strips were coated with a 0.3 mg/cm<sup>2</sup> layer of CD<sub>2</sub> and used to line the Lucite tubes. Since the cross-section for d,n reactions on carbon is much larger than that for p,n reactions, it should be possible to determine where most of the accelerated ions originate and where they strike the wall. Although there was some shot-to-shot variation, most of the accelerated ions came from the first half of the drift tube. A segmented mylar liner, which was placed in the downstream portion of the drift tube as shown in Fig. 6, was used to determine the distribution of ions accelerated into the wall. Inspection of the histograms shows both an axial and azimuthal variation. More activity was produced in the center band than in either the upstream or downstream band, and section #7 had more than 7 times the activity of the nearby #13. These results indicate that the electron beam and ion acceleration mechanism do not manifest either axial uniformity or azimuthal symmetry.

### Conclusions

The major goal of these experiments -- to demonstrate that this mechanism can accelerate ions to many times the electron energy with a high current, high voltage accelerator -- was realized. Ion acceleration depended strongly upon diode geometry and both radial and axial acceleration of ions were observed. For the transport configuration with the planar diode, the propagated current decreased linearly with tube length. Because the optimum geometry for ion acceleration differed from that for propagation, increased ion energy with tube length was not observed because of poor current transport efficiency for the longer tubes.

It is evident from these results that the experimental parameters were not optimized. Since the primary energy loss mechanism was beam-front erosion, the dielectric guide may provide an efficient means for transporting electron beams of

longer duration. Ion acceleration might be improved by appropriately tailoring the guide and the injected current pulse shape (e.g., a triangular pulse with a relatively long rise time could allow scaling of ion energy with guide length).

#### Acknowledgments

The authors thank A. Greenwald for his many discussions and suggestions during the course of this work. W. Doggett, D. Pershing, and D. Price participated both in taking the data and analyzing the results. We appreciate the assistance of F. Young in providing and setting up the nuclear diagnostics. The authors of this paper are listed on the title page in alphabetical order.

### References

1. S. E. Graybill and J. R. Uglum, J. Appl. Phys. 41, 236 (1970).
2. B. Ecker, S. Putnam, "Collective Ion Acceleration and Power Balance in Intense Electron Beams in Neutral Gas," Physics International Report PIIR-8-76, November, 1976.
3. C. L. Olson, Physics of Fluids 18, 585 (1975).
4. C. L. Olson, "Collective Ion Acceleration with Intense Electron Beams," IEEE Trans. on Nucl. Sci. NS-22, June, 1975.
5. R. B. Miller and D. C. Straw, J. Appl. Phys. 47, 1897 (1976).
6. M. L. Sloan, W. E. Drummond, Phys. Rev. Lett. 20, 1234 (1973).
7. J. S. Luce, Ann. N. Y. Acad. Sci. 251, 217 (1975).
8. R. F. Hoeberling, "Collective Ion Acceleration on the PR 1590," Proc. of the 3rd International Conference on Collective Methods of Acceleration (Laguna Beach Conference), May, 1978.
9. W. W. Destler, H. Kim, G. Zorn, R. F. Hoeberling, "Helix Controlled Collective Ion Acceleration," Proc. of Laguna Beach Conf.
10. O. Zucker, J. Wyatt, H. Sahlin, J. S. Luce, B. Freeman, and R. Gullickson, "Collective Field Acceleration by the Interaction of a Relativistic E Beam with an Apertured Solid Dielectric Anode," Proc. of Laguna Beach Conf.
11. C. L. Olson, "Experiments and Scaling of the IFA," Proc. of the Laguna Beach Conf.
12. J. R. Uglum, H. A. Davis, D. E. Hasti, and T. P. Starke, "The Auto-Resonant Accelerator Experimental Program," Laguna Beach Conf.
13. R. Adler, G. Gammel, J. A. Nation, G. Providakes, and R. Williams, "Propagation and Control of Slow Space Charge Waves on Electron Beams," Laguna Beach Conf.

14. J. Pasour, R. K. Parker, R. L. Gullickson, W. O. Doggett, D. Pershing, "Collective Ion Acceleration and Intense Electron Beam Propagation Within an Evacuated Dielectric Guide," Laguna Beach Conf.
15. A. Greenwald, "Dielectric Guide Controlled Collective Ion Acceleration," Laguna Beach Conf.
16. A. V. Agaronov, A. A. Kolomensky, E. G. Nrastelev, A. M. Lebedev, and B. N. Yablokov, "REB Propagation in Vacuum Dielectric Channels Accompanied by Ion Acceleration," Laguna Beach Conf.
17. A. Greenwald, R. Lowell, R. Little, Bull. Am. Phys. Soc. 21, 1147 (1976).
18. R. K. Parker and M. Ury, IEEE Trans. NS-22, 983 (1975).
19. F. C. Young, IEEE Trans. NS-22, 718 (1975).
20. F. C. Young, J. Golden, and C. A. Kapetanacos, Rev. Sci. Instrum. 48, 432 (1977).
21. R. B. Miller and D. C. Straw, AFWL-TR-75-236 Air Force Weapons Lab., April, 1976.
22. R. B. Miller, private communication.



### Figure Captions

1. Experimental configuration: A, cathode; B, anode foil; C, dielectric guide; D, outer conductor; E, graphite current collector; F, Faraday cup. (a) propagation configuration. (b) acceleration configuration.
2. Variation of electron beam transport with axial magnetic field. The space-charge limited current is shown in dashed lines for the  $B = 4$  kG case.
3. Electron beam energy transport vs guide length and cathode diameter.
4. Electron beam front propagation time vs guide length.
5. Proton energy spectra from stacked foil targets with (a) a smooth guide and (b) a ribbed guide.
6. Segmented liner geometry and relative activity induced in each segment showing radial proton acceleration.

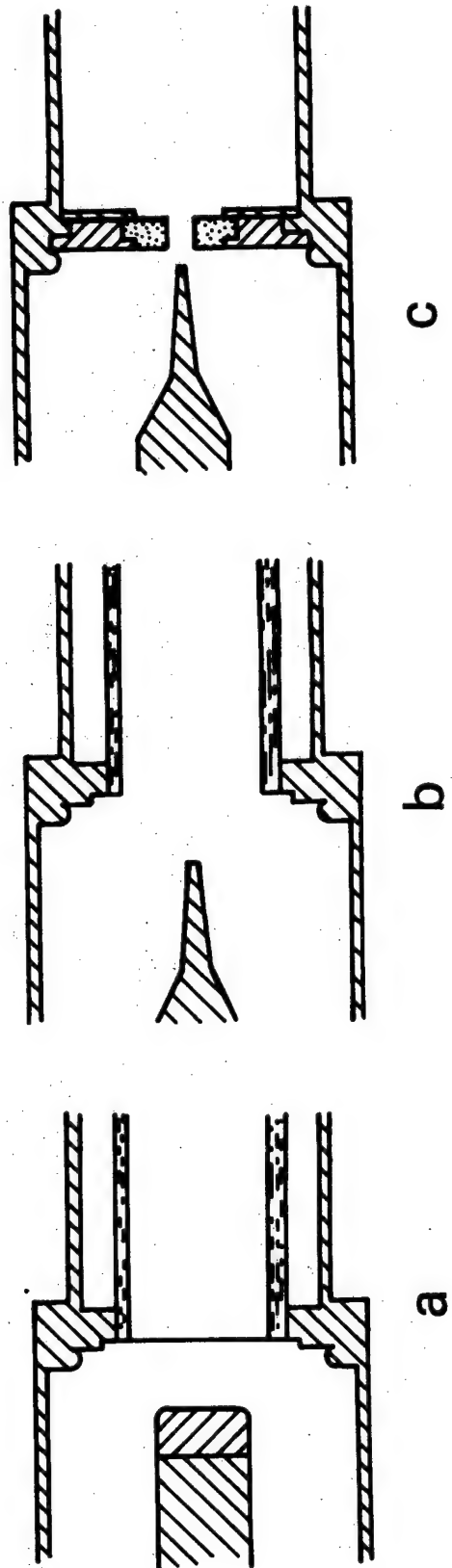
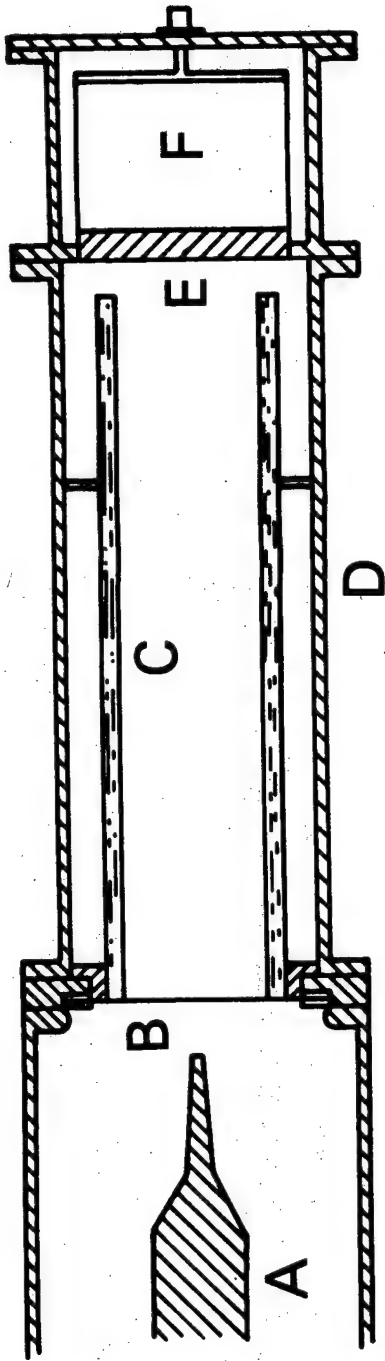


Figure 1

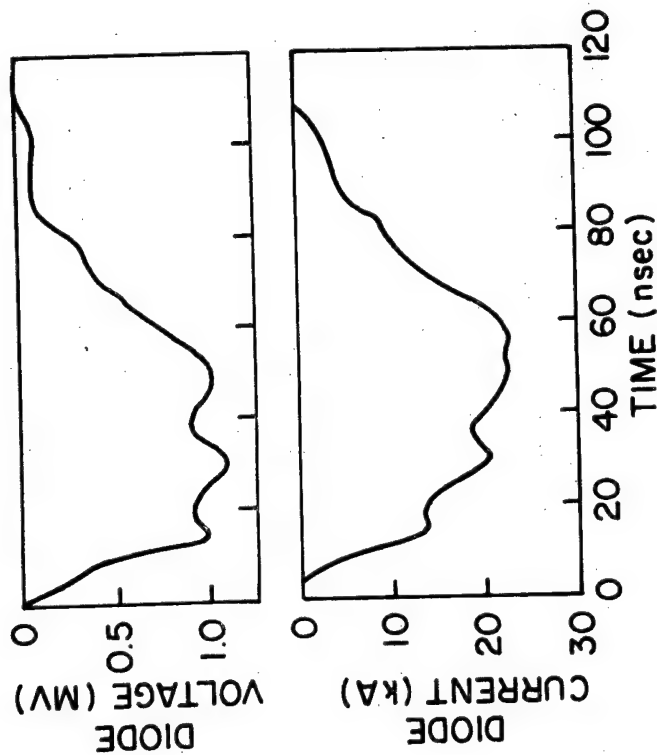
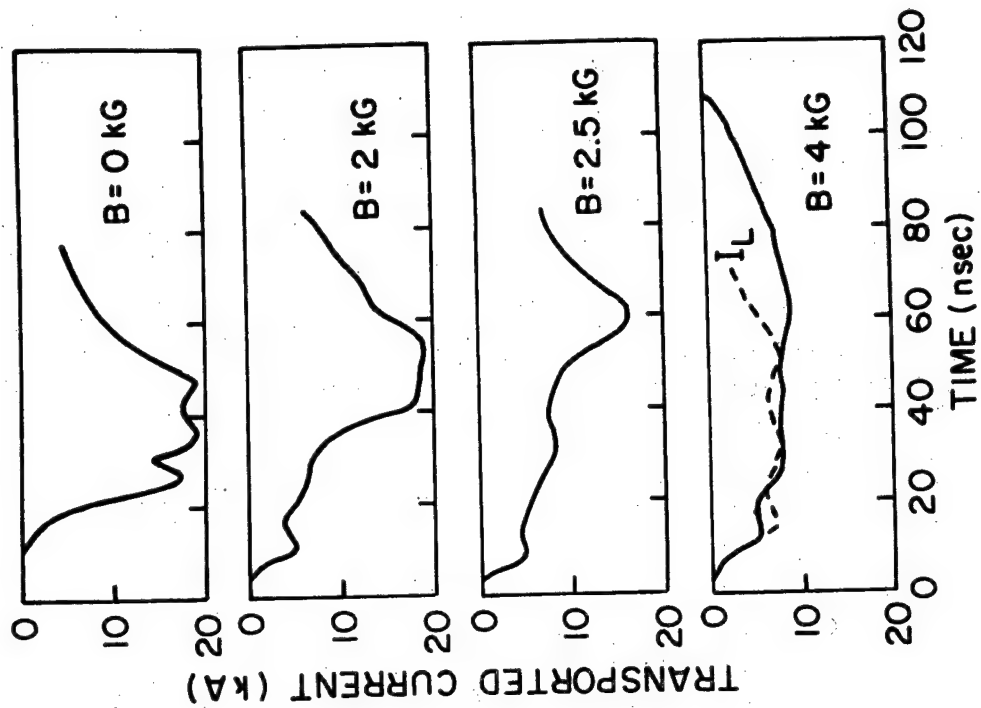


Figure 2

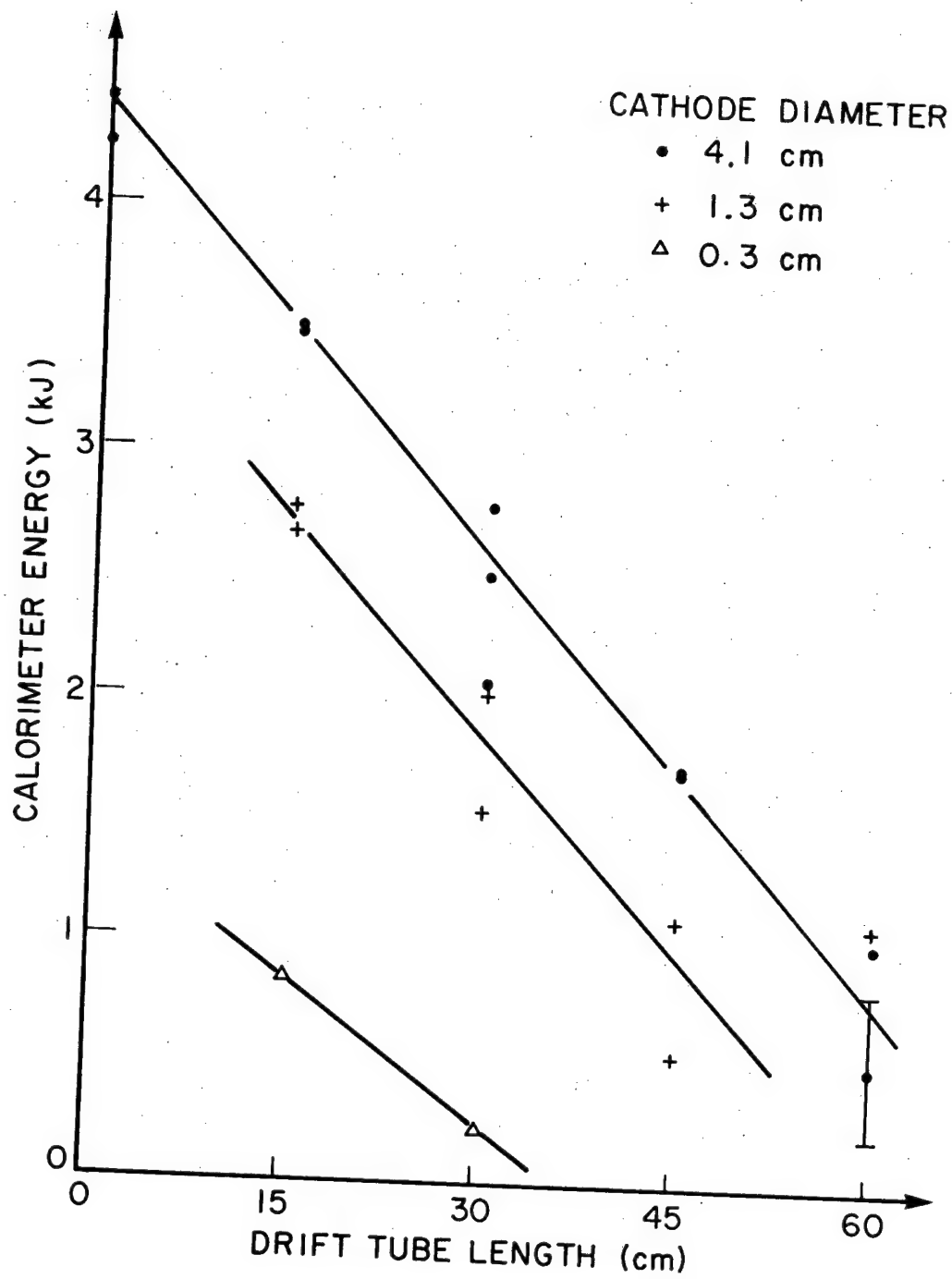


Figure 3

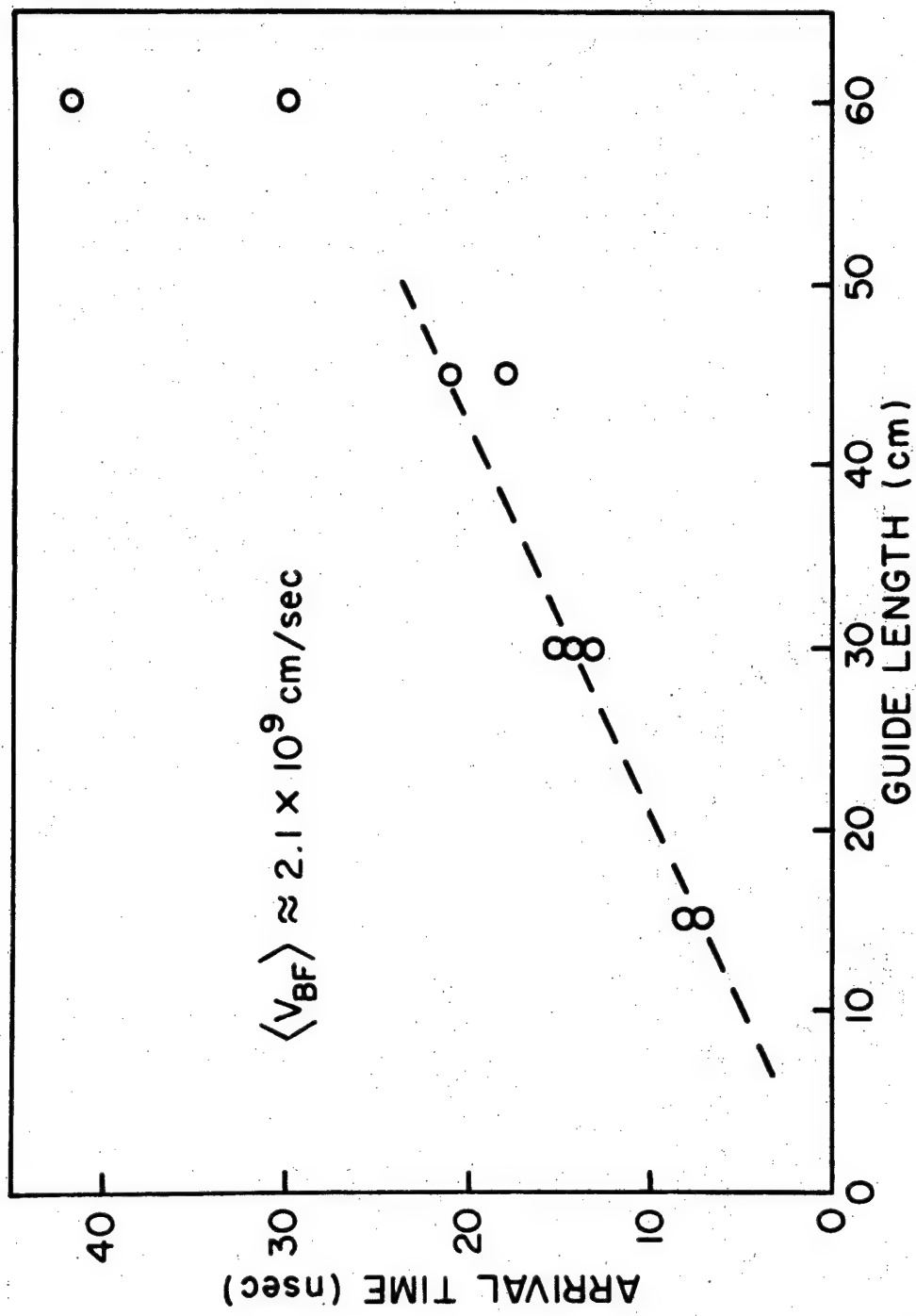


Figure 4

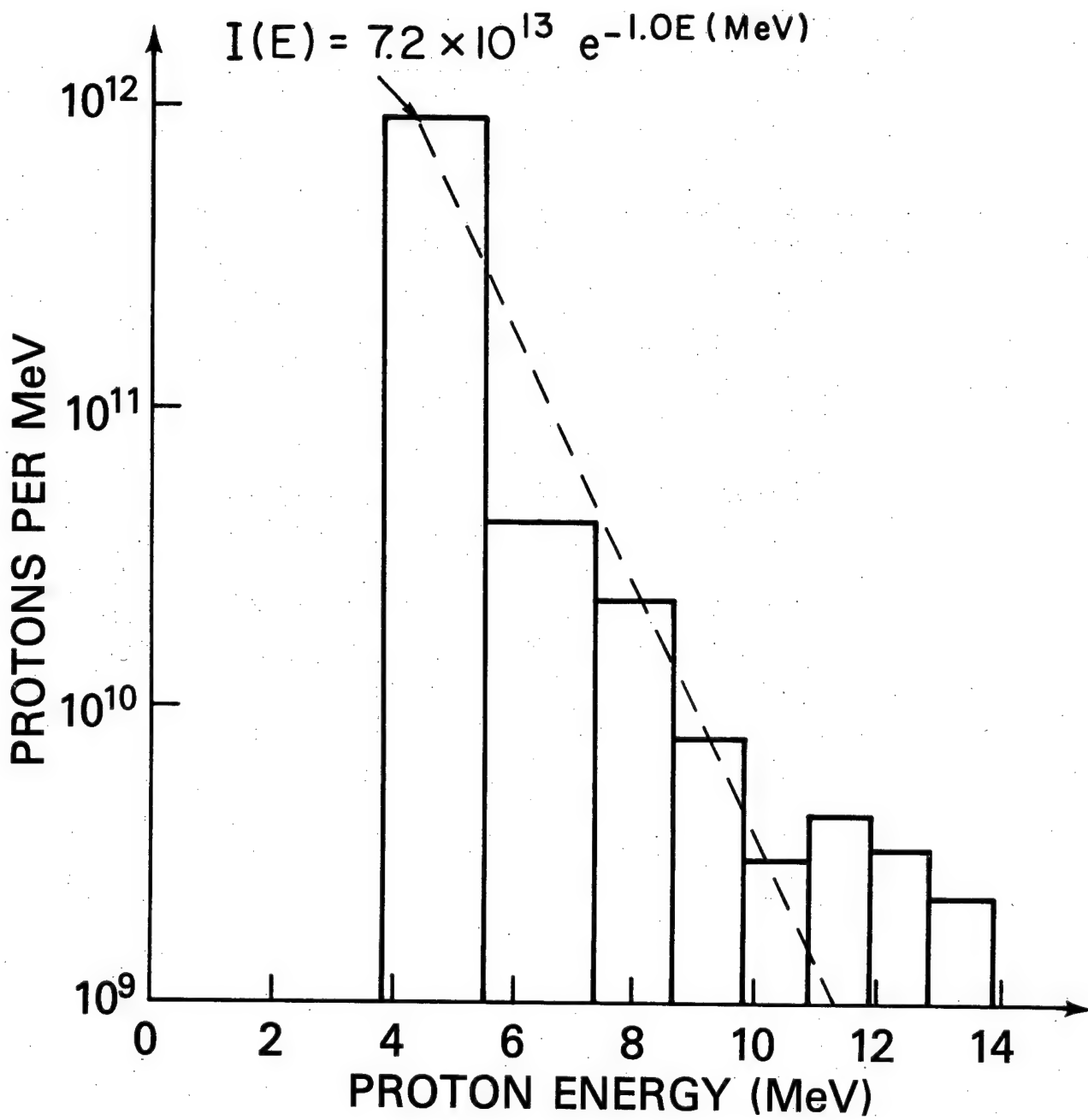
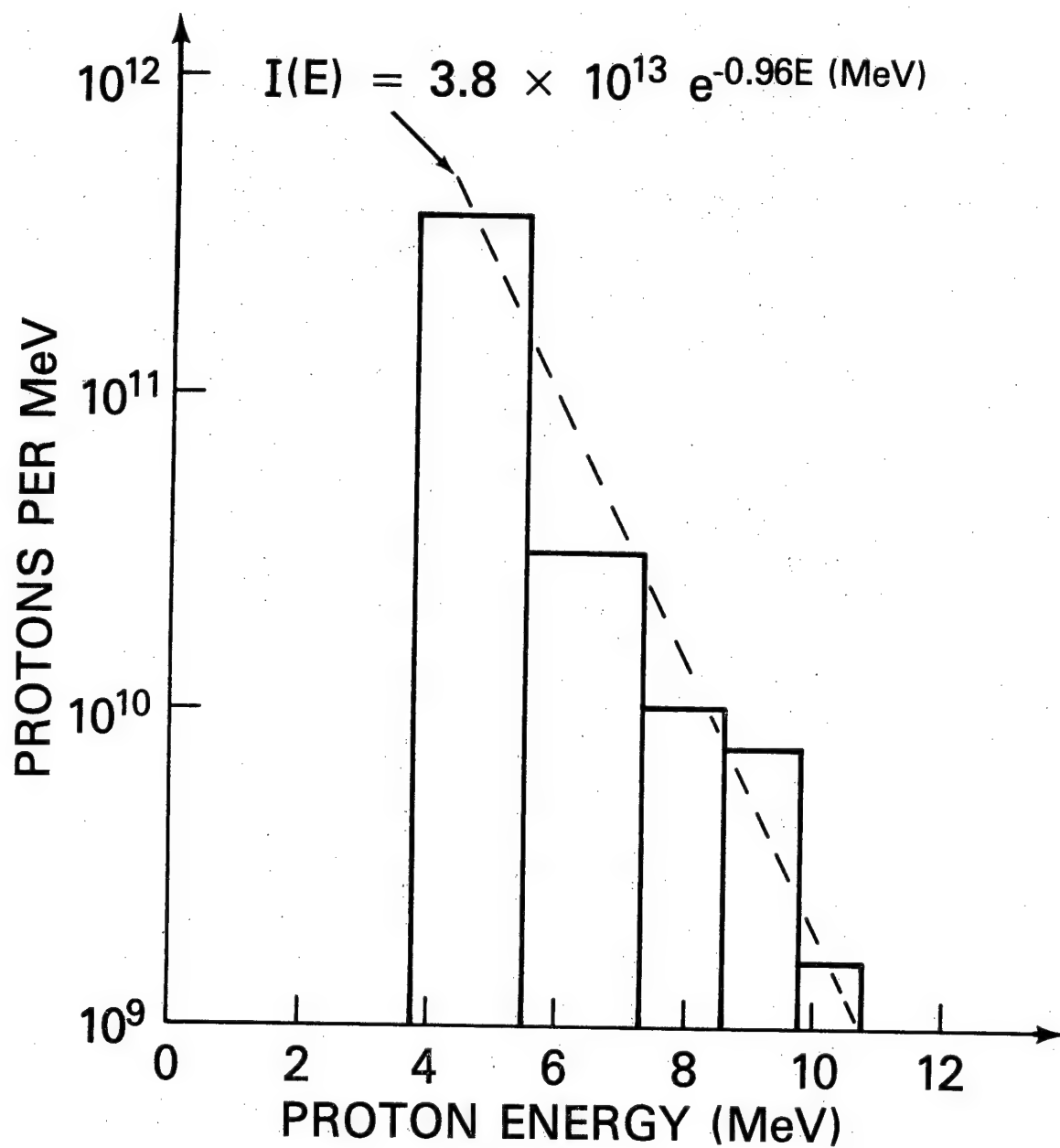
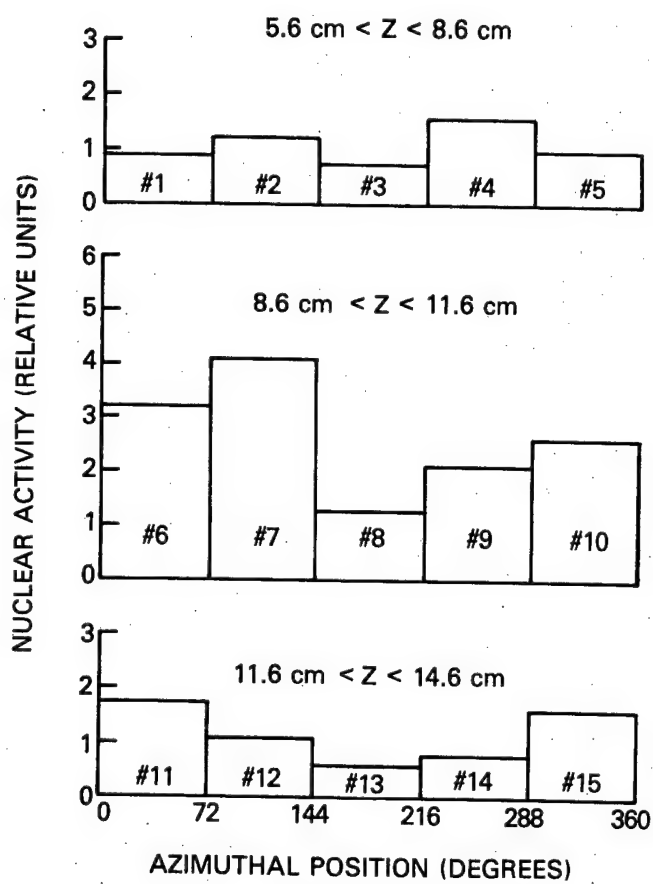
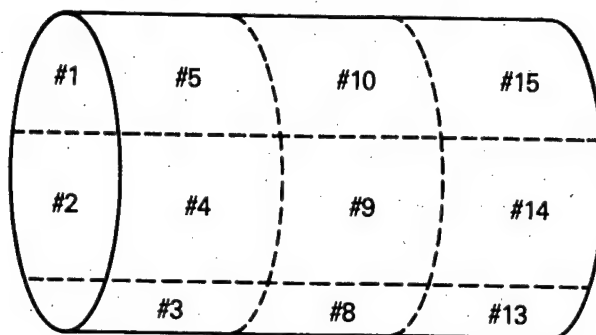


Figure 5a



## SEGMENTED LINER GEOMETRY





## Biographical Sketches

### R. L. Gullickson

Capt Gullickson received his B. S. degree in physics from the University of Michigan in 1965 and was commissioned in the Air Force following an AFROTC program. He was granted a delay from active duty to pursue graduate studies at Michigan and received his M. S. E. in Nuclear Engineering in 1968.

In 1967 he began his active duty at the Air Force Weapons Laboratory, where he worked on plasma radiation sources for nuclear weapons effects simulation. In 1972 he was assigned to the Lawrence Livermore Lab as a Military Research Associate in the Theoretical Physics Division doing experiments on collective ion acceleration and on the plasma focus device. Capt Gullickson continued his graduate studies at Livermore on a part-time basis at the Department of Applied Science, University of California, Davis/Livermore.

Since 1975, Capt Gullickson has been a Program Manager for Particle Beam and Plasma Physics Research in the Physics Directorate, Air Force Office of Scientific Research. Since coming to AFOSR, he has continued his research activities by consulting at the Lawrence Livermore Lab and Naval Research Lab. Capt Gullickson is a registered Professional Nuclear Engineer, is a member of the Plasma Division of the American Physical Society, and has been involved in the organization of a number of technical meetings.

### John A. Pasour

John A. Pasour was born in Gastonia, North Carolina on July 25, 1950. He graduated as valedictorian of his class from North Carolina State University in 1972, receiving a B. S. degree in physics. In that same year, he entered graduate school at North Carolina State University under a Phi Kappa Phi fellowship. While a graduate student, he held summer positions at the Los Alamos Scientific Laboratories and the Naval Research Laboratory.

Pasour performed his dissertation research at the Naval Research Laboratory with funding from the Air Force Office of Scientific Research. This work involved the reflection of microwaves from relativistic electron beams to produce short bursts of high power millimeter waves. After receiving

his Ph.D in physics in 1977, Pasour accepted a National Research Council Associateship in the Naval Research Laboratory's Ion Ring Program. In addition to papers on microwave scattering and ion rings, he has published papers dealing with collective ion acceleration, intense proton beam generation, proton-beam-pumped lasers, and diagnostics for high-power, pulsed proton beams and millimeter waves. Pasour received an IEEE Nuclear and Plasma Sciences Graduate Student Award (1977) and a Naval Research Laboratory Publication Award (1978). He is a member of the American Physical Society and a Fellow of Phi Kappa Phi.

Robert K. Parker

Robert K. Parker graduated from Allegheny College, Meadville, PA, with a B. S. in physics in 1964. He went on active duty as a 2LT in the Air Force at this time and was assigned to the Air Force Institute of Technology, Wright-Patterson AFB, Ohio. He received his M. S. degree in space physics there in 1966. He then was assigned to the Air Force Weapons Lab, Kirtland AFB, New Mexico where he conducted research on radiation sources for nuclear weapons effects simulation. In 1970 Capt Parker received a scholarship from the University of New Mexico to work on a doctorate in nuclear engineering. He conducted his thesis research at AFWL and completed his dissertation research on "Explosive Emission and the Characteristics of High-Current Electron Flow," in 1971. Dr. Parker was then assigned to the Defense Nuclear Agency, Alexandria, Virginia where he served as a program manager in the Atmospheric Effects Division until 1972. He left the Air Force in 1972 to accept a civilian position at the Naval Research Lab in the Electron Beam Applications Branch of the Plasma Physics Division. Since that time, Dr. Parker has worked in the area of pulsed power technology development for relativistic electron beam machines. He now directs an experimental program on the generation of high power microwave and submillimeter wave radiation with relativistic electron beams. Dr. Parker is a member of the Plasma Physics Division of the American Physical Society, Tau Beta Pi Engineering Honorary Society, and has been the recipient of several NRL Publication Awards. As a major in the Air Force Reserves, he is the director of a reserve group which evaluates technology in the field of intense particle beams.

HIGH SPATIAL RESOLUTION OPTICAL OBSERVATIONS  
THROUGH THE EARTH'S ATMOSPHERE

BY

Simon P. Worden, Captain, USAF

Space Physics Division

Air Force Geophysics Laboratory  
Hanscom AFB, Massachusetts

# High Spatial Resolution Optical Observations Through The Earth's Atmosphere

## Abstract

Turbulence in the Earth's atmosphere degrades telescope images to about one arc-second angular resolution. For a 4-meter diameter telescope this degradation is a factor of thirty worse than the instrument's theoretical resolution of .03 arc-second. The technique known as speckle interferometry entails taking very short exposures of objects through a large telescope. If these exposures are short enough to "freeze" the turbulence, about .01 sec., then a telescope behaves as a multiple aperture interferometer. From such a device, information can be extracted down to the theoretical resolution limit. We have developed both computer processing methods and instrumentation to implement speckle interferometry on several telescopes. For bright objects, like the solar surface, we can reconstruct images with .1-.2 arc-second resolution. For faint objects, like high altitude satellites, we use a television camera and computer to identify individual photon locations within an image. From these data we can then derive size and shape information about the object. We are now using these methods and instruments to study several problems. These include assessing the applicability of speckle interferometry for satellite surveillance, and studying the fine scale solar magnetic structure. We have also begun a program to adapt new multiple-mirror ground-based telescopes for speckle interferometry. With large instruments of the kind now being designed, it may be possible to achieve the full angular resolving capability of a 25 meter diameter telescope. The resulting resolution of .005 arc-second would correspond to better than 1 meter resolution at synchronous satellite altitudes.

## Introduction

Telescope images have a theoretical angular resolution limit (diffraction limit) which is inversely proportional to the diameter of the main light-collecting mirror or lens. For existing large telescopes, which are about 5 meters in diameter, this limit is .02 arc-second. However, turbulence within the Earth's atmosphere severely degrades resolution on objects such as satellites observed through the atmosphere. This degradation is visible to the naked eye; e.g. in the twinkling of stars and is known as "seeing". Seeing degrades telescope images to about 1 arc-second angular resolution, the resolution limit of a small 10 cm telescope. No matter how large the telescope, images are never any better than a 10 cm instrument could obtain. In Table 1 I have listed the effects of this seeing limit on angular resolutions for satellites along with the resolution possible without seeing. Clearly, effective surveillance of high altitude and synchronous objects is impossible unless seeing effects are eliminated.

Table 1

### Large Telescope Resolution Capabilities

| Orbital<br>Altitude (km) | Atmospheric<br>Limit<br>1 arc-sec | 4 Meter Limit<br>.028 arc-sec | 25 Meter Limit<br>.004 arc-sec |
|--------------------------|-----------------------------------|-------------------------------|--------------------------------|
| 150                      | 72 cm                             | 2 cm                          | 0.2 cm                         |
| 1000                     | 5 m                               | 13 cm                         | 2 cm                           |
| 10000                    | 50 m                              | 1.3 m                         | 20 cm                          |
| 40000 (sync)             | 200 m                             | 5 m                           | 80 cm                          |
| $1.5 \times 10^8$ (Sun)  | 700 km                            | 20 km                         | 3 km                           |

For over a century astronomers have made observations of binary star angular separations considerably in excess of the seeing limit and approaching the telescope diffraction limit. These scientists accomplish this resolution by looking for good images inside of the atmospherically degraded images. In 1970 a French astronomer, A. Labeyrie, explained this phenomenon as an

optical interference effect. He pointed out that telescope photographs with exposure times shorter than about .05 sec effectively freeze the turbulent motions within the Earth's atmosphere. Light arriving at opposite sides of the telescope mirror during this instant will interfere with itself and produce an image which has information on scales down to the telescope diffraction limit. An instant later the turbulence has moved and blurred the image. Examples of these short exposure photos for several stars are displayed in Figure 1. The small scale structure inside these images is near the telescope diffraction limit, even though the total image remains 1 arc-second in size. The mottled or speckled appearance is very similar to laser speckle interference patterns and this phenomenon is known as stellar speckle interferometry.

To use speckle interferometry for recovering high resolution information I have identified each "speckle" as a diffraction limited telescope image. Why I make this identification and how it is used is covered in the following sections. Although astronomers have used speckle interferometry to study bright stars, there are several complications in applying it to military applications. Satellites which shine by reflected sunlight have a substantially lower surface brightness than do stellar surfaces. We have therefore developed efficient detection systems in order to detect and record short exposure data for faint and low surface brightness objects. The low brightness necessarily means there will be few photons to detect for faint objects, so we have also developed methods to process such faint object data. In this respect we are now confident we can derive accurate size and shape information for high altitude satellites. Since it is usually desirable to derive images as well as size and shape information we have pursued techniques for retrieving diffraction limited images as well. Since the largest existing telescopes are only 5 meters in diameter, even diffraction limited images would provide only coarse resolution on synchronous objects. I have therefore concluded this paper with a discussion on efforts to develop and adapt for speckle interferometry low-cost multiple mirror telescopes with effective apertures near 20 meters.

## Image Formation Through The Earth's Atmosphere

Non-uniform heating of the Earth's atmosphere results in small scale temperature perturbations within the atmosphere. The scale of this temperature structure has been measured to be about 10 cm. If these perturbations did not exist light from a distant star or satellite would arrive at the telescope in the form of plane waves. That is, the peaks and troughs in the light wave would arrive at the same time at every point in the telescope aperture as shown in Figure 2a. The resulting image would be diffraction limited with a resolution inversely proportional to the telescope diameter. However the temperature changes also change the index of refraction in the air. These changes shift the location of the peaks and troughs or phase of the incoming light differently for each 10 cm patch of the telescope aperture. The image shown in Figure 2b still has the same amount of light as without the phase shifts but the mean image resolution is now typical of only a 10 cm telescope, namely 1 arc-second. The locations and phase shifts of each 10 cm patch changes with time and further blurs the image. Labeyrie pointed out that short exposure photos freeze these motions and that while the phase is not the same for the entire telescope aperture it is the same for some 10 cm pieces over the whole aperture. This situation is similar to an optical device known as a multiple aperture interferometer shown in Figure 2c.

A multiple aperture interferometer has a series of evenly spaced holes which let light of a constant phase pass through. The image of an object observed with this device would look like a multiple exposure or "fly's eye" view of the object. Each image would be a diffraction limited image as if observed with the whole aperture. However, the images would be shifted relative to one another and they would be modulated by a function appropriate to the size of each hole. Since the 10 cm patches are more or less evenly distributed in a real telescope then a short exposure speckle photo looks like a photo taken through a multiple aperture interferometer. The speckle photos in Figure 1 may be easily understood as the superposition of many diffraction limited images modulated by a 1 arc-second function which is the diffrac-

tion size of a 10 cm hole. The fact that speckles are images is especially noticable for the binary star where close inspection shows each speckle doubled.

### Computer Processing of Speckle Interferometry Data

A direct way to produce a reconstructed image from speckle photos is to extract one of the individual speckle images. In collaboration with two Kitt Peak National Observatory scientists, I used this method in 1975 to produce the first picture of a stellar surface other than the Sun. In that work we used a computer to locate and add together speckle images from many speckle frames to produce a good image of the bright supergiant star Betelgeuse. However, this method only works well for relatively small, bright, and uniform objects like stars. For large and more complex objects it becomes impossible to pick out individual speckle images since they overlap one another. Moreover, faint objects, like satellites, just don't put out enough light to identify individual speckles in a short exposure photo.

I have developed a general purpose method for extracting size and shape information from speckle photos. I look for preferred scales or correlation distances within each speckle frame. When I find these correlation distances I can then interpret them with respect to the size of the object being observed. Although other investigators have used this method it had proved difficult to calibrate accurately enough so as to provide precise size results. The problem occurs because a large part of the correlation signal is caused by seeing rather than the object being observed. In my method I use the cross-correlation between separate speckle photos to obtain a precise estimate for this effect so that I can remove it. This method has the added advantage of using the same set of data both for calibration and deriving results. I have used this method to obtain the first direct angular size measurement for the asteroids Vesta and Pallas. Asteroids are suitable test objects since they are faint and shine by reflected sunlight as do satellites. However, correlation methods provide only size and shape information. A more useful, fully reconstructed image cannot yet be directly derived from correlations.



We are currently investigating several methods to reconstruct images from speckle observations. A sophisticated imaging scheme using Fourier mathematics has been proposed by two University of Rochester optical physicists. However, this method has proved useful only for bright objects like the solar surface. We are currently using this method in a collaborative project with astronomers at Harvard University to study solar magnetic features. In very recent work, J. Feinup of The Environmental Research Institute of Michigan proposed a method to construct images directly from correlation data alone. We plan to apply his method to our correlation results in order to determine its applicability for speckle imaging.

#### Using Speckle Interferometry to Observe Very Faint Objects

Synchronous satellites are faint enough so that speckle interferometry becomes difficult. A typical synchronous satellite has brightness near + 13 stellar magnitudes which means that only about 100 photons reach the telescope during a .01 second speckle exposure. Photographic material is not sensitive enough to accurately detect such a small number of photons. Therefore, I have developed in collaboration with P. Strittmatter and G. Hubbard of the University of Arizona, a system for identifying and computer processing individual photons in a speckle exposure without using photographs.

The Arizona speckle system consists of an electronic image intensifier coupled to a television detector and computer processor. The image intensifier converts a single incoming photon to a large pulse of light which is detectable on one element of the television detector. The computer identifies and records the coordinates of each arriving photon. We can then use the same computer to determine the correlation distances and resulting object size and shape as described earlier. An example of the photon data is shown in Figure 3, a speckle photo of Saturn's moon Iapetus, showing approximately 200 photons for this magnitude 11.5 object. To test this method we have used it to derive angular diameters for a number of asteroids and outer planet moons in the magnitude range + 10 to + 13. The excellent agreement between our size determinations and those derived by other means is a clear indication that our method will work well on

synchronous satellites. To further demonstrate our capabilities we plan to observe faint, high altitude satellites.

#### The Development of Very Large Optical Telescopes for Speckle Interferometry Work

The largest existing telescopes are not large enough to obtain good resolution on synchronous satellites. Even a 5 meter telescope would resolve nothing smaller than 5 meters at synchronous altitudes. To make useful synchronous measurements we require an instrument larger than 20 meters with angular resolution near 1 meter. A rough estimate for the cost of such an instrument made from a single mirror would be over 1 billion dollars. However, new telescope technology is rapidly becoming available to reduce substantially this cost.

Large telescopes can now be built by combining light from many small mirrors. The University of Arizona and Harvard University are currently completing a telescope which combines light from six 2-meter mirrors. This instrument, shown in Figure 4, has the theoretical resolving power of a conventional 7-meter telescope, yet it cost about the same as a conventional 3-meter telescope. Although this telescope is not specifically designed for speckle interferometry, I believe we will be able to adapt it for this purpose. The Air Force Geophysics Laboratory is currently funding a program to determine whether we will be able to hold each mirror stable to a few microns while speckle observations are underway. Regardless of our results with this instrument, it is possible to design a low cost multiple mirror instrument which would be optimized for speckle work. Under National Science Foundation Support, the Kitt Peak National Observatory has designed a 25 meter multiple mirror instrument well suited for speckle work. This instrument, shown in Figure 5, would cost less than \$50 million.

#### Summary

Turbulence in the terrestrial atmosphere degrades all telescope images so that angular resolution of the largest instrument is not better than a 10 cm diameter telescope. Speckle interferometry is a technique for recovering the full theoretical resolving power of large telescopes. The basis of speckle interferometry is to

obtain telescope exposures short enough to "freeze" the turbulent motions in the atmosphere. The resulting speckled image is basically an optical interference pattern which contains information on scales representing the full resolving power of the telescope. A number of techniques exist for recovering the information lost by atmospheric degradation.

The Air Force Geophysics Laboratory has been working to adapt speckle interferometry for use in observing Earth orbital satellites. We are able to recover full diffraction limited images for bright objects. This work has resulted in the first images of a stellar surface other than the Sun and we are also using it to study magnetic fields which occur on the solar surface. In order to extend speckle techniques to faint objects, such as synchronous satellites, we have developed a technique to obtain size and shape information for those objects. We have also constructed a computer-controlled television speckle camera capable of detecting individual photons in order to obtain speckle data on faint objects. With this system and method we have obtained the first direct measurements of the sizes of asteroids. Based on results for these low surface brightness test objects we are proceeding to demonstrate this system for actual satellite observations.

To transform our concepts into a working high altitude satellite surveillance system we are working on two additional aspects. We feel that we will be able to develop a system capable of recovering images for faint objects as well as bright ones. We are also investigating using a new multiple mirror telescope in Tucson, AZ for speckle interferometry. Since we need a telescope larger than 20 meters for effective resolution at synchronous altitudes, and multiple mirrors are the only practical way to construct such an instrument, it is important to understand the design considerations for large multiple mirror instruments.

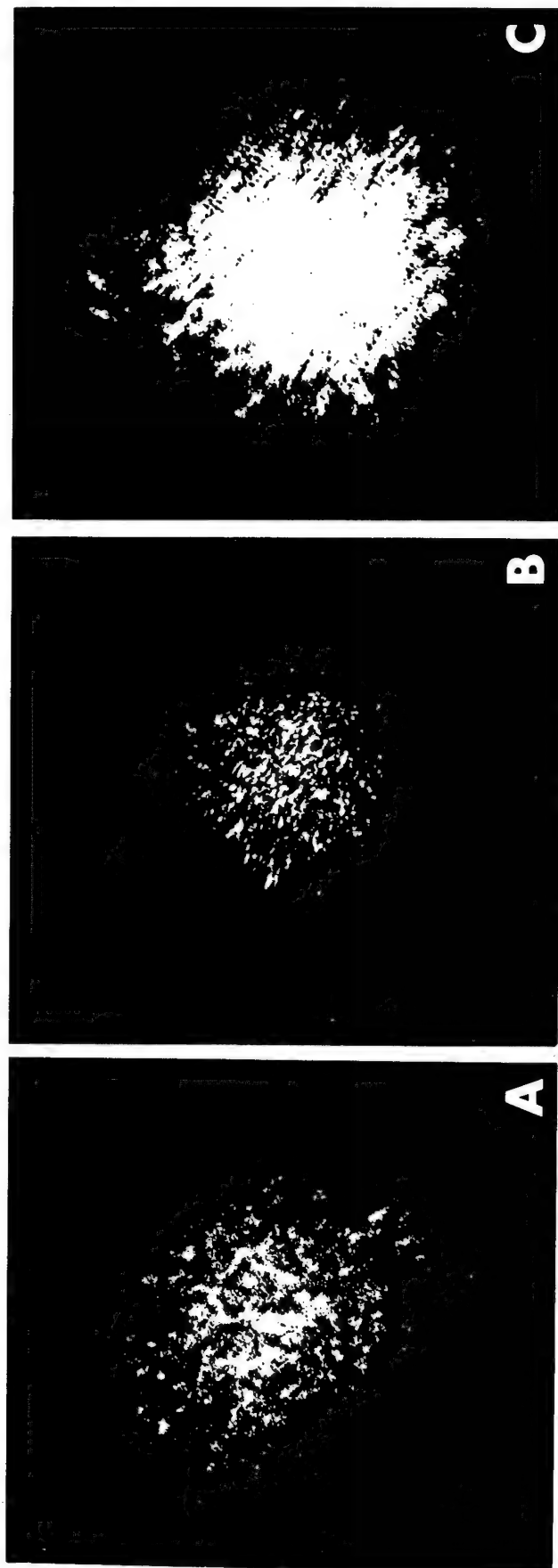


Figure 1. Short exposure ( $\tau=0.02$  sec) speckle snapshots from the Kitt Peak National Observatory 4-meter telescope (diffraction limit 0.030 arc-seconds). A) The bright red supergiant star Betelgeuse ( $\alpha$  Orionis). This star is resolved by the 4-meter telescope since its angular diameter is 0.060 arc-seconds. B) The unresolved point source star Bellatrix ( $\alpha$  Orionis). C) The Binary star Copella ( $\alpha$  Auriga). The two component stars have an angular separation of 0.050 arc-seconds. Note that the individual speckles for Copella are double and that the speckles for Betelgeuse are larger than those for the unresolved star.

UNCLASSIFIED

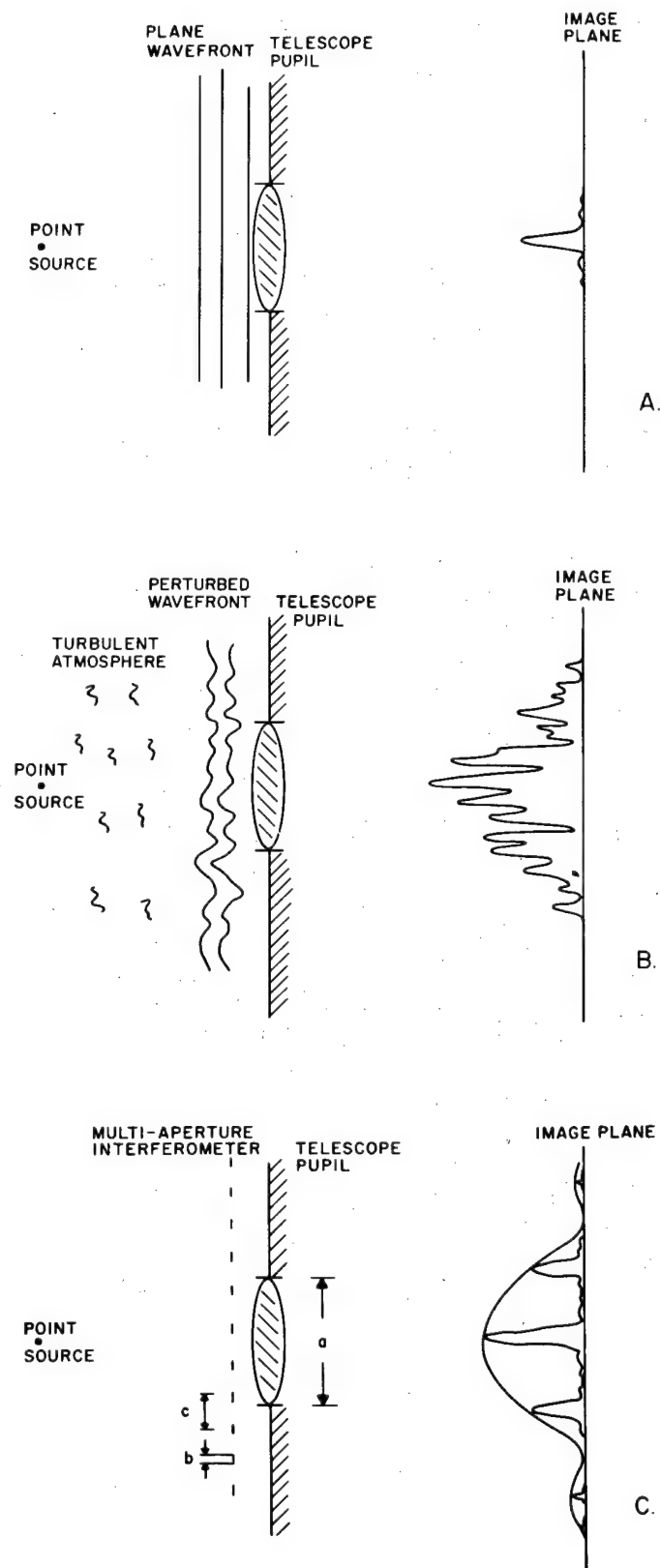


Figure 2. Schematic design of telescope image formation process: A) In the absence of an atmosphere light arrives at the telescope as a plane wave, B) Phase shifts with a scale of 10 cm produced by turbulence in the atmosphere, C) Multi-aperture interferometry, a rough model of a speckle snapshot. UN-CLASSIFIED.

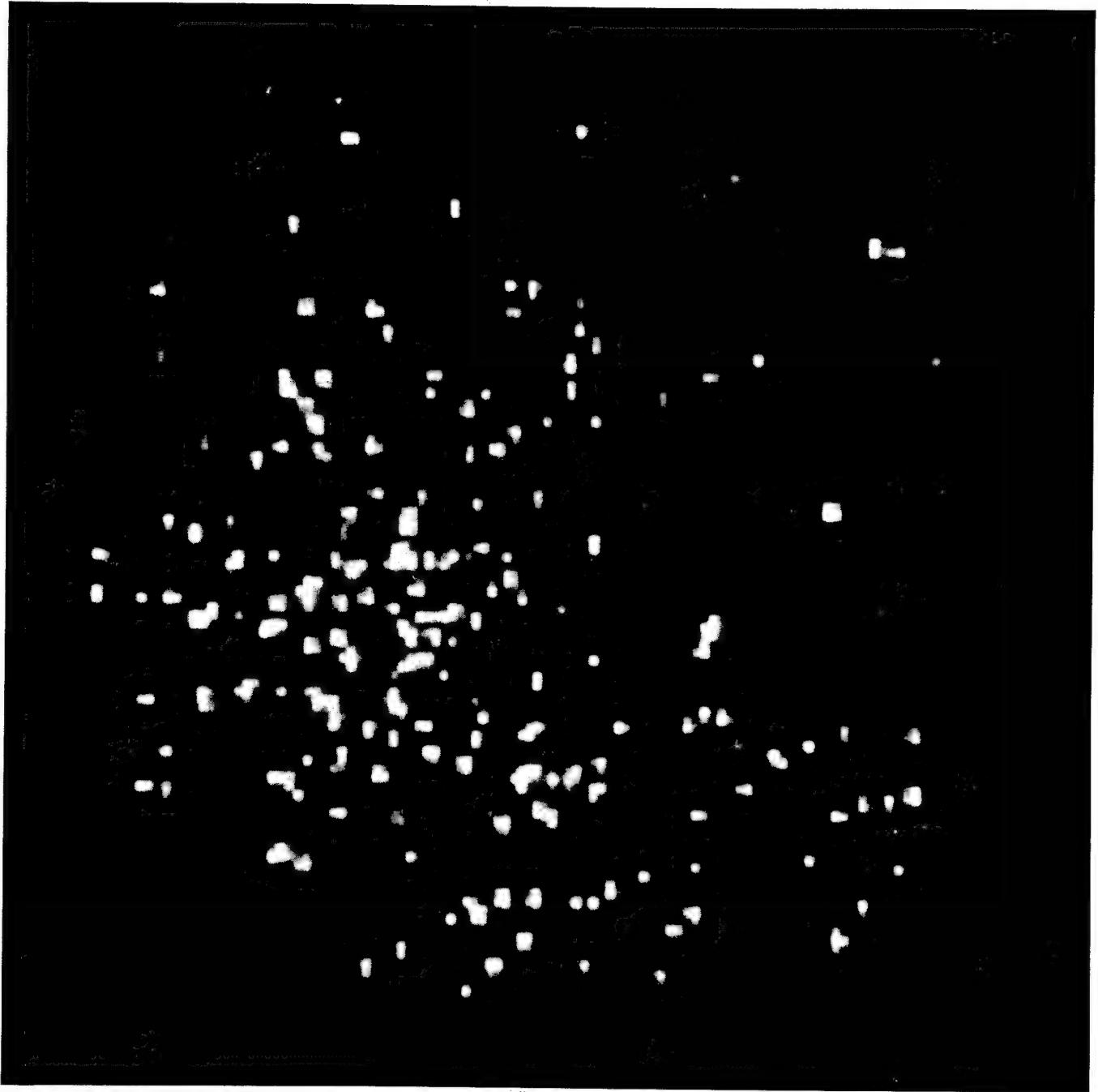
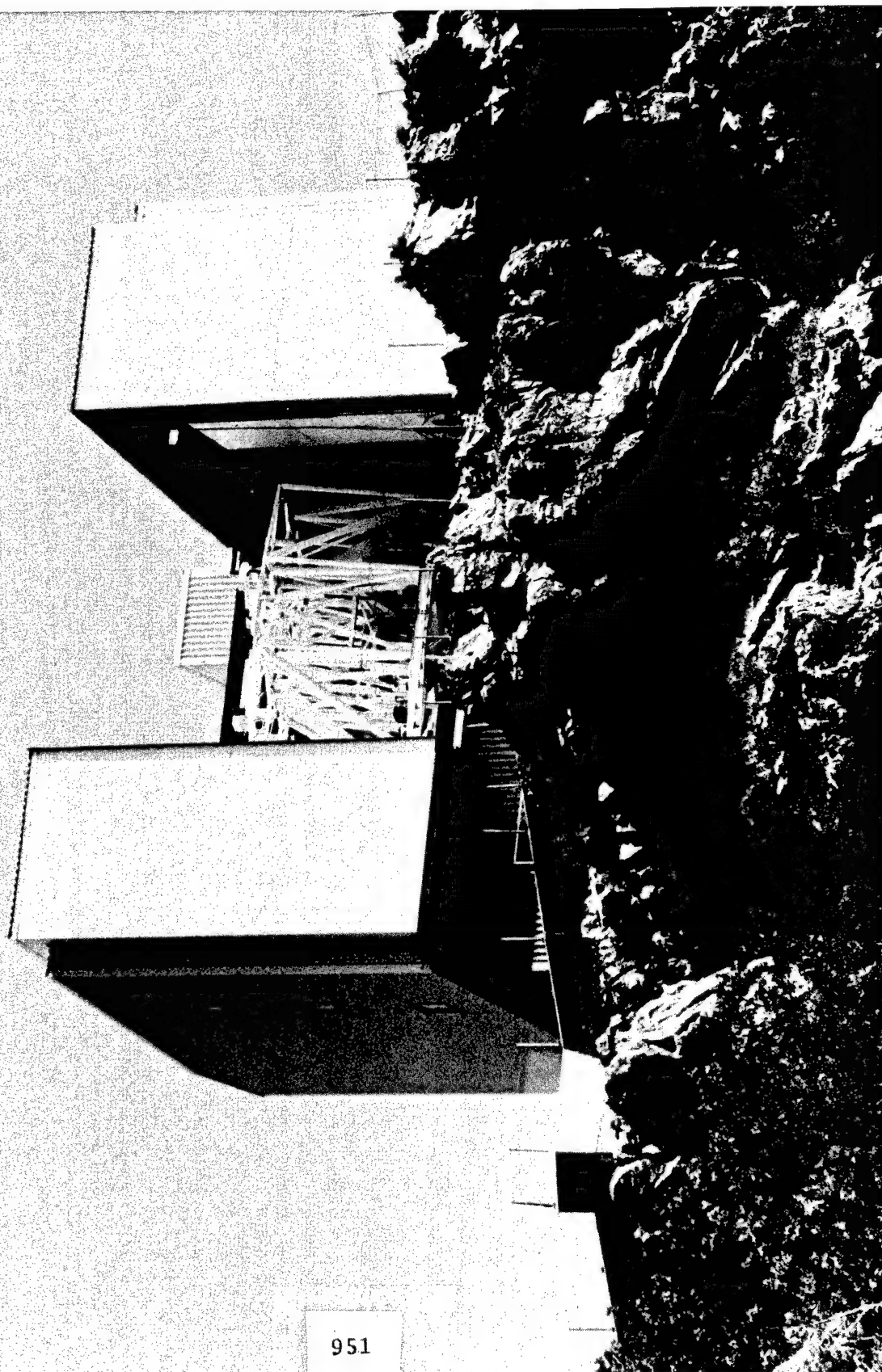
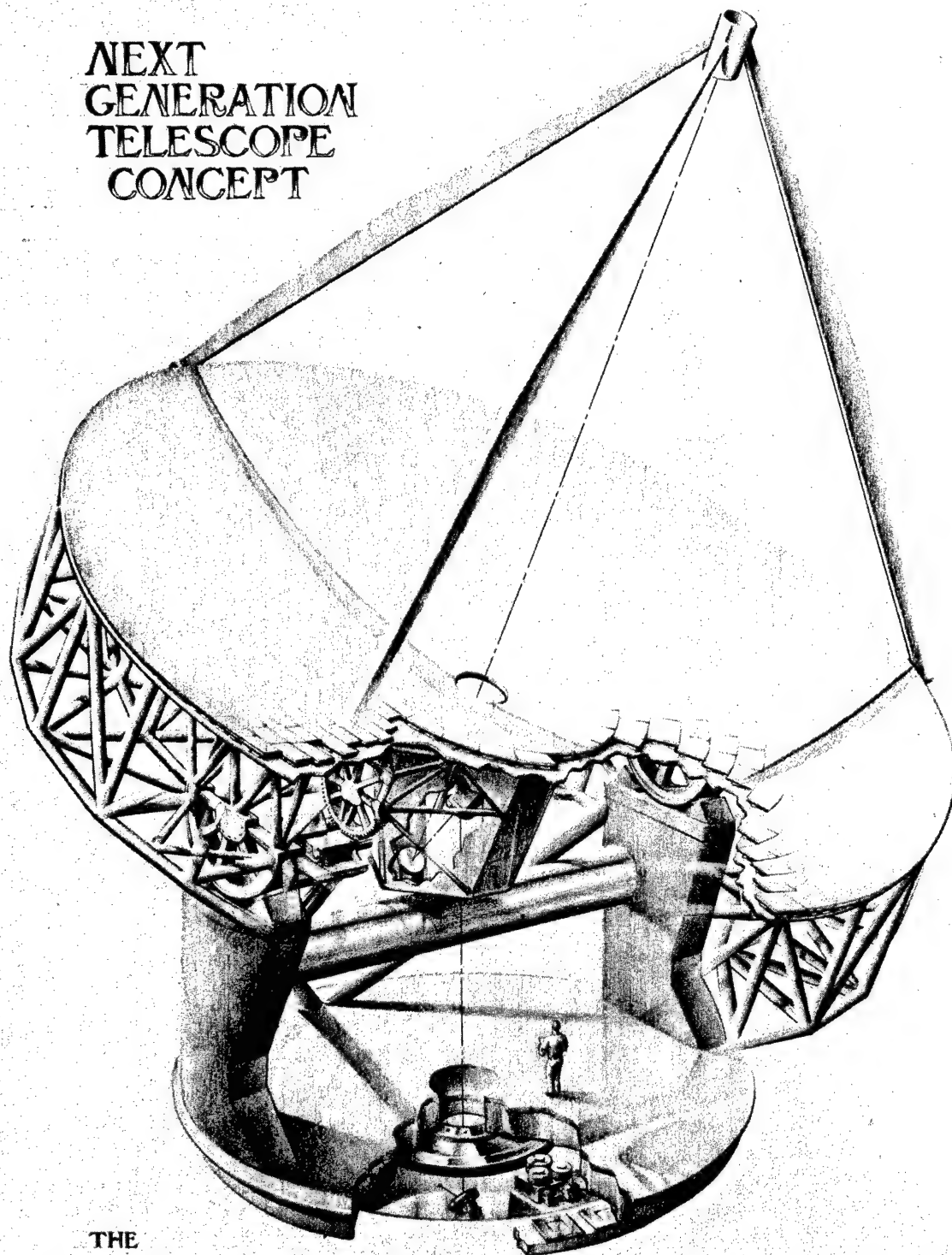


Figure 3. Television and computer obtained speckle snapshot of Saturn's moon Iapetus. This exposure shows several hundred individual photons. UNCLASSIFIED

Figure 4. University of Arizona/Harvard University multiple mirror telescope.  
The effective image forming aperture is close to 7 meters in diameter  
(Photo courtesy of The University of Arizona) UNCLASSIFIED



# NEXT GENERATION TELESCOPE CONCEPT



## THE STEERABLE DISH

R.N. SHOWALTER  
'77

952

Figure 5. Design for a potential 25 meter multiple mirror telescope suitable for speckle interferometry. (Photo Courtesy of the Kitt Peak National Observatory) UNCLASSIFIED



### Biographical Sketch

Captain Simon Peter Worden was born in Mount Clemens, Michigan on 21 October 1949. He graduated with highest distinction from the University of Michigan in 1971 with a B.S. degree in Physics and Astronomy. He was commissioned in the Air Force as a distinguished graduate of the AFROTC program and was granted a delay from extended active duty in order to pursue graduate studies in Astrophysics at the University of Arizona. He was awarded a Ph.D. by Arizona in 1975.

In May, 1975 Captain Worden began active duty at the Air Force Geophysics Laboratory Solar Research Branch in Sunpot, New Mexico. His research interests are wide ranging. He has published over forty papers since 1973 on such topics as global models of solar activity and variability, solar-type activity in other stars, and nucleosynthesis. His recent work has concentrated on developing techniques for recovering telescope images free from atmospheric degradation. Captain Worden is a co-investigator on a Spacelab II solar experiment and he is a member of the NASA working group on the detection of extra-solar planets. He is a member of the American Astronomical Society, The Astronomical Society of the Pacific, The Royal Astronomical Society, and Phi Beta Kappa. He was recently awarded one of four Air Force Research and Development Awards in 1977 for his work in image reconstruction.

HIGH BURNOUT SCHOTTKY BARRIER MIXER DIODES FOR X-BAND  
AND MILLIMETER FREQUENCIES

BY

A. CHRISTOU, CODE 5215

Department of the Navy  
Electronics Technology Division  
Naval Research Laboratory  
Washington, D. C. 20375

## High Burnout Schottky Barrier Mixer Diodes for X-Band and Millimeter Frequencies

### Abstract

The objective of this investigation was to develop x-band Schottky barrier diodes for the new version Sparrow Missile and Advanced Missile Systems. The resultant diodes are more rugged, with high burnout resistance to RF pulses and also exhibit less susceptibility to static charge damage. Receiver antennas in F4J, F14, F15 and F4B aircrafts are also susceptible to RF power degradation. RF burnout can be improved in Schottky barrier diodes by the greater reflection capability of certain refractory metals. The choice of metal, in turn, determines the local oscillator power required for operation (1 mW or less for military systems). Silicon and GaAs diodes were both investigated.

Ti-Mo-Au and Pt-Ti-Mo-Au silicon Schottky diodes were tested for NF and RF burnout performance in the appropriate mount. The diodes were tuned for low VSWR (less than 1.5) at 1 mW RF power level. Noise figure was measured at 9.375 GHz at a local oscillator power level of 1 mW using a gas discharge tube. Noise figure of an IF amplifier was 1.5 dB and a 100 ohm load resistor was used for the measurements. Results show that both Ti-Mo-Au and Pt-Ti-Mo-Au exhibit noise figure close to 7.0 dB.

RF burnout tests were also conducted at 9.375 GHz using an X-band pulsed magnetron. Pulsewidth ( $\tau = 1 \mu\text{sec}$ ) and repetition rate (1000 pulses per second) were used for measurements. The Pt-Ti-Mo-Au Schottky diodes exhibited low noise figure of 6.3 to 6.5 dB at a local oscillator power level of 1.0 mW and high burnout performance of 11.0 to 15.0 watts to 1.0  $\mu\text{sec}$  RF pulses. Ion implantation of the silicon has allowed us to attain the same performance at 0.75 mW local oscillator power.

GaAs Schottky barrier diodes have been fabricated for X-band and high frequencies utilizing refractory metallizations and ion implantation. These new diodes exhibit a low noise figure of 6.5 dB at .75 mW, with burnout levels of 8-10 watts at X-band.

## Introduction

Mixer diodes have seen wide application at microwave frequencies primarily in military radar receivers. However, these diodes are subject to burnout (catastrophic failure) from enemy jammers or by accidental irradiation from friendly aircraft transmitters. Typical effects of mixer diode failures results in the degradation in the missiles rear locking sensitivity and in channel mixer degradation (fuze). With a fifty foot missile to illuminator separation, a peak power of 50 watts is calculated to be induced at the mixer diode. Present system diodes are rated at 15-25 watts peak power and 1-2 watts CW. The survival rate for these diodes (such as found in the AIM-7F) would be less than 10 percent for the above field environment.

Point contact diodes have been used for mixer and detector applications at microwave frequencies for some time. They are relatively unsophisticated devices consisting of a metal whisker making a pressure contact with a semiconductor chip. In the early 1960's, Schottky barrier diodes were introduced for similar applications. The Schottky diode is also a metal semiconductor rectifying junction and is formed by depositing a metal on the semiconductor material by chemical deposition, evaporation or sputtering as shown in Figure 1.

In general, Schottky's have superior noise figure and better mechanical and environmental reliability when compared to equivalent point contact diode. However, Schottky diodes have proven to be less resistant to RF burnout in high frequency radar systems where short RF pulses are often incident on the diode.

NRL in FY 76 became aware of the problem of degradation of the mixer diode in the Sparrow AIM 7F system through the NRL Physics of Failure Program (Code 5215) which had been studying reliable metallization systems for L-band power transistors. Metal systems developed during 1974-75 were quickly applied to mixer diodes in order to significantly improve reliability. Based on the 6.1 effort at NRL, a 6.2 program was initiated in FY 77 with the objective of developing a high burnout Schottky diode. The specific goal of the FY 77 program at Microwave Associates was to develop X-band diodes with a noise figure of 7.0 dB at 1.0 mW local oscillator power level and with RF pulse burnout of 10 watts minimum to 1 microsecond RF pulses. The

second goal was to achieve 80 watts to 3 nanosecond pulses. The success of the FY 77 program sponsored by NAVELEX resulted in a FY 78 design refinement program. In FY 79 a manufacturing technology program will be initiated in order to reduce diode cost from 30 dollars to less than 10 dollars. Hence, the present program illustrates the successful movement of a concept from 6.1 to 6.2, 6.3 and finally to an MT phase. Table I illustrates the improvement in diode burnout achieved in FY 78.

TABLE I

RF Burnout Improvement for Schottky Diodes

|              | 1974      | 1975 | 1976<br>(6.1) | 1977<br>(6.2) | 1978<br>(6.3) | 1979<br>(MT) |
|--------------|-----------|------|---------------|---------------|---------------|--------------|
| Noise Figure | 7.0 dB    | 6.8  | 6.0           | 6.0           | 6.0           | 6.0          |
| CW Burnout   | 1-2 watts | 2-3  | 8-10          | 11-14         | 12-15         | 12-15        |
| RF Burnout   | 25 watts  | 35   | 80            | 100           | 100           | 100          |
| L.O. Power   | .7mW      | .8   | 1.0           | 1.0           | .75           | .75          |

The diodes which will become available for missile radar will be low cost (less than 10 dollars each) and will have significantly high burnout levels of 12-15 at CW and greater than 100 watts at RF. In the remainder of the paper we will concentrate on the techniques used to obtain the significant improvement.

Burnout at X-Band Frequencies

During the last decade, significant progress has been made in understanding the burnout mechanism and improving the power handling capabilities of Schottky-barrier diodes. DC pulse burnout test methods such as Torrey-line and mercury-relay pulser do not give a valid measurement of the RF-burnout resistance of a mixer diode because the diode encounters a different environment in a radar set than in the test setup. A newly developed RF-pulse burnout system which simulates actual radar conditions (with a TR tube) and uses PIN switches was used in this work.<sup>1</sup>

Lepselter, et al<sup>2</sup> have succeeded in improving the reliability and burnout performance of low-frequency Schottky

diodes (up to 4 GHz) by introducing a diffused guard-ring structure at the Schottky-barrier edge. This technique, however, increases the total capacitance of the device. Furthermore, it is extremely difficult to fabricate devices with diffused guard-ring structures with a geometry suitable for X-band and higher frequencies. Another type of guard ring was formed by proton implantation around the periphery of the metal dot<sup>3</sup> in GaAs Schottky barrier diodes for Ku-Band frequencies. The protons converted the N-type GaAs to semi-insulating ( $10^6$  -cm) material.<sup>4</sup> The diodes fabricated from this technique did not exhibit parasitic losses and showed a 3 dB improvement in burnout. Test data<sup>5</sup> showed that tripod inverted mesas have improved CW burnout at S-band frequencies.

Schottky-barrier diode burnout mechanisms are not completely understood. It is experimentally observed that the high-burnout point contact diodes have self-protecting behavior at high power levels by mismatching the line and reflecting much of the power back to the RF source. This behavior may be due to variation of the barrier capacitance.<sup>6</sup> Generally, Schottky barrier diodes mismatch the line to a lesser extent, and therefore absorb more of the incident RF energy. In an RF nanosecond environment ( $\tau \approx 50$  nsec) a point-contact diode can also withstand large reverse currents or voltages (due to varactor type behavior at high power levels) without degradation. The Schottky diode, on the other hand, tends to avalanche at the periphery of the junction due to high electric fields and fails catastrophically due to a localized alloyed site in the metal semiconductor junction. The use of higher eutectic temperature-barrier metal systems generally results in higher burnout resistance Schottky diodes to nanosecond RF pulses. In the long pulse condition, the diodes fail in the center of the<sup>7,8</sup> junction indicating a thermal dissipation phenomenon.

#### Optimum Design of High-Burnout Schottky Barrier Diodes (NAVY 6.2 and 6.3 Programs)

The 6.1 effort at NRL was conducted in order to pinpoint the exact cause of failure observed on diodes in the AIM 7E missiles. These experiments<sup>9</sup> using scanning electron microscopy and Auger spectroscopy have shown that CW or microsecond RF pulse burnout is due to thermal dissipation and causes diffusion of gold in silicon, particularly at the center of the Schottky junction as shown in Figure 2.

The overlay and barrier metals were removed by chemical etching to observe the failure points. The diodes failed at the center of junction due to excessive heating. With longer pulses, the heat flow reaches equilibrium and the center of the diode is hotter than the outer portion so that burnout usually occurs near the center. In contrast, diodes subjected to nanosecond pulses were characterized by edge burnout as shown in Figure 3. Since the heat generated in the diode does not have time during the short nanoseconds pulse to spread or reach equilibrium, the diode fails at the periphery due to high electric fields.

A number of high-temperature barrier metals were investigated such as Pt, Pd, Ti, and Mo. The main features of interest in the different barrier metals were the barrier height and the eutectic temperature of the silicon-barrier-metal system. Low-barrier height is necessary to meet the 1.0 mW local oscillator power requirement and the high-temperature silicon-barrier metal system is needed for high RF power handling capability of the Schottky diode. The Pt-Ti-Mo-Au system exhibited the best burnout performance as shown in Table II, and was chosen as the optimum system for the mixer diodes.

Table II

RF Burnout of X-BAND Silicon Mixer Diodes

| Metal Scheme | RF Burnout<br>3 nsec pulses | RF Burnout<br>1 $\mu$ sec pulses | Barrier<br>Height |
|--------------|-----------------------------|----------------------------------|-------------------|
| PD           | 10-15 watts                 | .2 - .4 watts                    | .45 eV            |
| Ti-Mo-Au     | 12-25                       | 1 - 2                            | .40               |
| Mo-Au        | 40-60                       | 2 - 3                            | .65               |
| Pt-Ti-Mo-Au  | 60-100                      | 12 - 15                          | .80               |
| Ta-Pt-Ta-Au  | 80-100                      | 10-12                            | .75               |

Performance of the High Burnout Silicon Diodes at X-Band

Pt-Ti-Mo-Au Schottky diodes were tested for NF and RF burnout performance. The diodes were matched in a tunable mount I.D. 2967 for low VSWR (less than 1.5) at 1 mW RF power level. Then the noise figure (NF) was measured using a gas-discharge tube at 9.375 GHz at the same local oscillator power level.<sup>11,12</sup> Noise figure of the IF amplifier was

1.5 dB and a 100 ohm load resistor was used for the measurements. Results are given in Table II and show that both Ti-Mo-Au and Pt-Ti-Mo-Au exhibit a noise figure close to 7.0 dB at 9.375 GHz. The performance of these diodes were also compared with the "old" Ti-Mo-Au diodes previously used for the Sparrow Missile.

RF burnout tests were also conducted at 9.375 GHz using an X-Band pulsed magnetron.<sup>1</sup> Pulsewidths of  $T=1\mu\text{sec}$  and repetition rates of 1000 pulses per second were used for the measurements. Fifty diodes of each type were subjected to increasing power levels for 30 second periods until at least a 1 dB degradation of noise figure was observed. Results are given in Table III and show that Ti-Mo-Au metalized devices burnout when 1.75 to 3.0 watts RF power is applied. The Pt-Ti-Mo-Au Schottky diodes exhibited similar noise figures at a local oscillator power level of 1.0 mW however, a higher burnout performance (12.0 to 15.0 watts) with  $1.0\mu\text{sec}$  RF pulses was observed. This represents a significant improvement over the Ti-Mo-Au diodes.

Table III  
DC and RF Burnout Tests of Ti-Mo-Au and Pt-Ti-Mo-Au Schottky Diodes

|                  | $R_s$ (ohms) | $V_B$ (volts) | NF (dB) | RF Burnout watts |
|------------------|--------------|---------------|---------|------------------|
| Ti-Mo-Au (Si)    | 12-16        | 6-8           | 6.5-7.5 | 2-3              |
| Pt-Ti-Mo-Au (Si) | 8-12         | 14-18         | 6.0-7.0 | 12-15            |
| *Implanted       |              |               |         |                  |
| Pt-Ti-Mo-Au (Si) | 10-12        | 16-18         | 6.0     | 12-15            |

\*Implanted with  $1 \times 10^{14}$  Sb to lower the Barrier Height.

The Pt-Ti-Mo-Au Schottky diodes exhibit a barrier height of 0.80 eV as compared to 0.5 eV for Ti-Mo-Au diodes.<sup>7</sup> This implies that electrons in the Pt-Ti-Mo-Au Schottky diodes require higher energy (in the form of local oscillator power or DC bias) to cross the metal-semiconductor interface.<sup>3</sup> A degradation in noise figure occurs for the Pt-Schottky diodes, while Ti-Schottky diodes maintain a noise figure in the 6.5-7.0 dB range even below 1.0 mW.

There are many advanced avionic systems that operate under starved local oscillator conditions and have 0.5-0.75 maximum local oscillator power available for the mixer diode.



These systems cannot use the Pt-Ti-Mo-Au diodes without further modification. Utilizing the ion implantation technology, the barrier height of a Pt-Ti-Mo-Au Schottky diode can be reduced without degrading the overall performance of the device.<sup>13,14</sup> The implanted Pt-Ti-Mo-Au diodes therefore resulted in the same noise figure as the unimplanted diodes, with the added advantage that they require local oscillator power of 0.75 mW instead of 1.0 mW. Hence, the optimum configuration is the implanted Pt-Ti-Mo-Au silicon mixer diode.

#### High Burnout GaAs Diodes (X-Band and mm-wave)

As an outgrowth of NRL's technology programs in GaAs materials and devices, investigations were successfully carried out in the development of high burnout GaAs diodes for future missile applications. GaAs offers the possibility of improved performance at X-band and higher frequencies. Low barrier Schottky diodes have been developed by implantation of Ge or S into epitaxial GaAs at energy of 5 keV and fluences of  $5 \times 10^{12} \text{ cm}^{-2}$  and  $1 \times 10^{13} \text{ cm}^{-2}$ .<sup>15</sup> The metal schemes utilized were Pt-Ti-Mo-Au and Ta-Pt-Ta-Au. In both cases the barrier height was reduced from .8 eV to .5-.4 eV allowing for operation at low local oscillator power. Burnout levels achieved for these devices were 8-10 watts, CW at X-band, thus making GaAs mixers a competitor to Silicon mixers for high burnout applications. Potential noise figures of 3.5 to 4.5 dB can be attained with GaAs.

The same device structures, but with a thinner GaAs epitaxial layer thickness and active area radius were fabricated for mm-wave applications. In a mixer configuration at 35 GHz, a conversion loss below 5.0 dB and less than 6.5 dB noise figure was realized. This device can be used in front-end receivers, as efficient detectors at millimeter wavelengths and as a high speed switch. The mm-wave devices due to their small size (less than .5  $\mu\text{m}$  radius and less than .2  $\mu\text{m}$  thick epitaxial layer) did attain a burnout level of only 20-25 mWatts. Table IV summarizes the GaAs results at X-band and mm-wave frequencies.

TABLE IV  
GaAs Mixer Diodes Pt-Ti-Mo-Au, Implanted

|                 | X-Band     | mm-wave, 35GHz |
|-----------------|------------|----------------|
| Conversion Loss | -          | 5.0 dB         |
| Noise Figure    | 6.0 dB     | 6.5 dB         |
| Burnout Level   | 8-10 Watts | 20-25 mWatts   |

Potential burnout levels of 500 mWatts are possible at 35 GHz after a development effort in order to improve metallizations and device configuration.

### Conclusions

High burnout Silicon mixer diodes have been developed for missile applications. This program illustrates the successful transfer of technology from 6.1 through 6.3 and manufacturing technology in order to achieve a significant cost reduction. The research and development program was undertaken in order to solve a specific problem in the fleet and represents a successful utilization of basic research at affordable costs.

### References

1. Anand, Y. and Howell, C., "The Real Culprint in Diode Failure," *Microwaves*, August 1970, pp. 1-3.
2. Lepselter, M.P., and SZE, S.M., "Silicon Schottky Barrier Diodes with Near Ideal I-V Characteristics," *Bell System Tech. Journal*, Vol. 47, pp. 195-208 (1968).
3. Anand, Y. and Moroney, W.J., "Microwave Mixer and Detector Diodes," *Proc. IEEE*, Vol. 59, No. 8, August 1970, pp. 1182-1190.
4. Foyt, A.G., et al, "Isolation of Junction Devices in GaAs Using Proton Bombardment," *Solid State Electronics*, February 1969.
5. Day, H.M. and Macpherson, A.C., "Design and Fabrication of High Burnout Schottky Crystal Video Diodes," *Solid State Elec.*, Vol. 15, No. 4, 1972, pp. 409-416.
6. Anand, Y., "RF Burnout Dependence on Variation in Barrier Capacitance of Mixer Diodes," *Proc. IEEE*, Vol. 61, Feb. 1973, pp. 247-248.
7. Anand, Y., "X-Band High Burnout Resistance Schottky Barrier Diodes," *IEEE Trans. on Electron Devices*, Vol. 24, pp. 1330-1336 (1977).
8. Anand, Y., "High Burnout Mixer Diodes," *IEEE Elec. Device Conf.*, Washington, D.C., Dec. 1974.
9. Weisenberger, W.H., Christou, A., Anand, Y., "High Spatial Resolution Scanning Auger Spectroscopy Applied to Analysis of X-Band Diode," *J. Vac. Sci. Technol.*, Vol. 12, No. 6, Nov/Dec 1975, pp. 1365-1368.
10. Copeland, J.A., "A Technique for Directly Plotting the Inverse Doping Profile of Semiconductor Wafers," *IEEE Trans. on Electron Devices*, Vol. ED-16, pp. 445-449, May 1969.

11. Mumford, W.W., and Scheibe, E.H., "Noise Performance Factors in Communications Systems," Horizon House, Inc. 1968.
12. Torrey, H.C. and Whitmer, C.A., Crystal Rectifiers, Radiation Lab Series, Vol. 15, pp. 199-234, Boston Technical Publishers, Lexington, MA., 1964.
13. Andrews, J.M. and Ryder, R.M., United States Patent No. 3,964,084 (1976).
14. Shanon, J.M., Applied Physics Letters, Vol. 25, No. 1, p. 75 (1974).
15. Christou, A., Anand, Y., and Dietrich, H., "Low Barrier Height Ion Implanted X-Band Diode," IEEE Elec. Device Conference, Washington, D.C., 1977.

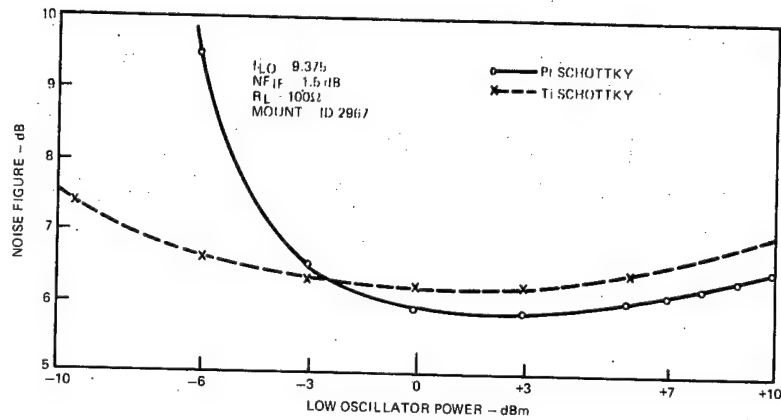
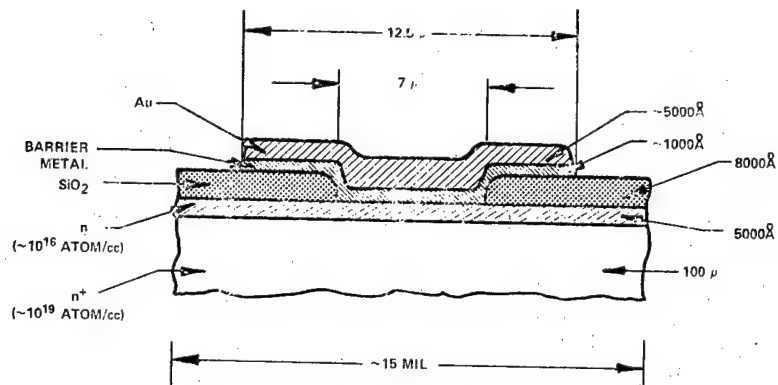
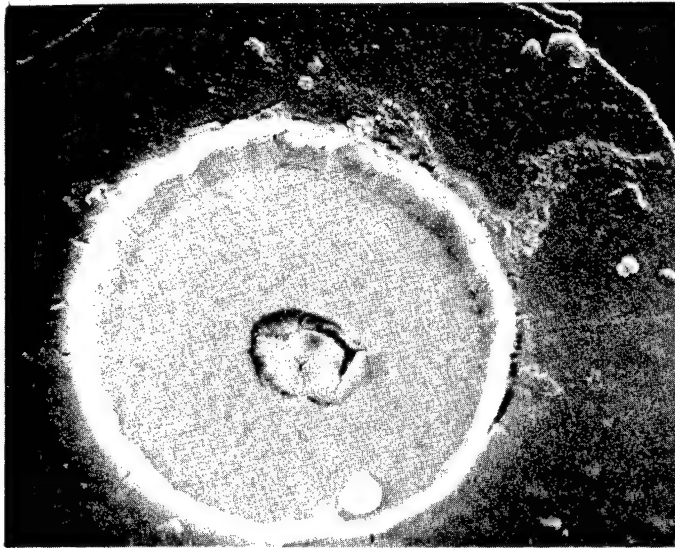


Figure 1. Cross section of a Silicon Mixer Diode showing a 7  $\mu$ m active area. Also shown is the dependence of noise figure on local oscillator power.



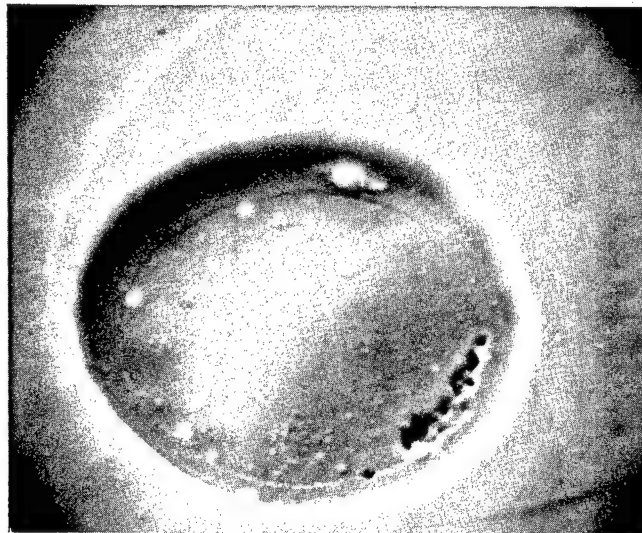
7600X

RF POWER = 8 WATTS,  $\tau = 1 \mu s$



21,600X

Figure 2. Scanning electron micrograph of an X-band mixer which failed under "CW" conditions. Interdiffusion between the metal constituents was the major failure mode.



10,000X

RF POWER = 20 WATTS,  $\tau = 10$  ns



13,900X

RF POWER = 100 WATTS,  $\tau = 3$  ns

Figure 3. Scanning electron micrograph of an X-band mixer subjected to nsecond pulses. Edge burn-out is shown.

### Biographical Sketch

Dr. Aristos Christou graduated from Columbia University in 1967 and from the University of Pennsylvania in 1968 having received the B.A. and M.S. degrees respectively in Physics. In 1971 he received the PhD. degree in Materials Science by the University of Pennsylvania.

In May 1969 he joined the Naval Surface Weapons Center in Dahlgren, Virginia as a research metallurgist. Dr. Christou in Dahlgren was involved in a number of programs in the area of micro-electronics reliability and failure analysis. In 1970-72 he conducted basic research on the effects of rf energy on diodes and transistors. His research also included phase transformation in advanced materials of interest to the Navy.

In October 1972 he joined the Electronics Technology Division of the Naval Research Laboratory where he was responsible for the reliability and failure analysis of microwave power transistors to be used in phased array radars. Presently, he is head of the Reliability and Failure Analysis Section responsible for failure physics programs in Silicon and GaAs devices and hybrids.

NEW ENERGETIC PLASTICIZERS:  
SYNTHESIS, CHARACTERIZATION AND POTENTIAL APPLICATIONS

By

Robert A. Hildreth, Captain, USAF

Richard L. Wallace, 2nd Lt, USAF

Melvin L. Druelinger, URRP Visiting Scientist

Ben A. Loving, Lt Colonel, USAF

Directorate of Chemical Sciences

Frank J. Seiler Research Laboratory (AFSC)  
U.S. Air Force Academy, Colorado



NEW ENERGETIC PLASTICIZERS:  
SYNTHESIS, CHARACTERIZATION AND POTENTIAL APPLICATIONS

Abstract

A class of fluorodinitroalkyl ether plasticizers for use in explosive and propellant formulations has been synthesized via triflate intermediates. The new energetic plasticizers, bis-2-fluoro-2,2-dinitroethoxymethylenes, which for brevity were given the trivial name FEME, were prepared by condensation of fluorodinitroethanol with the appropriate alkyl ditriflates. These plasticizers have been developed specifically for use with the dinitropropylvinyl ether polymer (DNPVEP) previously developed and reported from this laboratory. These new plasticizers may also be replacements for FEFO or nitroglycerin which have availability and/or sensitivity problems. Preliminary evaluation of these plasticizers indicates a high degree of both thermal and hydrolytic stability. DNPVEP plasticized with FEME showed excellent physical properties. Chemical integrity of this plasticizer is such that compatibility with normal explosive and propellant ingredients, such as TNT, HMX, RDX, and ammonium perchlorate is expected.

The DNPVEP energetic binder with or without the fluorodinitroethoxymethylene ether plasticizers (FEME) has attracted considerable developmental interest. Although no developmental formulations with FEME have been prepared, explosive formulations with DNPVEP are being investigated by the Air Force Armament Laboratory, Los Alamos Scientific Laboratory and the Lawrence Livermore Laboratory. Applications in nitramine gun propellant formulations are in the earliest stages of investigation; however, theoretical considerations suggest a possible break-through.

## Introduction

The energetic materials technology base is being taxed by current requirements for explosive and propellant systems for advanced weaponry. So much so that in the development of new high impulse propellants, such as that for the SRAM missile, structural integrity and shelf life have been sacrificed to obtain increased impetus by increasing percent solid oxidizer loadings to the maximum. Composite explosives and propellants differ largely in the rate of energy release. That is, one obtains deflagration in propellants as opposed to detonation in explosives. Basically these composite energetic materials are composed of approximately 85% energetic material, 10% binder and 5% various additives to improve physical properties and combustion characteristics. The energetic material component is divided approximately 70% oxidizers, such as ammonium perchlorate, and about 15 to 20% fuel, such as aluminum powder. The remaining 10% polymeric binder materials are normally considered inert due to their low energy contribution. To alleviate this problem, propellant formulators, both missile and gun, are now using nitramines such as HMX and RDX, long known high energy materials, in new formulations. The tradeoffs between energy and structural integrity clearly illustrate the constraints of binder and oxidizer materials capabilities.

Historically, the largest expenditure in energetic materials research and basic development has been in efforts to improve the energy content of the oxidizer and fuel fractions. This seems like the highest area of payoff since they constitute the largest percentage of the composite mixture. In recent years only limited progress has been made in improving these materials. The binder fraction of these formulations received some attention until eight or ten years ago. However, most of the materials in use are commercially available polymers developed for domestic purposes which have been known for at least fifteen years. Therefore, combination of good binder structural properties with energetic oxidizer moieties in one polymeric material appeared as an attractive research goal with high potential payoff.

A few years ago a program was initiated at the Seiler Laboratory to design, based on sound molecular architecture, a new binder system composed of both an energetic polymer and an energetic plasticizer. Binder molecular architecture determines bulk properties and the percent loading that can be obtained. The chemical moieties and bonding linkages in polymer molecules determine factors such as chemical reactivity (stability and sensitivity), energy content, and the mechanical properties of both neat polymer and any explosive or propellant formulation utilizing it. The current state-of-the-art in molecular design has established that ether or carbon-carbon backbones provide the best mechanical properties. An extensively used polymer of this later type is hydroxy-terminated polybutadiene which provides great structural integrity and

high loading density. Various polyethers, such as polyethyleneglycol, have been investigated with energetic plasticizers such as fluorodinitroethyl formal (FEFO) and nitroglycerine (NG), however, in these systems a large amount of polymer is required to obtain the desired mechanical properties of the propellant. Furthermore FEFO is hydrolytically unstable and nitroglycerine is not as insensitive as one might desire. The oldest energetic binder is nitrocellulose which originally was used in a double base propellant plasticized with nitroglycerine. It may also be plasticized with FEFO. Nitroglycerine and nitrocellulose are nitrate esters which exhibit certain burning characteristics at high pressure that appear to indicate a basic incompatibility when used in nitramine propellant formulations.<sup>1</sup>

In an effort to design a polymeric material embodying both structural integrity and high energy oxidizer properties, a facile synthesis for dinitropropyl vinyl ether and fluorodinitroethyl vinyl ether was developed in this laboratory.<sup>2</sup> These synthetic techniques were transferred to the Los Alamos Scientific Laboratory where polymerization methods were developed resulting in a class of energetic vinyl ether polymers (Figure I). This work was reported last year at the AFSC Science and Engineering Symposium.<sup>3</sup> Preliminary developmental work has shown that this energetic vinyl ether polymer when used in pressed formulations is very stable, has a low impact sensitivity, excellent mechanical properties, permits a high loading density, and is compatible with all ingredients so far formulated with it. These include RDX, HMX, ammonium perchlorate, and aluminum. These findings confirmed the anticipated properties which were based on the molecular design embodied in the dinitropropyl ether and fluorodinitroethyl ether structures.

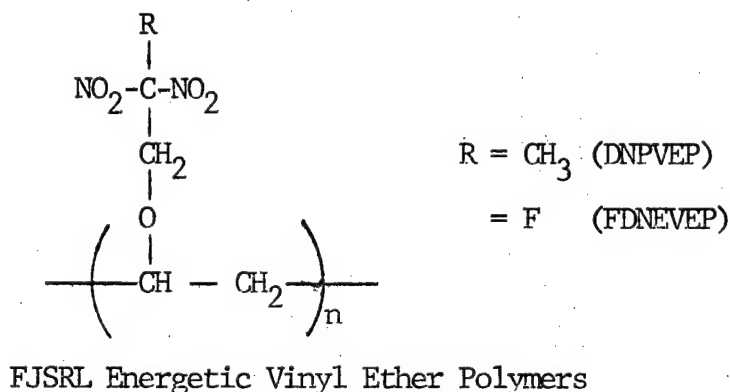


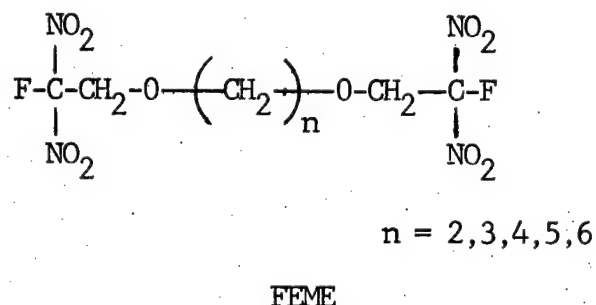
Figure I.

It was then concluded that an improved energetic plasticizer was needed since the two heretofore used in operational formulations both have disadvantages. FEFO, the most important energetic plasticizer

today, has excellent energetic properties. However, it has an acetal linkage which is hydrolytically unstable. Formulations in which it is most commonly employed are based on polyethers which are somewhat hydrophylic in nature. These propellant formulations then do have moisture present in the propellant matrix. Another disadvantage with both nitroglycerine and FEFO is migration. This problem could be reduced by increasing the molecular length and weight. The excellent energy and plasticizing properties of FEFO would also be expected to remain if the central linkage were converted to an ether or diether, thus eliminating the problem of hydrolytic instability. Other workers realized this potential and prepared closely related compounds<sup>4</sup> but no synthetic technique was developed for these ethers.

### Discussion

It was the purpose of our study to develop a new class of energetic plasticizers based on the union of 2-fluoro-2,2-dinitroethanol via an ether linkage through a carbon chain. This homologous series of compounds (bis-2-fluoro-2,2-dinitroethoxypolymethylenes) differs only in the value of  $n$  shown in Figure II for the central number of methylene



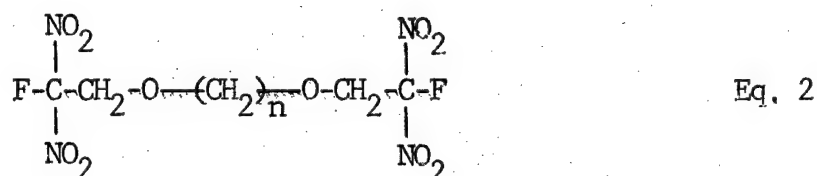
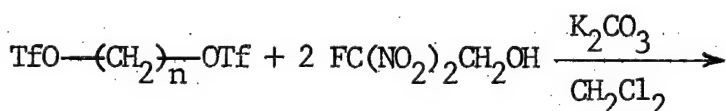
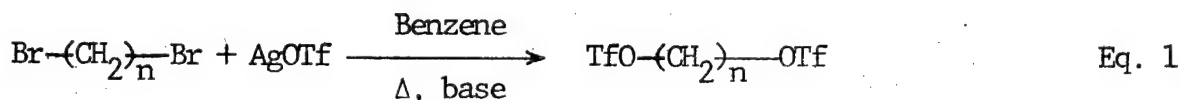
(Bis-2-fluoro-2,2-dinitroethoxypolymethylenes)

Figure II.

groups in the plasticizer molecule. In an effort to provide an easily used nomenclature we have given this series the trivial name FEME. FEME compounds should be highly stable both thermally and hydrolytically as demonstrated for the fluorodinitroethoxy grouping in the energetic vinyl ether polymers. Their flexible ether linkage should provide increased internal lubricity. The high number of polar groups (ether, nitro, and fluoro) should increase hydrogen bonding and adhesion to solid fillers such as HMX, RDX, aluminum, and ammonium perchlorate. Nitro groups, being strong oxidizers, impart increased energy. Furthermore, the C-nitro linkage, as opposed to the nitrate ester, provides decreased

sensitivity to impact initiation. Lastly, the terminal fluoro groups embodied in this molecular architecture impart thermal stability and increased density. Explosive/propellant energy release has been shown to increase with the square of material density.

Employing newer synthetic techniques involving triflate,<sup>5</sup> tosylate, and mesylate intermediates, synthesis of the desired series of bis-2-fluoro-2,2-dinitroethoxypolymethylenes was attempted. To date mesylate and tosylate processes, which promise to be less expensive, have not been fruitful,<sup>6</sup> however, the triflate technique has given up to 85% yields. This synthesis is effected in two steps (Equations 1 and 2). First a ditriflate is prepared by reaction of a 50% excess of silver triflate with the corresponding dibromoalkane in benzene solvent at reflux with a catalytic amount of proton scavenger for approximately six hours. Elution through a short silica gel column yields approximately 80% of the ditriflate. In the second step, condensation of the ditriflate and fluorodinitroethanol is effected in methylene chloride with potassium carbonate at room temperature for a few hours. The desired ethers (80% yield) were purified by chromatography on silica gel providing the plasticizers as colorless oils in an overall yield of approximately 50%.



It is not the intention here to imply that this is an optimized process, but only proof of principle that these materials will be good plasticizers and can be synthesized in good yields by practical techniques. Further synthetic studies to optimize the synthetic conditions for improved yields are planned. Synthesis of the ditriflate from the dialcohol and triflic anhydride has been used in one case where an excellent yield was obtained. This modification will reduce cost by elimination of silver salts. The most expensive remaining reagent, triflic anhydride, could be recovered as triflic acid from the reaction residues and recycled. Use of toluene as a reaction medium replacing

benzene is expected to reduce reaction time. Similar synthetic approaches employing mesylate as the leaving group rather than triflate have to date been unsuccessful. However, if proper reaction conditions were found, this would greatly reduce cost.

The physical properties of these plasticizers are attractive. They are all colorless oils with expected densities of up to 1.4 grams per cc. The energetic vinyl ether polymers, which are hard friable materials, were plasticized with 20% FEME to yield elastomeric materials. Differential thermal analysis (DTA) of these plasticizers reveal onset of decomposition at about 200°C. DTA of DNPVEP plasticized with FEME energetic plasticizers also showed onset of thermal decomposition above 200°C. The decomposition exotherms exhibited a maxima near 250°C. The exotherm maxima of the HMX mixes are not significantly different from HMX alone. Compatibility with other explosive and propellant ingredients, such as TNT, RDX, ammonium perchlorate and aluminum, are expected. Differential thermal analysis characteristics of several mixtures are shown in Table I. These data are highly encouraging when compared to the low thermal stability of FEFO (max = 115°C).

TABLE I  
FEME ENERGETIC PLASTICIZER  
DTA THERMAL STABILITY PROPERTIES

| COMPOUND                  | NEAT <sup>b</sup>      | DTA ( $\Delta H$ ) EXOTHERM <sup>a</sup> in °C |                         |
|---------------------------|------------------------|--|-------------------------|
|                           |                        | DNPVEP <sup>c</sup>                            | HMX/DNPVEP <sup>d</sup> |
| FEFO                      | 105 (115) <sup>7</sup> |  |                         |
| DNPVEP                    | 220 (257)              |  |                         |
| HMX                       | 282 (284)              | 220 (257) <sup>e</sup>                         |                         |
| FEME-3                    | 200 (250)              | 205 (263) <sup>f</sup>                         |                         |
| FEME-4                    | 192 (247)              | 207 (249)                                      | 279 (281) <sup>g</sup>  |
| FEME-5                    | 190 (248)              | 200 (249)                                      |                         |
| FEME-6                    | 207 (241)              | 217 (256)                                      |                         |
| 3-Oxa FEME-5 <sup>h</sup> | 187 (233)              | 198 (251)                                      | 277 (279) <sup>g</sup>  |

<sup>a</sup>Differential Thermal Analysis (DTA) figures reflect onset of exothermic reaction and (the maximum observed). <sup>b</sup>Purity determined by NMR: FEME-3, -5, and -6 were 90+% pure; FEME-4 and 3-Oxa FEME-5 were 99+% pure.

<sup>c</sup>Binder: DNPVEP (60%) plasticized with FEME (40%). <sup>d</sup>HMX (80%), DNPVEP (12%), FEME (8%). <sup>e</sup>HMX (95%), DNPVEP (5%), no FEME (ref 3). <sup>f</sup>DNPVEP (80%) plasticized with FEME-3 (20%). <sup>g</sup>For major exotherm; minor exotherm occurs at 259 and 261° for FEME-4 and 3-Oxa FEME-5 respectively. <sup>h</sup>Bis-2-(2-fluoro-2,2-dinitroethoxy) ethyl ether.

### Conclusion

It is anticipated that additional research and developmental studies will be continued on this new class of plasticizer materials by various agencies interested in energetic materials. To date a number of agencies (the Air Force Armament Laboratory, the Los Alamos Scientific Laboratory, the Lawrence Livermore Laboratory, the Stanford Research Institute, and the AF Rocket Propulsion Laboratory) have complementary follow-on efforts on the DNPVEP binder system. All of their studies have employed conventional plasticizers and not the energetic plasticizers reported here. However, all indications are that these plasticizers could be an important advance. LASL has obtained good results with pressed explosive formulations of DNPVEP and HMX (95% loading). They did observe that the conventional plasticizers used were not compatible with HMX, but that the DNPVEP was compatible with both HMX and plasticizer. The Livermore Laboratory, in conjunction with the Stanford Research Institute, has prepared test quantities of the fluorodinitroethyl vinyl ether polymer (FDNEVEP) which they also find encouraging. In order to modify the DNPVE polymer for use in castable explosive formulations, the Air Force Armament Laboratory and the Naval Weapons Center (White Oak) have converted some of the nitro groups in dinitropropylvinyl ether polymer to hydroxyl groups. This effort to obtain cross linking with the conventional diisocyanate cure has met with preliminary success. Expressions of interest have been received from a number of industrial sources.

One of the more exciting potential applications is in nitramine gun propellants now under consideration by the Air Force Armament Laboratory. Experimental nitramine gun propellant formulations employing nitrocellulose binders exhibit pressure excursions at normal gun operating pressures. This may be due to nitramine decomposition catalyzed by nitrous oxide produced by the lower burning nitrocellulose. Decomposition of DNPVEP and FEME plasticizer materials does not yield nitrous oxide. This, in conjunction with their high decomposition temperature, more nearly coincident with that of the nitramine, is highly encouraging.<sup>8</sup> Conventional gun propellant extrusion techniques should be feasible with this binder system inasmuch as it is readily soluble in the conventional solvents. Two hundred grams of DNPVE have been synthesized by LASL for this feasibility study. Thermodynamic calculations on hypothetical HMX formulations project excellent gas production and energy properties.

Using our synthetic procedures, large quantities of FEME plasticizers could be produced for use in feasibility studies with HMX and the DNPVEP binder. Additional members of this class of plasticizers will be prepared and efforts will also be directed towards improving the synthetic methods described in this report.



## Experimental

All starting materials were obtained from commercial sources. The dibromoalkanes were distilled and stored over molecular sieves. The proton sponge (2,6-di-*t*-butyl-4-methylpyridine) was chromatographed on silica gel (hexane) and stored at 0°. Proton nmr spectra were determined with a Varian T-60 spectrometer using tetramethylsilane as an internal standard. Benzene was dried over sodium and freshly distilled before use. Hexane (analytical reagent grade) was distilled from sodium hydroxide and the center cut stored over molecular sieves, as was freshly distilled methylene chloride.

General Procedure for Preparation of Ditriflates. The following procedure for the synthesis of alkyl ditriflates is illustrative of the method used for all of the ditriflates used in this work, except the one in the next section.

In a 100 ml round bottom flask equipped with a stirring bar, reflux condenser and drying tube were placed benzene (30 ml), dibromoalkane (6.15 mmol), silver triflate (18.4 mmol), and the proton sponge (1.9 mmol). The flask was wrapped in aluminum foil and heated to reflux in oil bath for 5 h. Aliquots were taken periodically and examined by nmr. The reaction was completed in this time period with virtually total conversion, alkylated benzenes being the minor by-product. The reaction mixture was filtered through a fritted funnel and a pad of magnesium sulfate and/or silica gel and washed with benzene to remove most silver salts. The solvent was removed on a rotary evaporator and cold carbon tetrachloride was added to the residue. The filtration was repeated, solvent removed and the product examined by nmr. Crude yields were 80-85%. This material was suitable for use in the conversion to the fluorodinitroethyl ethers in the next step, however, purification was effected using silica gel column chromatography and varying mixtures of hexane-methylene chloride.

Ditriflate of Diethyleneglycol. In a 100 ml round bottom flask equipped as above were placed triflic anhydride (30.0 mmol) and the proton sponge (32.4 mmol) in methylene chloride (25 ml). The dialcohol in methylene chloride (25 ml) was added dropwise over 90 min to the reaction mixture cooled to 0°C. The mixture was allowed to warm to room temperature and after two hours the reaction was complete (nmr analysis). The mixture was filtered and the solvent was removed. The crude ditriflate was purified by column chromatography on silica gel using varying mixtures of hexane-methylene chloride. The isolated yield of purified mixture was 61%.

General Procedure for Preparation of Fluorodinitroethoxymethylenes (FEME). In a 50 ml round bottom flask equipped with a stirring bar and a drying tube were placed the ditriflate (5 mmol), 2-fluoro-2,2-dinitroethanol (20 mmol), potassium carbonate (83.5 mmol) and methylene



chloride (20 ml). The heterogeneous yellow mixture was stirred at ambient temperature for several hours (3-18). Reaction was essentially complete in most cases in less than 5 h (nmr analysis). The mixture was diluted with water and the product was extracted with methylene chloride dried over magnesium sulfate, filtered and stripped of solvent (rotary evaporation). Alternatively, the heterogeneous mixture was filtered directly using a fritted funnel. The solid was washed copiously with methylene chloride. This procedure avoided emulsion problems. The products were purified using silica gel column chromatography and varying amounts of hexane-methylene chloride. The resulting colorless oils were obtained in purified yields of 50-60%.

Differential Thermal Analysis Conditions. DTA measurements were carried out on a Perkin Elmer DSC-2 with a Scanning Auto Zero attachment. Sample sizes were 1.5-2.5 mg for binder/plasticizer mixtures and 0.6-1.2 mg for high explosive mixtures. The DSC range was 5 mcal/second. The scanning range was 420-600°K and the heating rate was 10°K per minute. A scanning auto zero attachment was used to insure a flat baseline over the entire range.

## References and Notes

1. Private communication with Capt Robert Powers (AFATL).
2. S. A. Shackelford, R. R. McGuire, and R. E. Cochoy, Patent Secrecy Order, 10 June 1976.
3. S. A. Shackelford, R. E. Cochoy, M. D. Coburn, and G. J. Marchand, "New Energetic Binder Breakthrough: One-Step Monomer Synthesis and Polymer Characterization", Proceedings of the 1977 Air Force Systems Command Science and Engineering Symposium.
4. H. G. Adolph, "Synthesis and Properties of Bis(2-Fluoro-2,2-dinitroethyl) ether and the Lower Bis(2-Fluoro-2,2-dinitroethyl) polyoxymethylenes", Naval Ordnance Laboratory, White Oak, MD, MOL TR 67-48, 1 June 1967.
5. C. D. Beard, K. Baum, and V. Grakauskas, J. Org. Chem., 3673 (1973).
6. The authors wish to recognize significant preliminary experimental contributions by Lt J. P. Smith, Lt S. L. Clift, Capt W. Avila, Capt S. A. Shackelford, and Maj R. E. Cochoy.
7. K. Scribner, R. Elson, R. Fyfe, and J. P. Cramer, Proceedings of the Sixth Symposium (Intl.) on Detonation, Naval Surface Weapons Center, White Oak, MD, 466 (1976).
8. Attempts to take advantage of the low burning temperature, low molecular weight combustion gases, and high energy of nitramines in gun propellants have been tried for over 30 years. Problems of propellant explosion at gun operating pressures have never been solved. At the lower chamber pressures of rocket motors, successful use of nitramines has been possible, however, Trident propellants have exhibited some recent problems. Combustion of nitrate esters produces nitrous oxide. Russian workers have demonstrated that nitrous oxide catalyzes decomposition of nitramines. Recent studies in our laboratory suggest that DNPVEP and FEME, which are C-nitro compounds, do not yield nitrous oxide as a primary mass fragmentation product. Furthermore, nitrocellulose (NC) begins decomposition at 165°C vs HMX at 282°C. High speed photography of burning HMX/NC propellants show particles of HMX flying out of the burning NC matrix. Capt R. Powers and workers (AFATL) have observed that pressure excursions of nitramine propellant may be caused by premature decomposition of HMX catalyzed by nitrous oxide. They have postulated that these pressure excursions could be controlled if an energetic binder other than nitrocellulose were available which co-combusted with the nitramine and did not produce nitrous oxide. The higher combustion temperature and non-catalytic nature of DNPVEP/FEME in nitramine propellant formulations then suggests a possible break-through.

### Biographical Sketches

Captain Robert Alan Hildreth was born in Mattoon, Illinois on June 6, 1949. He graduated from Eastern Illinois University in 1971, receiving a B.S. degree in Chemistry, Physics, and Mathematics. He entered graduate school at Texas A&M University in 1971 and was commissioned in the Air Force through the AFROTC program in 1973 and was granted a delay from extended active duty in order to complete his graduate studies. He was awarded the Ph.D. degree in Chemistry by TAMU in 1976. In July, 1976 he began active duty at the Frank J. Seiler Research Laboratory (FJSRL). His interests have been primarily in the synthesis of nitroaliphatic compounds with potential uses as energetic plasticizers and monomers for energetic binders for rocket propellants and explosives. He is currently Task Chief for Energetic Materials Chemistry at FJSRL. Captain Hildreth was recently appointed as Secretary to the Joint Technical Coordinating Group for Munitions Development, the Working Party for Explosives. He is a member of the American Chemical Society and Sigma Pi Sigma.

Second Lieutenant Richard L. Wallace was born in Nagoya, Japan on November 1, 1955. He graduated from the United States Air Force Academy in 1978, receiving a B.S. degree in Chemistry. He is currently performing TDY at the Frank J. Seiler Research Laboratory while awaiting entry into Undergraduate Pilot Training at Vance Air Force Base, Oklahoma. He is currently working on the synthesis of energetic plasticizers.

Dr. Melvin Druelinger was born in South Bend, Indiana on December 7, 1940. He graduated from Indiana University in 1962 (B.S.) and from the University of Wisconsin in 1967 (Ph.D.). After spending a year at Iowa State University with Dr. O. L. Chapman as a postdoctoral research associate, he joined the faculty at Indiana State University where he is an Associate Professor of Chemistry. He has also spent a sabbatical year at Colorado State University in the research group of Dr. A. I. Meyers and a summer at the Frank J. Seiler Research Laboratory at the United States Air Force Academy as a USAF-ASEE Research participant. He is currently on leave from ISU as a University Resident Research Program participant (AFOSR) at the Frank J. Seiler Research Laboratory. His research interests include organic photochemistry, heterocycles, reactive intermediates, strained rings and cycloadditions as well as energetic binder precursors, energetic plasticizers and the chemistry of xenon difluoride.

Lieutenant Colonel Ben A. Loving (b. Edgewood, TX Dec 29, 1933) attended East Texas State University (B.S.) and was commissioned (AFROTC) in 1956; and the University of Texas at Austin (M.A. 1959). He resumed graduate study in 1965 and was awarded the Ph.D. in Physical Organic Chemistry with a minor in Fuels Engineering from the University of Utah in 1968. After serving as Asso. Prof. at Carroll College, Waukesha, Wis.,

and NSF Research Fellow at the Institute of Paper Chemistry, Appleton, Wis. (1959-60), Colonel Loving entered onto active duty in September, 1960. He served as a Munitions Test Engineer at Hill Air Force Base, Utah (AFLC) (1960-62) and as Chief, Technical Br., AF Aerospace Fuels Field Office (AFLC), Tokyo, Japan (1962-65). After receipt of his doctoral degree, he was assigned to the AF Materials Lab (1968-72). There he developed and evaluated a less flammable hydraulic fluid (synthetic hydrocarbon) now procured under MIL-H-83282; served as staff scientist in the Technical Operations Office; and as Chief of the Chemical Physics Branch, Electronics Div., where he was responsible for work in dye lasers, liquid crystals, thermo and impact physics. From 1972-75 he was Research Manager for Chemistry and Weaponry, Director of Science and Technology, AF Systems Command, Andrews AFB, Washington, D.C. Since July 1975 he has been Director of Chemical Sciences, Frank J. Seiler Research Laboratory (AFSC), USAF Academy, CO with programs in Energetic Materials, Electrochemistry, and Molecular Dynamics. He has 13 technical publications, is a member of the American Chemical Society, Sigma Xi; and will be listed in the 14th Ed of American Men and Women in Science. He currently serves on the DOD JTCG/MD/Working Party for Explosives, is listed as an authority in DEAs with the Republic of France and is an approved National Research Council Post Doctoral Research Director for research related to lasers and energetic materials.

IMPROVED CORROSION AND MECHANICAL BEHAVIOR  
OF ALLOYS BY MEANS OF ION IMPLANTATION

BY

JAMES K. HIRVONEN

AND

JAMES W. BUTLER

RADIATION TECHNOLOGY DIVISION

NAVAL RESEARCH LABORATORY  
WASHINGTON, D.C. 20375

Improved Mechanical and Corrosion Behavior of Alloys  
By Means of Ion Implantation

Abstract

Ion implantation is being investigated as a technique for the beneficial modification of surface-sensitive, life-limiting properties of metals, including resistance to corrosion, wear, and fatigue. Ion implantation is a process of accelerating ions to high velocities and directing them into the near-surface regions of materials (e.g., alloys) to produce in essence a different material (alloy) in the near-surface region. Ion implantation can produce a graded alloy from the surface to the unchanged underlying bulk alloy so that both the surface alloy and bulk alloy can be independently optimized. It may be emphasized that no coating is involved, and hence there are no adhesion problems or macroscopic dimension changes such as those associated with coatings. On a laboratory scale it has already been demonstrated that ion implantation can produce corrosion resistant surfaces on an otherwise corrosion susceptible material. For example, the corrosion (pitting) resistance of M-50 bearing alloy (extensively used in turbojet engines) has been demonstrated to be improved when implanted with high concentrations of chromium. The technique promises the ability to produce unique metastable corrosion-resistant surface alloys without additional processing steps. The sliding wear rate between various steel alloys has been reduced by as much as two orders of magnitude as a result of implantation with selected elemental species, including nitrogen, cobalt, and titanium. (This technique is already being exploited by industry in England, where much of its development is occurring.) The implantation technique has also been used to increase fatigue lifetimes in a number of alloys, including low-carbon steel (by a factor of 50 to 100), titanium, stainless steel, and maraging steel (by a factor of 8 to 10). Experimentation is now being directed toward other materials of major DoD interest, such as titanium alloys.

## Introduction

This paper describes the application of ion implantation (a relatively new technology for semiconductor materials) to some of the oldest problems affecting equipment: problems that lead to deterioration, malfunction, and eventual breakdown. These problems include corrosion, wear, and fatigue. All three problems are surface-sensitive and have been found to be amenable to amelioration by ion implantation surface treatment.

Corrosion, wear, and metal fatigue are extremely costly to all DoD services. The cost of corrosion alone to DoD has been estimated to exceed eight billion dollars a year. The additional factors of high reliability and maintainability generally desired of DoD equipment provide an added impetus for solving such problems. One response to these problems has been the (intensive) development of new materials; another response has been the development of surface protective coatings.

In spite of these advances there still exist specific problem areas not amenable to either improved bulk alloys or protective coatings. A given application is likely to involve several incompatible requirements for an alloy: reasonable cost, machineability, desirable surface properties (e.g., corrosion resistance), and desirable bulk properties (e.g., hardness, strength, or toughness). Surface coatings are sometimes used in attempts to optimize independently the surface and bulk properties required and can have several advantages, including low cost, relative ease of application, and ability to cover complicated geometries. For certain applications, however, coatings have limitations, e.g., adhesion problems, nonuniformity, porosity, and macroscopic dimensional changes of the treated surface.

The remainder of this paper discusses ion implantation as an alternative surface treatment method which shows promise of ameliorating corrosion, wear, and fatigue problems within DoD. Ion implantation is not a coating technique. Implantation consists of forcibly injecting selected elemental ion species beneath the surface of materials by means of a high-energy ion beam from an accelerator (usually at tens to hundreds of kilovolts). This injection process produces an intimate alloy of the implanted and host elements without producing a sharp interface characteristic of most coatings and hence avoids the related adhesion problems. The resultant depth distribution and alloy composition depend on the energy and atomic number of the projectile as well as on the atomic number of the host. Typically, depths of hundreds to thousands of angstroms are achievable with concentrations of up to 50 at. %. It should be stressed that ion implantation is not a thermodynamical equilibrium process and that metastable alloys can be formed without regard for the conventional considerations of solid solubility and diffusivity, since any elemental species can be implanted into any other material. Heating of the implanted alloy to sufficiently high temperatures will, of course, ensure equilibrium conditions, but several durable metastable (or amorphous) phases with potentially interesting physical properties have been formed by

implantation. Figure 1 summarizes many of these factors pertaining to ion implantation for materials modification. The ability to control and reproduce the ion beam parameters listed in Figure 1 is especially important to its large scale commercial usage for implanting (doping) semiconductor wafers with high reproducibility (typically less than 3% dose difference on different wafers or between different points on a single wafer).

Figure 2 shows a schematic diagram of a typical research-type ion implantation system. As depicted, atoms are ionized in an ion source, accelerated to the desired energy, analyzed according to mass by a magnet to select the desired species, and then electrostatically raster scanned over the target to ensure dose uniformity of the implantation. The implanted dose (in terms of impurity atoms per unit volume) is obtained from the ion beam charge, the implanted target area, and the implanted species depth distribution.

### Improving Corrosion Resistance

Implantation has been utilized as a research tool for studying basic corrosion mechanisms and also as a technique for improving the corrosion resistance of materials. Both aqueous corrosion and high-temperature oxidation phenomena have been experimentally studied.

#### Aqueous Corrosion

Corrosion is a significant factor for rejection of DoD equipment subcomponents, such as bearings, at Naval Air Rework Facilities. The annual cost for replacement of turbojet engine bearings from corrosion alone is estimated to exceed \$1.0 M. NRL is currently engaged in a project with the Naval Air Propulsion Center (Trenton, N.J.) to evaluate and develop ion implantation treatments for improving the pitting corrosion resistance of AISI M50 bearing alloy used extensively in Navy turbojet engines. In particular, it is found that engines which experience intermittent usage exhibit the worst corrosion problems. The corrosion is exhibited by local pitting at contact points between the bearing race and the rollers (or balls) after engine shutdown. Measurements at NAPC confirmed that the implantation of corrosion resistant elements (e.g., chromium) into M-50 test rods does not degrade the rolling-contact fatigue life of the bearing material. (Coatings usually do degrade fatigue life.) Initial simulated field service corrosion tests with a saltwater contaminated polyester lubricant (such as found in actual aircraft engines) show that the localized (pitting) corrosion resistance of chromium-implanted M-50 samples is significantly better than that of the unimplanted material. An illustration of these results is shown in Figure 3. These simulated field corrosion tests are being accompanied by standard electrochemical and surface analytical tests in order to characterize the implanted surface in an effort to optimize the choice of implantation variables (e.g., ion species, dose (concentration), and energy (depth)) for corrosion resistance. Although it is too early to evaluate implantation as a means of effectively controlling this problem, the results thus far look very promising. For



this application it should be noted that the technique has the important potential advantage of not changing the macroscopic dimensions of the precision bearings and should be applicable to otherwise finished components (i.e., the process can fit onto the end of an existing production line). The cost associated with implanting aircraft quality bearing components is estimated to be a small fraction of their initial cost.

#### High-Temperature Oxidation

The high-temperature oxidation resistance of several metals has also been improved by ion implantation. In some experiments the effect of the implanted species persists to depths much beyond that of the initial relatively shallow implanted depth concentration profile. Much of the published work in this area originates from the Atomic Energy Research Establishment at Harwell, England. Figure 4 shows the results of an NRL investigation of the oxidation kinetics of barium-implanted titanium. Implantation is found to reduce significantly the growth rate of the oxide for oxide thicknesses much greater than the initial depth of the implanted barium. Transmission electron microscopy studies of similar samples shows the formation of a perovskite-type structure (barium titanate) which has been postulated (by Harwell) to form along easy diffusion paths for oxygen (e.g., grain boundaries) and thus to serve to impede such diffusion.

Since most of these studies are still in a research stage, no general statements regarding applicability can yet be given. The Harwell group has, however, described the improvement in lifetimes of oil burner injection nozzles used in power generation plants in England by at least a factor of four by means of implanting species such as nitrogen and boron into the surfaces around the orifice. This is an example of an application where minimum equipment downtime is particularly important because of the associated high cost of shutdown.

#### Improved Mechanical Properties

In the past few years there has been increasing research interest in applying ion implantation to improve materials mechanical characteristics, such as hardness, friction, wear resistance, and fatigue lifetime. The following examples describe some of those efforts in which NRL is involved.

#### Surface Hardening of Gas Bearing Materials

Guidance and navigation equipment commonly uses gas under pressure to support and to lubricate bearing subcomponents during operation. For some of these applications powder-processed Be (containing BeO precipitates) is used as a bearing material because of its high rigidity, low mass (giving a low moment of inertia), and its thermal expansion properties. These relatively soft bearing component surfaces are currently coated with a hard material (such as chromium oxide) to reduce wear occurring mainly during startup and shutdown. These hard

coatings are expensive to machine and can suffer from adhesion and porosity problems. In an effort to reduce some of these problems a collaborative research program\* is being conducted by NRL and the Charles Stark Draper Laboratory, Inc. (Cambridge, MA) in order to examine the possibility of forming hardened (wear resistant) surface layers by means of ion implantation. The initial thrust of this work has been to perform multiple high-dose implantation of boron into beryllium at different energies to build up a uniform  $\text{Be}_{0.9}\text{B}_{0.1}$  alloy extending approximately  $0.8 \mu\text{m}$  into the bulk. Boron was chosen because certain Be-B phases are known to be very hard. The initial results of micro(indentation)hardness measurements made on these layers is shown in Figure 5 for various subsequent thermal annealing treatments. The microhardness values of the implanted layers are significantly increased to the point where the diamond stylus no longer leaves a permanent indentation for the heaviest load (5 gm) used. These increased hardness values presumably arise from the formation of a boron-beryllium phase. Although the microhardness values obtained with very light loads on such thin layers must be regarded as being only qualitative, they do serve as useful comparative guides.

Attempts have been made to thermally diffuse boron from an outer layer (diffusion source) into beryllium to harden the surface. However, it appears that beryllium atoms preferentially diffuse outward into the boron (rather than the boron diffusing into the beryllium) thus making this technique unsuitable for preparation of desired surface alloys. Whether implantation will prove to be an appropriate fabrication technique for this particular use requires further study. Nevertheless, this example serves to demonstrate the potential advantages of ion implantation as a surface modifying technique for small, critical parts. These potential advantages include the following: no macroscopic dimension changes, superior adhesion than coatings (because of no abrupt interfaces), and no porosity problems associated with some coatings for this application.

#### Sliding Wear Reduction

Following the early work on wear reduction at Harwell, researchers at NRL have investigated the effect of ion implantation on the sliding wear of type-416 stainless steel and AISI-52100 bearing alloy steel. The experimental apparatus consisted of either a ball-on-cylinder geometry (AISI-52100 steel tests) as shown in Figure 6 or a crossed cylinder-on-cylinder geometry (type-416 stainless steel tests). In both cases the upper part was under a deadweight load (2-kg), and the lower part (the race) was rotated while partially submerged in an polyester lubricant bath, resulting in boundary lubrication conditions. The amount of wear was determined by an optical-microscope examination of the wear scar on the upper stationary ball bearing (or on the upper stationary cylinder for the type-416 stainless steel alloy tested). As indicated in the figure of the test geometry, different portions of each component were implanted with nitrogen ions at an energy of 40 keV to a fluence of  $10^{17}$  nitrogen ions/cm<sup>2</sup> (about  $2 \mu\text{g}/\text{cm}^2$ ). The

\*Under Navy Strategic Systems Project Office support

nitrogen ions are expected to penetrate about 0.05 to 0.1  $\mu\text{m}$  into the steel surfaces, giving a local peak volume concentration of about 30 atomic percent. Although such wear tests commonly show significant problems regarding reproducibility, a factor-of-two improvement was commonly found for the nitrogen-implanted 52100 samples.

Since the type-416 stainless steel samples showed much greater wear rates than did the type-52100 bearing alloy steel samples, the type-416 samples were more suitable for determining the effect of the various parameters on the wear rate, hence were more suitable for a study of the mechanisms responsible for the wear reduction. Wear tests were performed for different combinations of unimplanted and implanted surfaces. The results are shown in Figure 7. These runs were all made with a 2-kg load for various times, which correspond to the total distances traveled as shown in the figure. The dimensionless wear volume has been arbitrarily normalized to unity for the unimplanted cylinder on the unimplanted race. The effect of implanting the rotating race (lower two curves) is seen to reduce the amount of wear by a factor of approximately 25 to 50 as compared with the unimplanted-race curves (upper curves). This large reduction in the wear is believed not to be merely the result of a nitriding of the alloy skin since the amount of material removed from the rotating member is greater than the penetration depth of the implanted nitrogen ions. The reduction has been attributed to nitrogen (a mobile-interstitial species) decorating dislocations produced during the wear, impeding their motion, and producing a hard skin. The persistence of the effect is attributed to the inward migration of the implanted (interstitial) nitrogen atoms under the high temperatures and stresses produced during the wear process. The figure also shows that implantation of argon, a chemically inert species, provides no improvement in wear resistance. Hence, the effect is not due solely to either the radiation damage or the compressive stresses that are produced by the implantation process. The reduction in wear was observed for both a complex lubricant (a polyester jet-engine lubricant) and a simple lubricant (polyphenol ether). Some other species (Ti, Co) provided a reduction in wear by a factor of eight to ten, whereas some species (Cr, Ni) gave no effect. The nitrogen implanted samples were also able to support appreciably higher loads than the unimplanted samples before experiencing catastrophic wear rates.

Several analytical techniques are currently being used for the investigation of these implantation effects, including Auger electron spectroscopy, transmission electron microscopy, scanning electron microscopy, and wear particle analysis. Wear particles from the tests shown in Figure 7 have been analyzed by a technique (Ferrography) that magnetically removes the wear particles from the lubricant and affixes them onto a surface for subsequent characterization of their concentration, sizes, and shapes either by means of optical or scanning electron microscopy. Results comparing unimplanted and implanted couples indicate that there is no significant change in the shape or size distribution of the wear particles produced even though they differ in quantity by a factor as much as several hundred. This observation suggests that implantation is reducing the initiation rate or growth rate of cracks.

Even though the basic and fundamental features of the responsible mechanisms are not known as yet, the systematic study of many wear systems by the Harwell group has allowed significant industrial exploitation of the process to reduce wear in a number of industrial situations. Some of these applications are described in a later section.

### Fatigue Lifetime

The Harwell group has reported that fatigue lifetimes for nitrogen-implanted stainless steel, titanium, and maraging steel are 8 to 10 times longer than for the unimplanted materials. On the basis of this report, a collaborative effort between researchers at NRL and at the State University of New York at Stony Brook was undertaken to study the effect of ion implantation on the fatigue lifetime of AISI 1018 steel. The preliminary results of this study are given below.

The experiments consist of measuring the time-to-failure of cylindrical samples (with a central reduced-cross-section segment) placed under alternate compression and tension while rotating under a fixed load (stress) in an apparatus such as that shown in Figure 8. The lifetime of unimplanted samples has been compared to that of samples whose central (reduced area) region has been implanted with 150-keV nitrogen ions ( $2 \times 10^{17}$  N ions/cm<sup>2</sup>). These tests have been performed for applied stresses intermediate in value between (i) the yield strength (the stress threshold for plastic deformation of the bulk material) and (ii) the endurance limit (the stress level at which the material will withstand flexing indefinitely). Preliminary results are shown in Figure 9; the applied stress level (ordinate) is plotted versus the number of cycles to failure (abscissa) on a semilogarithmic plot. The closed circles (unimplanted samples) are contained within a broad band whose width is indicative of the experimental scatter usually found in such measurements. The data for the implanted samples are represented in Figure 9 by open symbols. It is apparent that for stresses below the yield strength (viz., below 57 kpsi) the fatigue lifetimes of nitrogen-implanted type-1018 steel samples can be significantly improved. The datum points at  $10^8$  cycles represent implanted samples which have not yet failed even after having flexed 50 to 100 times as many cycles as the unimplanted samples at failure. These results are indicative of the formation of a nitrogen-rich atmosphere associated with surface dislocations; the nitrogen atoms presumably tend to suppress the movement of (i.e., to pin) the dislocations, which otherwise would coalesce to initiate cracks, leading to failure.

### Present Industrial Applications

To date, the only known industrial applications of this technique for nonsemiconductor purposes are those being pursued by the Harwell group in association with several industries. Because of the proprietary relationship which can exist between Harwell and private industry it is likely that many applications exist other than those described below. The applications can be grouped into three main areas: (I) cutting and slitting operations, (II) prevention of corrosive

and adhesive wear, and (III) extrusion operations and applications where large surface forces occur. Group I includes components (such as paper and synthetic-rubber slitters, punches, and taps) whose lifetimes were extended by a factor of two to twelve by nitrogen implantation. Group II includes tool inserts and forming tools where carbon or nitrogen implantation appreciably reduces the adhesive wear of the tools. Group III includes cemented tungsten carbide wire drawing dies. Implantation of carbon into these components increases the throughput (for a given permissible die size tolerance) by a factor of three to five.

### Ion Implantation Equipment

Although implantation in metals is mainly at the research stage, there exist high throughput production ion implanters for semiconductor processing which could be adapted for metals processing. There appear to be no fundamental problems of scaling up the present implanters to provide the higher beam currents necessary for the higher doses generally required for metals work. In addition, the rigid requirements for ion beam purity and dose uniformity that are encountered with semiconductor wafers can be significantly relaxed in the case of metals, resulting in simpler and cheaper machines. An important consideration for metals will be the development of dedicated-element ion sources and suitable vacuum chambers that will allow the desired areas of the intended targets to be uniformly exposed to the ion beam. Commercial prototypes of these are already being constructed at Harwell to allow components several feet in size to be implanted.

### Summary

The application of ion implantation to metals has shown several large, durable, and sometimes unpredicted beneficial effects on their chemical and mechanical properties. The basic understanding of some of these effects is still at a primitive stage; however, there exists sufficient information to permit industrial utilization for certain applications (Harwell). Potential applications require individual research and developmental study. There appear to be no fundamental technological problems in scaling up present ion implanters for treating high-dose, large-area metal components, given the need.

## ION IMPLANTATION PARAMETERS

- IMPLANTED ELEMENTS – VIRTUALLY ANY ELEMENT FROM HYDROGEN TO URANIUM CAN BE IMPLANTED.
- ION ENERGIES – NORMALLY 2 TO 200 KeV. ENERGIES UP TO 5 MeV MAY BE OBTAINED WITH THE VAN DE GRAAFF ACCELERATOR.
- ION RANGES – VARY WITH ION ENERGY, ION SPECIES AND HOST MATERIAL. RANGES NORMALLY 0.01  $\mu\text{m}$  TO 1.0  $\mu\text{m}$ .
- RANGE DISTRIBUTION – APPROXIMATELY GAUSSIAN. CHOICE OF ENERGIES ALLOW TAILORED DEPTH DISTRIBUTION PROFILES.
- CONCENTRATION – FROM TRACE AMOUNTS UP TO 50% OR MORE.
- HOST MATERIAL – ANY SOLID MATERIAL CAN BE IMPLANTED.
- SPECIAL EFFECTS – SPUTTERING, RADIATION DAMAGE, RADIATION ENHANCED DIFFUSION.

## ION IMPLANTATION SYSTEM

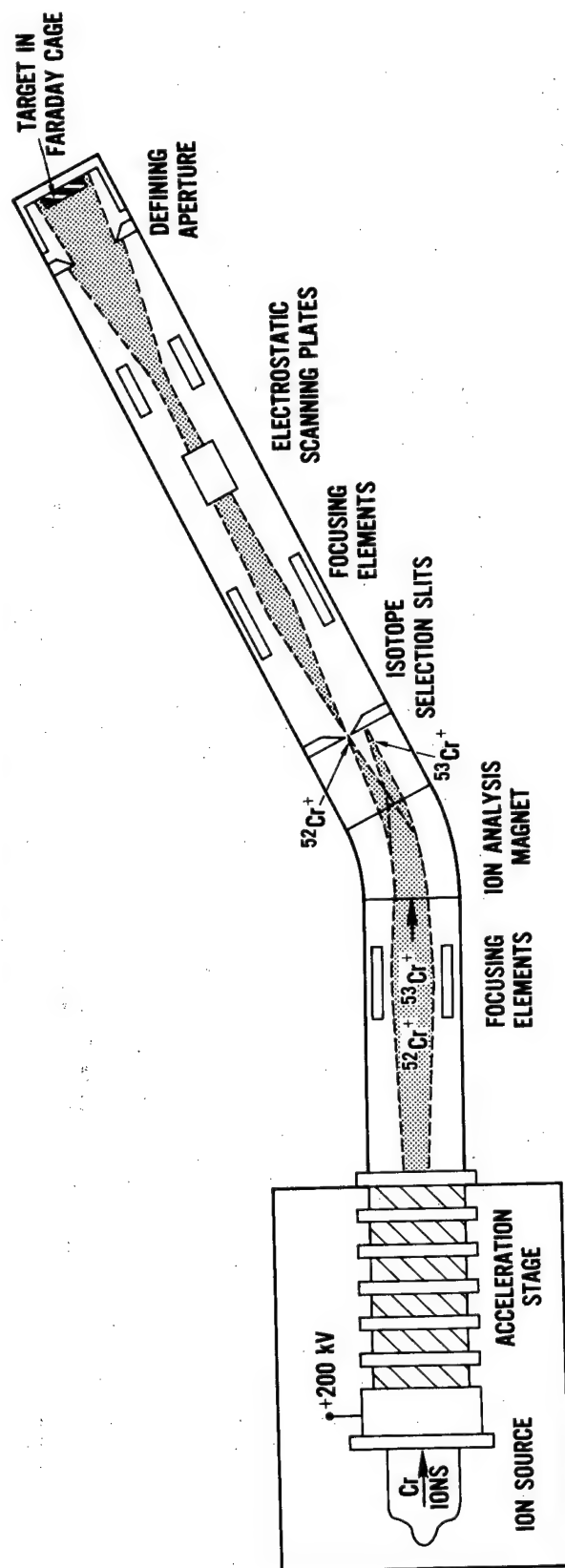


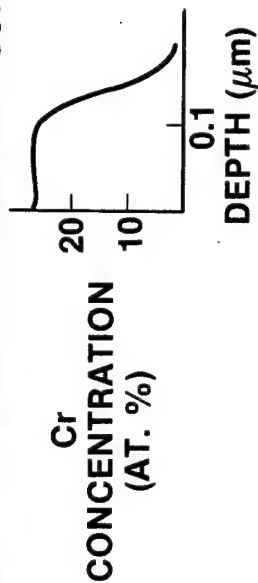
Figure 2. (U) Schematic diagram of research-type ion implantation system employed at NRL. It is basically the same as an isotope separator except that the acceleration potential is high enough to produce significant penetration of the host substrate.



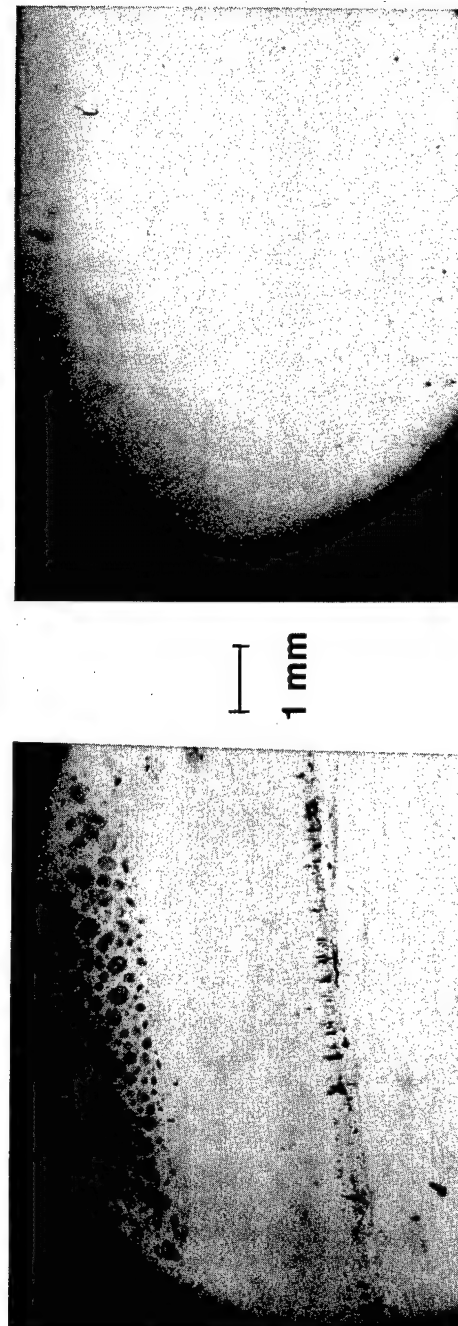
# CORROSION-RESISTANT BEARINGS BY ION IMPLANTATION

PROBLEM: PITTING CORROSION IN M50 ALLOY BEARINGS

APPROACH: PRODUCE CORROSION-RESISTANT SURFACE ALLOYS BY ION IMPLANTATION



RESULTS: M50 SURFACES FOLLOWING SIMULATED FIELD SERVICE TEST



## UNIMPLANTED

## Cr-IMPLANTED

Figure 3. (U) In the left-hand photograph we see the ordinary corrosion that occurs along the contact line between a rod and disk of M-50 alloy with a chloride-contaminated polyester lubricant between them. In the right-hand photograph we see less corrosion, with all conditions the same except that the M-50 surface was implanted with chromium ions.



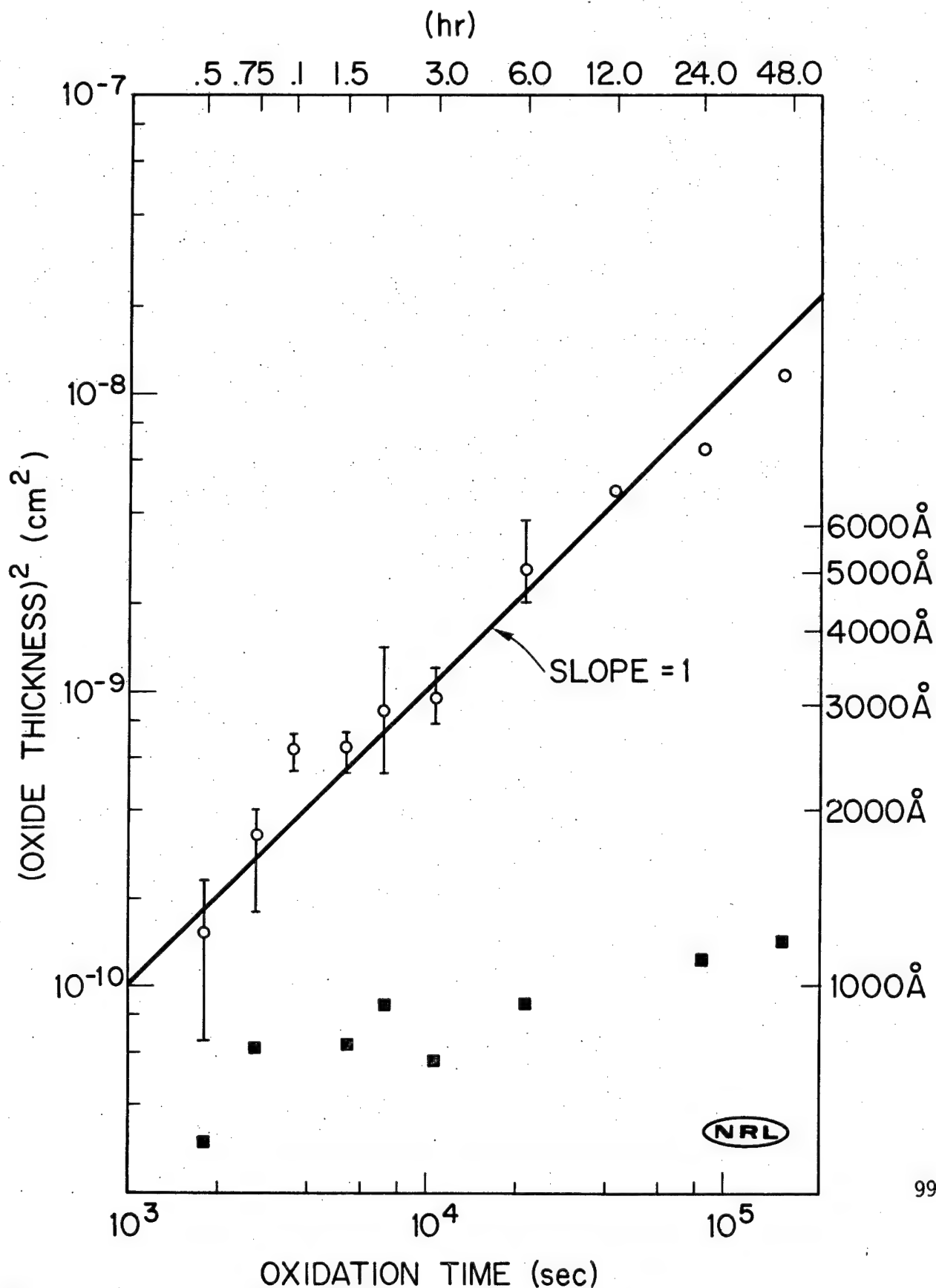


Figure 4. (U) Relationship between thickness of oxide layer on titanium and time in air at 600°C for unimplanted titanium (open circles) and barium-implanted titanium (closed squares).

# KNOOP MICROHARDNESS MEASUREMENTS ON BORON-IMPLANTED Be (~10 AT. % TO 0.8 $\mu$ M DEPTH)

| SAMPLE<br>TREATMENT         | LOAD | HARDNESS (KG/mm <sup>2</sup> ) |                     |
|-----------------------------|------|--------------------------------|---------------------|
|                             |      | UNIMPLANTED<br>REGION          | IMPLANTED<br>REGION |
| ALL VALUES ± 10%            |      |                                |                     |
| AS - IMPLANTED              | 5 GM | 490                            | 950                 |
|                             | 2    | 570                            | 1520                |
|                             | 1    | 540                            | NO DEPRESSION       |
| POST 437°C<br>ANNEAL (1 HR) | 5    | 460                            | 1150                |
|                             | 2    | 330                            | 1830                |
|                             | 1    | 240                            | NO DEPRESSION       |
| POST 650°C<br>ANNEAL (1 HR) | 5    | 400                            | NO DEPRESSION       |
|                             | 2    | 310                            | NO DEPRESSION       |
|                             | 1    | 230                            | NO DEPRESSION       |

994

Figure 5. (U) Microhardness values (indentation) for unimplanted and boron-implanted beryllium gas bearing material as a function of load and thermal annealing treatments.

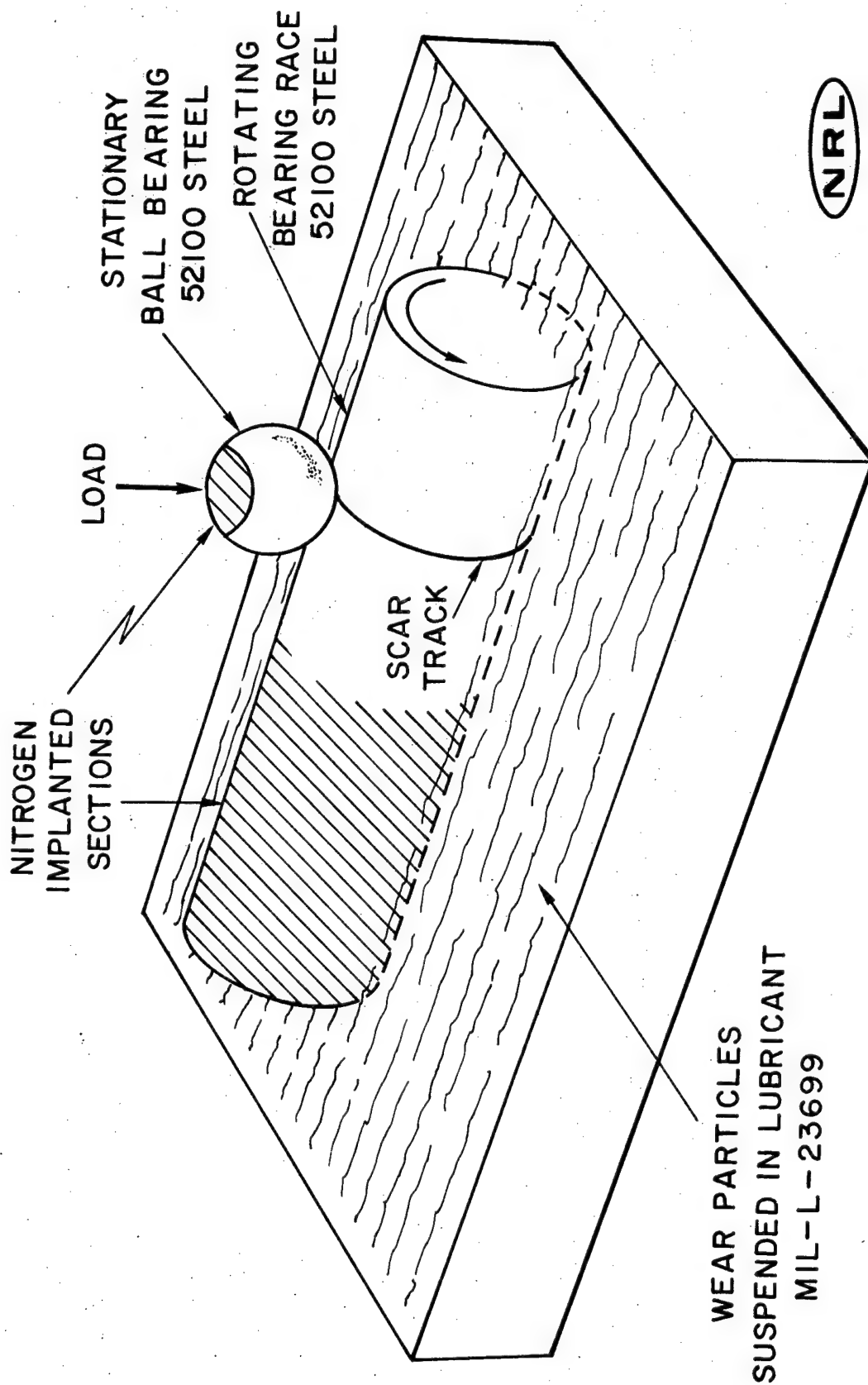


Figure 6. (U) Schematic drawing of ball-on-cylinder test arrangement for measuring sliding-wear rates of implanted and unimplanted specimens.

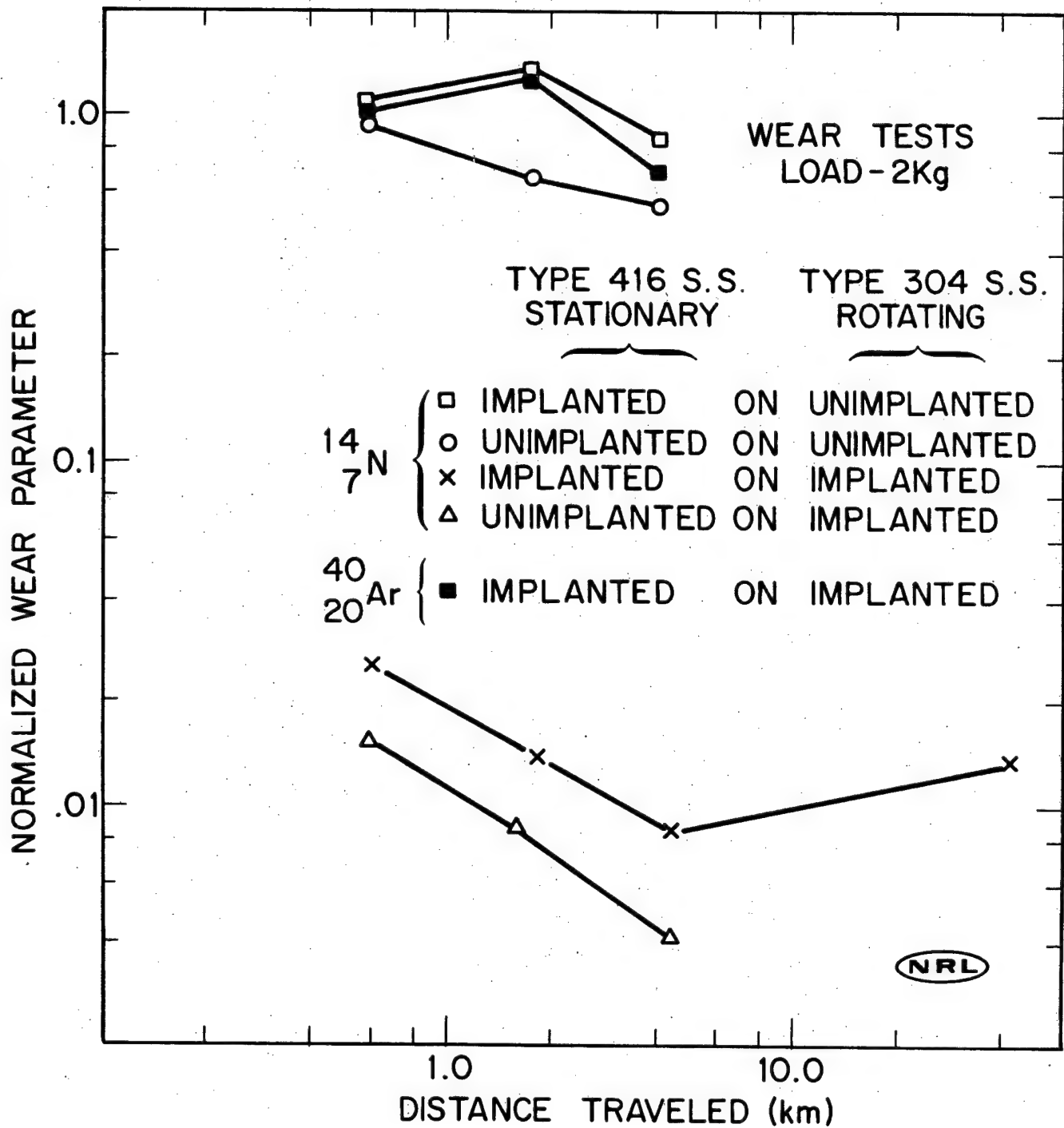
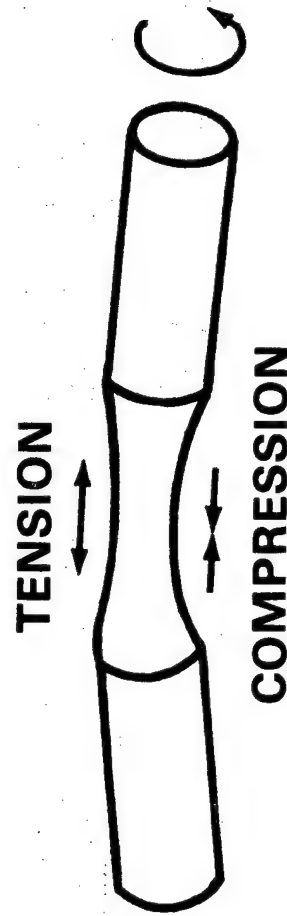
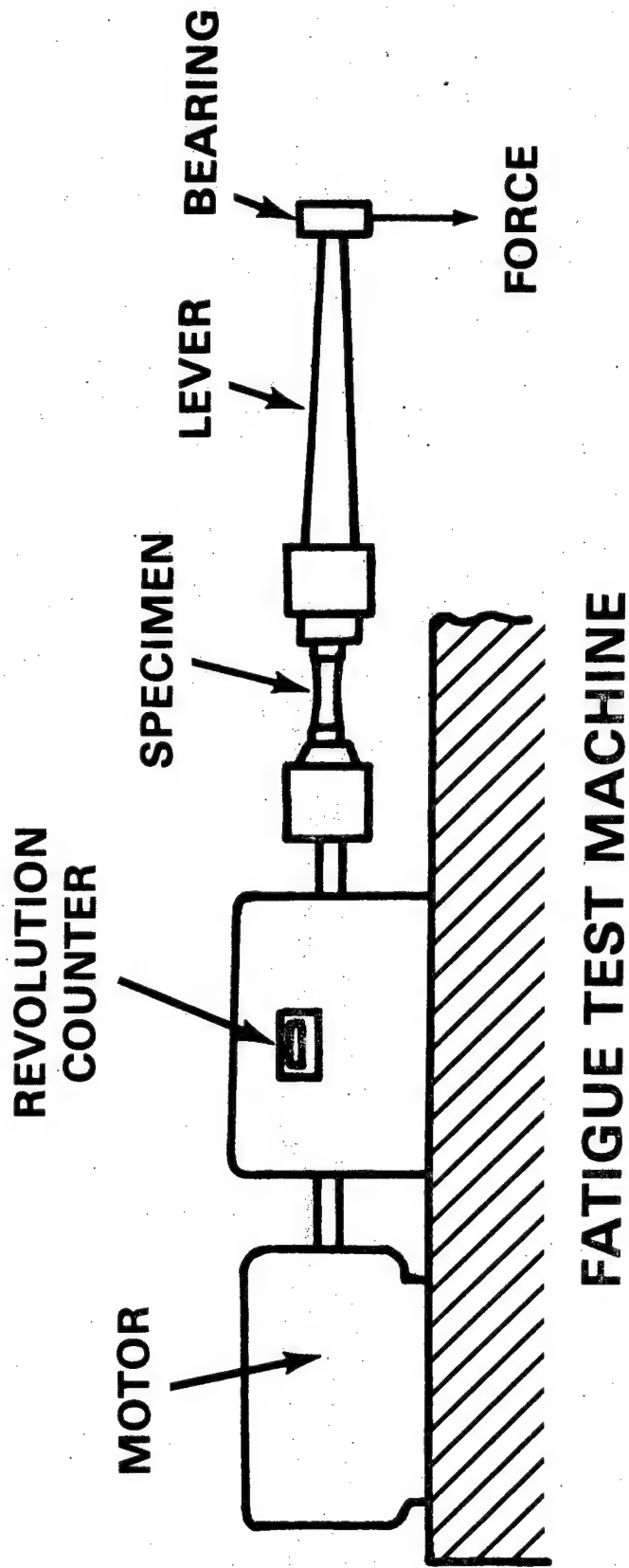


Figure 7. (U) Normalized wear rates for a variety of situations in which a fixed cylinder of type-416 stainless steel is held under a deadweight load against a rotating cylinder of type-304 stainless steel.



## FATIGUE — TEST SAMPLE

Figure 8. (U) Schematic diagrams of rotating-beam fatigue-test machine and fatigue-test specimen. Each point on the surface of the specimen undergoes alternating tensile and compressive stress.

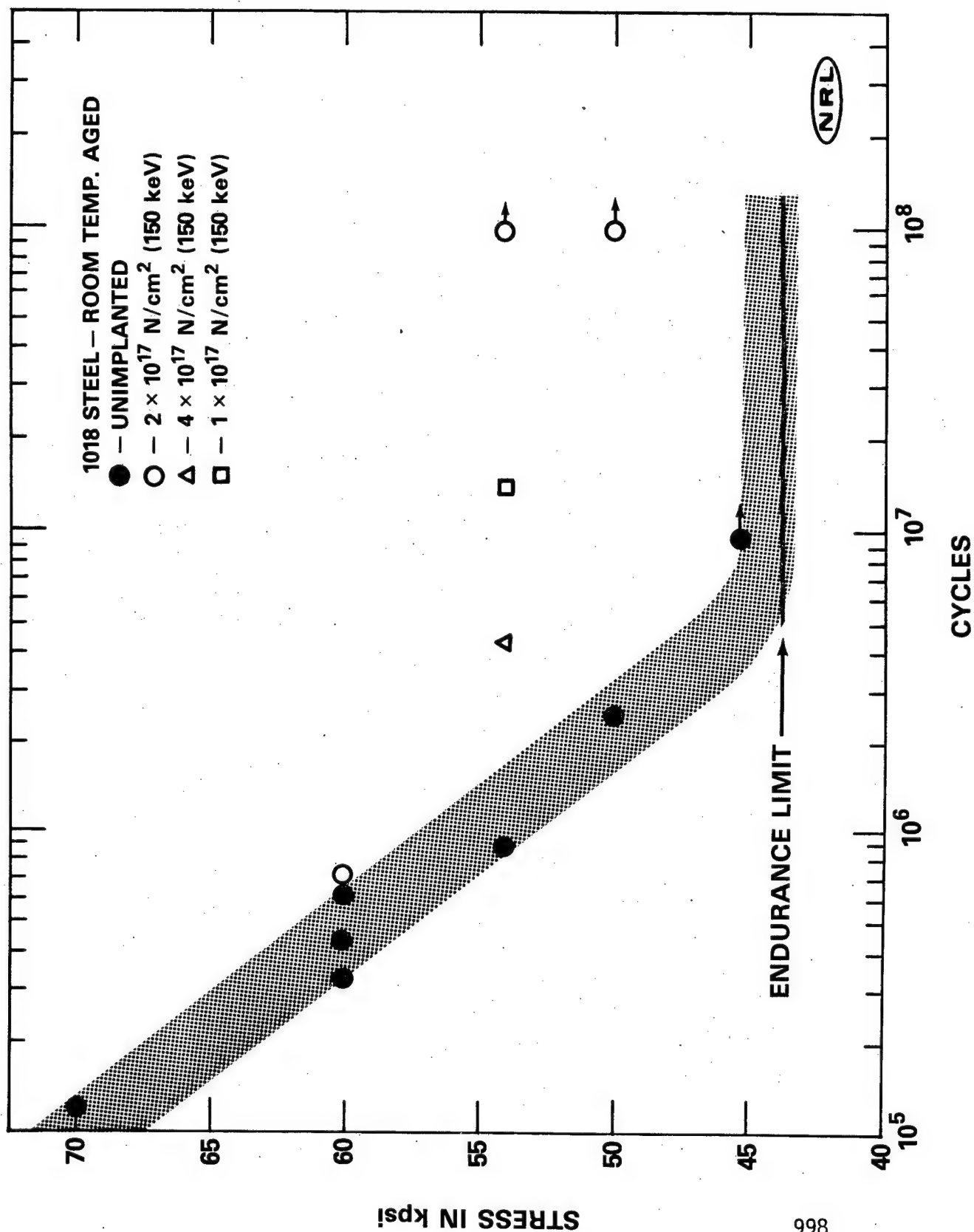


Figure 9. (U) Lifetime (in units of cycles) of fatigue crack growth for various neutron doses

### Biographical Sketches

After obtaining a Ph.D. degree in physics (1971) under a joint Rutgers University/Bell Laboratories graduate research program, James K. Hirvonen joined the Naval Research Laboratory. His research interests and publications have been in the area of applying high-energy ion beams for near-surface materials analysis and also for modification of the surface properties of materials. He is Head of the Ion Implantation Section of the Radiation Technology Division at NRL. He is currently editing a book on nonsemiconductor applications of ion implantation and serving as the Navy liaison representative to a National Materials Advisory Board committee which is evaluating the potential of ion implantation for DoD applications. He is a member of the Bohmische Physical Society.

James W. Butler received a Ph.D. degree in physics from Rice University in 1951 and joined the Naval Research Laboratory. At NRL he has worked on a wide variety of projects, ranging from basic research in experimental nuclear physics to radiation hardening of satellites to certain nonacoustic methods involved in antisubmarine warfare. He is Head of the Materials Modification and Analysis Branch, which has a broad program of research in the modification of the surface properties of materials by means of ion implantation and in the analysis of the near-surface regions of materials by means of high-energy ion beams. He was one of the editors of the Proceedings of the Third International Conference on Ion Beam Analysis (1977). These Proceedings appeared in two issues of the journal Nuclear Instruments and Methods (1978).

SYMMETRIC BODY VORTEX WAKE CHARACTERISTICS  
IN SUPERSONIC FLOW

BY

William L. Oberkampf, Ph.D.

Donald C. Daniel, Ph.D.

Air Force Armament Laboratory

Armament Development and Test Center  
Eglin AFB, Florida

1000



### List of Symbols

|            |   |
|------------|---|
| $d$        | Body diameter   |
| $h$        | Circulation contour size (square $h \times h$ )               |
| $M$        | Mach number   |
| $P_o$      | Total pressure  |
| $R_d$      | Reynolds number based on body diameter                        |
| $R_c$      | Cross flow Reynolds number ( $R_d \sin \alpha_b$ )            |
| $u, v, w$  | Velocity components in body axis system (Fig. 1)              |
| $U_c$      | Magnitude of cross-flow velocity ( $\sqrt{v^2 + w^2}$ )       |
| $U_\infty$ | Freestream speed  |
| $x, y, z$  | Body coordinate system (Fig. 1)                               |
| $\alpha_b$ | Angle of attack of the body                                   |
| $\Gamma$   | Local circulation in cross-flow plane (contour $h \times h$ ) |
| $\Gamma_t$ | Total circulation cross-flow plane                            |
| $\psi$     | Stream function   |

### Subscript

|          |                       |
|----------|-----------------------|
| $\infty$ | Freestream conditions |
|----------|-----------------------|

Symmetric Body Vortex Wake Characteristics  
in Supersonic Flow

Abstract

High angle of attack aerodynamics has become increasingly important for highly maneuverable fighter aircraft and tactical missiles. At these high angles vortices, which can create very difficult controllability problems, form on the leeward side of the airframe. In order to obtain a better basic understanding of the body vortex phenomena, a series of experiments were conducted in Supersonic Wind Tunnel A at the Arnold Engineering Development Center. Over 6000 total pressure, Mach number, and orthogonal velocity component measurements were made at various survey planes on the leeward side of a pointed body of revolution for angles of attack up to  $25^\circ$ . Measurements were made at two freestream Mach numbers and two Reynolds numbers. The results presented provide the first accurate characterization of the geometry and flow properties of the supersonic body vortex wake. These results include cross-flow plane velocity, pressure and Mach number distributions. Local and total vortex circulation strengths are also presented. These basic research results should be of great value in verifying future, advanced fluid dynamics computations of three dimensional viscous separated flows for aircraft and missiles.

## Introduction

During the last several years there has been considerable interest in the aerodynamics of aircraft and missiles at high angles of attack. This interest has been generated primarily by desires, and requirements, to have more highly maneuverable fighter aircraft and tactical missiles. From man's earliest experiences with airframes, it has been realized that increasing the angle of attack generally creates more lift which, with proper orientation, can be used to achieve desired, and often rapid, changes in a flight vehicle's trajectory.

Unfortunately, as the angle of attack of a missile or aircraft is increased beyond certain limits, complex flow phenomena can result. In the case of tactical missiles, which tend to have long body lengths compared to their maximum diameter, vortices form along the leeward side of the body. These vortices come into existence at angles of attack of approximately  $10^\circ$  as a result of separation of the boundary layer from the surface of the missile's body. The vortices initially form in symmetric pairs (see Figure 1) and they become larger as the distance from the nose increases. Maintaining control of a missile whose fins or wings are immersed in these vortices is often very difficult, and a better understanding of the basic phenomena is of great importance to the designers of present and future USAF conventional munitions.

The formation of body vortices at high angles of attack was first noted by Allen and Perkins<sup>1</sup> of the National Advisory Committee for Aeronautics (NACA), Ames Research Center in the early 1950's. Later Jorgensen, also of NACA, and Perkins<sup>2</sup> conducted pioneering body vortex flow measurements about a tangent ogive cylinder in supersonic flow using a pitot-survey rake and conical pressure probe. In the late 1950's Mello<sup>3</sup> conducted a more complete, but still somewhat limited, investigation for Mach 2 flow about a cone-cylinder body. Beyond these early investigations, there have been no detailed measurements of the supersonic body vortex wake. In subsonic flow, body vortex wake surveys have been conducted by Tingling and Allen,<sup>4</sup> Fiechter,<sup>5</sup> and Grosche<sup>6</sup> using conical probes. Limited wake surveys using a laser anemometer in subsonic flow have also been conducted recently by Fidler, Nielsen, and Schwind,<sup>7</sup> Yanta and Wardlaw,<sup>8</sup> and Owen.<sup>9</sup>

The present paper describes the most comprehensive experimental investigation to date on the symmetric vortex wake of a pointed body of revolution. The experiments were conducted in Supersonic Wind Tunnel A at the USAF Arnold Engineering

Development Center. Over 6000 total pressure, Mach number, and orthogonal velocity component measurements were made at various survey planes on the leeside of a tangent ogive cylinder for angles of attack up to  $25^\circ$ . Measurements were made at a nominal Mach number of 2.0 for two Reynolds numbers and at Mach number 3.0 for one Reynolds number. The higher Reynolds number condition ( $R_d = 1.75 \times 10^6$ ) is a factor of four increase over previously published data for supersonic flow. This is particularly important since Reynolds number is a key factor in matching sub-scale wind tunnel experimental results to full-scale flight vehicles.

The flow field surveys were taken at three positions along the body for angles of attack of  $10^\circ$ ,  $15^\circ$ , and  $20^\circ$  and at two body positions at  $25^\circ$  angle of attack. The measurements were made using a conical pressure probe that was computer manipulated in angular orientation and position in the wind tunnel. In addition to the computer driven probe, the experiments also involved simultaneous interaction of a theoretical model of the flow field and real time data quality optimization.

The experimental program was jointly planned and executed by the Air Force Armament Laboratory (AFATL), the University of Texas at Austin, and the Arnold Engineering Development Center (AEDC). Due to the magnitude of the experiments, only a portion of the results are presented in this paper. Full details are given in Reference 10.

The equipment, instrumentation and experimental procedure are discussed in the following section of the paper. This is followed by presentation and discussion of the results, including general characteristics of the body vortex wake, effects of Reynolds number, and effects of Mach number. Conclusions and a brief discussion of other AFATL research related to the present paper are presented last.

## Experimental Investigation

### Equipment and Instrumentation

The wind tunnel experiments were conducted in Supersonic Tunnel A of the von Karman Gas Dynamics Facility (VKF), AEDC. Tunnel A is a continuous flow, closed-circuit, variable density wind tunnel with an automatically driven flexible-plate nozzle and a 1.02 m by 1.02 m (40 in. by 40 in.) test section. The tunnel can be operated at Mach numbers from 1.5 to 6 at stagnation pressures from 200 to 1380 kPa (29 to 200 psia).

The model was a 76.2 mm (3 in.) diameter circular cylinder with a two caliber tangent ogive nose and a total length of 1.143 m (45 in.). The model was supported by a sting and strut assembly attached to the main model support system of the wind tunnel. Wake flow measurements were made using a biconic shaped pressure probe with a diameter of 3.17 mm (.125 in.). A drawing of the probe is given in Figure 2. The pressure port at the tip of the probe senses the local total pressure of the flow, i.e., the stagnation pressure, and the four surface pressure orifices on the cone portion sense a pressure near the local static value. The probe was supported by a double offset wedge-shaped support strut. The support strut was attached to the Captive Trajectory System (CTS) of the wind tunnel. The CTS is a sophisticated computer controlled electro-mechanical drive system, which can be manipulated in six degrees of freedom. The CTS was originally designed for simulation of store separation from a parent body in the wind tunnel. In the present experiment, however, the CTS was used to vary the pitch angle and yaw angle of the probe in the vortex wake in order to reduce the local angle of attack of the probe. Reduction of the local angle of attack of the probe while in the vortex wake is of crucial importance because of possible interference of the probe on the wake. A photograph of the model and probe installation is shown in Figure 3.

### Experimental Procedure

During the flow field probing phase, the CTS was controlled by the VKF CDC-1604B computer which was programmed to position the probe at a series of grid points in the model cross-flow plane, i.e., the y-z plane shown in Figure 1. Data were taken in the right-half of the cross-flow plane on the leeside of the body. This was done because the vortex wake was symmetric with respect to the x-z plane for the angles of attack and body stations surveyed. Two or three axially

located grids were surveyed, depending on the body angle of attack. A grid point spacing of 5.17 mm (0.225 in.) was used in the present experiment. This was a much finer spaced survey field than that used by previous investigators. The size of each survey field depended on axial location and model angle of attack. A summary of wind tunnel freestream conditions, model angles of attack, axial grid locations, and number of data points is presented in Table I.

The probe was set at pitch and yaw angles such that it would be nominally aligned with the local velocity vector, i.e., near zero local angle of attack. This was done because as the angle of attack of the probe increases, the accuracy of the data decreases for the three following reasons. First, the probability of probe interference on the vortex flow greatly increases. Second, the pitot pressure begins to deviate from the total pressure behind the shock wave of the cone probe. Third, the average value of the surface pressures from the cone begins to approach the pitot pressure making calculation of Mach number inaccurate. The appropriate probe angles were estimated using available theoretical techniques. The mathematical flow model developed in References 11 and 12 was used to predict the local velocity vectors in the vortex wake. Using this theory, the pitch and yaw angles of the probe were chosen such that the probe was nominally aligned with the local velocity at each grid point. This technique was generally successful and only a small percentage of the initial survey points were repeated because of large angle of attack of the probe. The average angle of attack of the probe for the final data set was  $8.2^\circ$ , whereas the velocity vector in the wake varies up to  $60^\circ$ .

During the experiment a new type of computer/wind tunnel interaction was employed to allow real time analysis of the data. Immediately after a body station was surveyed, all of the local flow parameters as well as local angle of attack of the probe and local flow circulation were calculated. These data were manually scanned for large values of probe angle of attack and also for any required improvements in the size and shape of the survey region. Improvements in probe angle of attack and in the region surveyed were promptly effected by reprogramming the CTS computer.

## Discussion of Results

### General Characteristics of the Vortex Wake

The general characteristics of the symmetric body vortex wake will be discussed first. All of the data presented in this section will be for a freestream Mach number of 2.0 and Reynolds number (based on diameter) of  $1.75 \times 10^6$ . This Reynolds number is representative of the value for a full scale missile (with a diameter of 6 inches) flying at an altitude of approximately 40,000 feet. The changes in the wake as a function of body length and angle of attack will be detailed first using various quantities which were measured. The effect of variations in freestream Mach number and Reynolds number will be discussed later.

The velocity components measured in the cross-flow plane for  $\alpha_b = 15^\circ$  and  $x/d = 7, 10, 13$  are shown in Figure 4. The view in the figures is from the rear of the body looking upstream. The base of each vector plotted is the location of a grid point in the cross-flow plane. The vortex is identified above the arc of the body surface as the region of roughly circular, counter-clockwise motion. This sequence of cross-flow vector plots clearly shows how the vortex gradually moves away from the body and increases in strength as it moves along the body. The vortex obtains its strength from the viscous flow in the boundary layer on the surface of the body. As the fluid flows from the windward side of the body, i.e., negative  $z$ , to the leeward side, the boundary layer separates from the body. This is due to the increasing static pressure as the flow attempts to decelerate on the leeside of the body. The separation point can be seen at each body station shown in Figure 4 as the region on the right side of the body where the velocity vectors are small in magnitude and generally point in the positive  $y$  direction.

Figure 5 shows a set of perspective plots of the local total pressure in the cross-flow plane for the same conditions as given in Figure 4. The value of  $p_o$  is normalized by the freestream total pressure  $p_{o\infty}$ . The perspective view is from above a three dimensional surface of  $p_o/p_{o\infty}$  as a function of  $(y,z)$  and looking in the positive  $y$  and negative  $z$  directions. The "blank" portion in the upper right portion of the plot represents one quadrant of the body in the cross-flow plane and also the grid points near the body surface where data were not obtained. Lines hidden from the viewer are plotted as dashed lines. The surface of the perspective plot is numerically constructed by connecting the measured value at

the grid points with straight lines. The body vortex can be identified as the region of low total pressure. The total pressure is low in the vortex because the fluid in the vortex has primarily come from fluid that had earlier been in the boundary layer on the surface of the body. This fluid lost a large amount of total pressure due to viscous deceleration in boundary layer.

For the most forward body station shown in Figure 5a ( $x/d = 7$ ) the vortex is very concentrated. The total pressure of the fluid drops off very rapidly in the core of the vortex. The nondimensional total pressure drops from .98 to .20 over a distance of only 2 grid points, i.e., 11 mm. As one moves down the body (see Figure 5b and 5c) the increase in size of the vortex can be clearly seen. At 13 diameters from the nose the vortex spreads roughly one body radius in the y-direction and two radii in the z-direction. Another region of low total pressure can be identified at each body station of Figure 5; this is the vortex sheet. It extends from the separation point on the body toward the left side, as viewed in Figure 5, of the vortex. The vortex sheet is the path the separating flow in the boundary layer takes on its way to the body vortex. The vortex sheet can be seen in each part of Figure 5 as a valley of low total pressure; the bottom of which can only be seen as a dashed line. The floor of the valley rises as fluid from the boundary layer mixes with external fluid of high total pressure.

The axial velocity component, that is, the velocity component parallel to the body axis, is shown in Figure 6 for  $\alpha_p = 20^\circ$  and  $x/d = 6, 8.5$ , and 11. Figure 6 shows that the axial component of velocity is affected by the vortex wake to a much lesser degree than the total pressure. This implies that the flow about a missile at angle of attack is primarily two-dimensional in the cross-flow plane. This assumption has been heavily used in theoretical approaches to high angle of attack aerodynamics, but this is the first experiment in which the accuracy of this assumption has been quantified. The nondimensional axial velocity, far from the vortex, is  $u/U_\infty = \cos 20^\circ = 0.94$ . In the core of the vortex for  $x/d = 6$ , Figure 6a, a defect in velocity exists, i.e.,  $u/U_\infty < \cos \alpha_p$ . As the vortex develops down the length of the body the defect disappears. This characteristic is very similar to the decay of axial velocity defects in wing tip vortices generated by an aircraft.

Using the cross-flow velocity data  $U_c = v\vec{j} + w\vec{k}$ , the local circulation was calculated in each of the cross-flow survey planes. Circulation, or vorticity, is a measure of



local rotational motion of a fluid particle. It is of great importance in devising theoretical models for the flow field. In regions of the flow where circulation is nonzero, theoreticians cannot use inviscid potential flow theory with accuracy. Local circulation  $\Gamma(y,z)$  was calculated for a square with side,  $h = .0375d$ , i.e., one-half of the survey grid size. Using the definition of circulation one has

$$\Gamma \equiv \oint_R \vec{V} \cdot d\vec{s} = \int_{y,z}^{y+h,z} v \, dy - \int_{y,z+h}^{y+h,z+h} v \, dy + \int_{y+h,z}^{y+h,z+h} w \, dz - \int_{y,z}^{y,z+h} w \, dz$$

where  $\Gamma$  is positive counterclockwise. Several numerical procedures were required before the line integrals indicated above could be calculated. For complete details, the interested reader may see Reference 13.

Figure 7 gives a perspective plot of the local circulation for the same conditions given in Figure 6. A region of fairly concentrated vorticity is seen in the core of the body vortex for  $x/d = 6$ . As the vortex develops along the body,  $x/d = 8.5$  and 11, the vorticity diffuses over a large portion of the wake due to viscosity. The vortex sheet is identified as the very high ridge of vorticity extending from the separation point in the  $z$ -direction. The large negative value of circulation for  $x/d = 6$  is due to a secondary separated flow region near the surface of the body. This secondary region lies underneath the vortex sheet, between the primary separation point on the side of the body and the secondary separation point on the leeward generator. The angular rotation in this separation bubble is clockwise thereby producing the large negative circulation shown in Figure 7a.

A perspective plot of the local Mach number in the wake for  $\alpha_b = 25^\circ$  and  $x/d = 6$  and 9 is shown in Figure 8. Several very interesting features of the distribution can be seen. For  $x/d = 6$  (Figure 8a) the Mach number varies in the  $z$ -direction approximately 1.9, far from the body, to a peak of 3.16 near the body. Then, a strong embedded shock wave passing normal through the angle of attack plane drops the Mach number to 2.2. The shock wave can be seen to extend in the  $y$ -direction for two grid spacings (11 mm) and then vanish into the low Mach number flow of the vortex core. Quantitative measurements of this shock wave aid in the proper interpretation of vapor screen photographs which have been taken by many previous investigators (see, for example, Reference 14).

During the early part of the present experiment a few vapor screen photographs were taken for  $\alpha_b = 25^\circ$ ,  $M_\infty = 2.0$ ,  $R_d = 1.75$ . Figure 9 shows one of the photographs in the cross-flow plane at  $x/d = 6$ . The air flow in Figure 9 is from left to right, the laser source is on the right, and the camera was positioned upstream of body station  $x/d = 6$  looking partially downstream. The symmetric pair of vortices are clearly shown as the dark, roughly elliptic areas above the missile body. The region between the two vortices which becomes progressively darker as the body is approached is the previously discussed region of rapidly increasing Mach number. The sharp change from dark to light near the body is the embedded shock wave. Also seen on the photograph are several other embedded shock waves outboard of the body vortices. The first wave near the crest of the body can be clearly identified on the Mach number distribution (Figure 8a). The second and third waves are not distinguishable in Figure 8a.

Another feature of the Mach number distribution shown in Figure 8a are two points of very low Mach number just above the vortex. After examining all of the survey planes of data it was found that this feature occurred at other angles of attack, body stations, and freestream conditions. This feature is due to a small secondary vortex located above the primary body vortex. It leaves the surface of the body near the nose and, consequently, it is referred to as a secondary nose vortex. Werle<sup>15</sup> and Hsieh<sup>16</sup> suggest the existence of such a vortex on blunt cylindrical bodies at high angle of attack. The present measurements prove the vortex exists, even on pointed bodies of revolution. This experiment also shows, from the circulation distribution corresponding to Figure 8a, that the secondary nose vortex rotates in the opposite rotational sense of the primary body vortex. This small secondary vortex does not appear to be significant with respect to missile flight dynamics, but it is an interesting fluid dynamic discovery.

#### Effect of Reynolds Number

In order to obtain a detailed understanding of the sensitivity of the body vortex wake to Reynolds number, the entire set of survey measurements were repeated for free-stream conditions of  $M_\infty = 2.0$  and  $R_d = 0.48 \times 10^6$ . Comparisons between these results and those discussed previously for  $R_d = 1.75 \times 10^6$  at  $M_\infty = 2.0$  are presented in this section.

A novel means of qualitatively evaluating effects of Reynolds number is by comparing numerically generated streamline patterns. In steady flow the streamlines are coincident with the path a particle traverses in the field. The stream function requires that the three dimensional continuity equation,

$$\frac{\partial u}{\partial x} + \frac{\partial v}{\partial y} + \frac{\partial w}{\partial z} = 0$$

be reduced to a two-dimension form by requiring  $\partial u / \partial x = 0$ . However, analysis of the data for  $\partial u / \partial x$  indicated that it was near zero for only the aft body stations. This should be expected from earlier comments concerning the variation of the axial velocity component with body station.

The streamlines were numerically generated from the governing equation

$$\psi_B - \psi_A = \int_A^B w \, dy - \int_A^B v \, dz.$$

A cubic integration method, similar to the one used in circulation calculations referenced previously was utilized.

Figure 10 shows streamline plots for  $\alpha_b = 15^\circ$  and  $x/d = 13$  for both Reynolds numbers. This station is sufficiently far aft for the flow in the cross-flow plane to be two dimensional. A comparison of the streamline contours in Figure 10 clearly shows the elongation of the vortex with an increase in Reynolds number. The low Reynolds number condition displays a vortex which is much more circular than the vortex formed at high Reynolds number. The primary separation point for the low Reynolds number appears to be very near the crest of the body (Figure 9a) whereas the separation point for the high Reynolds number appears to be farther downstream. The low Reynolds number condition should have laminar boundary layer separation, with a cross-flow Reynolds number,  $R_c$ , of  $0.12 \times 10^6$ , and the high Reynolds number condition should exhibit turbulent separation,  $R_c = 0.45 \times 10^6$ .

#### Effect of Freestream Mach Number

The influence of Mach number on the body vortex wake was evaluated by repeating all of the survey grids for a free-stream Mach number of 3.0 while holding the Reynolds number

very near the high Reynolds number value for the previous survey at  $M_\infty = 2.0$ .

Figure 11 shows the Mach number distribution for  $M_\infty = 3.0$ ,  $R_d = 1.70 \times 10^6$ ,  $\alpha_b = 25^\circ$  and  $x/d = 6$  and  $9$ . The sharp changes in Mach number near the core of the body vortex are striking. In the inviscid flow just outside the core the Mach number is near  $4.0$  and in the core the Mach number is near  $2.0$ . Changes of this magnitude did not occur for  $M_\infty = 2.0$  (Figure 8). Approaching the body along the  $z$ -axis for  $x/d = 6$  the Mach number increases similar to  $M_\infty = 2.0$ . Very near the body, however, the Mach number increases again contrary to what was seen for the lower freestream Mach number. This increase in Mach number near the body was also observed for an angle of attack of  $20^\circ$ . At  $x/d = 9$  all of the Mach number variations along the  $z$ -axis which occurred at  $x/d = 6$  have been dissipated by viscosity. The location of the embedded cross-flow shock from the crest of the body has changed from  $M_\infty = 2.0$ , as would be expected. For  $M_\infty = 3.0$  it appears to originate further past the crest of the body than what was observed for  $M_\infty = 2.0$ . But it is difficult to determine from comparing Figures 8 and 11 because the decrease in the shock wave angle for  $M_\infty = 3.0$  has changed substantially the path of the embedded wave through the cross-flow plane. The path of the embedded wave can be seen in Figure 11b as a drop-off in Mach number whose angle is roughly  $60^\circ$  from the  $y$ -axis. The trace of other embedded waves higher in the wake can be seen in both Figures 11a and b.

The final results, Figure 12, show the relationship between the total circulation in the survey grid as a function of body length for  $\alpha_b = 10^\circ, 15^\circ, 20^\circ$ , and  $25^\circ$ ,  $M_\infty = 2.0$  and  $3.0$ , and  $R_d \approx 1.70 \times 10^6$ . For  $\alpha_b = 10^\circ$  and  $15^\circ$  a clearly linear variation of total circulation with body length is demonstrated. For  $\alpha_b = 20^\circ$  and  $25^\circ$ , the variation is not as definite because many of the survey grids did not completely capture all of the circulation. That is, the flagged symbols in Figure 12 indicate that significant circulation passed over the top boundary of the grid. Consequently, the flagged symbols are a lower bound on the total circulation in the cross-flow plane. For  $\alpha_b = 10^\circ$  and  $15^\circ$  it is seen that the free-stream Mach number change from  $2.0$  to  $3.0$  has little effect on total circulation in the field. For  $\alpha_b = 20^\circ$  and  $25^\circ$  the data indicate that the Mach  $2.0$  wake contains significantly more circulation than the Mach  $3.0$  wake. To obtain an indication of the relationship of total circulation to angle of attack of the body, a least squares fit of the data was calculated. Using the total circulation data for  $x/d = 8$  and  $11$

and  $\alpha_b = 10^\circ, 15^\circ, \text{ and } 20^\circ$ , a fit of  $\Gamma_t$  as a function of  $\sin^m \alpha_b$  was effected. The values of  $m$  for  $M_\infty = 2.0$  and  $R_d = .48 \times 10^6$ ,  $M_\infty = 2.0$  and  $R_d = 1.75 \times 10^6$ , and  $M_\infty = 3.0$  and  $R_d = 1.70 \times 10^6$  were 2.82, 2.33 and 1.90, respectively. The correlation coefficients for the power fits were approximately 0.99, indicating that the plot of  $\log \Gamma_t$  vs  $\log \sin \alpha_b$  is very close to linear. The fit of the data demonstrates that the total circulation grows with angle of attack at a substantially lower rate as the Reynolds number and Mach number increases.

## Conclusions and Related Research

### Conclusions

An experimental program which characterizes the symmetric body vortex wake for supersonic flow has been presented. The data have shown that even at  $10^\circ$  angle of attack, a well defined body vortex of significant size and strength exists.

It has been shown that the shape of the body vortex changes from circular to a more elongated shape as angle of attack, distance aft of the nose and Reynolds number increases. This is contrary to previous findings in incompressible flow where the large circular vortices cause a large diversion of flow around the vortex. Mathematical modeling of these compressibility effects will be required in future theoretical research if accurate computation of the symmetric body vortex wake for supersonic flow is to be achieved.

The experimental results have confirmed that flow about a missile body at high angles of attack is primarily two dimensional in the cross-flow plane. It has also been shown that the local wake vorticity becomes extremely diffuse as angle of attack and distance aft of the nose increase. Finally, it has been shown that the total circulation of the symmetric body vortex wake increases with angle of attack, but at a decreasing rate as Reynolds number and Mach number increase.

The experimental research results summarized in this paper represent the most comprehensive examination to date of the symmetric body vortex wake of a pointed body of revolution in supersonic flow. They should be of great value in providing insight for future theoretical research on three dimensional, viscous separated flows and for verifying fluid dynamics computations using these theories.

### Related Research

The experimental results presented in this paper are only a portion of a very large AFATL research program in high angle of attack aerodynamics.<sup>17</sup> Other experimental research includes detailed time varying and time averaged surface pressure measurements on bodies of revolution at angles of attack up to  $70^\circ$ ; supersonic flow field measurements using newly developed laser velocimeter techniques; and, generation and comparison of aerodynamic force and moment coefficients from wind tunnel and free flight experiments. Finally, theoretical research is being conducted in mathematically modeling the very complex flow field about airframes at high angles of attack. It is anticipated that this total research program will ultimately contribute greatly to the design of future highly maneuverable USAF tactical missiles.

### Acknowledgements

In an experimental program that is as large and complex as the one described herein, many people obviously are involved and make significant contributions. The authors would like to thank all of those at AFOSR, AFATL, AEDC and the University of Texas at Austin who helped make this a successful research effort. Particular gratitude is due to Mr. Timothy J. Bartel, formerly of the University of Texas at Austin, for the many hours that he spent reducing and analyzing the data. Special thanks also go to Mr. Bill Martindale and Mr. Terry Penny of AEDC who served as Project Engineers for the wind tunnel experiments.

## References

1. Allen, H. J., and Perkins, E. W., "A Study of Viscosity on Flow Over Slender Inclined Bodies of Revolution," NACA Report 1048, 1951.
2. Jorgensen, L. H., and Perkins, E. W., "Investigation of some Wake Vortex Characteristics of an Inclined Ogive-Cylinder Body at Mach No. 2," NACA Report 1371, 1955.
3. Mello, J. F., "Investigation of Normal Force Distributions and Wake Vortex Characteristics of Bodies of Revolution at Supersonic Speeds," Journal of the Aeronautical Sciences, Vol 26, March 1959, pp. 155-168.
4. Tingling, B. E., and Allen, C. Q., "An Investigation of the Normal Force and Vortex Wake Characteristics of an Ogive Cylinder," NASA TN D-1297, April 1962.
5. Fiechter, M., "Uber Wirbelsysteme an Schlanken Rotationskorpern und Ihren Einfluss auf die Aerodynamischen Beiwerte," Deutsch-Franzosisches Forschungsinstitut, Saint-Louis (I.S.L.) Bericht 10/66, 1966.
6. Grosche, F. R., "Wind Tunnel Investigation of the Vortex System Near an Inclined Body of Revolution With and Without Wings," Aerodynamic Interference, AGARD-CP-71-71, January 1971.
7. Fidler, J. E., Nielsen, J. N., and Schwind, R. G., "An Investigation of Slender-Body Wake Vortices," AIAA Journal, Vol 15, No. 12, December 1977, pp. 1736-1741.
8. Yanta, W. J., and Wardlaw, A. B., "Laser Doppler Velocimeter Measurements of Leeward Flowfields on Slender Bodies at Larger Angles of Attack," AIAA Paper 77-660, June 1977.
9. Owen, F. K., "Wake Vortex Measurements of Bodies at High Angle of Attack," AIAA Paper 78-23, January 1978.
10. Oberkampf, W. L., and Bartel, T. J., "Supersonic Flow Measurements in the Body Vortex Wake of an Ogive Nose Cylinder," AFATL-TR-78-XX, to be published.



11. Oberkampf, W. L., and Nicolaides, J. D., "Aerodynamics of Finned Missiles at High Angle of Attack," AIAA Journal, Vol 9, No 12, December 1971, pp. 2378-2384.
12. Oberkampf, W. L., "Prediction of Roll Moments on Finned Bodies in Supersonic Flow," Journal of Spacecraft and Rockets, Vol 12, No 1, January 1975, pp. 17-21.
13. Oberkampf, W. L., and Bartel, T. J., "Symmetric Body Vortex Wake Characteristics in Supersonic Flow," AIAA Paper 78-1337, August 1978.
14. Jones, J. H., and O'Hare, J. E., "Flow Visualization Photographs of a Yawed Tangent Ogive Cylinder at Mach Number 2," AEDC-TR-73-45, March 1973.
15. Werle, H., "Separation on Axisymmetric Bodies at Low Speed," La Recherche Aeronautique, No 90, September - October 1962.
16. Hsieh, T., "An Investigation of Separated Flows About a Hemisphere-Cylinder at Incidence in the Mach Number Range from 0.6 to 1.5," AIAA Paper 77-179, January 1977.
17. Daniel, D. C., "Research in Conventional Weapons Aerodynamics," Air Force Armament Research and Technology Plan, Part 2 - Research Programs, FY 79-83, RCS-DLX-(A)-7402, September 1977, pp. 15-18.

Table I. Summary of Experimental Conditions and Survey Grid Points

| $\alpha b$<br>(Deg) | $x/d$ | Number of Survey Grid Points<br>(excluding repeat data points) |  |  |
|---------------------|-------|--|--|--|
|                     |       | $M_\infty=2.0$<br>$R_d=1.75 \times 10^6$                       | $M_\infty=2.0$<br>$R_d=0.48 \times 10^6$ | $M_\infty=3.0$<br>$R_d=1.70 \times 10^6$ |
| 10                  | 8     | 78   | 78                                       | 78                                       |
| 10                  | 11    | 128  | 128                                      | 128                                      |
| 10                  | 14    | 179  | 179                                      | 158                                      |
| 15                  | 7     | 97   | 98                                       | 98                                       |
| 15                  | 10    | 168  | 168                                      | 163                                      |
| 15                  | 13    | 224  | 224                                      | 205                                      |
| 20                  | 6     | 127  | 129                                      | 127                                      |
| 20                  | 8.5   | 189  | 213                                      | 201                                      |
| 20                  | 11    | 222  | 261                                      | 234                                      |
| 25                  | 6     | 147  | 169                                      | 147                                      |
| 25                  | 9     | 189  | 213                                      | 198                                      |
| Totals              |       | 1748   | 1860                                     | 1734                                     |

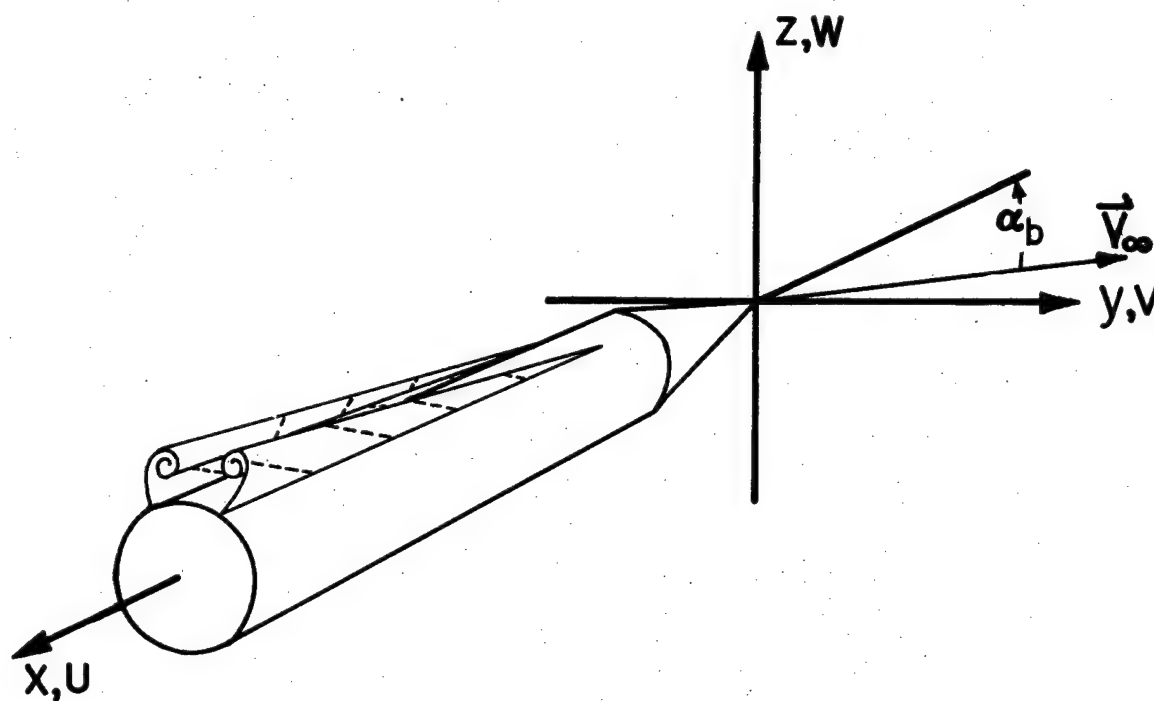


Figure 1. Body Vortex Wake and Coordinate System

ALL DIMENSIONS IN mm  
EXCEPT AS NOTED

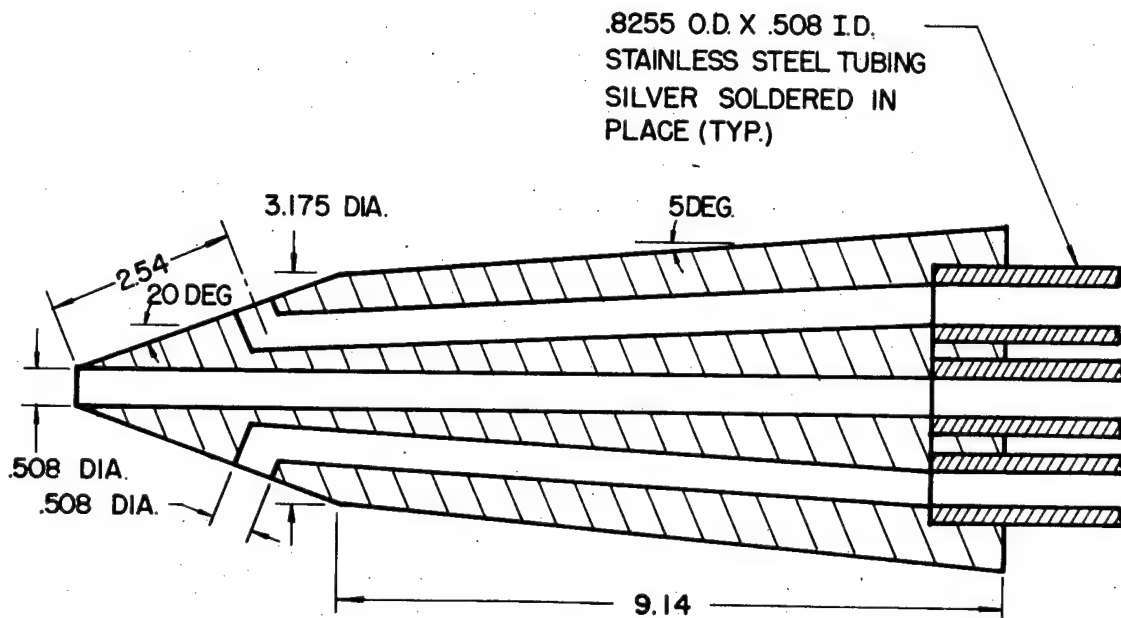


Figure 2. Conical Pressure Probe



Figure 3. Model and Probe Wind Tunnel Installation 1021

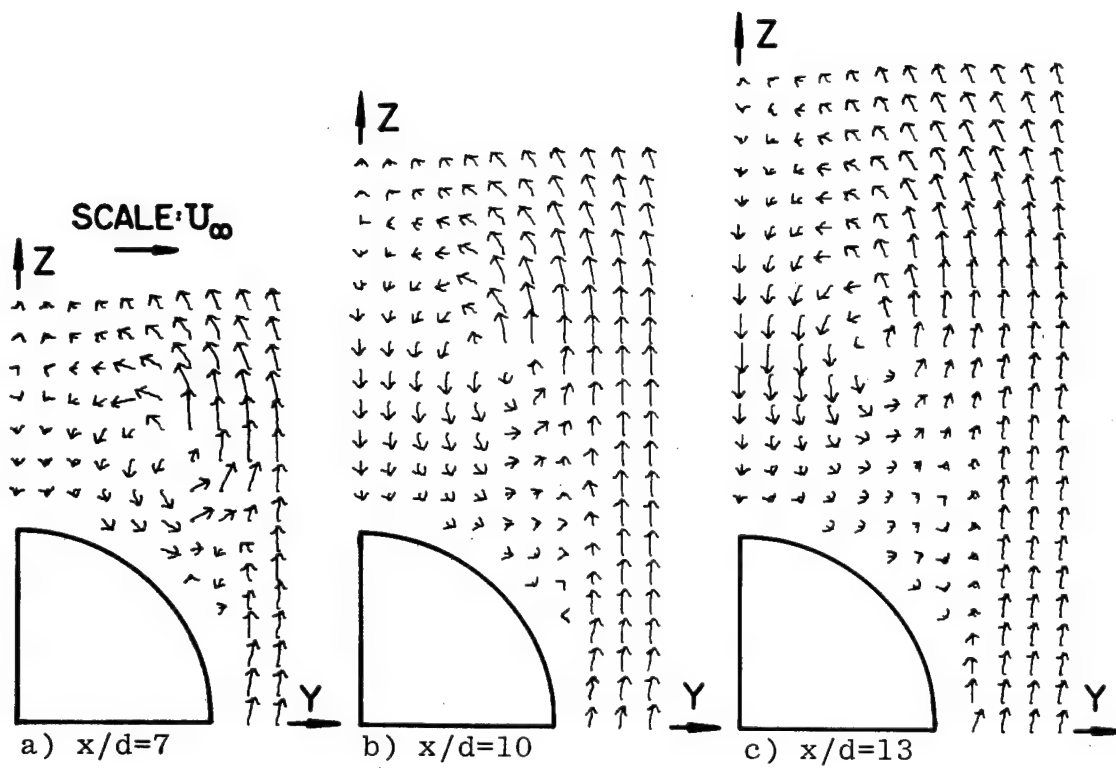


Figure 4. Cross-Flow Plane Velocity Vectors For  $\alpha_b = 15^\circ$ ,  $M_\infty = 2.0$ ,  $R_d = 1.75 \times 10^6$

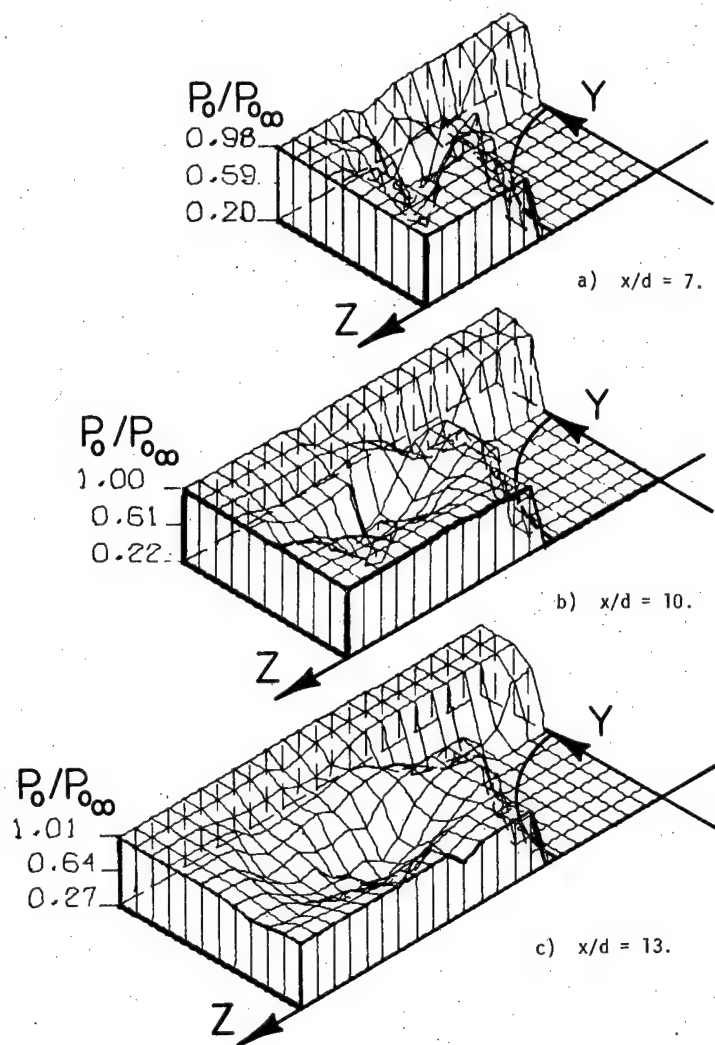


Figure 5. Variation of Total Pressure in the Cross Flow Plane for  $\alpha_b = 15^\circ$ ,  $M_\infty = 2.0$ ,  $R_d = 1.75 \times 10^6$

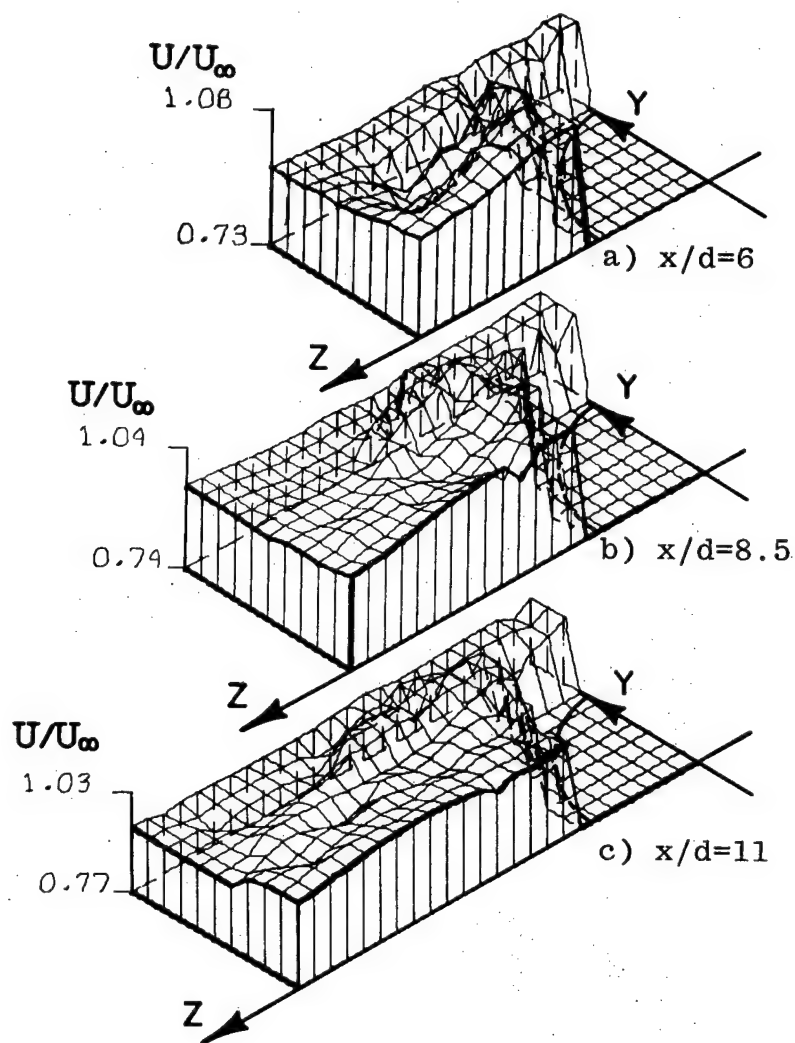


Figure 6. Variation of Axial Velocity in the Cross-Flow Plane for  $\alpha_b = 20^\circ$ ,  $M_\infty = 2.0$ ,  $R_d = 1.75 \times 10^6$



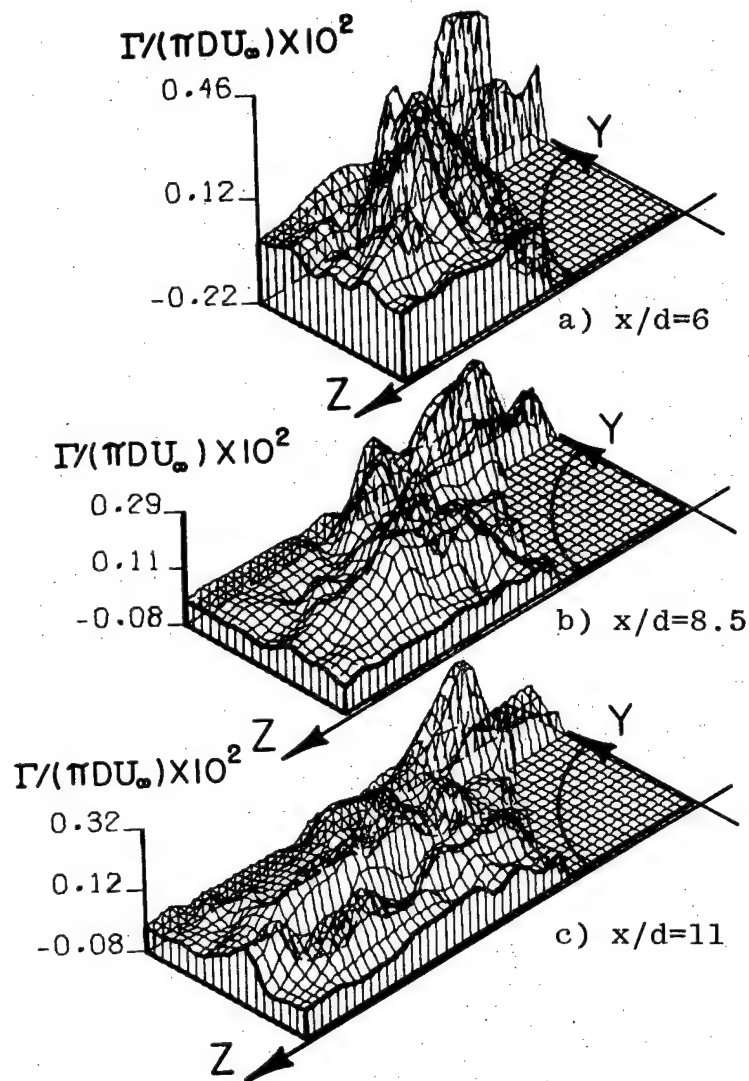


Figure 7. Variation of Local Circulation in the Cross-Flow Plane for  $\alpha_b = 20^\circ$ ,  $M_\infty = 2.0$ ,  $R_d = 1.75 \times 10^6$

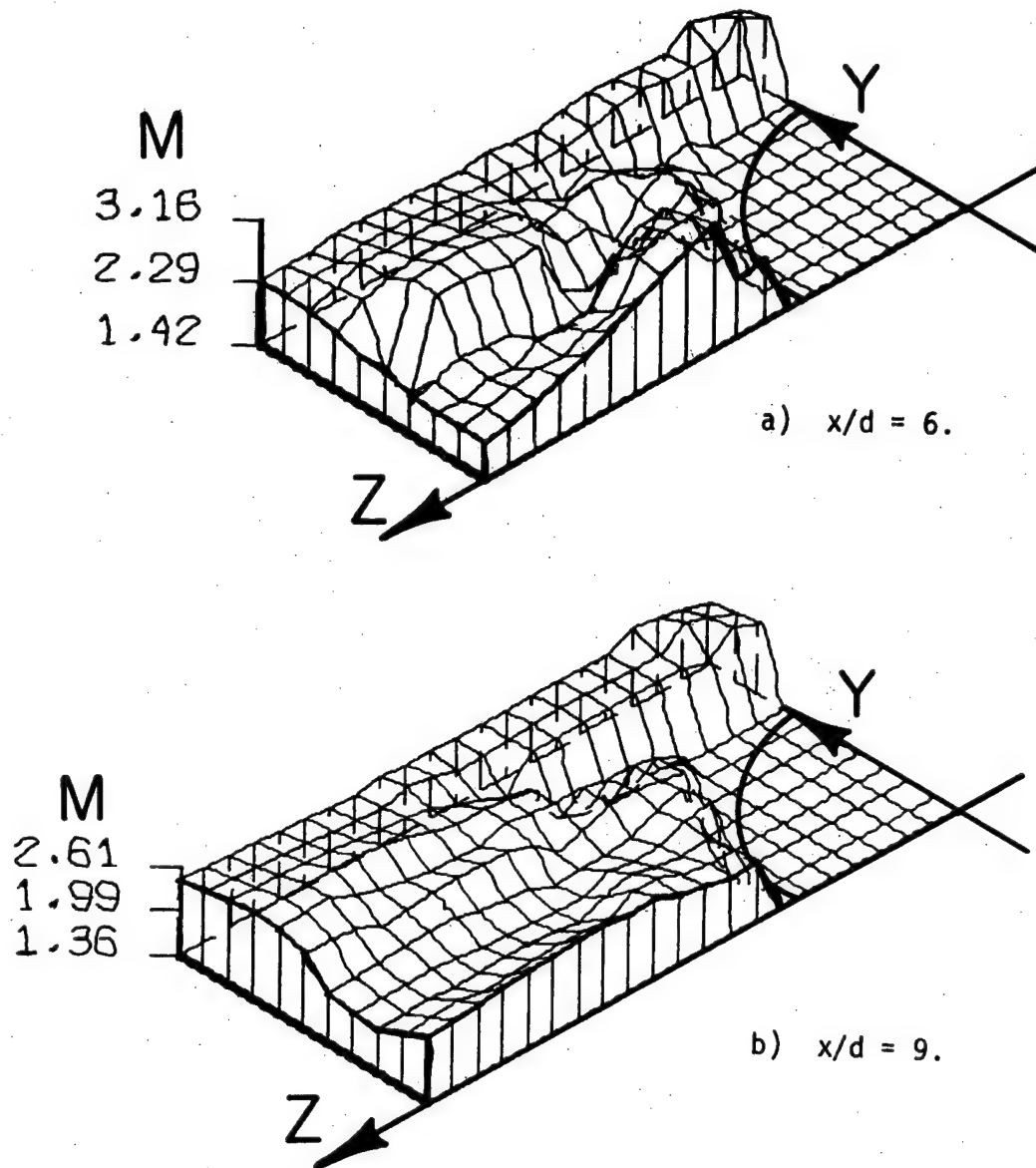
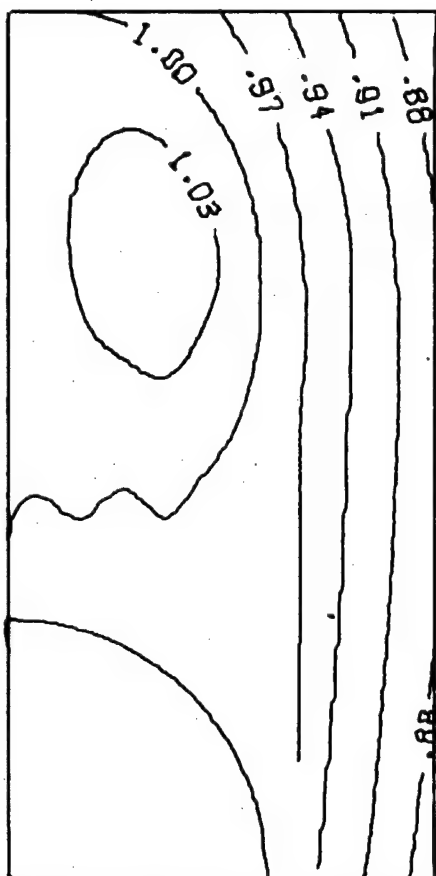


Figure 8. Variation of Local Mach Number in the Cross Flow Plane for  $\alpha_b = 25^\circ$ ,  $M_\infty = 2.00$ ,  $R_d = 1.75 \times 10^6$

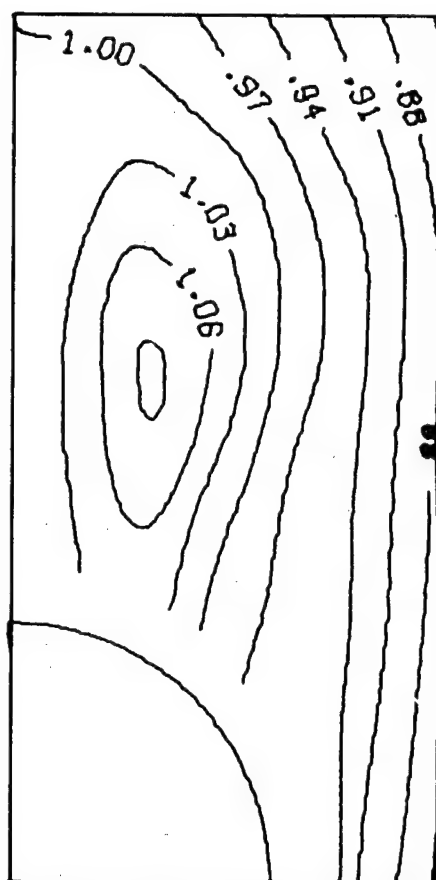


1027

Figure 9. Vapor Screen Photograph of Symmetric Body Vortex Wake



a)  $M_\infty = 1.95$  and  
 $R_d = 0.48 \times 10^6$



b)  $M_\infty = 2.00$  and  
 $R_d = 1.75 \times 10^6$

Figure 10. Reynolds Number Effect on Streamlines in the Cross-Flow Plane for  $\alpha_b = 15^\circ$ ,  $M_\infty = 2.0$ ,  $x/d = 13$

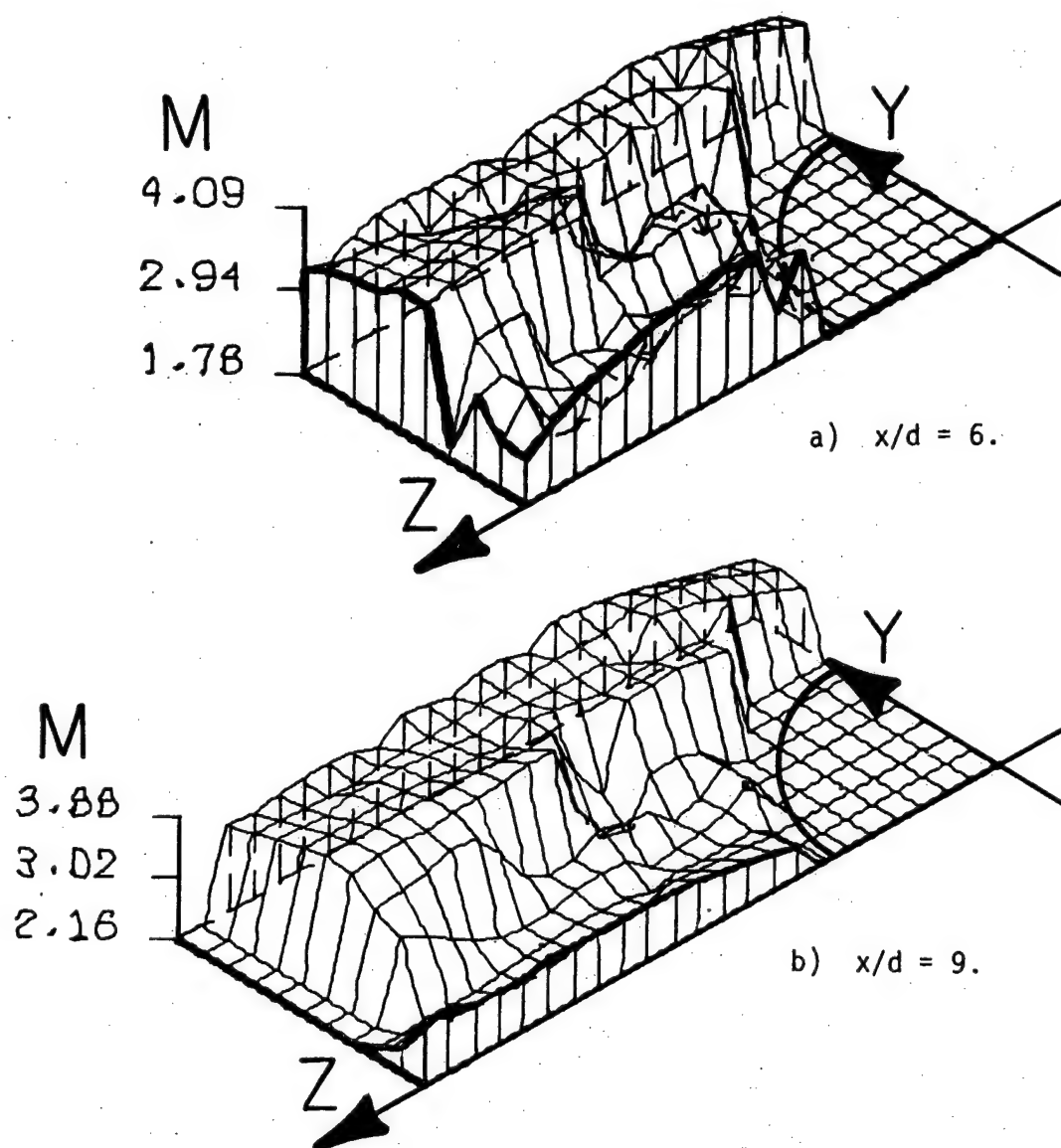


Figure 11. Variation of Local Mach Number in the Cross-Flow Plane for  $\alpha_b = 25^\circ$ ,  $M_\infty = 3.0$ ,  $R_d = 1.70 \times 10^6$

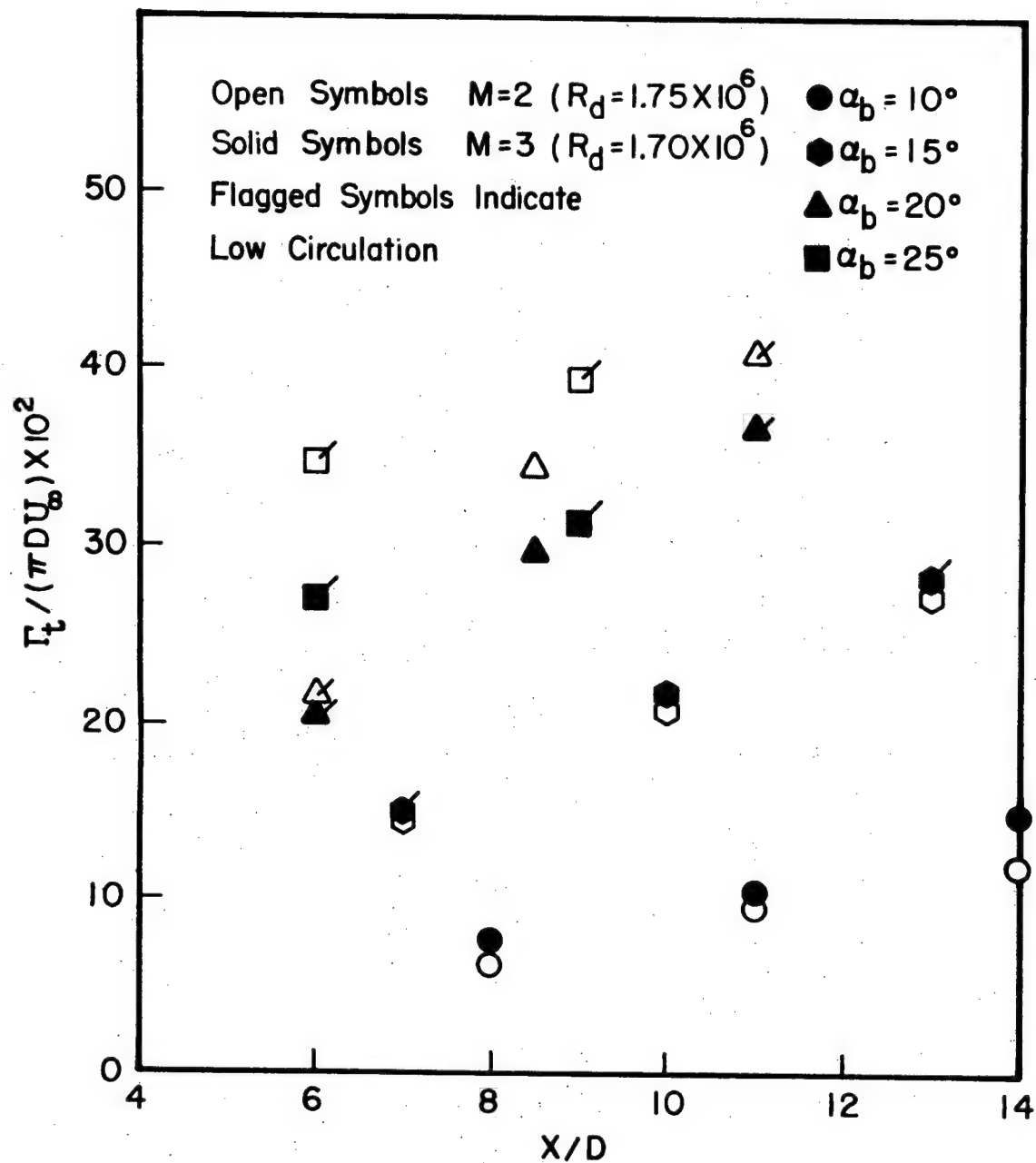


Figure 12. Variation of Total Circulation With Body Length

### Biographical Sketch

Donald C. Daniel was born in Atlanta, Georgia on May 21, 1942. He received the Bachelor of Aerospace Engineering Degree from the University of Florida in 1964. He later received the Master of Science in Engineering and Doctor of Philosophy Degrees, also from the University of Florida, in 1965 and 1973, respectively.

From August 1972 to the present time, Dr. Daniel has been employed as an Aerospace Engineer at the Air Force Armament Laboratory. His assignments have included serving as Chief of the Aeroballistic Research Facility, Technical Director of the Ballistics Branch, Special Assistant to the Commander, and presently, Aerodynamics Research Manager. Prior to his employment with AFATL, he was a Research Engineer with the Boeing Company and a Research Associate with the University of Florida. His principal fields of interest are atmospheric flight mechanics, aerodynamics and astrodynamics.

Dr. Daniel is an Associate Fellow of the American Institute of Aeronautics and Astronautics (AIAA) and serves on the AIAA's national Atmospheric Flight Mechanics Technical Committee. He is also a past Chairman of the AIAA's Northwest Florida Section. In addition, Dr. Daniel is a member of the Engineering Management Society of the Institute of Electrical and Electronic Engineers (IEEE) and an Adjunct Assistant Professor of Aerospace Engineering at the Eglin Graduate Center of the University of Florida.

William L. Oberkamp was born on October 19, 1944 in New Braunfels, Texas. He attended the University of Notre Dame where he earned his Bachelor of Science Degree in Aerospace Engineering in 1966. In the fall of 1966 he entered the graduate school of the University of Texas at Austin and completed the Master of Science Degree in Mechanical Engineering in 1967. He then returned to the University of Notre Dame and completed the Doctor of Philosophy Degree in 1970.

Dr. Oberkamp accepted the position of Assistant Professor of Mechanical Engineering at the University of Texas at Austin in 1970. In 1976 he was promoted to Associate

Professor and presently holds that position. He spent the summer of 1976 at the Air Force Armament Laboratory under the auspices of the AFOSR/ASEE Summer Faculty Program. His principal fields of interest are aerodynamics and computational fluid dynamics.

Dr. Oberkampf is a member of the American Institute of Aeronautics and Astronautics (AIAA) and the American Society of Mechanical Engineers (ASME). He is a Registered Professional Engineer in Texas and a member of the Mechanical Engineering Honor Society Pi Tau Sigma. He has been Director of the Mechanical Engineering Laboratory, Balcones Research Center, a member of the Texas Institute for Computational Mechanics, and Chairman of the AIAA San Antonio Section's Education Committee.



MATERIALS EFFECTS IN HIGH REFLECTANCE COATINGS

BY

H. E. Bennett, Ph.D.

Physics Division

Michelson Laboratories  
Naval Weapons Center  
China Lake, CA 93555

## MATERIALS EFFECTS IN HIGH REFLECTANCE COATINGS

H. E. Bennett

Michelson Laboratories, Physics Division  
Naval Weapons Center, China Lake, CA 93555

### Abstract

High reflectance and antireflectance multilayer optical coatings have applications in missile technology, laser gyro development, FLIR systems, laser designators, and many other areas of optics of interest to the Navy and DoD. One of the most difficult of these applications involves components for high power lasers. Absorption levels of only half a percent are often intolerable, and the reflectances or transmittances of these multilayer-coated components are sometimes higher than 99.9%. Since the absorption in the filming materials is typically very low, it is usually assumed to be negligible in thin film calculations. However, in these components it is the limiting factor. Typically, thin film absorption, which occurs both within the films and at interfaces between them, and which involves light which is absorbed through scattering as well as light which is absorbed directly, is orders of magnitude higher than would be expected from the bulk absorption coefficients of the filming materials. Our limited understanding of materials effects such as the influence of crystalline defects, surface topography, and impurity centers on optical absorption restricts our ability to develop lower absorption optical films. Research at the Naval Weapons Center (NWC) and elsewhere is slowly improving this situation. Knowing what the effective absorption coefficients of the films are allows us to predict multilayer behavior. Simple closed-form expressions have now been developed at NWC which predict the decrease in reflectance of multilayer films as a function of effective film absorption coefficients. Experimental techniques for separating and measuring thin film and interface absorption directly have also been developed at NWC and will be discussed. Using these data, we can predict what the multilayer film reflectance will be from relevant thin film parameters and infer how to improve multilayer coating performance both for high power lasers and for other DoD applications.

## Introduction

High reflectance or antireflectance multilayer optical coatings are crucial to the performance of missiles, laser gyros, FLIR systems, laser designators, and many other areas of optics of interest to the Navy and DoD. One of the most difficult of these applications involves components for high power lasers. Absorption levels of only half a percent are often intolerable, and reflectances or transmittances must sometimes be higher than 99.9%. The bulk absorption coefficients of the dielectric materials used in these multilayer films are typically much less than  $1 \text{ cm}^{-1}$ , and in theory such performance should be readily achieved by adding enough layers. However, in practice, the performance of actual multilayers is often very disappointing. Materials in thin film form typically absorb orders of magnitude more light than would be expected from their bulk absorption coefficients. The reason for this unexpected behavior is not well understood and presents an intriguing problem in solid state and surface physics. In addition to absorption in the volume of the film there is also surface absorption, which exists in astonishing amounts at interfaces between films or at the film substrate or air-film interfaces. What evidence there is suggests that this surface absorption occurs within a depth of only 1000 or 2000 Å.<sup>1</sup> The absorption coefficients in this region must therefore be over 100,000 times higher than that of the bulk material.

In addition to light which is absorbed directly, some light is also scattered in the volume of the film or at the interfaces. Appreciable scattered light is intolerable in applications such as laser gyro mirrors, where it limits the system performance by coupling the two beams traveling around the gyro in opposite directions. It also may result in additional absorption, since some of it will be scattered internally at angles large enough so that the light is trapped and cannot escape before being absorbed by the film. Some of this scattered light is caused by microvoids or other imperfections in the volume of the film. Most of it, however, is scattered at the interfaces by microirregularities only a hundredth of a wavelength or so in height. Understanding the relationship between surface microtopography and scattered light, devising ways for measuring these quantities, and learning to make surfaces which reduce this scattering by orders of magnitude represent challenging problems. Considerable progress has been made here, although much remains to be done.

Once scattering and absorption mechanisms at interfaces and in the volume of the material are partially understood, the next problem

is to predict what the influence of such defects will be on the performance of a multilayer high reflectance or antireflectance film. Multilayer calculations are usually quite involved and were not done until impedance theory was applied to optics about 1950. Since then many programs have been developed which make it possible to obtain exact numerical solutions to multilayer problems. Usually the films are assumed to be nonabsorbing, but recently programs have been developed which make it possible to include volume absorption in the films. To our knowledge, no programs currently incorporate interface absorption, but now that it is recognized as an important factor and methods for measuring it have been developed, a simple program modification could be made to do this. A fundamental difficulty with the computer approach, however, is that there is no apparent functional dependence to guide us in estimating how much effect absorption or scattering at various positions in the multilayer stack will have on component performance and how the design of the multilayer can be modified to minimize it and optimize component performance. In this paper a brief description of methods developed at the Naval Weapons Center (NWC) for predicting and measuring scattered light and for determining surface and volume absorption in films will be given, and then a simple approximate calculational technique for applying these results to predict the performance of either high reflectance or antireflectance films of various designs without a computer will be discussed.

### Scattered Light

Light scattered from single interfaces is usually a monotonically decreasing function of wavelength.<sup>2</sup> In the visible, ultraviolet, and near infrared regions of the spectrum it typically results primarily from microirregularities only tens of angstroms in height which cover the entire surface of all optically polished materials. The width of the irregularities that contribute ranges from a minimum value equal to half the wavelength of the incident light to a maximum value which is determined by how close to the specular direction scattered light can be measured. If we arbitrarily choose  $1^\circ$  from the specular direction as a typical value, the irregularities contributing to scattered light in the visible region range from about  $0.25 \times 10^{-4}$  cm to  $15 \times 10^{-4}$  cm in width, with heights typically of  $10^{-6}$  to  $10^{-7}$  cm. Since these heights are much smaller than the wavelength of light, we are dealing with a diffraction phenomenon. The light scattered into all directions by these irregularities is determined only by their heights,<sup>3,4</sup> and decreases exponentially with wavelength, as illustrated in Figure 1. The angular dependence of this scattered light is more complicated and

is determined by the surface autocovariance function as well as by the height distribution function.<sup>5</sup> It also, however, decreases monotonically with increasing wavelength.

In the infrared region microirregularity scattering becomes low enough so that scattering from particulates, dust, scratches, etc. becomes important.<sup>2</sup> For poorly polished or badly contaminated surfaces these scattering centers can even affect the scattered light observed at the shorter wavelengths. Except for resonance scattering from very fine particles, however, this macroirregularity scattering is describable by geometrical optics and is nearly independent of wavelength. Volume scattering in the bulk of a transparent material caused by voids or other imperfections large compared to a wavelength is also nearly independent of wavelength.<sup>6</sup>

Light scattered in a multilayer film presents a strong contrast to the single interface or volume scattering cases in that it is a strong function of wavelength. The theoretical variation in scattered light with wavelength for a typical multilayer film is illustrated in Figure 2. This theory, which was derived by Elson,<sup>7</sup> takes into account the wavelength variation in local fields in the multilayer stack and also includes possible multiple reflections of the scattered light. Some of this scattered light will be absorbed either in the component itself or by the component holder and will contribute to thermal absorption. The magnitude of this absorption can be estimated calorimetrically by monitoring the instantaneous rise in apparent temperature of a test sample when light passes through it.<sup>8,9</sup> If scattering centers are concentrated in certain layers or at certain interfaces, scattered light can be minimized by designing the multilayer film so that the local field at those positions is a minimum.

#### Volume Absorption

A comparison of absorption coefficients at a wavelength of 10.6  $\mu\text{m}$  for various materials in thin film form and in bulk form is given in Table I. Differences of several orders of magnitude are apparent for most materials. Exceptions are  $\text{As}_2\text{S}_3$  and  $\text{As}_2\text{Se}_3$ , amorphous coatings which were the first coatings shown to have bulk properties. Initial measurements were reported by NWC.<sup>10</sup> Other laboratories subsequently verified them.<sup>11</sup> The reason for the large differences in film and bulk absorption coefficients found in most coating materials and particularly evident for crystalline materials, is not well understood. It probably results at least in part from impurity effects. Sparks<sup>12</sup> has pointed out that levels in the ppb

range for some common impurities would be sufficient to cause the observed increases in absorption in some cases, and considerable effort has gone into purifying the starting materials and in using techniques such as ultrahigh vacuum deposition to prevent contamination during the evaporation process itself. Another contributing factor is diffusion of impurities into the film, which is often not completely dense and thus is more susceptible to penetration than is the bulk material. A third factor may be the film structure itself. The fact that bulk absorption coefficients have been obtained in glassy films, which are amorphous and thus do not have a crystalline array, but not in crystalline films, suggests that structural disorder may affect the allowed transitions in some cases. Clearly, the origin of the additional volume absorption in thin films is obscure and requires further investigation. However, its reality is beyond question and must be considered when designing multilayer stacks for critical applications.

### Interface Absorption

Even more obscure than the anomalously high volume absorption in thin films is the origin of surface absorption at the film-substrate, film-film, or film-air interfaces. It may result from surface contamination, from diffusion of impurity atoms to interfaces, or from some other source, and has only recently been measured experimentally even on bulk material. Initially, it was determined calorimetrically<sup>13</sup> by measuring bulk samples of varying lengths and noting that the resultant absorption when extrapolated to zero sample thickness was not zero. Later, Hass, of the Naval Research Laboratory,<sup>14</sup> developed a long bar technique for separating surface and volume absorption on a single sample by noting the time response of a detector centered along the sample length, and Rehn and Burdick<sup>15</sup> developed a prism technique for separating volume and surface absorption in bulk materials. Burdick applied this technique<sup>16</sup> to thin films and now Temple *et al.*<sup>17</sup> have succeeded in measuring the surface as well as the volume absorption of thin films calorimetrically with high accuracy. The essentials of Temple's method are shown in Figure 3. By utilizing a novel, high precision adiabatic calorimeter designed and constructed by Decker,<sup>18</sup> he has increased the signal-to-noise ratio for incident power levels of the order of 1 watt so that he can accurately track across a wedged film and note the variation in absorption with film thickness. This absorption is caused by (1) absorption in the substrate, which is independent of beam position on the wedged film, (2) volume absorption in the film, which increases linearly with film thickness when measured at the quarter- or half-wave thickness points on the film, (3) film-substrate

interface absorption, and (4) vacuum-film interface absorption. The substrate plus substrate-vacuum interface can be determined from measurements on an uncoated region of the substrate. The volume absorption of the film is obtained from the slope of the curve connecting the measured absorption values at the multiple half-wave or odd quarter-wave film thicknesses. Since the fields at the front and back interfaces of the film are equal for multiple half-wave film thicknesses but are unequal for multiple odd quarter-wave film thicknesses, the maxima and minima corrected for volume absorption in the film and substrate absorption give the surface absorption at the vacuum-film interface and the difference between the film-substrate and vacuum-substrate interface absorption. This technique was only reported last month. For one film of  $\text{As}_2\text{Se}_3$  deposited on  $\text{CaF}_2$ , the film-substrate interface absorption at  $2.87 \mu\text{m}$ , measured using this technique, was 40 times the volume absorption in a quarter-wave layer, whereas the film-vacuum interface absorption was negligible. Using conventional calorimetric measurement techniques all of this absorption would have been erroneously assumed to be volume absorption in the film itself.

Only film-substrate and vacuum-film interface absorption measurements have been demonstrated thus far. However, it is clear that once a particular film-substrate combination is understood, that film can be deposited in a uniform thickness on the substrate and a wedged film of a different material deposited on that and measured. We then have a means for determining the film-substrate and film-film interface absorptions as well as the film-vacuum interface absorption. A requirement is that the film properties be reproducible from evaporation to evaporation. In NWC evaporation chambers this requirement appears to be met provided that no changes in the chamber, evaporant, or conditions are made between runs. The next question is how the information about single film volume and interface absorption can be used to predict multilayer coating performance and ultimately to produce lower absorption coatings.

#### High Reflectance Multilayers

A high reflectance multilayer is made by depositing alternate high and low index dielectric layers on a metal or dielectric substrate. With each multilayer pair the reflectance increases, and if the substrate is initially coated with a metal of high reflectivity such as silver, only four or five multilayer pairs may be required in principle to reach very high reflectivities. If no high reflectance metals exist, as is true, for example, in the ultraviolet region of the spectrum, or if an all-dielectric design is desired,

many more multilayer pairs may be required, and 40 or more layers are not uncommon. In the general case, the equations describing the performance of such a multilayer stack are formidable and are best solved by iteration using a computer. However, in the special case in which the layers are all a quarter wavelength (or multiples thereof) in optical thickness, and the reflectance is nearly unity, Sparks<sup>19</sup> has shown that a great simplification occurs, making it possible to develop simple approximate closed-form expressions for multilayer films on dielectric substrates. We find that these expressions often agree with exact calculations of the reflectance to four significant figures or better for reflectances above 99%, the region of most interest for many high reflectance applications, and can be extended to cover metal as well as dielectric substrates. Fortunately, the requirement that the layers be a quarter-wave in optical thickness, or multiples thereof, is not a significant restriction since most high reflectance coatings have such a design.

The key to the simplification which occurs lies in the multiplicative nature of the standing wave field. Consider an all-dielectric high reflectance multilayer film on a dielectric substrate. As shown in Figure 4, the standing wave field outside the multilayer film is  $2E_0$  where  $E_0$  is the amplitude of the incident light. The amplitude goes to zero at the entrance face of the multilayer film, assumed to have a high index outer layer, so that contamination on the outer surface of the film will have little effect on film absorption. However, it reaches a maximum again at the first high-low (HL) film interface and at each succeeding HL interface thereafter. The amplitude at each succeeding HL interface is reduced by a factor  $n_L/n_H$ , the ratio of the high and low film indices, and the standing wave in each film layer is sinusoidal. The average field in a layer is then  $\bar{E} = E/\sqrt{2}$  and the volume absorption  $A_v$  in that layer is, utilizing the Poynting theorem,

$$A_v = \beta \ell \overline{nE^2/E_0^2} = (\beta\lambda/8)(E/E_0)^2, \quad (1)$$

where  $(E/E_0)^2$  is given by Figure 4. Here,  $\beta$  is the volume absorption coefficient of the film of index  $n$  and  $\ell$  is its physical thickness. At the LH interfaces the field is to a first approximation zero, so that interfacial absorption at these interfaces can be neglected. However, at the HL interfaces the field is a maximum. Interfacial absorption occurs in a small depth near the interface and should be treated just as volume absorption except that  $E$  is substituted for  $\bar{E}$ . However, we know neither what the depth of the layer in which interfacial absorption occurs nor the absorption coefficient, which



is surely varying with depth. The experimentally measured parameter is the interface absorption itself, which is proportional to  $(E/E_0)^2$  and may be represented by  $A_I(E/E_0)^2$  where  $A_I$  is determined by the calorimetric technique described previously and incorporates, if necessary, the contribution to absorption made by light scattered at the interface. Since evaporated films contour the surface on which they are deposited quite accurately, to a first approximation the contribution to  $A_I$  made by scattered light is proportional to the square of the rms microroughness of the substrate surface. Additional roughness or void structures developed in the films during deposition may make this approximation optimistic.

The resultant reflectance  $R$  of a high reflectance multilayer on a dielectric substrate is then obtained by summing the contributions from each dielectric pair, giving

$$(1-R) = \left[ \frac{\lambda}{2} (\beta_L + \beta_H) + 4A_I \right] \left[ 1 - \left( \frac{n_L}{n_H} \right)^{2N+1} \right] \left[ n_H^2 - n_L^2 \right]^{-1} + \frac{4n_S}{2} \left( \frac{n_L}{n_H} \right)^{2N}, \quad (2)$$

where the last term represents the intensity of the traveling wave transmitted into the dielectric substrate when a high index film is next to the substrate. If a low index film is next to the substrate, this term becomes  $(4/n_S)(n_L/n_H)^{2N}$ . Here, H, L, and S are subscripts indicating the high index film, low index film, or substrate, respectively, and  $N$  is the number of film pairs deposited. To maximize  $R$  we need to minimize the right-hand side of Eq. (2). As the number of film pairs  $N$  becomes larger the contribution from the substrate term decreases rapidly. However, the multilayer film term (first term) increases equally rapidly, so that volume and interfacial absorption in the film quickly increase in importance and ultimately dominate reflector performance. If the number of layer pairs becomes sufficiently large and interface absorption is neglected, the second term in brackets goes to unity, the last term goes to zero, and we have Koppelman's well-known equation<sup>20</sup> for a semi-infinite multilayer stack.

If the final layer is a metal rather than a dielectric or if a metal substrate is used, the dielectric layer next to the metal is modified in thickness so that the phase change on reflection seen by the rest of the dielectric stack is unchanged. The phase change  $\delta$  from a metal substrate is given by

$$\tan \delta = \frac{2nk_S}{n^2 - n_S^2 - k_S^2}, \quad (3)$$

where  $n$  is the index of the dielectric film nearest the substrate and the complex index of refraction  $\bar{n}_S$  of the metal is

$$\bar{n}_S = n_S - ik_S. \quad (4)$$

If the high index film is next to the metal, its optical thickness is made greater than a quarter wavelength and is given by

$$n_H \ell = \frac{\lambda}{4} \left(1 + \frac{\delta}{\pi}\right). \quad (5)$$

It is more efficient to put the low index film next to the metal since its thickness is less than a quarter wavelength and is given by

$$n_L \ell = \frac{\lambda}{4} \left(\frac{\delta}{\pi}\right). \quad (6)$$

In either case, the resultant admittance  $n_S^+$  of the dielectric film-metal combination is real and can be treated as a dielectric material so far as the reflectance of the multilayer stack is concerned. It is given by

$$n_S^+ = \frac{n_S}{\frac{1 + \cos \delta}{2} \left[ \left(\frac{k_S}{n}\right)^2 + \left(\frac{n_S}{n}\right)^2 \right] + \frac{1 - \cos \delta}{2} - \frac{k_S}{n} \sin \delta}. \quad (7)$$

By substituting  $n_S^+$  for  $n_S$  we may then use Eq. (2) to calculate the reflectance of multilayer dielectric films on metals as well as on dielectrics.

A comparison of reflectances and absorptances calculated from Eq. (2) for metal and dielectric substrates with the exact values is shown in Table II. For reflectances above 0.99 the discrepancies are typically  $\sim 10^{-4}$  or less. The analysis for high reflectance mirrors given above and antireflection films given below were presented at the 1978 Conference on Laser Induced Damage in Optical Materials.<sup>20</sup>

Although significantly fewer dielectric layers are required to reach a given reflectance when metal substrates are used, the light

energy striking the substrate is higher and hence absorption at the substrate interface is more important than in the case of dielectric substrates. Polished metal surfaces typically exhibit significant cold-working and often have absorption values several times as high as an undisturbed metal surface. The most promising method of correcting this situation is by diamond-turning the metal components.<sup>22</sup> This new technique for producing mirrors promises to revolutionize the optical fabrication industry, since in addition to producing better components it can turn them in a few minutes at a fraction of the cost of conventional techniques. NWC now has<sup>23</sup> the only operational diamond-turning facility in DoD. Figure 5 shows this system, which was designed jointly by Decker of NWC and by the staff at Pneumo Precision, Inc. It was installed at NWC this year, and is the first operational machine designed specifically for diamond-turning. Surface quality obtained with this machine is outstanding, and it is now being used in a research program to improve diamond-turning technology and to encourage industry to utilize diamond-turning as a production technique.

#### Antireflection Films

The performance of antireflectance films may be calculated from the interfacial and volume absorption of the filming materials in much the same way as that for high reflectance mirrors. The filming materials used in both applications are typically the same. However, there is a very significant difference between high reflectance and antireflectance coatings. In the former, enough layers could be added to minimize interfacial absorption at the substrate; whereas, for antireflection coatings, the fields at the substrate interface are necessarily virtually the same as those incident on the front side of the component. Perhaps for this reason antireflection-coated components typically have a lower laser damage threshold than do high reflectance components.<sup>24</sup> If the origin of interfacial absorptance were understood and steps could be taken to modify it, possibly this situation would change.

In the high reflectance case, the approximation made was that the fields in the film structure resulted from perfect reflection of all incident light. In the antireflection case, we assume perfect transmission of the incident light. The resulting fields, which may be obtained from the Poynting theorem, are shown in Figure 5. Calculating the volume absorption from Eq. (1) and the surface absorption as before, we obtain for a single-layer quarter-wave antireflection film

$$A_1 (\beta_L \lambda / 8 n_S) (n_S + 1) + A_{OL} + A_{LS} / n_S^{1/2}, \quad (8)$$

where  $A_1$  is the absorption of the film,  $A_{OL}$  is the air-film interface absorption,  $A_{LS}$  is the film-substrate interface absorption, and the other quantities were defined previously. The total absorption of a component antireflected on both sides would then be approximately  $2A_1 + \beta_S \tau$ , where  $\beta_S$  is the volume absorption coefficient of the substrate material and  $\tau$  is its thickness. If volume and interfacial absorption remain constant, the lowest total absorption will be obtained for the highest index substrate material, assuming, of course, that a suitable index material can be used to antireflect it.

Index requirements are much more readily met for a two-layer quarter-wave antireflection coating than they are for a single-layer coating. The absorption per coating is then  $A_2$ , where

$$A_2 = \beta_L \lambda / 8 \left( \frac{n_S^2 + n_H^2}{n_H^2} \right) + \beta_H \lambda / 8 \left( \frac{n_S^2 + n_H^2}{n_S n_H^2} \right) + A_{OL} + A_{LH} (n_S^{1/2} / n_H) + A_{HS} n_S^{-1/2}. \quad (9)$$

For a three-layer quarter-wave coating the absorption can be determined following a similar procedure. A broader band three-layer coating can be obtained, however, by utilizing a quarter-half-quarter-wave coating. The absorption penalty in this case, however, may be severe if the half-wave filming material has a significant volume or interface absorption. The absorption per surface for a three-layer quarter-half-quarter-wave coating is  $A_3$ , where

$$A_3 = A_2 + \frac{\beta_h \lambda}{4 n_S} \left( \frac{n_S^2}{n_H^2} + \frac{n_H^2}{n_h^2} \right) + \frac{n_S^{1/2}}{n_H} (A_{Lh} + A_{hH} - A_{LH}) \quad (10)$$

and the h subscripts refer to the half-wave layer.

Two- or three-layer antireflection coatings which do not contain quarter- or half-wave layers are not only possible, but often desirable since they can result in more perfect matching of available index materials. In most cases there are two solutions for a two-layer antireflectance stack of appropriate filming materials which

result in perfect matching. A Schuster diagram is helpful in determining what these appropriate materials are.<sup>25</sup> There are a semi-infinite number of three-layer solutions, some of which can result in significant reductions in absorption relative to two-layer solutions if one of the filming materials has a large absorption coefficient. Simple mathematical relationships governing the design of three-layer antireflectance coatings have been reported by Baer<sup>26</sup> for nonabsorbing coatings of arbitrary thickness. An alternate approach utilizing Herpin equivalent indices is discussed by Ohmer.<sup>27</sup> Quarter-wave coatings are useful, however, in forming a baseline for coating optimization and also in indicating the influence of interface and volume absorption in the films on coating performance. Frequently, they perform very well indeed.

### Conclusions

Low absorption multilayer film coatings are important for most DoD programs which involve optics. The absorption in these coatings is caused by three factors: (1) scattered light which is trapped internally and ultimately absorbed; (2) the anomalously high absorption coefficients of materials in thin film form; and (3) interface absorption. Scattered light arises from microirregularity scattering at interfaces, a diffraction effect involving coherent scatterers for which a model has been developed which is in good agreement with experiment. Another source is incoherent scattering from surface particulates, which is also a diffraction effect for which models exist. A third source is scattering by scratches, pits, and other macroirregularities, which is describable by geometrical optics. Some light is also scattered by voids and other imperfections in the films themselves. Scattered light may be reduced by superpolishing the substrates on which films are to be deposited, by reducing particulate contamination, and by using deposition techniques which produce uniform films which are fully dense.

The origin of the anomalously high absorption coefficient of materials in thin film form is obscure as is the origin of interface absorption. It is almost certainly, at least in part, an impurity effect. Techniques have now been developed to separate interface and volume absorption in single thin films and to measure each. Substrate surface absorption may also be important; it can be minimized by diamond-turning, and there is now an operational diamond-turning facility at NWC.

A simple set of closed-form approximate expressions has been developed for obtaining accurate absorption values of high reflectance or antireflectance multilayer coatings on dielectric or metal

substrates from interface and volume absorption parameters. These expressions also make it possible to see functional relations between the film or interfacial absorption in various layers or at the substrate and the resultant multilayer performance. This information will be useful both in designing lower absorptance multilayer coatings and in suggesting directions for further research aimed at reducing multilayer absorption.

#### References

1. M. J. Soileau, H. E. Bennett, J. O. Porteus, P. A. Temple, and M. Bass, in *Proceedings of the Fifth Annual Conference on Infrared Laser Window Materials*, C. R. Andrews and C. L. Strecker, eds. (DARPA, 1976), pp. 392-417.
2. H. E. Bennett, *Opt. Engr.* 17, 480 (1978).
3. H. E. Bennett and J. O. Porteus, *J. Opt. Soc. Am.* 51, 123 (1961).
4. J. O. Porteus, *J. Opt. Soc. Am.* 53, 1394 (1963).
5. J. M. Elson and J. M. Bennett, *J. Opt. Soc. Am.* (in press).
6. H. C. van de Hulst, *Light Scattering by Small Particles* (John Wiley and Sons, New York, 1957).
7. J. M. Elson, *J. Opt. Soc. Am.* (in press).
8. H. V. Winsor, in *Proceedings of the Third Conference on High Power Infrared Laser Window Materials*, C. A. Pitha and B. Bendow, eds. (AFCRL Special Report 174, 1974), pp. 1069-1082.
9. J. A. Detrio and J. Fox, in *Proceedings of the High Power Laser Optical Components Topical Meeting*, Lowry Air Force Base, September 1978 (in press).
10. T. M. Donovan and A. D. Baer, in *Proceedings of the Fifth Annual Conference on Infrared Laser Window Materials*, C. R. Andrews and C. L. Strecker, eds. (DARPA, 1976), pp. 291-300.
11. J. A. Harrington, E. J. Rudisill, and M. Braunstein, *Appl. Opt.* 17, 2798 (1978).
12. M. Sparks, "Theoretical Studies of Materials for High-Power Infrared Coatings," Sixth Technical Report, December 1975, ARPA Order 1969, pp. 31-50.

13. T. F. Deutsch and R. I. Rudko, in *Second Conference on High Power Infrared Laser Window Materials*, AFCRL Special Report No. 162, June 1973, pp. 201-221.
14. M. Hass, J. W. Davisson, H. B. Rosenstock, and J. Babiskin, *Appl. Opt.* 14, 1128 (1975).
15. V. Rehn, D. L. Burdick, and V. O. Jones, in *Laser Induced Damage in Optical Materials: 1977*, A. J. Glass and A. H. Guenther, eds. National Bureau of Standards, Washington, D.C. (NBS Special Publication 509), pp. 132-136.
16. D. L. Burdick, *Op. cit.*, pp. 352-357 (ref. 15).
17. P. A. Temple, D. L. Decker, T. M. Donovan, and J. W. Bethke, in *Laser Induced Damage in Optical Materials: 1978*, A. J. Glass and A. H. Guenther, eds. (in press).
18. D. L. Decker and P. A. Temple, in *Laser Induced Damage in Optical Materials: 1977*, A. J. Glass and A. H. Guenther, eds., National Bureau of Standards, Washington, D.C. (NBS Special Publication 509), pp. 281-285.
19. M. Sparks, *J. Opt. Soc. Am.* 67, 1590 (1977).
20. H. E. Bennett and D. K. Burge, in *Laser Induced Damage in Optical Materials: 1978*, A. J. Glass and A. H. Guenther, eds. (in press).
21. G. Koppelman, *Ann. Phys. (Leip.)* 7, 388 (1960).
22. H. E. Bennett, M. J. Soileau, and P. C. Archibald, in *Laser Induced Damage in Optical Materials: 1975*, A. J. Glass and A. H. Guenther, eds. National Bureau of Standards, Washington, D.C. (NBS Special Publication 435), pp. 49-56.
23. D. L. Decker and D. J. Grandjean, in *Laser Induced Damage in Optical Materials: 1978*, A. J. Glass and A. H. Guenther, eds. (in press).
24. J. J. Apfel, in *Laser Induced Damage in Optical Materials: 1977*, A. J. Glass and A. H. Guenther, eds., National Bureau of Standards, Washington, D.C. (NBS Special Publication 509), pp. 251-254.
25. J. T. Cox and G. Hass, *Physics of Thin Films*, G. Hass and R. E. Thun, eds., Vol. II (Academic Press, New York, 1964), pp. 258-265.

26. A. D. Baer, in *Laser Induced Damage in Optical Materials: 1976*, A. J. Glass and A. H. Guenther, eds. National Bureau of Standards, Washington, D.C. (NBS Special Publication 462), pp. 221-229.
27. M. C. Ohmer, "Antireflection Coatings for Calcium Fluoride Laser Windows for 5.3 Microns," AFML-TR-76-103 (1976).

TABLE I. Coating Materials for 10.6 Microns.

| Material                | Index | Bulk absorption coefficient, $\text{cm}^{-1}$ | Film absorption coefficient, $\text{cm}^{-1}$ |
|-------------------------|-------|---|---|
| $\text{SrF}_2$          | 1.36  | 0.65  | 24  |
| $\text{BaF}_2$          | 1.40  | 0.19  | 6   |
| $\text{ThF}_4$          | 1.50  | ....  | 6   |
| $\text{ZnS}$            | 2.16  | 0.38  | 2-3   |
| $\text{CdS}$            | 2.21  | 0.032   | (>10)   |
| $\text{ZnSe}$           | 2.35  | 0.005   | (~10)   |
| $\text{CdSe}$           | 2.44  | 0.03  | (>10)   |
| $\text{As}_2\text{S}_3$ | 2.38  | 0.7   | 1-3   |
| $\text{In}_2\text{S}_3$ | 2.47  | ....  | 7.7   |
| $\text{CdTe}$           | 2.67  | 0.002   | 1-2   |
| $\text{ZnTe}$           | 2.71  | 0.38  | 2-4   |
| $\text{GaAs}$           | 3.30  | 0.006   | Very large                                    |
| $\text{Ge}$             | 4.00  | 0.03  | 30  |



TABLE II. Mirrors: Comparison With Exact Calculations.

| Infrared, metal substrate (ZnSe/ThF <sub>4</sub> ) <sup>N</sup> ZnSeMo   |                   |        |                        |        |         |        |
|--|-------------------|--------|------------------------|--------|---------|--------|
| N  | A <sub>film</sub> |        | A <sub>substrate</sub> |        | R       |        |
|  | Approx.           | Exact  | Approx.                | Exact  | Approx. | Exact  |
| 0  | 0.0006            | 0.0002 | 0.0199                 | 0.0194 | 0.9794  | 0.9804 |
| 1  | 0.0012            | 0.0011 | 0.0063                 | 0.0061 | 0.9925  | 0.9928 |
| 2  | 0.0014            | 0.0013 | 0.0020                 | 0.0019 | 0.9966  | 0.9967 |
| 3  | 0.0014            | 0.0014 | 0.0006                 | 0.0006 | 0.9979  | 0.9980 |
| 4  | 0.0015            | 0.0014 | 0.0002                 | 0.0002 | 0.9983  | 0.9984 |
|  |                   |        |                        |        |         |        |
| Ultraviolet, dielectric substrate (HfO <sub>2</sub> /SiO <sub>2</sub> ) <sup>N</sup> HfO <sub>2</sub> SiO <sub>2</sub> |                   |        |                        |        |         |        |
| N  | A <sub>film</sub> |        | T <sub>substrate</sub> |        | R       |        |
|  | Approx.           | Exact  | Approx.                | Exact  | Approx. | Exact  |
| 1  | 0.0029            | 0.0025 | 0.7231                 | 0.5171 | 0.2740  | 0.4803 |
| 3  | 0.0042            | 0.0040 | 0.1973                 | 0.1783 | 0.7985  | 0.8177 |
| 5  | 0.0045            | 0.0045 | 0.0538                 | 0.0521 | 0.9417  | 0.9434 |
| 7  | 0.0046            | 0.0046 | 0.0147                 | 0.0145 | 0.9807  | 0.9809 |
| 9  | 0.0046            | 0.0046 | 0.0040                 | 0.0040 | 0.9914  | 0.9914 |
| 11   | 0.0046            | 0.0046 | 0.0011                 | 0.0011 | 0.9943  | 0.9943 |
| 13   | 0.0046            | 0.0046 | 0.0003                 | 0.0003 | 0.9951  | 0.9951 |

### Figure Captions

Figure 1. Wavelength dependence of the light scattered into all angles except the specular direction by an aluminum-coated superpolished fused quartz optical flat. Circles are the measured values and the solid theoretical curve is calculated assuming a value of  $12.8 \text{ \AA}$  for  $\delta$ .

Figure 2. Calculated scattering and polarization dependence of a multilayer dielectric film on a dielectric substrate.

Figure 3. Calorimetrically measured absorption of a wedged single-layer film as a function of beam position on the sample. The points on the left are for the uncoated substrate.

Figure 4. Standing wave electric fields in a dielectric multilayer which is perfectly reflecting.

Figure 5. Facility for diamond-turning optical components which was recently installed at the Naval Weapons Center.

Figure 6. Electric fields in a three-layer antireflecting coating which is perfectly transmitting.

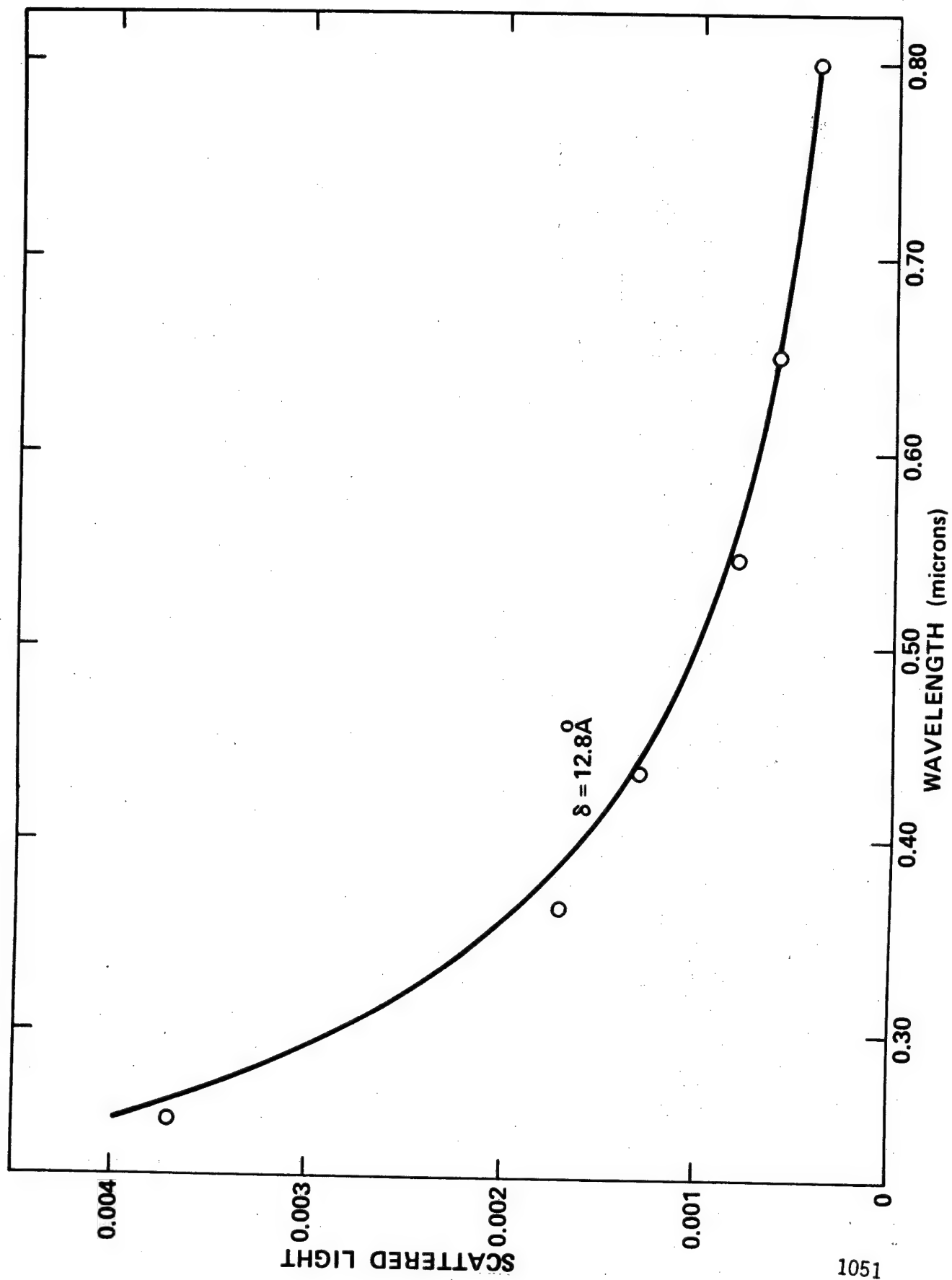


Fig.1

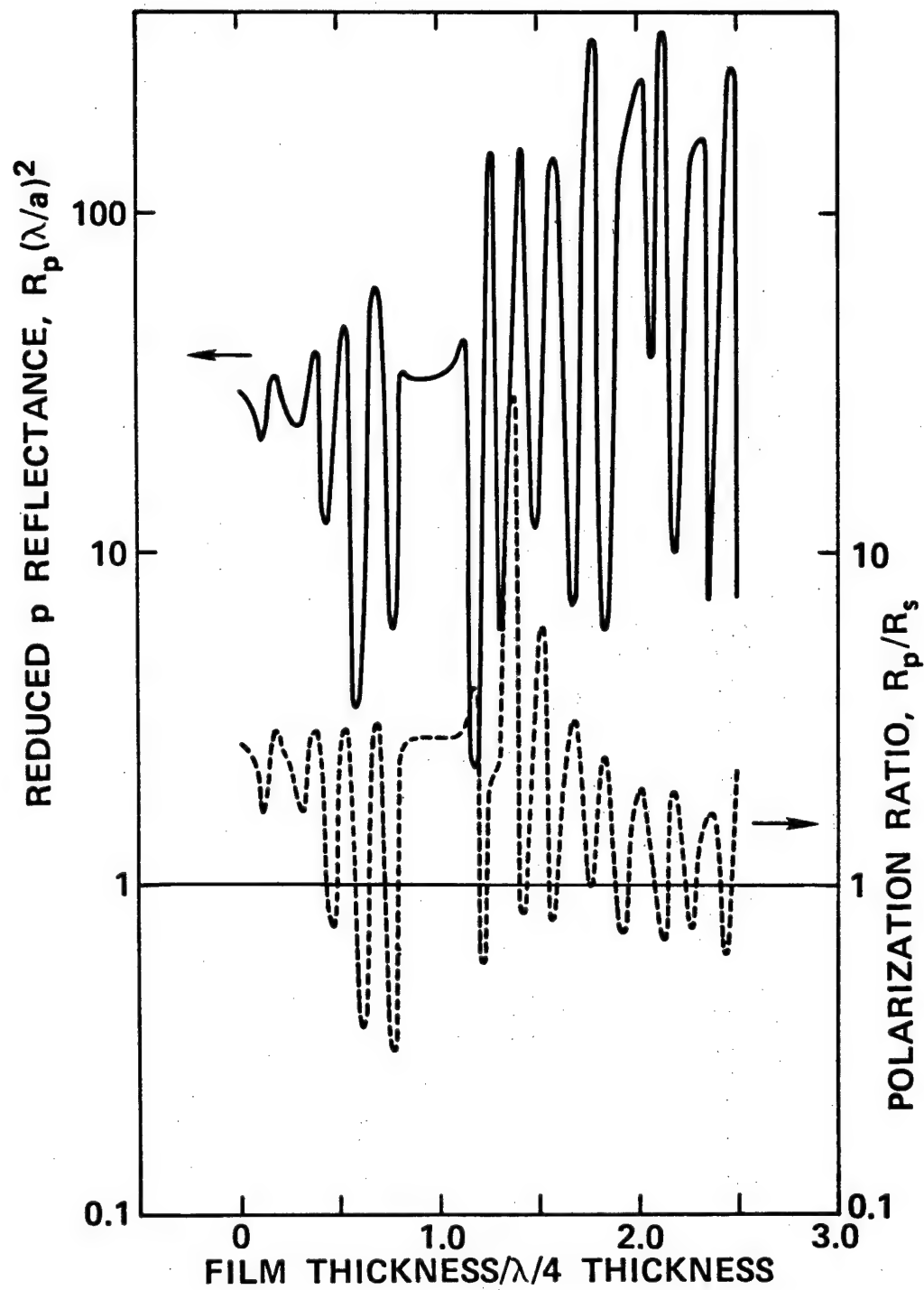


Fig.2

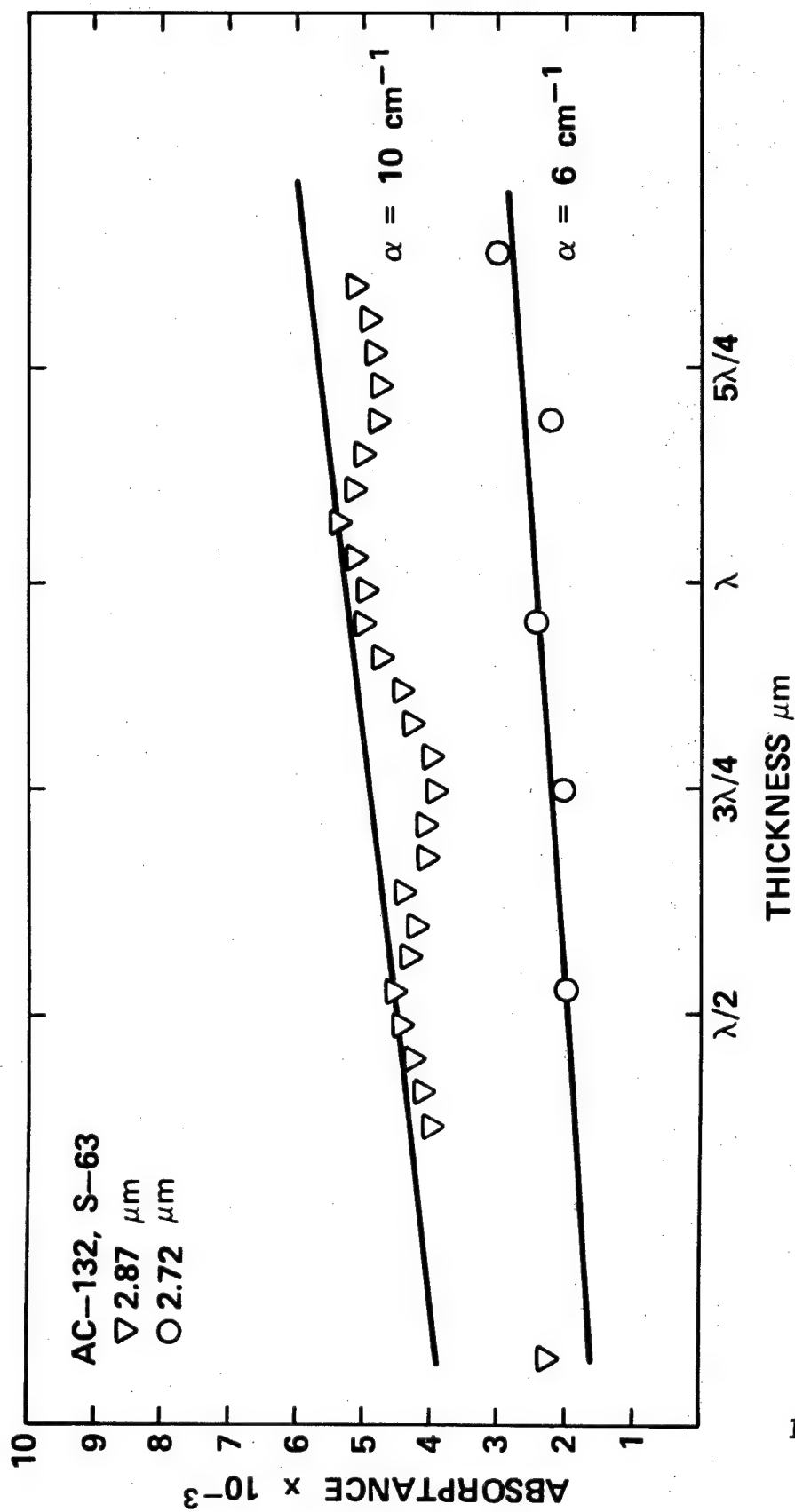


Fig. 3

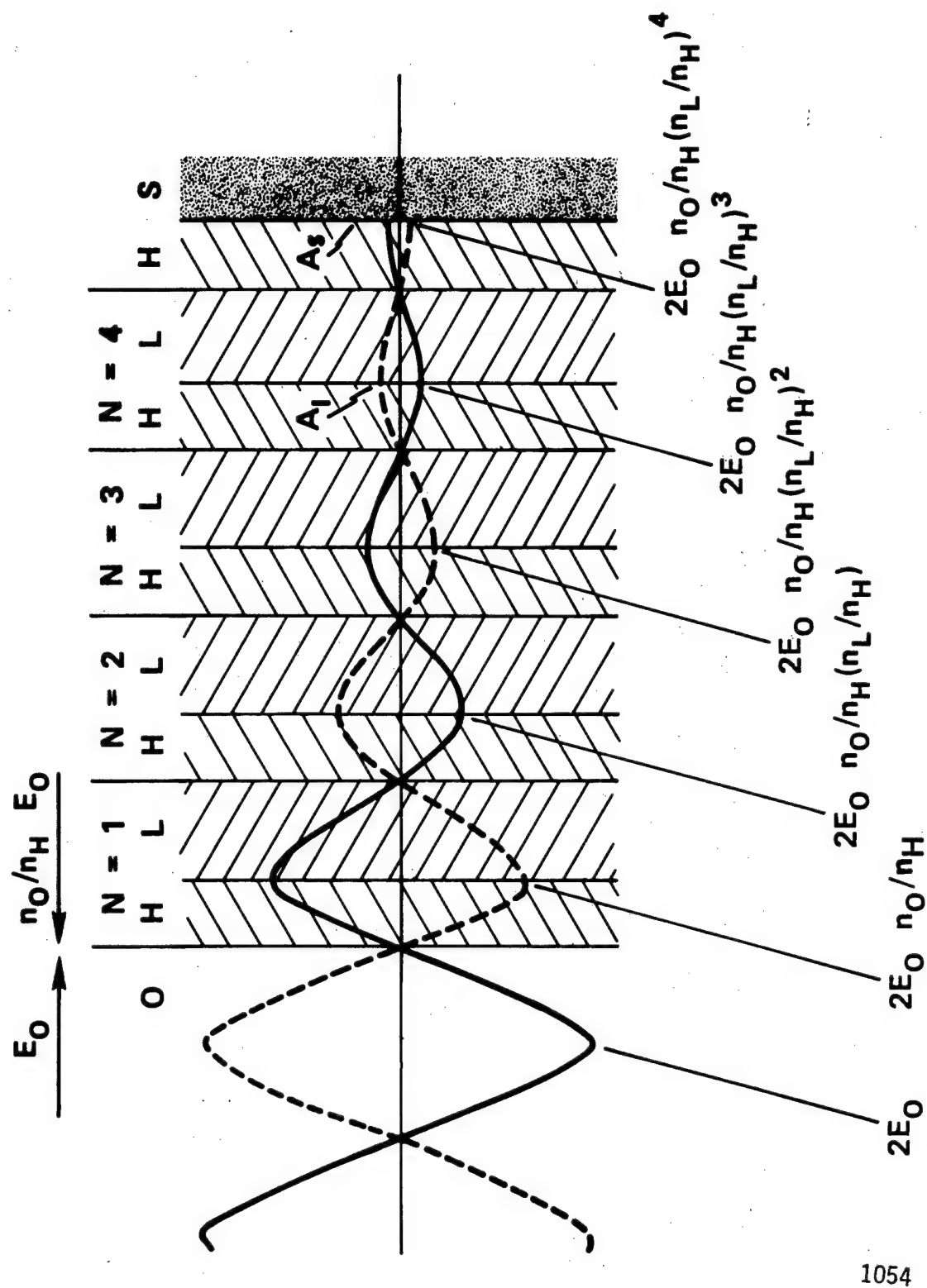


Fig. 4

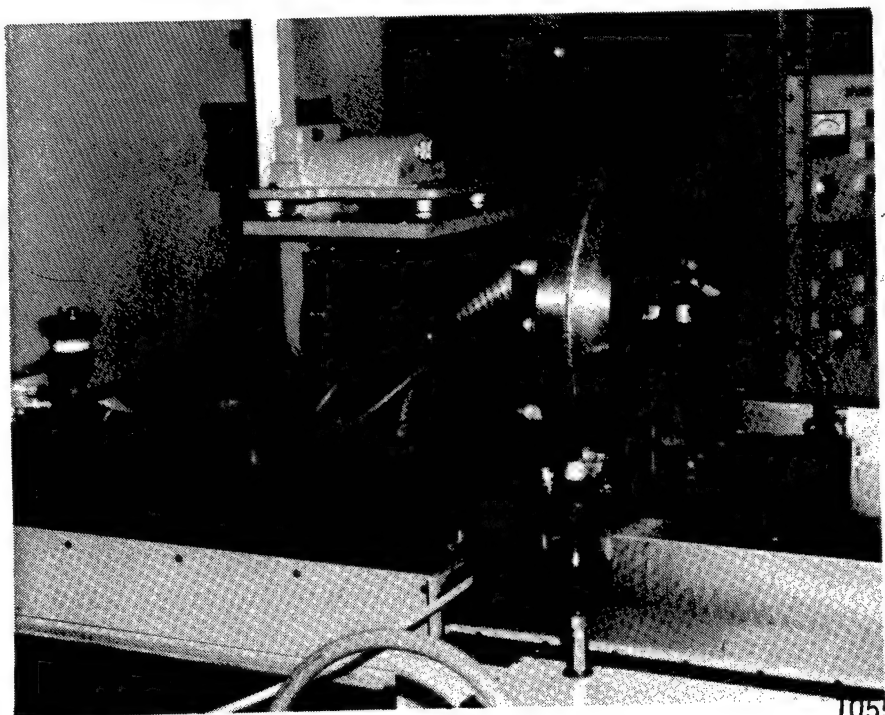


fig. 5

1055

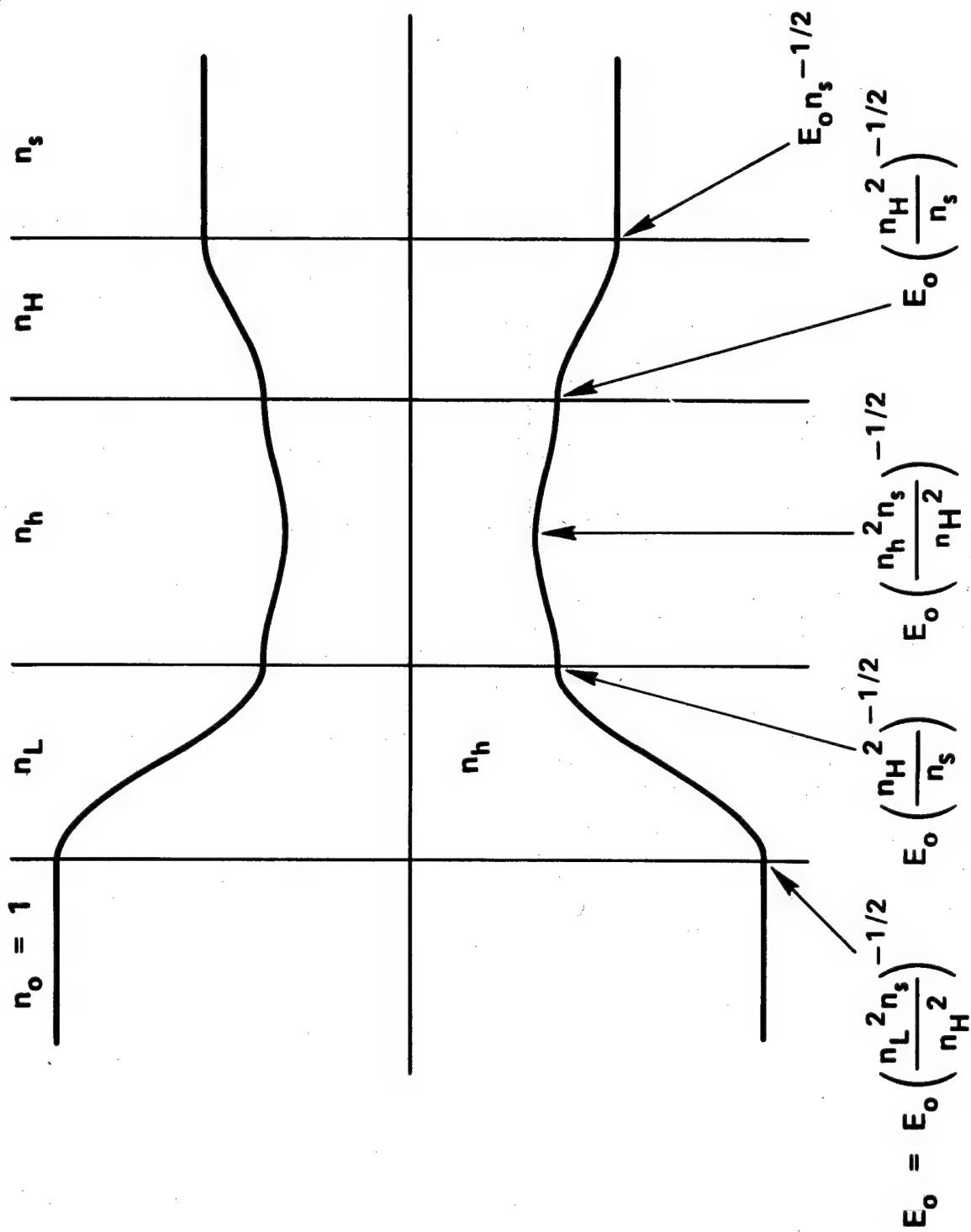


fig. 6



### Biographical Sketch

Dr. Harold E. Bennett was born in Missoula, Montana on February 25, 1929. He received his BA degree from the University of Montana in 1951 with a double major in physics and mathematics and a minor in history. He then attended Pennsylvania State University, where he received an MS degree in physics in 1953, and a PhD degree in physics in 1955 in the field of molecular spectroscopy under Dr. D. H. Rank.

Before graduation he worked briefly at the National Bureau of Standards in Washington, D.C., and after graduation he spent one year at the Wright Air Development Center in Dayton, Ohio before moving to the Naval Weapons Center, where he has remained. He is now Head of the Optical Components Technology Program Office and Associate Head of the Physics Division in the Research Department.

Dr. Bennett holds seven patents and has authored more than 80 publications on optics and related phenomena covering the general areas of spectroscopy of solids, thin film physics, solid state physics, scattered light, laser effects on materials, atmospheric optics, and optical instrumentation. He has served as Associate Editor of the Journal of the Optical Society of America and Advisory Editor of Optics Communications. At present, he is editing a special issue of Optical Engineering. He has served as a member of the International Commission for Optics and was a Director of the Optical Society of America from 1973 to 1975. In 1974 he received the LTE Thompson Award from the Naval Weapons Center, its highest civilian award. He is a member of numerous honorary societies, of the American Physical Society and is a Fellow of the American Optical Society.

IMPROVED SUBSTRATE MATERIALS FOR  
SURFACE ACOUSTIC WAVE (SAW) DEVICES

BY

Robert M. O'Connell, Captain, USAF

Electromagnetic Sciences Division

Rome Air Development Center  
Deputy for Electronic Technology  
Hanscom AFB, Massachusetts 01731

## Improved Substrate Materials For Surface Acoustic Wave (SAW) Devices

### Abstract

Surface acoustic wave (SAW) devices are becoming increasingly attractive for a variety of signal processing functions primarily because they are relatively small, lightweight, and inexpensive. Fundamental to the design of a SAW device is the choice of substrate material upon which the device is to be fabricated. For broad bandwidth requirements, the only substrate material currently available is lithium niobate, which suffers from a large sensitivity to temperature fluctuations; consequently, in applications requiring both wide bandwidth and temperature stability, it is necessary to use lithium niobate and bulky, costly ovens to accurately control the temperature. One approach to relieving this requirement has been to search for new substrate materials which have the temperature stability of quartz and the piezoelectric coupling (and hence the bandwidth capability) of lithium niobate. Toward this end, significant progress has been made at the RADC Deputy for Electronic Technology with two new materials, berlinite,  $\text{AlPO}_4$ , and lead potassium niobate,  $\text{Pb}_2\text{KNb}_5\text{O}_{15}$ . For berlinite, experimental measurements confirm our earlier theoretical prediction that it be temperature-stable at room temperature; furthermore, the measured piezoelectric coupling is almost twice as large as that of quartz. For lead potassium niobate, theoretical calculations show that it is temperature-stable with up to 17 times the piezoelectric coupling of quartz. Although these new materials are not yet readily available, they promise to make it possible to build temperature-stable SAW devices with far greater bandwidth than that possible with quartz, and without the bulky temperature control schemes necessary with lithium niobate.

## Introduction

Because they are relatively small, lightweight, and inexpensive, surface acoustic wave (SAW) devices are becoming increasingly attractive for a variety of signal processing functions. A few examples are delay lines, filters, encoders, decoders, correlators, and oscillators, all of which have Air Force applications. While a good deal of effort has been devoted to the improvement of these components, the ultimate performance of any SAW device is limited by the fundamental properties of the piezoelectric substrate material upon which it is fabricated. Depending upon the type of device and the specific application, certain fundamental material properties take on more importance than others.

In the important class of SAW devices which require temperature stability and broad bandwidth, the important material requirements are for a zero temperature coefficient of time delay and a large piezoelectric coupling coefficient. Unfortunately, there are currently no materials available which can satisfy both requirements. To overcome this deficiency, various investigations have been conducted over the past several years to find new, temperature-stable, high-coupling materials. Two of the more promising candidates to come from these investigations are berlinite,  $\text{AlPO}_4$ , and lead potassium niobate,  $\text{Pb}_2\text{KNb}_5\text{O}_{15}$ .

It is the primary purpose of this paper to present the results of experimental measurements on berlinite and theoretical calculations on lead potassium niobate which show that both materials are temperature-stable with greater bandwidth capability than that of quartz. To clarify and emphasize the problem, a brief description of SAW device operation is given first, followed by an example which dramatically shows the need for temperature stability. A few of the more important early results in the search for temperature-stable, high-coupling materials are discussed next, with the remainder of the paper devoted to the more recent results obtained at the RADC Deputy for Electronic Technology with berlinite and lead potassium niobate.

## Temperature Stability and High Piezoelectric Coupling

As an aid to understanding the operation of a SAW device, consider Figure 1. The basic device consists of a pair of interdigital transducers on a piezoelectric substrate. By means of the piezoelectric effect, an electromagnetic signal applied to the input transducer is converted to a Rayleigh type

surface acoustic wave which is confined to within a few wavelengths of the surface. The center frequency of the device  $f$  can be expressed as

$$f = v/\lambda \quad (1)$$

where  $v$  is the velocity of the surface wave on the piezoelectric medium and  $\lambda$  is defined by the geometry of the interdigital transducer. The surface wave propagates to the output transducer where the reverse piezoelectric effect converts it back to an electromagnetic signal. Notice that the device delays the electromagnetic signal by the amount of time it takes the surface wave to travel from the input transducer to the output transducer. The delay time  $t$  can be written as

$$t = \ell/v \quad (2)$$

where  $\ell$  is the spacing between the transducers and  $v$  has been defined above. A typical SAW velocity is 3000 m/sec, which is  $1/100,000$ th the speed of light. Thus, to electromagnetically produce the same amount of time delay as a 1cm long SAW delay line would require a kilometer of coaxial cable! This is just one of the many advantages of SAW technology.

In the time delay equation (2) above,  $\ell$  is related to the substrate's coefficients of thermal expansion and  $v$  is related to its thermoelastic constants. Since  $\ell$  and  $v$  are functions of temperature, so, too, is  $t$ , and the quantity used to describe this dependence is the temperature coefficient of time delay. A dramatic demonstration of the need for temperature stability (that is, a zero temperature coefficient of time delay) was provided by scientists at the Air Force Cambridge Research Labs (AFCRL) in 1972. Using a SAW correlator fabricated on a cut of quartz which is not temperature-stable, they showed (see Figure 2) that for a temperature difference of  $160^{\circ}\text{C}$ , the correlation peak disappears completely, rendering the device useless.

Piezoelectric coupling is simply a measure of the efficiency with which electromagnetic energy is converted to surface acoustic energy at the interdigital transducer. In order to design broadband SAW devices with acceptable levels of insertion-loss, it is necessary to use a substrate material whose piezoelectric coupling is high.

Many Air Force applications require temperature-stable, broadband devices. Currently, the most widely used SAW substrate materials are quartz and lithium niobate,  $\text{LiNbO}_3$ . The popular ST cut of quartz, discovered by scientists at the Raytheon Research Division in 1970, is temperature-stable, but lacks sufficient piezoelectric coupling for broadband applications. Lithium niobate, on the other hand, has the necessary coupling, but is not temperature-stable. In order to satisfy both requirements, therefore, it has been necessary to use lithium niobate and ovens to control the temperature. Especially for airborne applications, these ovens represent a less-than-ideal solution. They are large and expensive, and require either long warm-up times or excessive amounts of power for short warm-up times.

### Early Progress in Finding Improved Materials

In order to fill the need for a substrate material with the temperature stability of ST cut quartz and the piezoelectric coupling of lithium niobate, several investigations were begun in the early seventies. At that time the state-of-the-art in SAW materials could be described by Figure 3. One measure of piezoelectric coupling is a quantity known as  $\Delta v/v$ ; it is plotted on a logarithmic scale on the ordinate of the figure. The temperature coefficient of time delay is plotted on a linear scale along the abscissa, with zero on the far right. The important points to note are the ST cut of quartz with its zero temperature coefficient of time delay and the various cuts of lithium niobate with their much better coupling and much worse temperature coefficients. Lithium tantalate ( $\text{LiTaO}_3$ ), also shown in the figure, has found use as a compromise material. In terms of Figure 3, the goal of the various programs has been to find materials in the upper right-hand corner.

Since quartz is temperature-stable, scientists at the Pennsylvania State University (under RADC contract) sought to learn why, and to use their findings to make predictions about other materials that might be temperature-stable. The result of their study was a heuristic model which states that temperature-stable materials possess either of the following anomalous properties: 1) a positive temperature coefficient of an elastic constant, or 2) a negative coefficient of thermal expansion. On the basis of this model, at least three materials have been predicted and shown to be temperature-stable. One of them, Beta eucryptite,  $\beta\text{-LiAlSiO}_4$ , has been shown to be unattractive for various other reasons, and is no

longer of interest. The other two are berlinite and lead potassium niobate, each of which is discussed in a separate section below.

Another approach has been to consider the sulfosalts, a class of materials of the form  $Tl_3BX_4$ , where B can be V, Nb, or Ta, and X can be S or Se. Scientists at the Westinghouse Research Laboratories and at the University of Maine have shown that at least two of these materials are temperature-stable with significantly larger piezoelectric coupling than ST cut quartz. However, their SAW velocities are much slower than those of quartz or lithium niobate, and it can be seen from the frequency equation (1) above that the sulfosalts are applicable to lower frequencies than quartz or lithium niobate. They are considered complimentary to, rather than competitive with, berlinite and lead potassium niobate.

A third approach to the problem, pursued by scientists at the Raytheon Research Division, has been to develop a temperature-stable composite structure by sputtering a film of silicon dioxide on lithium tantalate. While this composite has significantly larger piezoelectric coupling than ST cut quartz and a similar SAW velocity, it suffers from fabrication difficulties, dispersion, and excessive losses at high frequencies.

### Berlinite

Although the results obtained with the materials discussed in the previous section demonstrate that progress has been made toward finding better SAW substrate materials, the most promising results to date have been obtained with berlinite and lead potassium niobate. Both of these materials were initially identified as being potentially temperature-stable by researchers at Pennsylvania State University. Subsequent investigations at the RADC Deputy for Electronic Technology and elsewhere have confirmed this and shown that they both have greater piezoelectric coupling than ST cut quartz.

Like quartz, berlinite is of the  $D_3(32)$  crystal class and has a positive temperature coefficient for one of its elastic constants, thereby satisfying the Penn State heuristic model. Motivated by this, we conducted a theoretical investigation of berlinite's surface acoustic wave properties in 1976. The investigation consisted of using an iterative computer program to calculate various SAW quantities for different crystallographic orientations. The computer program was

written by scientists at The Hughes Aircraft Company in 1968 and is the solution of the problem of acoustic wave propagation on an arbitrary anisotropic piezoelectric medium.

An example of the type of theoretical information which the computer program provided for berlinite is shown in Figure 4. The inset in the upper frame defines the initial crystallographic orientation and how it is to be varied. The case of Figure 4 is called an X-axis boule; the direction of SAW propagation is fixed along a previously defined X-axis, and the plate-normal direction is rotated about the propagation direction as shown. At each position of the plate normal (the abscissa in Figure 4), three SAW properties are calculated: SAW velocity (in the upper frame), the  $\Delta v/v$  piezoelectric coupling number (in the center frame), and the temperature coefficient of time delay (in the lower frame). As the lower frame of Figure 4 shows, the temperature coefficient of time delay is zero at two crystallographic orientations, indicating that berlinite is temperature-stable. Only the orientation at  $\mu = 80.4^\circ$  is interesting, though, because its  $\Delta v/v$  piezoelectric coupling is four times larger than that of ST cut quartz.

Having obtained this and other exciting theoretical results, we sought to experimentally verify them. Berlinite is presently available only in limited research-produced quantities, and we were fortunate to obtain a sample from the Naval Weapons Center. The sample was cut by technicians at Manlabs, Inc., to the X-axis boule  $80.4^\circ$  orientation discussed above, and a delay line of the type described earlier was fabricated photolithographically by our own technicians.

The SAW velocity of the sample was measured using the frequency equation (1). The quantity  $\lambda$  is fixed by the master used to fabricate the transducers, and is very accurately known. The center frequency  $f$  was obtained by measuring the insertion-loss versus frequency of the delay line with a spectrum analyzer and defining  $f$  as the frequency corresponding to minimum insertion-loss. Using these values of  $\lambda$  and  $f$  in equation (1), we obtained a measured SAW velocity of 2743 m/sec, which agreed quite well with the theoretically calculated value of 2751 m/sec.

To measure the temperature coefficient of time delay, the delay line was used as a feedback element between the output and input terminals of an amplifier to form an oscillator circuit. The delay line was enclosed in a temperature chamber and the frequency of oscillation measured as a function of



temperature. The results are shown in Figure 5. The fact that the curve "turns over" at 25°C means that the first order temperature coefficient of frequency (or time delay) is zero at room-temperature, which verifies the theoretical prediction. This technique for measuring a material's time delay versus temperature behavior was first described in 1969 by scientists at the Royal Radar Establishment in England.

Finally, the piezoelectric coupling coefficient was estimated from the input impedance of the delay line as measured with a network analyzer. This technique requires the use of a circuit model for the interdigital transducer, and various assumptions about the values of the elements in that circuit. The analysis yielded a piezoelectric coupling coefficient which is only half as large as the theoretically predicted value, but which is still twice as large as that of ST cut quartz. The experimental value of the piezoelectric coupling may well approach the theoretical value as better quality crystals become available.

#### Lead Potassium Niobate

The newest material is lead potassium niobate (PKN),  $\text{Pb}_2\text{KNb}_5\text{O}_{15}$ , which occurs in the tungsten bronze structure and belongs to the orthorhombic crystal class  $\text{mm}2(\text{C}_{2v})$ . Several of PKN's elastic constants have positive temperature coefficients, and so it, too, satisfies the Penn State heuristic model.

Using the previously described computer program, we calculated the SAW properties of PKN and found several crystallographic orientations for which the material is temperature-stable. The most exciting result of those calculations is that the piezoelectric coupling coefficients of the temperature-stable orientations are up to 17 times as large as that of ST cut quartz.

Like berlinite, very few samples of PKN are currently available. Scientists at Penn State University, under contract with the RADC Deputy for Electronic Technology, have made significant progress in solving many of the problems associated with the growth of PKN, and they have recently provided us with a modest-sized, single-crystal sample. That sample, shown in Figure 6, is currently being prepared for an experimental assessment of PKN's SAW potential.

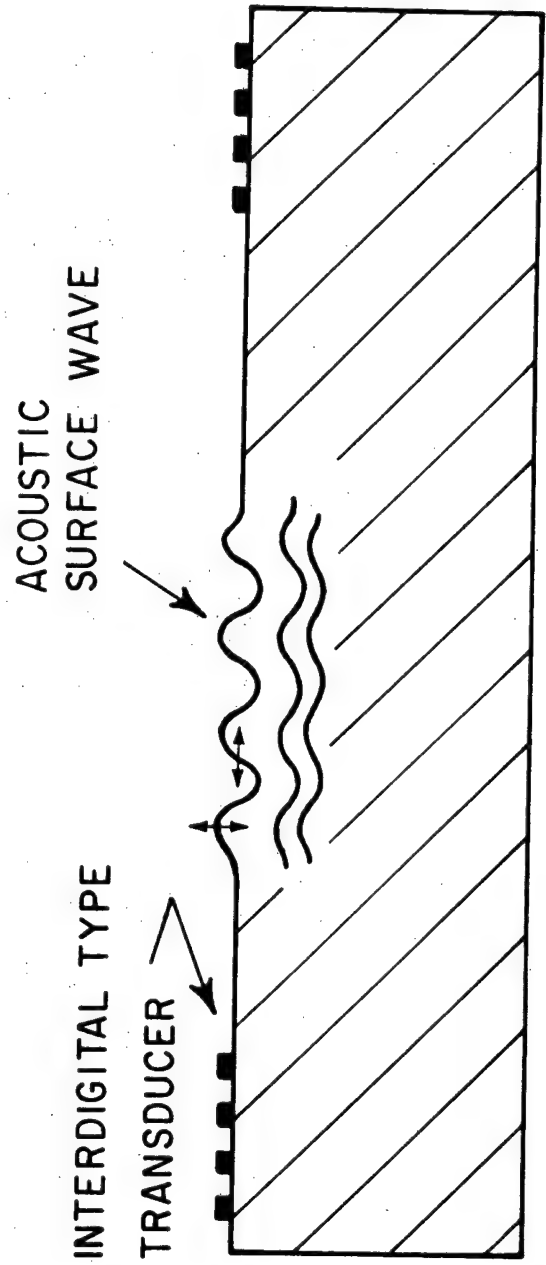
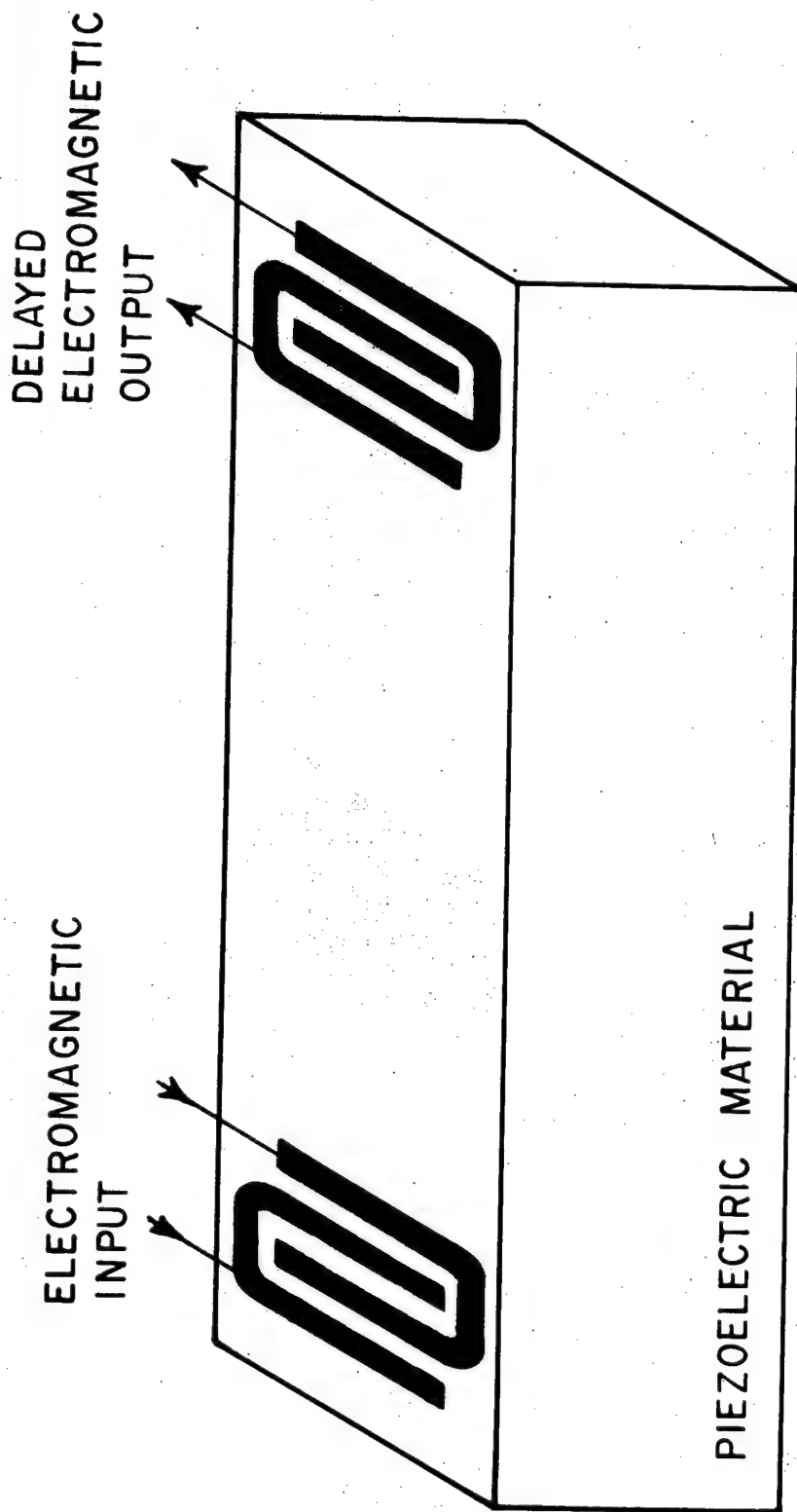
#### Conclusion

The current state-of-the-art in SAW materials is shown in Figure 7; and it includes all of the temperature-stable

materials which have been discussed above. These new materials are all in early stages of their development, and are not yet commercially available. For berlinite and lead potassium niobate, the most promising of these, many growth related problems must still be solved before more accurate determinations of their SAW potential can be made. Despite this, it is clear from Figure 7 that a great deal of progress has been made in closing the piezoelectric coupling gap that exists between quartz and lithium niobate. When these and other new materials become readily available, it will be possible to build temperature-stable, low insertion-loss SAW devices with far broader bandwidth than that possible with quartz, and without the undesirable temperature-control schemes necessary with lithium niobate.

### Figure Captions

- Figure (1) The basic elements of a surface acoustic wave device.
- Figure (2) The effect on the correlation peak of a SAW correlator due to changing temperature when the substrate material is not temperature-stable.
- Figure (3) The state-of-the-art in SAW materials prior to the search for temperature-stable, high piezoelectric coupling materials.
- Figure (4) Theoretical surface acoustic wave data for X-axis boule berlinite. The inset defines "X-axis boule", and the quantities calculated are SAW velocity (upper frame),  $\Delta v/v$  piezoelectric coupling coefficient (center frame), and temperature coefficient of time delay (lower frame).
- Figure (5) Relative frequency shift versus temperature for a SAW oscillator with the berlinite delay line as feedback element. The turn-over at 25°C shows that berlinite's first order temperature coefficient of time delay is zero at room temperature.
- Figure (6) A single-crystal sample of lead potassium niobate, grown at The Pennsylvania State University. The sample has been cut as shown, and the piece on the left is currently being prepared for an experimental assessment of PKN's SAW potential.
- Figure (7) The current state-of-the-art in temperature-stable, high-coupling SAW materials. The most promising new materials are berlinite and lead potassium niobate.

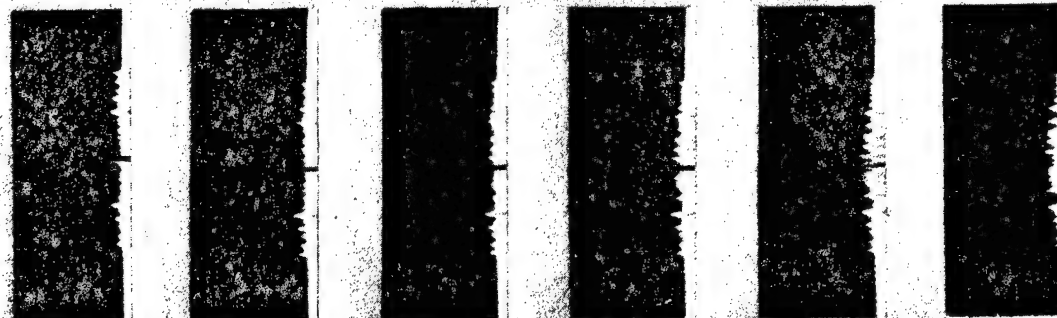
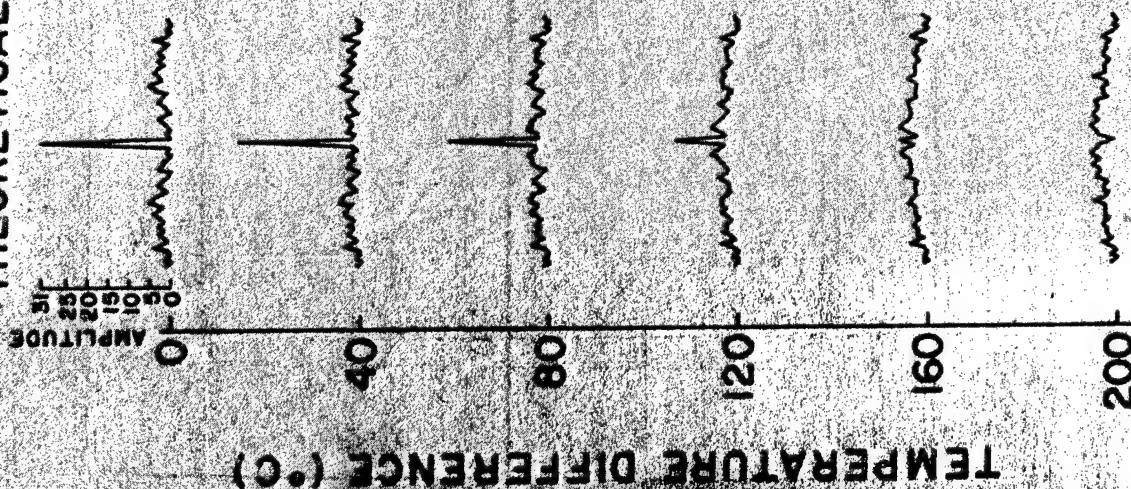


1068

FIG. 1

# CORRELATION FUNCTION vs $\Delta T$ ON Y-X QUARTZ

THEORETICAL EXPERIMENTAL



1  $\mu$  sec/DIV

FIG. 2

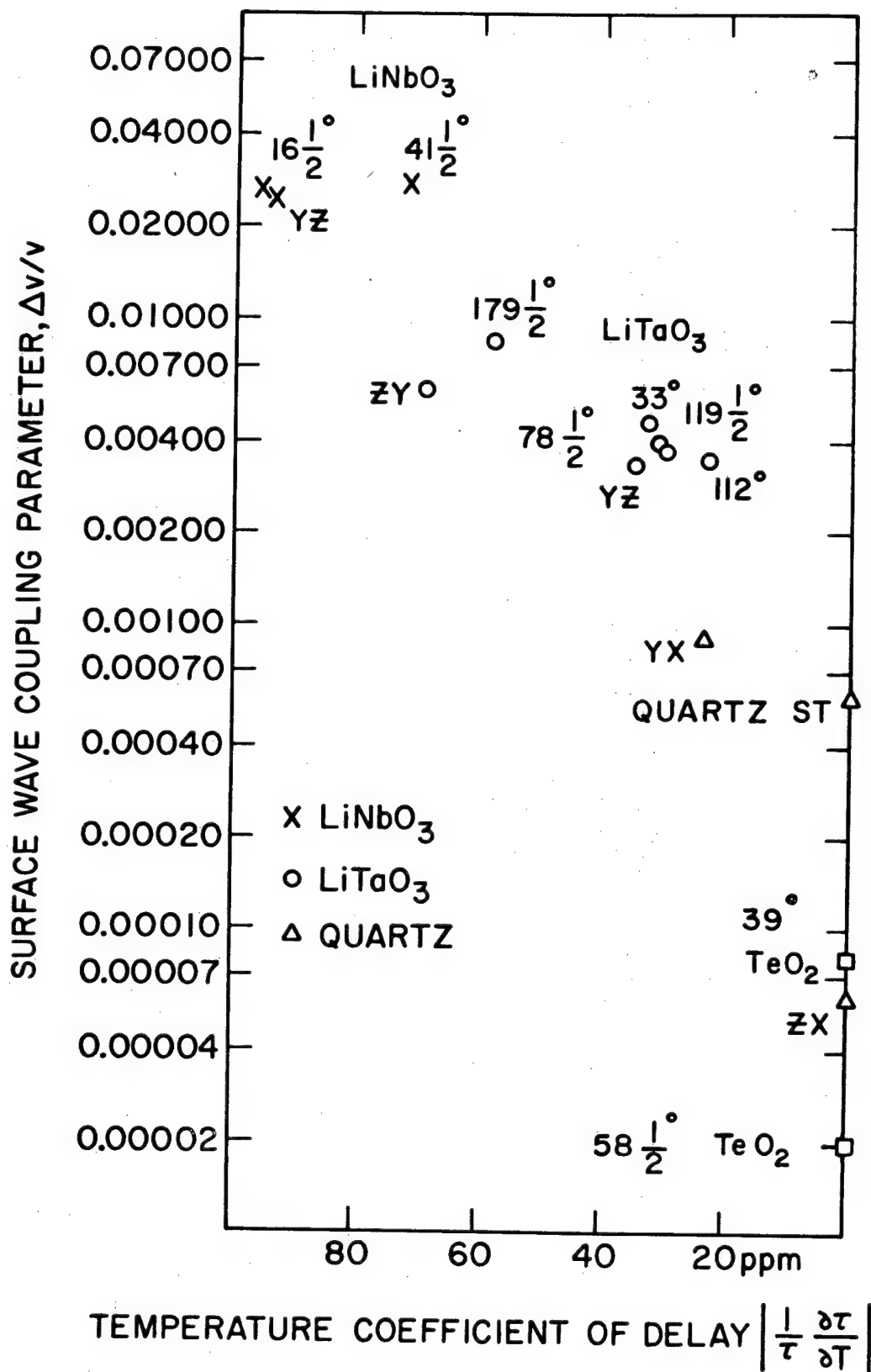


FIG. 3

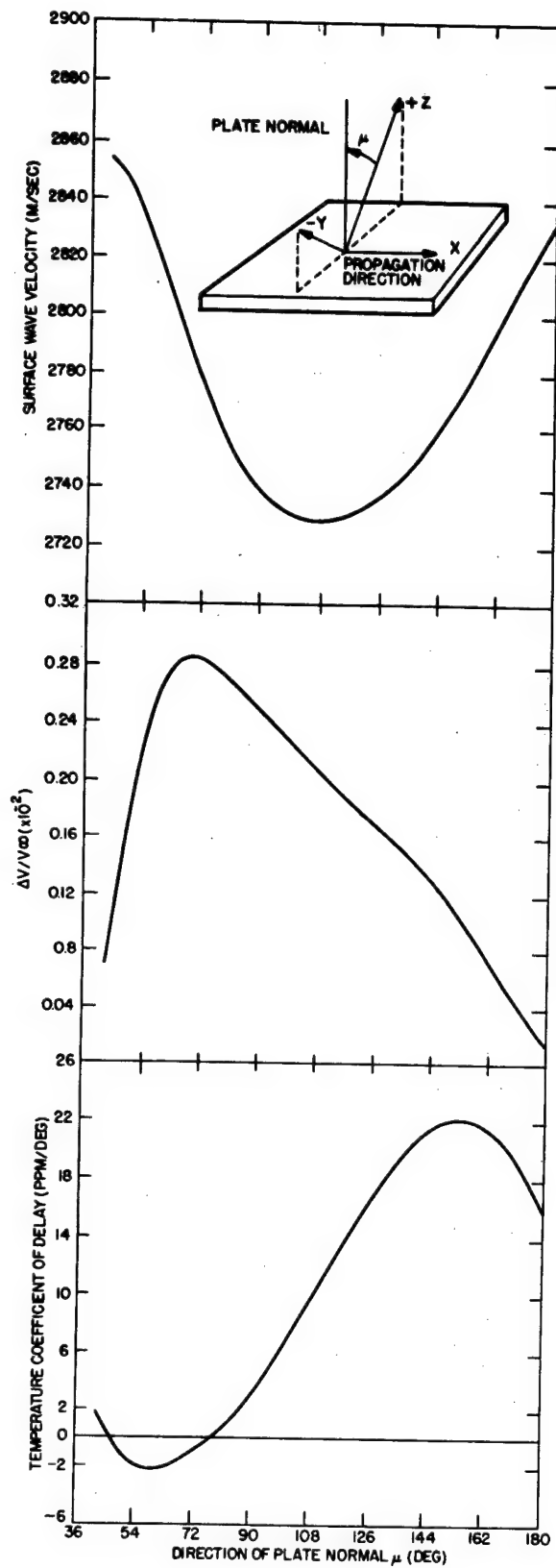


FIG. 4

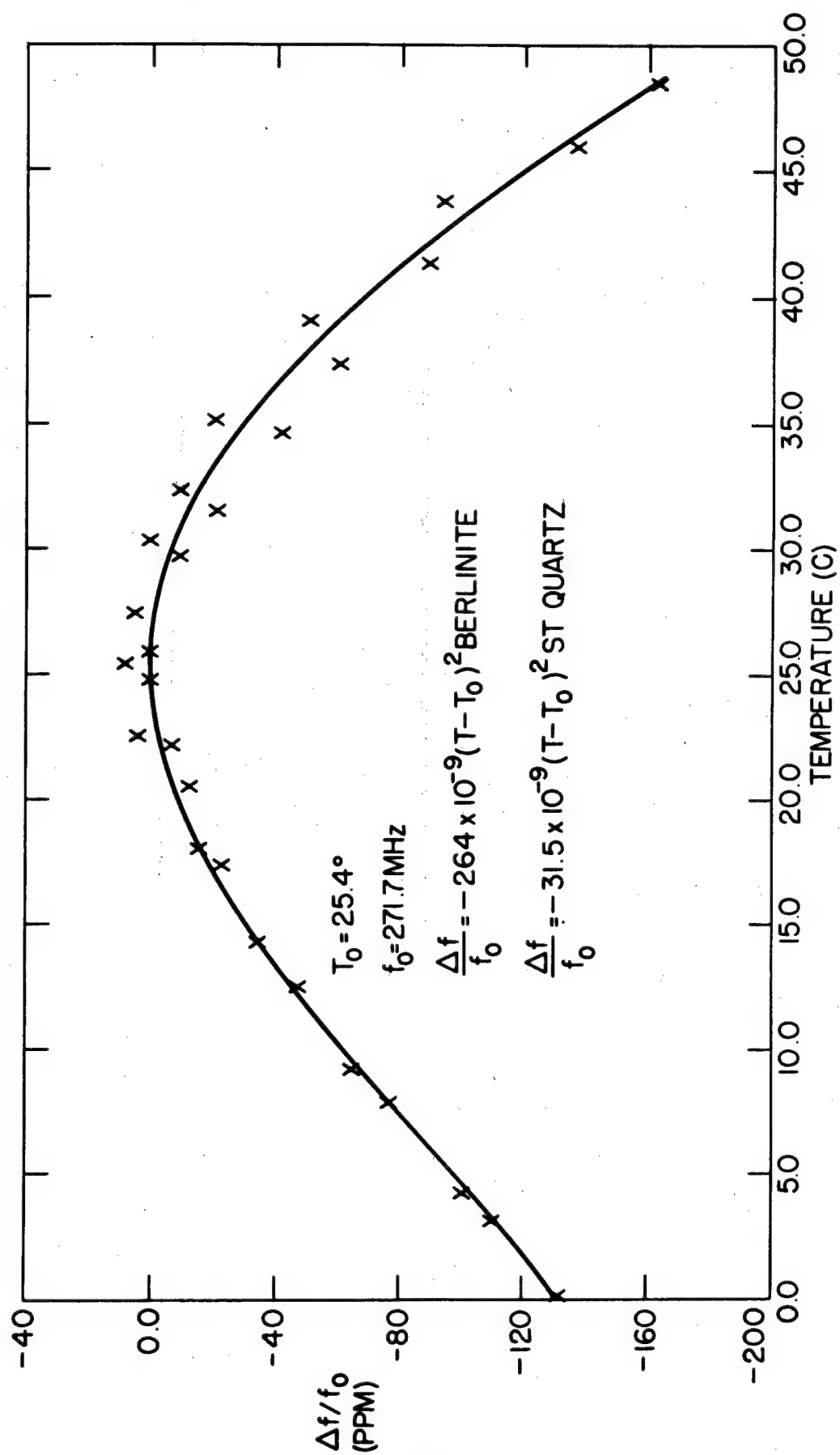


FIG. 5





FIG. 6

1072

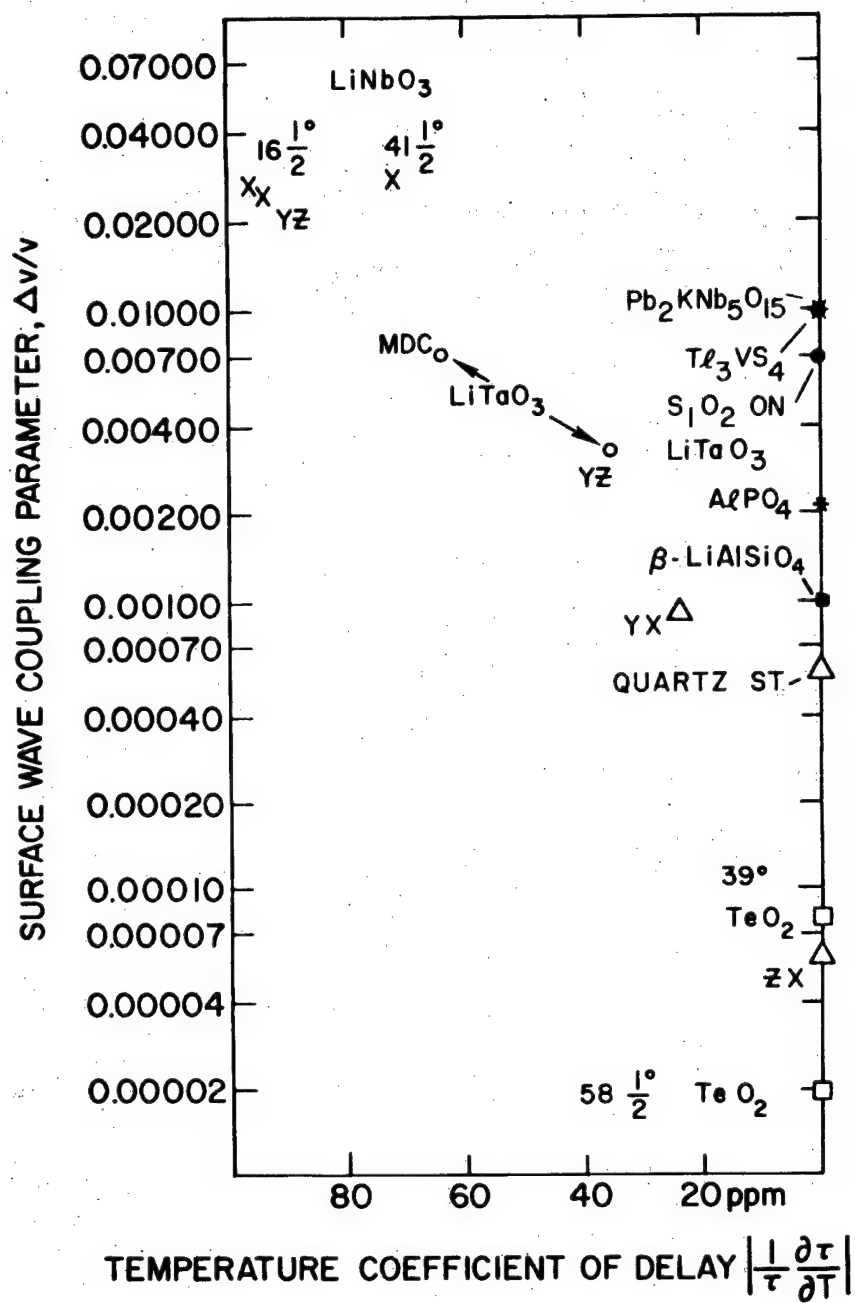


FIG. 7

### Biographical Sketch

Captain Robert Michael O'Connell was born in New York, New York on March 9, 1949. In 1971 he graduated from Manhattan College, New York, with a BE degree in electrical engineering and was commissioned in the Air Force through the AFROTC program. He attended the University of Illinois on an educational delay, and received the M.S. and Ph.D degrees in electrical engineering in 1972 and 1975, respectively.

Since October, 1975, he has been on active duty with the Rome Air Development Center Deputy for Electronic Technology at Hanscom AFB, Massachusetts. He has been engaged in research on new piezoelectric materials for surface acoustic wave (SAW) applications, and has written eight papers on that subject. In addition, he has been the technical monitor of several SAW technology research and development contracts. Captain O'Connell is a member of the IEEE, Eta Kappa Nu, Tau Beta Pi, and Sigma Xi.

A SIMPLE PREDICTION METHOD FOR  
VISCOUS DRAG AND HEATING RATES

BY

Tse-Fou Zien, Ph.D., USN

Research and Technology Department

Naval Surface Weapons Center  
White Oak Laboratory  
Silver Spring, Maryland

A Simple Prediction Method for Viscous  
Drag and Heating Rates

Abstract

A simple integral method is presented which provides accurate estimates of friction drag and heating rates on aerodynamic bodies. The basic idea of the method lies in the use of integral expressions for various aerodynamic quantities on the surface of the body under study. Applications of the method are given in skin-friction and convective heat-transfer calculations for laminar boundary-layer flows, three-dimensional boundary layer calculations and transient ablation problems, all based on somewhat idealized, but representative, models. Approximate solutions are compared with available exact solutions to determine the accuracy of the method. They are also compared with the classical integral solutions to assess the degree of improvements achieved. It is amply demonstrated that the present method provides accurate solutions to the model problems with remarkable simplicity.

## 1. Introduction

The fluid dynamic phenomena associated with the operation of most high-speed aerodynamic weapons, such as reentry vehicles, are generally very complex. In order to analyze these phenomena and to provide their predictions for design purposes, simple analytical methods need to be developed. Such methods have the unique advantage of providing considerable insight into the physical problem under study without the expenditure of an undue amount of computational efforts. The design procedure for advanced aerodynamic weapons can thus be substantially economized.

In this paper, a simple integral method is presented which is especially suitable for accurate predictions of the friction drag and heating rates on aerodynamic bodies. These quantities are believed to have critical effects on the performance of aerodynamic vehicles in general. The method has found its applications in such areas as boundary-layer flows and transient heat conduction, and these applications are also illustrated in the present paper. It is noted here that the mathematical descriptions of these physical problems all require nonlinear partial differential equations, and their solutions are generally extremely difficult. The ability of the present method in providing accurate solutions to these problems with great simplicity is particularly remarkable.

The basic ideas which form the basis of the present development first appeared in a brief article by Volkov<sup>(1)</sup>. These ideas have since been considerably generalized and successfully exploited by the present author in the approximate solution of problems in a wide variety of technical areas mentioned above (see, for example, Refs. (2,3,4,5,6)). The interested reader is referred to these references for more details of the discussion presented in this paper.

In the following, the basic ideas of the method are first described in section 2 by means of some examples of laminar skin-friction calculations for certain basic configurations. The application to laminar heat transfer calculations is next illustrated in section 3, and a

special limiting flow is solved as an example. In section 4, the method is applied to a relatively simple three-dimensional boundary layer with particular emphasis on cross-flow skin-friction calculations. One-dimensional transient heat conduction is the last area of application of the method discussed in this paper, and section 5 gives the solutions to a class of ablation problems in which the applied heat flux varies as a power of time. Finally, some concluding remarks are stated in section 6.

## 2. Basic Ideas and Skin-Friction Calculations

### 2.1 General Discussion

The central ideas of the present method can be most conveniently described by means of its simplest application, i.e., skin-friction calculations. For simplicity, we consider the two-dimensional, incompressible, laminar boundary layers on a porous surface. In practical applications, the surface porosity can be used for blowing and/or suction in transpiration cooling, boundary-layer control, etc. The inviscid flow outside the boundary layer is assumed to be the potential flow, and separated flow is thus ruled out by implication.

The governing equations of the boundary-layer flow are

$$\frac{\partial u}{\partial x} + \frac{\partial v}{\partial y} = 0 \quad (1)$$

$$u \frac{\partial u}{\partial x} + v \frac{\partial u}{\partial y} = u_e \frac{du_e}{dx} + \frac{1}{\rho} \frac{\partial \tau}{\partial y} \quad (2)$$

with the boundary conditions

$$u(x, 0) = 0 \quad (3a)$$

$$v(x, 0) = v_w(x) \quad (3b)$$

$$\lim_{y \rightarrow \infty} u(x, y) = u_e(x) \quad (3c)$$

In the above system and also in the discussion that follows,  $(x, y)$  forms an orthogonal coordinate system with  $x$  measuring the distance along the surface, and  $(u, v)$  is the corresponding velocity vector.  $\tau$ ,  $\rho$ , and  $v$  signify,

respectively, the shear stress, fluid density and kinematic viscosity. Conditions at the wall and at the outer edge of the boundary layer are represented by  $w$  and  $e$ , respectively. We note here that for laminar flows, the shear stress and the velocity field are simply related,

$$\tau = \mu \frac{\partial u}{\partial y} \quad (4)$$

where  $\mu (= \rho \nu)$  is the dynamic viscosity coefficient, and is generally a given quantity.

To proceed to an approximate solution of the problem, the momentum equation, Eq. (2), is first integrated over the entire boundary-layer thickness,  $y = \delta(x)$ , leading to the well-known Karman-Pohlhausen (K-P) momentum balance integral (MBI),

$$\frac{\tau_w}{\rho} = \frac{d}{dx} \int_0^\delta u(u_e - u) dy + \left( \frac{du_e}{dx} \right) \int_0^\delta (u_e - u) dy - u_e v_w \quad (5)$$

where Eq. (1) has been used to eliminate  $v$  in favor of  $u$ .

In the classical K-P technique, Eq. (5) is the only equation for the solution of the problem. After an appropriate velocity profile,  $f$ ,

$$\frac{u}{u_e} = f(x, y; \delta(x)) \quad (6)$$

is assumed and substituted for  $u$  in Eq. (5), the equation reduces to a first order ordinary differential equation for the profile parameter,  $\delta(x)$ .

Note here that in the classical technique, the wall shear stress is based on the derivative of the approximate profile, i.e.,

$$\tau_w = \mu u_e \left( \frac{\partial f}{\partial y} \right)_w \quad (7)$$

Since  $f$  is only an approximate (usually a crude approximation) velocity profile, its derivative is likely to incur additional inaccuracies in the approximation.

In the present approach, the MBI equation, (5), is only used as an expression for  $\tau_w$ , after  $u_e f$  is substitute



for  $u$  on the right-hand side of the equation. Therefore, the skin friction is not based on the derivative of the assumed profile at the wall. Instead, it is based on the integrals involving the assumed profile. The idea of using the integral expression for the skin friction is believed to be the key to the success of the present method.

A second equation is needed for the determination of the basic profile parameter,  $\delta(x)$ . Depending on how the second equation is generated, the present author<sup>(5)</sup> proposed two different schemes both of which have been used with equal success.

The  $y$ -moment scheme uses the  $y$ -moment integral of the momentum equation as the second equation, i.e.,

$$\int_0^\delta y \left( u \frac{\partial u}{\partial x} + v \frac{\partial u}{\partial y} \right) dy = \int_0^\delta y \left( u_e \frac{du_e}{dx} + \frac{1}{\rho} \frac{\partial \tau}{\partial y} \right) dy, \quad (8)$$

whereas the  $u$ -moment scheme uses the  $u$ -moment integral of the momentum equation as the second equation,

$$\int_0^\delta u \left( u \frac{\partial u}{\partial x} + v \frac{\partial u}{\partial y} \right) dy = \int_0^\delta u \left( u_e \frac{du_e}{dx} + \frac{1}{\rho} \frac{\partial \tau}{\partial y} \right) dy \quad (9)$$

The solution procedure is as follows. First, an appropriate velocity profile, Eq. (6), is assumed which satisfies the essential boundary conditions of the physical problem. Substituting the profile for  $u$  into either Eq. (8) or Eq. (9) results in an ordinary differential equation for the quantity  $\delta(x)$ . After  $\delta(x)$  is solved, Eq. (5) gives the skin friction through almost an algebraic process.

It should be noted that while Eq. (5) holds for turbulent boundary layers as well if  $u$  is taken to be the mean velocity and if the normal component of the Reynolds stress is small compared to the shear components, as is usually the case, the moment equations, (8) and (9), do require a knowledge of the turbulent shear stress distribution (hence a turbulence model) inside the boundary layer when applied to turbulent boundary layers.

## 2.2 Porous Plate: Uniform Blowing

We now specialize the above general formulation to the case of laminar boundary layers on a porous flat plate with uniform blowing. This is a case of nonsimilar boundary layers whose exact solution necessarily requires extensive numerical computations.

Here, we have  $u_e = u_o = \text{const.}$  and a constant blowing parameter,  $\epsilon$ ,

$$\epsilon \equiv \frac{v_w}{u_o} = \text{const.} \quad (10)$$

Four very different velocity profiles with a varying degree of complexity have been assumed in the calculation, and they are

$$f_1 = \eta \quad (11a)$$

$$f_2 = \eta(1 + m\eta)/(1 + m) \quad (11b)$$

$$f_3 = 2\eta - 2\eta^3 + \eta^4 \quad (11c)$$

$$f_4 = [2\eta + 6k\eta^2 - 2(1 + 4k)\eta^3 + (1 + 3k)\eta^4]/(1 + k) \quad (11d)$$

where  $u/u_o = f_n$  ( $n = 1, 2, 3, 4$ ),  $\eta \equiv y/\delta(x)$ ,  $m = \epsilon\Delta/2$ ,  $k = \epsilon\Delta/6$  and  $\Delta \equiv u_o\delta/\nu$ . The profiles  $f_2$  and  $f_4$  satisfy the wall compatibility condition whereas  $f_1$  and  $f_3$  are oversimplified profiles deliberately chosen to test the capability of the method in handling crude approximations of the unknown velocity.

The y-moment scheme was used in the calculation, and the solutions corresponding to these four profiles were all obtained in closed form. The detailed solutions are omitted here to conserve space, but they can be found in Ref. 2 and the publications referred therein. The solution corresponding to  $f_2$  is shown below to indicate the general form of the present solutions:

$$m - \frac{9}{10} \ln(1 + m) + \frac{17}{10} m/(1 + m) + \frac{3}{20} \ln(1 + 2m + 4m^2/3) - \frac{63}{10\sqrt{3}} \tan^{-1} \frac{m}{\sqrt{3}(1 + m)} = 3\epsilon^2 \text{Rex} \quad (12a)$$

and

$$\frac{1}{2} C_f \text{Rex}^{\frac{1}{2}} = \frac{1}{2} \text{Rex}^{\frac{1}{2}} \left[ \frac{1}{3} \frac{(\frac{2}{5} m^2 + m + 1)(\frac{4}{3} m^2 + 2m + 1)}{m(m+1)(\frac{1}{9} m^2 + \frac{4}{15} m + \frac{1}{4})} - 2 \right] \quad (12b)$$

where  $\frac{1}{2} C_f \equiv \tau_w / \rho u_0^2$  and  $\text{Rex} \equiv u_0 x / \nu$ . Eqs. (12a,b) give a parametric representation of the solution  $\frac{1}{2} C_f \text{Rex}^{1/2}$  as a function of  $\epsilon \text{Rex}^{1/2}$  with  $m$  serving as a parameter.

These solutions are shown in Fig. 1 compared with the numerical solution of Catherall, et al.<sup>(7)</sup> which is used as the standard for comparison. The classical K-P solutions of the same problem based on the same profiles, Eqs. (11), are also shown in Fig. 1 compared with the numerical solution.

It is clear that the present solutions are all sufficiently accurate for most engineering purposes over a wide range of the blowing strength. A remarkable finding is that the results corresponding to the four very different profiles agree very closely, indicating the weak dependence of results on the assumed profile. This is obviously a highly desirable feature of the method, because the choice of a profile is never unique, and the suppression of the sensitivity of results to the choice of the profile enhances the reliability of the approximate solution.

The classical K-P solutions, on the other hand, are far less satisfactory. They are generally inaccurate, especially at large blowing rates where it fails to predict the "blow-off" phenomenon, and they are strongly dependent on the profile chosen in the calculation.

It will be revealed in the following that the characteristics of the present method as demonstrated in the solution of this particular problem prevail in other applications as well.

### 2.3 Impermeable Circular Cylinder

We next consider the laminar boundary layer on a circular cylinder with radius  $a$  in cross flow as an example of flows with pressure gradients. In this flow, we have  $u_e = 2u_\infty \sin\phi$  and  $v_w = 0$  where  $u$  is the uniform freestream velocity at upstream infinity (see Fig. 2).

Two simple polynomial profiles are used in the calculation, i.e.,

$$f_1 = \eta \quad (13a)$$

$$f_3 = 2\eta - 2\eta^3 + \eta^4 \quad (13b)$$

where  $u/u_e = f_\eta$  and, as before,  $\eta \equiv y/\delta$ . Note that these profiles are crude and oversimplified inasmuch as they presume similarity for the nonsimilar flow.

Substitution of Eq. (13a) or Eq. (13b) into the  $y$ -moment integral equation, (8), leads to an ordinary differential equation for the unknown  $\delta(\phi)$ . For  $u/u_e = f_1$ , the equation has the following form:

$$\sin\phi(d/d\phi)\bar{\delta}^2 + (6\cos\phi)\bar{\delta}^2 = 8/A \quad (14)$$

with the condition  $\bar{\delta}(0) < \infty$ , where  $\bar{\delta} \equiv \delta/a$  and  $A \equiv u_\infty a/\nu$ .

The solution of Eq. (14) is easily determined to be  $A\bar{\delta}^2 = (\sin\phi)^{-6}(-5\cos\phi + \frac{5}{6}\cos 3\phi - \frac{1}{10}\cos 5\phi + \frac{64}{15})$ , (15a)

and the skin friction follows from Eq. (15),

$$\frac{1}{2} C_f A^{\frac{1}{2}} = \frac{4}{3} \bar{\delta} A^{\frac{1}{2}} \sin\phi [\cos\phi + 2/(\bar{\delta} A^{\frac{1}{2}})^2] \quad (15b)$$

where  $\frac{1}{2} C_f \equiv \tau_w/\rho u_\infty^2$ .

Again, Eqs. (15a) and (15b) constitute the parametric representation of  $\frac{1}{2} C_f A^{1/2}$  as a function of  $\phi$  with  $\bar{\delta} A^{1/2}$  as the parameter.

For  $u/u_e = f_3$ , it is easy to show that the solution is given by the following pair of equations:

$$A \bar{\delta}^2 = 16.3 \int_0^\phi \sin^{4.467} \phi \, d\phi / (\sin^{5.467} \phi) \quad (16a)$$

$$\begin{aligned} \frac{1}{2} C_f A^{1/2} = & (A^{1/2} \bar{\delta} \sin \phi) [0.8553 \cos \phi \\ & + 3.8292 / (A \bar{\delta}^2)] \end{aligned} \quad (16b)$$

The above results are plotted in Fig. 2 along with the numerical solution due to Terrill<sup>(8)</sup> which is used here as the standard to establish the accuracy of the present solutions. It is clear that the approximate solutions are remarkably accurate from the stagnation point to the separation point ( $\tau_w = 0$ ). However, it must be stressed that the prediction of separation point here has only limited practical significance in view of the idealized model for the inviscid flow used in the calculations. In addition, the insensitivity of present results to the choice of profiles continues to prevail in the present example.

An interesting comparison of the present and other approximate methods of skin-friction calculations is given by Inger<sup>(9)</sup>

### 3. Convective Heat Transfer

The basic ideas presented in the last section will now be applied to the calculation of heat transfer in a transpired boundary layer. The procedure is basically the same except that attention is now focused on the thermal boundary layer. Thus, the first integration of the energy equation across the entire thermal boundary layer leads to an energy balance integral (EBI) which is to be used as an expression for the wall heat flux. An auxiliary equation is generated from a moment integral of the energy equation for the determination of the profile parameter of the assumed temperature profile. In order to present a self-consistent development of the procedure, we shall also use the approximate solution for the velocity by the present method in the solution of the energy equation.

For easy demonstration of the procedure, we again consider the simple case of two-dimensional, incompressible, laminar boundary layers. Only the results for an asymptotic flow corresponding to large Prandtl number and small surface mass transfer will be presented in this paper. The analytical derivation of such asymptotic limits is representative of the unique advantage of analytical methods. The derivation enhances physical understanding of the flow field and brings out similarity parameters to facilitate parametric studies. Results for moderate Prandtl numbers can be found in Ref. (10), where a compressible case is also treated.

The energy equation for incompressible, laminar flows in the boundary-layer approximations has the form

$$u \frac{\partial \theta}{\partial x} + v \frac{\partial \theta}{\partial y} = \alpha \frac{\partial^2 \theta}{\partial y^2} \quad (17)$$

where  $\theta \equiv (T - T_\infty)/(T_w - T_\infty)$  is the normalized temperature and  $\alpha$  is the thermal diffusivity. Note that the frictional heating is, as usual, neglected, in incompressible flows.

Integrating Eq. (17) over the thermal boundary-layer thickness,  $\delta_T$ , we get an expression for the Stanton number

$$St \equiv \frac{Nx}{Re_x Pr} = \frac{d}{dx} \int_0^{\delta_T} u^* \theta dy - \epsilon \quad (18)$$

where  $u^* \equiv u/u_\infty$ ,  $\epsilon \equiv v_w/u_\infty$ . Also,  $Nx = q_w x/k(T_w - T_\infty)$  is the Nusselt number,  $Re_x = u_\infty x/\nu$  is the Reynolds number, and  $Pr = \nu/\alpha$  is the Prandtl number. ( $k$  is the thermal conductivity of the fluid.)

In the present section, the EBI, Eq. (18), is used in conjunction with the y-moment integral of Eq. (17). An approximate temperature profile of the form

$$\theta = g(\eta_T), \quad \eta_T \equiv y/\delta_T \quad (19)$$

is chosen in which  $\delta_T$  is the basic profile parameter.

As an example of application of this method, let us consider the limit of large Prandtl number. In this limit,  $\delta_T$  becomes vanishingly small relative to  $\delta$ . Thus, heat transfer takes place in a very narrow region near the porous wall where the velocity distribution can be approximated by a linear form, i.e.,

$$u^* = \frac{1}{2} C_f \text{Ret } \eta_T \quad (20)$$

where  $\text{Ret} \equiv u_\infty \delta_T / \nu$ .

Substitution of Eqs. (19) and (20) into the y-moment integral of the energy equation leads to

$$\tilde{\alpha} \text{Ret} \frac{d}{d\text{Rex}} \left( \frac{1}{2} C_f \text{Ret}^2 \right) = \frac{1}{\text{Pr}} + \tilde{\beta} \epsilon \text{Ret} \quad (21)$$

The constants  $\tilde{\alpha}$  and  $\tilde{\beta}$  are profile-parameters defined as

$$\begin{aligned} \tilde{\alpha} = & \int_0^1 \eta_T g(\eta_T) d\eta_T + \frac{1}{2} \int_0^1 \eta_T^2 g(\eta_T) d\eta_T \\ & - \int_0^1 d\eta_T \int_0^{\eta_T} \eta_T g(\eta_T) d\eta_T \end{aligned}$$

and

$$\tilde{\beta} = \int_0^1 g(\eta_T) d\eta_T.$$

In Eq. (21), the three terms from left to right represent, respectively, the effect of convection, conduction and mass transfer. As  $\text{Pr} \rightarrow \infty$ , an interesting limit exists in which these three mechanisms of heat transfer still remain in balance. Such a distinguished limit can easily be deduced from Eq. (21) by requiring

$$\text{Ret}^3 \text{Rex}^{-3/2} \sim \text{Pr}^{-1} \sim \epsilon \text{Ret}, \quad (22)$$

from which it follows that

$$\epsilon \text{Rex}^{1/2} = O(\text{Pr}^{-2/3}) \rightarrow 0 \quad (23a)$$

and

$$\epsilon \text{Ret} = 0(\text{Pr}^{-1}) \rightarrow 0 \quad (23b)$$

Therefore, the transpiration rate,  $\epsilon \text{Rex}^{1/2}$ , must be small compared to that in the usual boundary-layer flows. Physically, this limit corresponds to the heat transfer in a nearly stagnant layer of fluid close to the solid surface with a small porosity.

In view of Eqs. (23), the following variables are appropriate for the study of this limiting flow:

$$\Lambda = \text{Pr}^{2/3} \epsilon \text{Rex}^{1/2} = 0(1) \quad (24a)$$

and

$$\Lambda_1 = \text{Pr} \epsilon \text{Ret} = 0(1) \quad (24b)$$

Thus,  $\text{Pr}^{2/3}$  and  $\epsilon \text{Rex}^{1/2}$  combine to form a single parameter,  $\Lambda$ , which characterizes the asymptotic heat transfer.

We shall specialize our discussion here to the case of a porous plate with similarity blowing (or suction). First of all,  $C_f$  takes on its value for a nonporous plate as the leading approximation. For the sake of self-consistency, we use the value based on the present solution discussed in section 1, i.e.,

$$\frac{1}{2} C_f = \frac{1}{3} \text{Rex}^{1/2}, \quad (25)$$

corresponding to a linear velocity profile.

For the case of similarity flow,  $\epsilon \text{Ret}$  is constant, and Eq. (21) can be easily integrated. The solution is expressed in the parametric (closed) form:

$$\Lambda_1^3 = 6\Lambda^3(1 + \tilde{\beta}\Lambda_1)/\tilde{\alpha} \quad (26a)$$

and

$$N_x/(\text{Rex}^{1/2} \text{Pr}^{1/3}) = 6^{-1/3} \tilde{\gamma} \tilde{\alpha}^{-2/3} (1 + \tilde{\beta}\Lambda_1) - \Lambda \quad (26b)$$

where  $\tilde{\gamma} = \int_0^1 \eta_T g(\eta_T) d\eta_T$  is another profile-parameter.



Two temperature profiles are used in the present calculation, i.e.,

$$\theta = g_1(\eta_T) = 1 - \eta_T \quad (27a)$$

and

$$\theta = g_4(\eta_T) = 1 - 2\eta_T + 2\eta_T^3 - \eta_T^4 \quad (27b)$$

which are again crude and oversimplified.  $(\tilde{\alpha}, \tilde{\beta}, \tilde{\gamma})$  for  $g_1$  and  $g_4$  are  $(1/8, 1/2, 1/6)$  and  $(1/28, 3/10, 1/15)$ , respectively.

The present solutions corresponding to  $g_1$  and  $g_4$  are plotted in Figure 3. Exact solutions to a class of self-similar flows in the same asymptotic limit have recently been obtained independently by Gersten(11), using a different approach. Figure 3 also includes the exact solution for comparison. Good accuracy and weak profile-dependence of the present solutions are again in evidence over a wide range of  $\Lambda$ . The present solutions can also be shown to reduce to the exact limit for large suction. Appreciable deviations from the exact solution occur only near thermal layer blow-off where the heat-transfer rate is very small. This is reminiscent of the difficulty encountered in the skin-friction calculations near the blow-off point(2).

Solutions to a nonsimilar flow in the same limit as well as solutions for small Prandtl number flows appear in Ref. (3).

#### 4. Three-Dimensional Boundary Layers

Despite the recent advances in computer technology and the related field of numerical methods for solving partial differential equations, the problem of three-dimensional flows, boundary-layer flows in particular, continues to be one of the most challenging problems to fluid dynamicists and engineers. Exact solutions are generally very difficult and costly, if not impossible.

In this section, the application of the basic ideas of the present integral method to the approximate calculation of three-dimensional boundary-layer flows is

illustrated. A relatively simple flow is studied as a first step in the approximate treatment of general flows. The work in this area is in its beginning stage, and more results are expected in the future.

Consider the incompressible, laminar boundary layer on a semi-infinite flat plate with an infinite span. Suppose that the inviscid velocity on the plate has the components  $u_0$  and  $bx$  in  $x$  and  $z$  directions, respectively ( $z$  being the spanwise direction), where  $u_0$  and  $b$  are constants. It is easily shown that the inviscid surface streamlines are parabolas,

$$z = z_0 + \frac{1}{2} \frac{b}{u_0} x^2 \quad (28)$$

with a constant spanwise pressure gradient given by

$$-\frac{1}{\rho} \frac{dp}{dz} = u_0 b. \quad (29)$$

This problem was first solved by Loos<sup>(12)</sup> who obtained the exact solution in similarity form.

The boundary-layer equations in the rectangular cartesian coordinate system  $(x, y, z)$  are

$$\frac{\partial u}{\partial x} + \frac{\partial v}{\partial y} = 0 \quad (30a)$$

$$u \frac{\partial u}{\partial x} + v \frac{\partial u}{\partial y} = \nu \frac{\partial^2 u}{\partial y^2} \quad (30b)$$

$$u \frac{\partial w}{\partial x} + v \frac{\partial w}{\partial y} = bu_0 + \nu \frac{\partial^2 w}{\partial y^2}. \quad (30c)$$

The boundary conditions are

$$y = 0: \quad u = v = w = 0 \quad (31a)$$

$$y \rightarrow \infty: \quad u \rightarrow u_0, \quad w \rightarrow bx \quad (31b)$$

$$x = 0: \quad u = u_0, \quad w = bx \quad (31c)$$

Note that the simplicity of the problem stems from the fact that the chordwise flow,  $u$ , is decoupled from the spanwise flow,  $w$ , and can be solved independently of

the latter. In fact, the chordwise flow is the well-known Blasius flow which has been solved approximately by the present method in section 1 as a special case ( $\epsilon \equiv 0$ ) of a more general flow. This approximate solution will be used in the solution of the spanwise flow,  $w$ .

The present procedure of solving the spanwise flow is as follows. First, the spanwise momentum equation, Eq. (30c), is integrated across the spanwise boundary-layer thickness,  $\delta_z$ , resulting in the spanwise momentum balance integral,

$$\frac{\tau_{wz}}{\rho} = \left(\frac{dw_1}{dx}\right) \int_0^{\delta_z} (u_o - u) dy + \frac{d}{dx} \int_0^{\delta_z} u (w_1 - w) dy \quad (32)$$

where  $\tau_{wz}$  is the spanwise skin friction.

Eq. (32) is to be used in conjunction with either the  $y$ -moment integral of Eq. (30c),

$$\begin{aligned} \int_0^{\delta_z} \frac{\partial}{\partial x} y u w dy + \int_0^{\delta_z} y \frac{\partial}{\partial y} u w dy &= \frac{1}{2} b u_o \delta_z^2 \\ &+ \nu \int_0^{\delta_z} y \frac{\partial^2}{\partial y^2} w dy \end{aligned} \quad (33a)$$

or the  $w$ -moment integral of Eq. (30c),

$$\begin{aligned} \int_0^{\delta_z} w \frac{\partial}{\partial x} u w dy + \int_0^{\delta_z} w \frac{\partial}{\partial y} u w dy &= b u_o \int_0^{\delta_z} w dy \\ &+ \nu \int_0^{\delta_z} w \frac{\partial^2}{\partial y^2} w dy \end{aligned} \quad (33b)$$

The use of Eq. (33a) corresponds to the  $y$ -moment scheme whereas the use of Eq. (33b) is referred to as the  $w$ -moment scheme.

The y-moment scheme will be used first. We assume the following simple profiles for  $u$  and  $w$ :

$$u/u_o = \eta_x ; \quad \eta_x \equiv y/\delta_x \quad (34a)$$

$$w/bx = \eta_z ; \quad \eta_z \equiv y/\delta_z \quad (34b)$$

where  $\delta_x$  is the chordwise boundary-layer thickness.

The chordwise-flow solution by the present method can be found in Ref. (1) as

$$\frac{\delta_x}{x} = \frac{4}{\sqrt{Re_x}} \quad (35a)$$

and

$$\frac{1}{3} C_{fx} \sqrt{Re_x} = \frac{1}{3} \quad (35b)$$

where  $\frac{1}{2} C_{fx} \equiv \tau_{wx}/\rho u_o^2$ .

Substituting Eqs. (34a) and (34b) into Eq. (33a) and assuming that

$$\Delta \equiv \delta_z/\delta_x < 1 \quad (36)$$

we obtain an ordinary differential equation:

$$\begin{aligned} \frac{1}{4} \frac{d}{dx} (\delta_z^2 \Delta x) - \frac{3}{8} \delta_z x \frac{d}{dx} (\Delta \delta_z) - \frac{1}{4} x \delta_z \Delta \frac{d\delta_z}{dx} \\ = \frac{1}{2} \delta_z^2 - \frac{vx}{u_o} \end{aligned} \quad (37)$$

Eq. (37) admits the simple solution of  $\Delta = \text{const}$ , with  $\Delta$  determined from the algebraic equation

$$3\Delta^3 - 8\Delta^2 + 1 = 0 \quad (38)$$

The only self-consistent solution of  $\Delta$  is

$$\Delta = 0.382 \quad (39)$$

and the corresponding solution for the spanwise skin friction is

$$\frac{1}{2} C_{fz} \sqrt{Rex} \equiv \frac{\tau_{wz}}{\rho u_o w_1} \sqrt{Rex} = 1.382 , \quad (40)$$

compared to the exact solution (12) of  $\frac{1}{2} C_{fz} \sqrt{Rex} = 1.414$ .

The problem is next solved using the w-moment scheme, and results are summarized in Table 1 where the corresponding solutions using the classical K-P method are also included.

Table 1. Spanwise Skin-Friction Results

| W PROFILE<br>( $u = u_o y/\delta_x$ )                              | PRESENT                |        | CLASSICAL K-P          |        |
|--|------------------------|--------|------------------------|--------|
|  | $1/2 C_{fz} R_x^{1/2}$ | ERROR  | $1/2 C_{fz} R_x^{1/2}$ | ERROR  |
| $\frac{w}{w_1} = y/\delta_z$                                       | 1.382                  | -2.3%  | 0.962                  | -32.0% |
| $\frac{w}{w_1} = 2(y/\delta_z) - 2(y/\delta_z)^3 + (y/\delta_z)^4$ | 1.374                  | -2.82% | 1.280                  | -9.5%  |

These results are certainly encouraging. The present solutions are clearly very accurate, and only weakly dependent on profiles.

##### 5. One-Dimensional Transient Heat Conduction

Conduction heat transfer plays an indispensable role in the reentry heating where the predominant

phenomena are melting, ablation, etc. These problems are inherently nonlinear, and their coupling with other heat transfer mechanisms existing in the attendant flow field necessarily makes the analysis of the overall heating phenomena extremely difficult. In view of the complexity of such aerodynamic heating problems, simple, analytical methods of approximate solution are highly desirable for engineering purposes.

The basic ideas of the present integral method have naturally found their applications in this area, since heat conduction bears a close similarity to boundary-layer flows in its mathematical description. In this section, a class of transient ablation problems is solved by the present method as an example of the application. Many details of the solution are omitted from this paper to conserve space, but appear in Refs. (5,6) where more examples can be found.

### 5.1 The Ablation Model

The model used here is a semi-infinite solid initially in a uniform temperature,  $T_{\infty}$ , lower than the phase-change temperature of the solid,  $T_p$ . An unsteady heat flux,  $q_0(t)$ , is then applied at the boundary until the boundary temperature reaches the phase-change temperature of the solid. This period is referred to as the preablation period. As the external heating continues, melting commences with the melting front progressing into the solid, and this period is referred to as the ablation period. In the idealized model, it is assumed that the molten solid is instantaneously and completely removed upon its formation say, by the action of some aerodynamic forces, so that the melting line acts like a new (moving) boundary upon which the external heat flux,  $q_0(t)$ , acts. This assumption is particularly appropriate for the ablation of subliming materials such as camphor, graphite, etc. Also, to simplify the calculations, the thermophysical properties of the solid are assumed constant. This model is the same as the one used earlier by Landau<sup>(13)</sup>, except that he considered only the special case of a constant  $q_0$ , and obtained solutions by entirely numerical means. The model is sketched in Fig. 4.

In terms of this idealized model, the governing equations and boundary conditions are as follows:

(1) Preablation period.

$$\frac{\partial T}{\partial t} = \alpha \frac{\partial^2 T}{\partial x^2}, \quad t_p > t > 0, \quad \infty > x > 0 \quad (41)$$

$$T(x, 0) = T(\infty, t) = T_\infty \quad (42a)$$

$$-k \left( \frac{\partial T}{\partial x} \right)_{x=0} = q_0(t) \quad (42b)$$

where  $\alpha$  and  $k$  are, respectively, the (constant) thermal diffusivity and heat conductivity of the solid. Also,  $t_p$  signifies the time at which the boundary temperature reaches  $T_p$ , i.e.,  $T(0, t_p) = T_p$ . Note that the preablation period can be treated as a linear problem.

(2) Ablation period.

$$\frac{\partial T}{\partial t} = \alpha \frac{\partial^2 T}{\partial x^2}, \quad \infty > t > t_p, \quad \infty > x > X(t) \quad (43)$$

$$T(x, t_p^+) = T(x, t_p^-) \quad (44a)$$

$$T(X, t) = T_p \quad (44b)$$

$$T(\infty, t) = T_\infty \quad (44c)$$

$$-k \left( \frac{\partial T}{\partial x} \right)_{x=X} + \rho Q_L \frac{dX}{dt} = q_0(t) \quad (44d)$$

Eq. (44a) ensures the continuity of the temperature distribution within the solid at the onset of ablation,  $t = t_p$ , and Eq. (44d) states the energy balance across the ablating front,  $x = X(t)$ . Note that the boundary condition, Eq. (44d), which relates the ablation speed,  $dX/dt$ , to the temperature gradient,  $(\partial T/\partial x)_{x=X}$ , is the basic source of the nonlinearity of the problem.

In the following, the special case of  $q_0 = At^m$  (where A and m are constants) will be studied, using the  $\theta$ -moment scheme<sup>(4,5)</sup> of the present integral method.

## 5.2 Preablation Solution

For the preablation period, an exponential profile for the temperature excess,  $\theta = T - T_\infty$ , is used in the calculation, i.e.,

$$f = \frac{q_0 \delta}{k} \beta \exp\left(-\frac{x}{\delta}\right). \quad (45)$$

The profile contains two parameters,  $\delta$  and  $\beta$ , and satisfies only the boundary of  $\theta_\infty = 0$ . Recall that the boundary flux is not to be obtained from  $(\partial f / \partial x)_0$  in the present method<sup>(4,5)</sup>.

Integrating Eq. (41) over the entire region of interest yields the heat-balance integral (HBI),

$$-\alpha \left(\frac{\partial \theta}{\partial x}\right)_0 = \int_0^\infty \frac{\partial \theta}{\partial t} dx \quad (46)$$

where the condition of  $\left(\frac{\partial \theta}{\partial x}\right)_\infty = 0$  is assumed. Eq. (46) can be rewritten as

$$\frac{\alpha}{k} q_0 = \int_0^\infty \frac{\partial \theta}{\partial t} dx \quad (47)$$

Eq. (47) expresses the conservation of heat in the entire solid. In the usual HBI method<sup>(14)</sup>, Eq. (47) is the sole equation for the problem once an approximate temperature profile is substituted into the equation. However, in the present approach, it is to be used with the  $\theta$ -moment integral of Eq. (41) for determining the two profile parameters. Thus, we have as the second equation,

$$\int_0^\infty \frac{\partial \theta^2}{\partial t} dx = 2k\theta_0 q_0 - 2\alpha \int_0^\infty \left(\frac{\partial \theta}{\partial x}\right)^2 dx. \quad (48)$$



Upon substitution of  $\theta$  by  $f$  (Eq. (45)) in Eqs. (47) and (48), the following two equations are deduced:

$$\frac{d}{dt} (q_0 \delta^2 \beta) = \alpha q_0 \quad (49)$$

and

$$\frac{1}{2} \frac{d}{dt} (\beta^2 q_0^2 \delta^3) = 2\alpha q_0^2 \beta \delta - \beta^2 \alpha q_0^2 \delta \quad (50)$$

Solutions of Eqs. (49) and (50) are easily obtained as

$$\delta/\sqrt{\alpha t} = 2/\sqrt{4m+5} \quad (51a)$$

$$\beta = (m+5/4)/(m+1) \quad (51b)$$

The boundary temperature,  $T_0$ , in dimensionless form is found from Eq. (45):

$$\theta_0 \equiv \frac{k(T_0 - T_\infty)}{q_0 \sqrt{\alpha t}} = \sqrt{m+5/4} / (m+1) \quad (52)$$

As is shown in Ref. (4), the boundary temperature as given by Eq. (52) agrees better than 1% with the exact solution for all  $m$  in the range  $0 \leq m < \infty$ .

Ablation starts when  $T_0 = T_p$ . From Eq. (52), the corresponding time,  $t_p$ , is determined as

$$t_p = \left[ \frac{k(m+1)(T_p - T_\infty)}{A\sqrt{(m+5/4)\alpha}} \right]^{\frac{1}{m+1/2}} \quad (53a)$$

The "penetration depth",  $\delta$ , at  $t_p$  follows from Eq. (51a),

$$\delta_p = \left[ \frac{k(m+1)(T_p - T_\infty)\alpha^m}{A\sqrt{m+5/4}} \right]^{\frac{1}{2m+1}} / \sqrt{m+5/4}. \quad (53b)$$

The quantities  $t_p$  and  $\delta_p$  are conveniently used as the scales for time and length, respectively, in the formulation of the ablation problem. However, since  $t_p$  and  $\delta_p$  given above are only approximate solutions dependent on the method of solution, it is desirable to use the characteristic time and length of the problem,  $t_c$  and  $\ell_c$ , as the scales for easy determination of the absolute accuracy of the solution. From a simple dimensional consideration, it is easily found that  $t_c$  and  $\ell_c$  of the problem can be defined by

$$t_c = [k(\Delta T)/A\sqrt{\alpha}]^{1/(m+1/2)} \quad (54a)$$

and

$$\ell_c = \sqrt{\alpha t_c} = [k(\Delta T)\alpha^m/A]^{1/(2m+1)} \quad (54b)$$

where  $\Delta T \equiv T_p - T_\infty$ .

Thus, we introduce the following two sets of dimensionless variables in the ensuing calculations:

$$\xi \equiv \frac{x}{\delta_p}, \quad \tau \equiv \frac{t}{t_p}, \quad \Delta \equiv \frac{\delta}{\delta_p}, \quad \lambda \equiv \frac{x}{\delta_p} \quad (55a)$$

and

$$\xi_1 \equiv \frac{x}{\ell_c}, \quad \tau_1 \equiv \frac{t}{t_c}, \quad \Delta_1 \equiv \frac{\delta}{\ell_c}, \quad \lambda_1 \equiv \frac{x}{\ell_c} \quad (55b)$$

Note, in particular, that at the onset of ablation,  $\tau_p = 1$  and

$$(\tau_{1p})_Z = [(m+1)^2/(m+5/4)]^{1/(2m+1)} \quad (56)$$

The accuracy of the present preablation solution may also be determined on the basis of a comparison of  $\tau_{1p}$  as given by Eq. (56) with that given by the exact solution. The exact  $\tau_{1p}$  can be found in Carslaw and Jaeger(15) as

$$(\tau_{1p})_E = [\Gamma(m + \frac{3}{2})/\Gamma(m+1)]^{1/(m + \frac{1}{2})} \quad (57)$$

where  $\Gamma$  is the Gamma function. It can be easily shown that  $\tau_{1p}$  of the present solution approaches the exact limit of  $\tau_{1p} = 1$  as  $m \rightarrow \infty$ .

The comparison between the approximate solution and the exact solution for  $\tau_{1p}$  is shown in Fig. 5. The present solution is practically indistinguishable from the exact solution in the entire range of  $m$ ,  $\infty > m > 0$ , the maximum error being about 1.8% at  $m = 0$ . It is interesting to note the existence of a maximum  $\tau_{1p}$  near  $m = 1.5$ . Also included in Fig. 5 is the HBI solution of the preablation time to indicate the degree of improvement achieved.

### 5.3 Ablation Solution

The ablation problem is then formulated in dimensionless form by using dimensionless variables  $\xi, \tau, \Delta, \lambda$  and  $\theta$ , where  $\theta = (T - T_\infty)/(T_p - T_\infty)$  is the normalized temperature.

An exponential profile for  $\theta$  is assumed,

$$f = \exp \left[ - \frac{x - X(t)}{\delta(t)} \right] \quad (58)$$

where  $X(t)$  is the (unknown) ablation line location, and  $X(t_p) = 0$ . Note that this choice of the temperature ensures the continuity of the temperature field at  $t = t_p$  if  $\delta(t)$  is assumed to be continuous at  $t_p$ .

With  $f$  substituting for  $\theta$ , the following equations are easily derived from the ablation line condition, Eq. (44d), the integration of Eq. (43) from  $\xi = \lambda$  to  $\xi = \infty$ , and the integration of the  $\theta$ -moment of Eq. (43), respectively

$$- (m + 5/4) \frac{\partial \theta}{\partial \xi} \Big|_{\lambda} = (m + 1) \tau^m - \nu \frac{d\lambda}{d\tau} \quad (59a)$$

$$\frac{d\Delta}{d\tau} + \frac{d\lambda}{d\tau} = - (m + 5/4) \frac{\partial \theta}{\partial \xi} \Big|_{\lambda} \quad (59b)$$

$$\frac{1}{2} \frac{d\Delta}{d\tau} + \frac{d\lambda}{d\tau} = - (m + 5/4) \left[ 2 \frac{\partial \theta}{\partial \xi} \Big|_{\lambda} + \frac{1}{\Delta} \right] \quad (59c)$$

where  $v = Q_L/C_p(T_p - T_\infty)$ .  $Q_L$  is the latent heat of ablation per unit mass and  $C_p$  is the specific heat of the solid.

In the present procedure, Eqs. (59) form the system for the three unknowns,  $\lambda, \Delta$  and the heat flux at the ablation front,  $-(\partial\theta/\partial\xi)\lambda$ .

Closed-form solution can be obtained for the special case of  $m=0$ , i.e., the case of a constant heat flux. For other values of  $m$ , solutions are obtained easily by numerically integrating an ordinary differential equation (see Ref. (6)).

Typical results for  $(m, v) = (0, \sqrt{\pi}/2)$  are shown in Fig. 6, compared with Landau's (13) numerical solution and the classical heat balance integral (HBI) solution based on similar temperature profiles. Note that the ablation thickness in Fig. 6 is normalized by its value at  $\tau = \infty$ , i.e.,

$$\lambda_n \equiv \lambda/\lambda_\infty$$

where

$$\lambda_\infty = \tau^{m+1}/(1+v).$$

It is clear that the present solution is very accurate and shows considerable improvements over the HBI solution.

Admittedly, the example treated here is highly idealized. Nevertheless, the essential features of the mathematical system of ablation problems are included in the model. The success of the method in this application is therefore indicative of its potential for providing approximate solutions to realistic conduction problems in general and ablation problems in particular.

## 6. Concluding Remarks

A simple integral method has been presented for approximate calculations of boundary-layer flows and heat transfer. Applications of the method have been illustrated in a variety of technological areas including

estimates of skin friction and convective heating rates on aerodynamic bodies and calculations of transient ablation pertaining to reentry vehicles. Calculation of the spanwise skin friction is also included as an example of application to three-dimensional boundary layers.

The accuracy of the method in these applications is determined by comparing the approximate solutions with existing exact (analytical or numerical) solutions. It is demonstrated that the method yields very accurate results with remarkable simplicity to problems whose exact solutions would require extensive numerical computations. The weak dependence of the approximate solution on the profile assumed in the calculation is also noteworthy.

Inasmuch as reliable exact solutions are available only for problems with idealized models and basic configurations, the applications discussed in this paper are, by necessity, also limited to idealized problems. However, since these models all possess the essential features of the more realistic models, it is believed that the potential of the method in realistic applications can be inferred.

The method is especially designed for accurate estimates of various surface properties in viscous flow and heat transfer problems, such as skin friction, surface heating rates, ablation front locations, etc. It is not intended to provide accurate details of the flow field or temperature field. The remarkable combination of simplicity and accuracy of the method as demonstrated in the paper is particularly attractive from economic considerations, and is indicative of the potential of the method for development into a practical tool for the aerodynamic design of advanced vehicles.

#### Acknowledgment

This research was supported by the Independent Research Program of the Naval Surface Weapons Center.

## References

1. Volkov, V. N., "A Refinement of the Karman-Pohlhausen Integral Method in Boundary-Layer Theory," Inzhenerno-Fizicheskii Zhurnal, Vol. 9, No. 5, 1965, pp. 583-588, (English translation in Journal of Engineering Physics, Vol. 9, No. 5)
2. Zien, T. F., "Skin Friction on Porous Surfaces Calculated by a Simple Integral Method," AIAA Journal, Vol. 10, No. 10, Oct 1972, pp. 1267-1268
3. Zien, T. F., "Approximate Analysis of Heat Transfer In Transpired Boundary Layer with Effects of Prandtl Number," International Journal of Heat and Mass Transfer, Vol. 19, No. 5, May 1976, pp. 513-521
4. Zien, T. F., "Approximate Calculation of Transient Heat Conduction," AIAA Journal, Vol. 14, No. 3, March 1976, pp. 404-406
5. Zien, T. F., "Study of Heat Conduction with Phase Transition Using an Integral Method," AIAA Progress in Astronautics and Aeronautics, Vol. 56: Thermophysics of Spacecraft and Outer Planet Entry Probes, (Edited by A. M. Smith), pp. 87-111, (Sept. 1977)
6. Zien, T. F., "Integral Solutions of Ablation Problems with Time-Dependent Heat Flux," AIAA Paper 78-864, presented at the 2nd AIAA/ASME Thermophysics and Heat Transfer Conference, Palo Alto, Calif., May 1978. Also to appear in AIAA Journal Vol. 16, No. 11 (Nov. 1978)
7. Catherall, D., Stewartson, K. and Williams, P. G., "Viscous Flow Past a Flat Plate with Uniform Injection," Proceedings of Royal Society, Series A, London, Vol. 284, 1965, pp. 370-396 (1965)
8. Terrill, R. M., "Laminar Boundary-Layer Flow Near Separation With and Without Suction," Philosophical Transactions of the Royal Society, London, Vol. A253, Sept. 1960, pp. 55-100

9. Inger, G. R., "Comment on 'Skin Friction on Porous Surfaces Calculated by a Simple Integral Method,'" AIAA Journal, Vol. 11, No. 9, Sep 1973, pp. 1356-1357
10. Zien, T. F., "An Approximate Calculation of Heat Transfer in Transpired Boundary Layers," NOLTR 73-17, Feb. 1973, Naval Ordnance Laboratory, White Oak, Silver Spring, Maryland
11. Gersten, K., "Wärme- und Stoffübertragung bei großen Prandtl-bzw. Schmidtzahlen," Wärme- und Stoffübertragung, Vol. 7, 1974, pp. 65-70
12. Loos, H. G., "A Simple Laminar Boundary Layer with Secondary Flow," Journal of the Aeronautical Sciences, Vol. 22, 1955, pp. 35-40
13. Landau, H. G., "Heat Conduction in a Melting Solid," Quarterly of Applied Mathematics, Vol. 8, 1950, pp. 81-94
14. Goodman, T. R., "Application of Integral Methods to Transient Nonlinear Heat Transfer," Advances in Heat Transfer, Vol. 1, 1964, pp. 51-122
15. Carslaw, H. S. and Jaeger, J. C., Conduction of Heat in Solids, 2nd ed., Oxford University Press, London, 1959, Chap. 2.

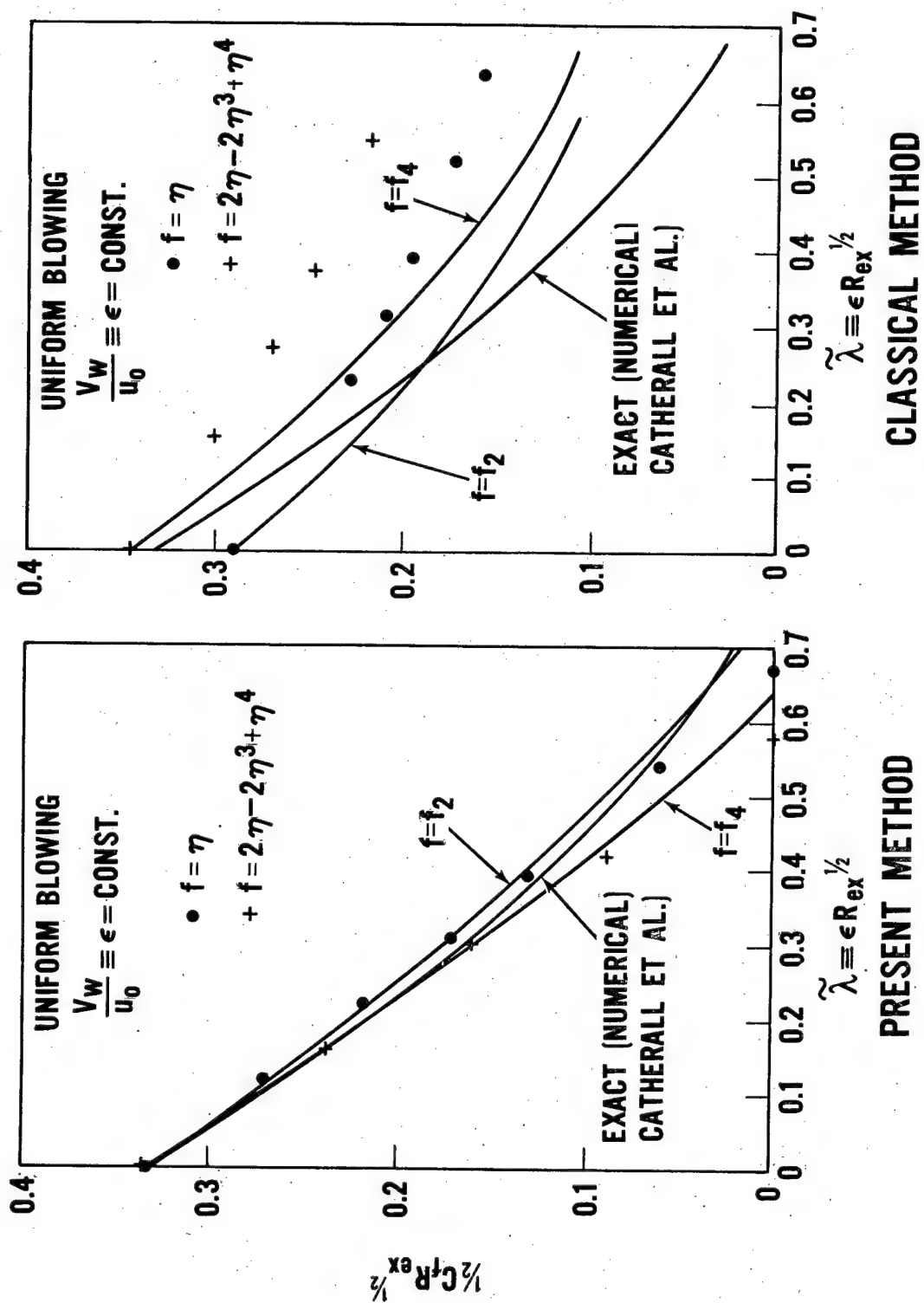


FIG. 1 SKIN FRICTION ON A POROUS PLATE WITH UNIFORM BLOWING  
 [UNCLASSIFIED]



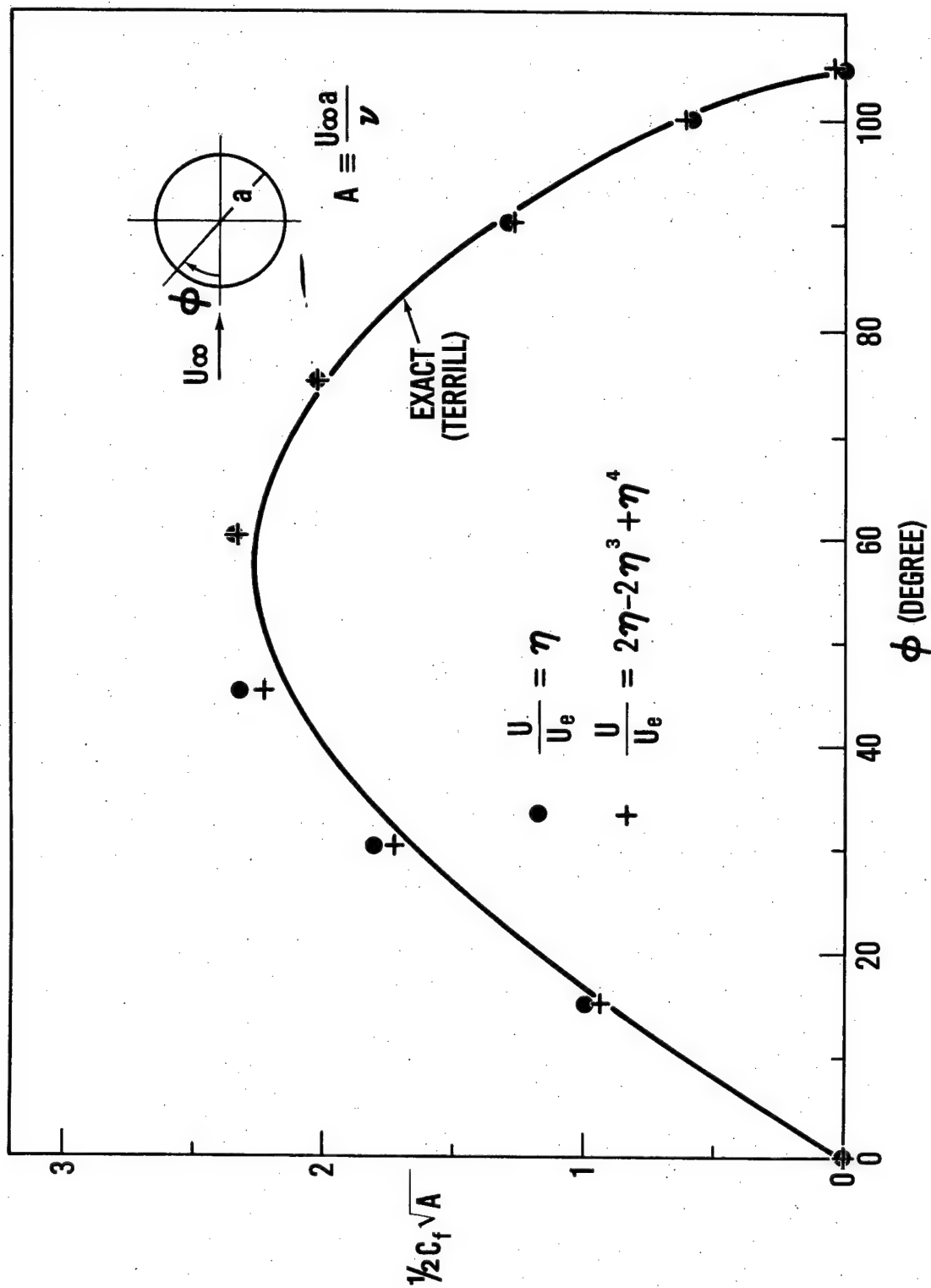


FIG. 2 SKIN FRICTION ON AN IMPERMEABLE CIRCULAR CYLINDER  
(UNCLASSIFIED)

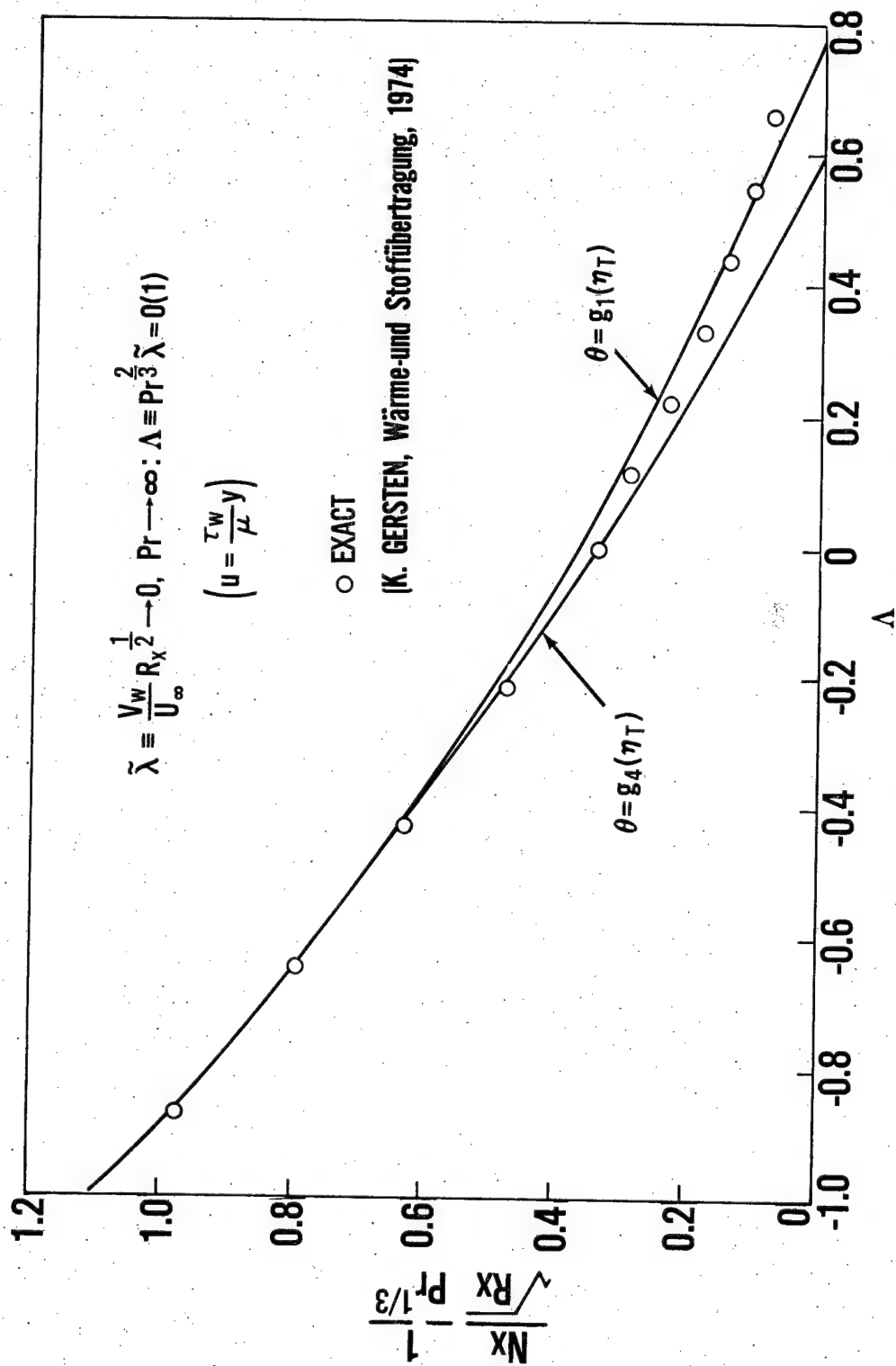
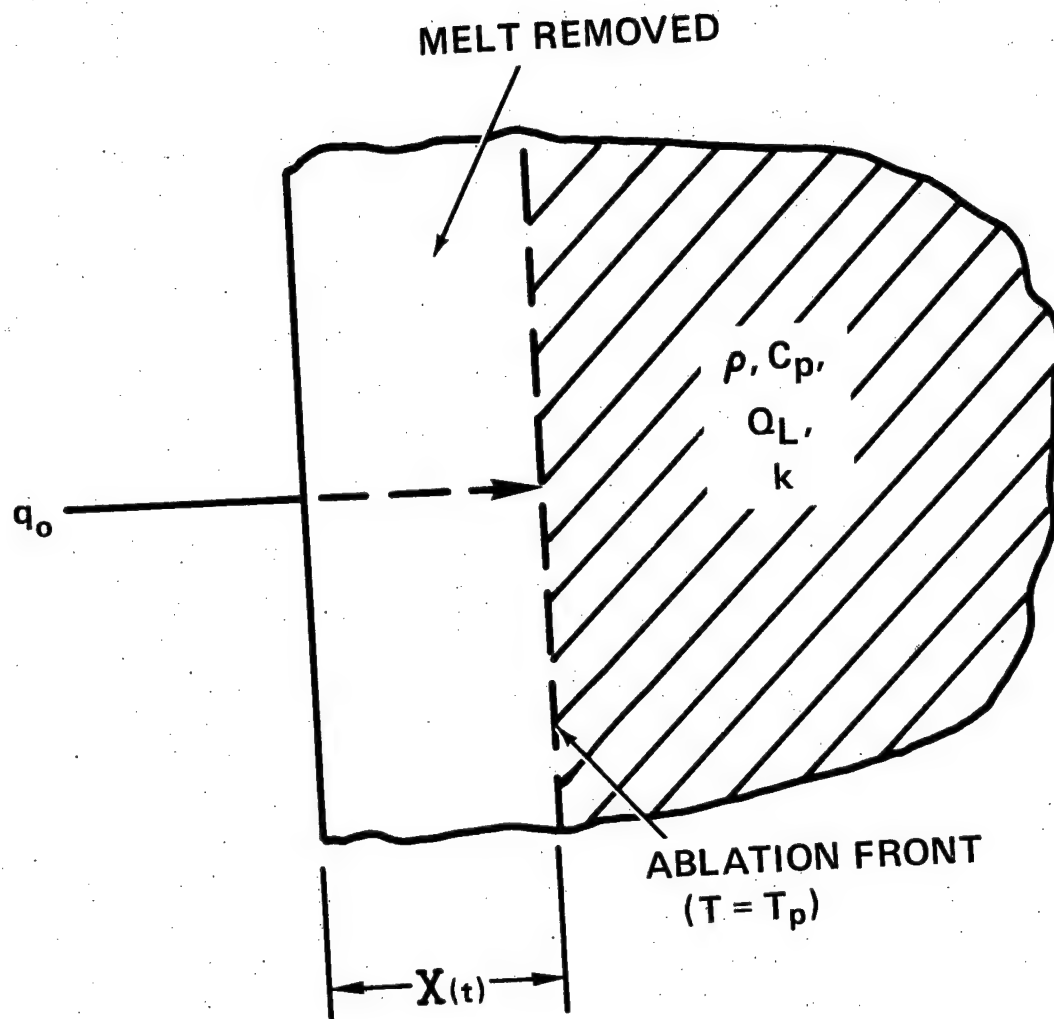


FIG. 3 ASYMPTOTIC HEAT TRANSFER ON A POROUS PLATE  
(UNCLASSIFIED)



$$x = X(t): q_o(t) = -k \frac{\partial T}{\partial x} + \rho Q_L \frac{dX}{dt}$$

**FIG. 4 ABLATION MODEL  
(UNCLASSIFIED)**

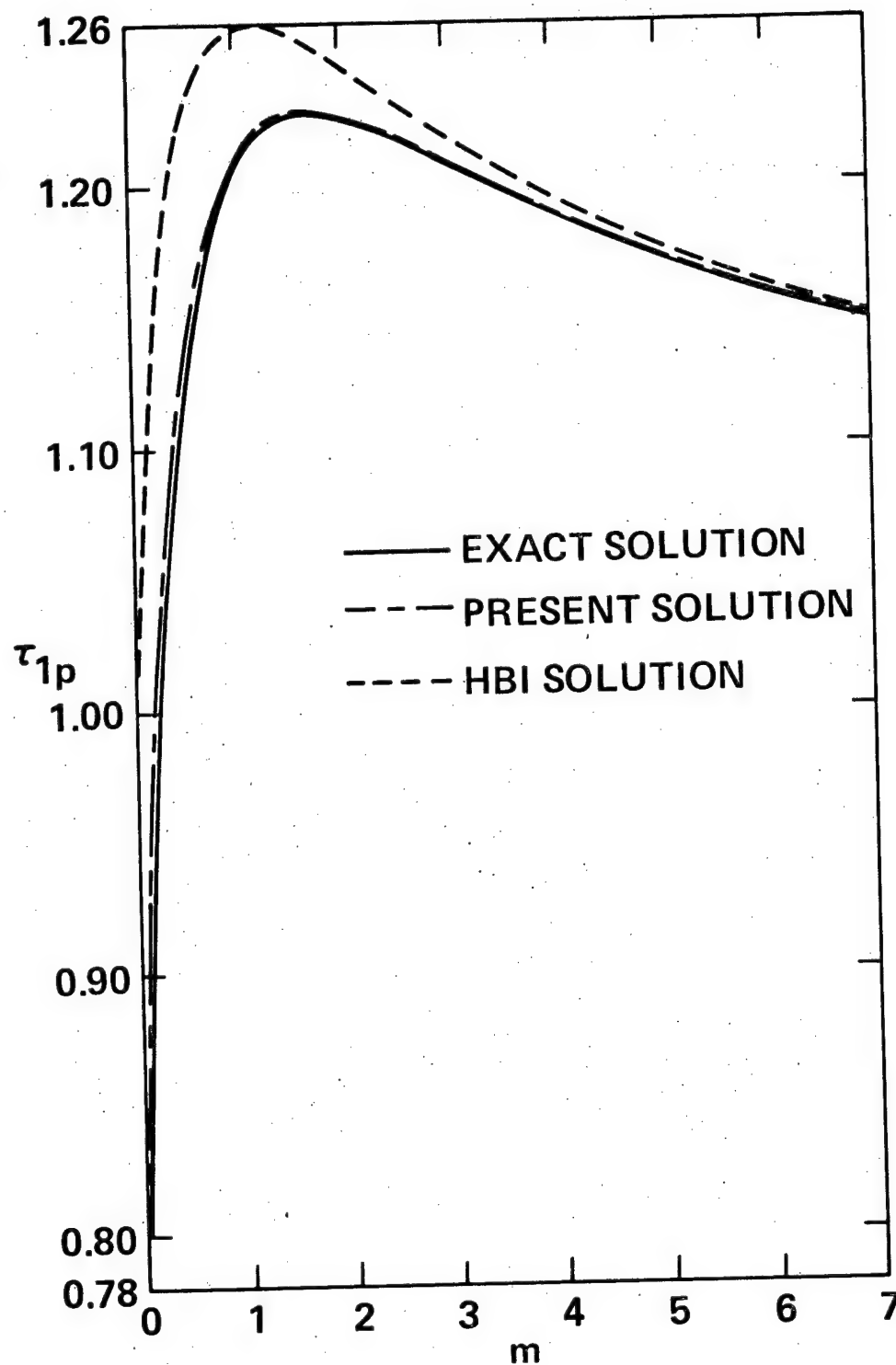


FIG. 5 PREABLATION TIME FOR  $q_0 = At^m$   
(UNCLASSIFIED)

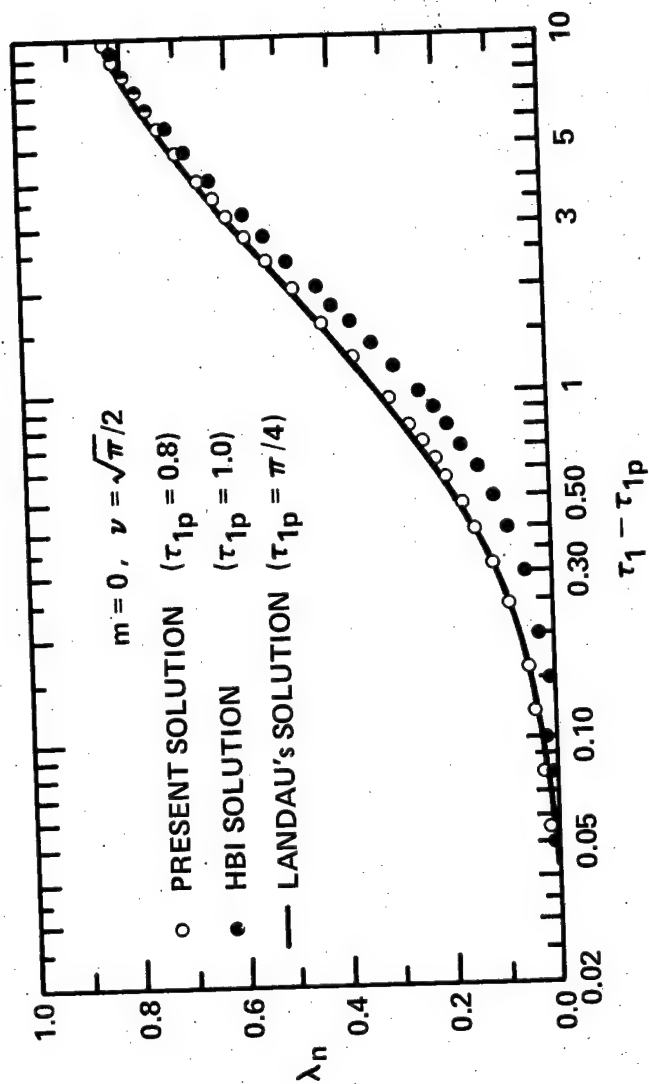


FIG. 6 ABLATION THICKNESS :  $q_0 = \text{CONST.}$   
 (UNCLASSIFIED)

### Biographical Sketch

Dr. Tse-Fou Zien received his B.S. degree in Mechanical Engineering from the National Taiwan University in 1958, M.S. degree in Engineering from Brown University in 1963 and Ph.D. degree in Aeronautics from the California Institute of Technology in 1967.

He joined the faculty of Case Western Reserve University in October 1967 where he was engaged in research in bio-medical fluid mechanics and unsteady viscous hypersonic flows. He also taught a graduate course in hypersonic flows. Since February 1970, Dr. Zien has been employed by the Naval Surface Weapons Center (NSWC) where he is presently a Research Aerospace Engineer in the Applied Mathematics Branch of the Research and Technology Department. At NSWC Dr. Zien has been working on problems of viscous flows and heat transfer, and has published numerous journal articles in this area. He also teaches basic fluid mechanics courses at the George Washington University holding a part-time faculty position.

Dr. Zien recently received, among many other honors and recognitions, the prestigious (1977) Annual Award for Scientific Achievement in Engineering Sciences from the Washington Academy of Sciences for his significant contributions to fluid mechanics and heat transfer. Dr. Zien has also been very active in various Navy committees on aeroballistic research, and has served as referee for professional journals in his field of specialty. Organizations in which he holds membership are American Institute of Aeronautics and Astronautics (Associate Fellow); American Physical Society, Washington Academy of Sciences (Fellow), and Society of Sigma Xi.

ASSESSING THE IMPACT OF AIR FORCE OPERATIONS ON THE  
STRATOSPHERE COMPOSITION

BY

Charles C. Gallagher

Robert V. Pieri, Captain, USAF

Aeronomy Division

Air Force Geophysics Laboratory  
Hanscom AFB, Massachusetts

## Assessing the Impact of Air Force Operations on the Stratosphere Composition

### Abstract

There is concern that the introduction of pollutants to the stratosphere may result in the reduction of the earth's protective layer of ozone. Contributions could come from Air Force aircraft and from diffusion upward of chlorofluoromethanes used by DOD. Determinations of stratospheric trace gas concentrations of NO, NO<sub>2</sub>, N<sub>2</sub>O, CFCl<sub>3</sub>, CF<sub>2</sub>Cl<sub>2</sub> and other compounds are made utilizing a balloon borne cryogenic, whole air sampler which obtains a one-mole sample at each of three altitudes per flight. Six altitudes (30, 25, 20, 18, 15 and 12 km) and five latitudes (9° to 64° N) are investigated. Sampling is controlled by a motor operated valve activated by ground command. Several precautions are taken to prevent contamination of the samples by the flight package. Subsequent analysis for NO and NO<sub>2</sub> content employs a chemiluminescent analyzer. The remaining gases of interest are analyzed using a gas chromatograph. Both dilution and permeation tube methods are used to calibrate both types of analytical devices. Results indicate daytime concentrations of NO and NO<sub>2</sub> generally in the 1 to 10 PPB range, and with N<sub>2</sub>O at 100 - 300 PPB, CFCl<sub>3</sub> and CF<sub>2</sub>Cl<sub>2</sub> at 10 to 100 PPT and with the latter three gases decreasing in concentration with increasing altitude and latitude. Present results are taken as baseline levels against which future changes, if any, can be compared. This assists the Air Force in the preparation of environmental impact statements where knowledge of present and projected future cumulative effects are required.



## Introduction

The stratosphere, that layer of the atmosphere extending from about 12 to 50 km in altitude, is receiving considerable attention of late because the introduction of pollutants to this region is predicted to result in the reduction of and possible eventual destruction of the earth's protective layer of ozone. The stratosphere is a stable region which means that introduction of even a small quantity of pollutants can be significant both because of the long residence times for such pollutants and because of the delicate chemical balance that presently exists there. Trace gas pollutants can enter the stratosphere in two ways: by injection as aircraft and spacecraft emissions and by diffusion from the atmospheric layer below, i.e. from the troposphere. Both of these sources are of concern to the Air Force, the former because of emissions from newer aircraft such as the F15 and F16 that operate in the stratosphere, the latter because of the wide use within DOD of chlorofluoromethanes, a series of compounds believed to be particularly damaging to the ozone layer. The chlorofluoromethanes (CFM's) are widely used within DOD (electronic and avionics cleaning compounds, aircraft surface cleaning compounds and spray lubricants) and slowly diffuse into the stratosphere at all latitudes and, in particular, upwell within tropical thunderstorms. The above considerations suggested that the initial trace gas compositions to be studied would be: nitric oxide (NO), nitrogen dioxide (NO<sub>2</sub>), nitrous oxide (N<sub>2</sub>O), CFM 11 (CFCl<sub>3</sub>) and CFM 12 (CF<sub>2</sub>Cl<sub>2</sub>). Since the composition of these gases varies with both altitude and latitude in the stratosphere, six altitudes (30, 25, 20, 18, 15 and 12 km) and five latitudes (90° N to 64° N) were chosen for investigation. The initial data gathering from all these locations would benefit the Air Force in the preparation of environmental impact statements and provide a baseline level against which future changes, if any, as stratospheric operations increased could be compared.

The approach utilized to determine stratospheric trace gas composition employs a balloon-borne cryogenic whole air sampler. This method provides a one mole sample from each altitude studied per flight, a sufficient quantity to permit extensive analyses in the laboratory subsequent to flight. The analytical equipment include a chemiluminescent analyzer and a gas chromatograph.

## 2. The Tri-Sampler

The initial cryogenic sampler obtained a single, one mole sample per flight, thus requiring six flights to investigate all altitudes of interest. The second generation device employs the same design principles but is larger and contains three sample chambers. Any additional chambers would unduly complicate the flight logistics. The tri-sampler obtains a one mole sample at each of three altitudes per flight. A cross section of the device is shown in Fig. 1. Only one of the three identical sample cylinders is illustrated. The dark shaded area represents the liquid helium well which maintains the inner wall of the sample cylinder at just above 4° K. To keep the liquid helium boiloff rate sufficiently low so as to permit the required multi-hour flight times, a liquid nitrogen chamber (lightly shaded area) and a vacuum jacket (unshaded area) serve to insulate the liquid helium. The sampling valve for each chamber is motor operated and is remotely activated by ground command. Air passes from the valve to the sample cylinder via a long small bore tube, the diameter of which is chosen for sampling at a specific altitude. The criteria is that a one mole sample be obtained in one hour. In that way, air molecules tend to freeze on first contact, thereby eliminating a pressure buildup in the chamber which in addition to increasing the chances for chemical reactions which could destroy the integrity of the sample, also would accelerate the liquid helium boiloff rate. A separate valve on each inlet is required for sample chamber pumpout. Although the sample is intended to remain frozen until transformed for analysis, the tri-sampler is designed to accommodate the warmed up sample without damage; however, as a precaution against the unlikely situation of having an oversize sample which then warmed in the tri-sampler, a safety blow-off disc is mounted on each inlet. Overall tri-sampler height is 50 inches and diameter is 18 inches. Under no-load conditions, the cryogen hold time is about one day.

Fig. 2 is a photo of the upper portion of a tri-sampler. The motor driven valves were standard valves modified so that air could flow continuously through the valve bodies. A removable manifold (not shown) permits air to be drawn through the valves by a downstream fan. The fan is turned on throughout the sampling period and helps to ensure that a continual supply of non-stagnant air is available for sampling. A second manifold interconnects the three sample cylinder pumpout valves and leads to an ion pump system. This manifold is removed prior to flight.

Fig. 3 is a full length photo of a tri-sampler. The pumpout manifold projects at the top right. The pumpout valve for the guard vacuum projects from the tri-sampler base. Overall tri-sampler weight, including cryogenics, is 380 lbs. During flight, the tri-sampler rests on a foam base, blown with nitrogen rather than the usual

chlorofluoromethane in order to eliminate a potential contaminant from the flight package.

### 3. The Flight Package

The tri-sampler is evacuated and then chilled with the cryogens in preparation for flight. It then becomes part of the flight package shown in Fig. 4. The tri-sampler and associated electronics are mounted in a six foot diameter gondola, of tubular aluminum frame construction and spherical in shape except for a flat bottom. When outfitted for flight, the gondola has a low center of gravity. Thus, since most flights involve ground recovery, the gondola will roll to an upright position, thereby eliminating excessive cryogen losses. A 20 ft. length of stainless steel bellows tubing is suspended from the air intake system to minimize the chances of sampling air contaminated by outgassing from flight package components. A 200 ft. load line increases the separation between gondola and balloon and is an added precaution against polydust from the balloon surface ever reaching the air intake tube. Control of sampling valve and fan operation are by ground command. Confirmation of these commands and the monitoring of various flight package parameters are transmitted to the ground control station. The remainder of the flight package includes standard items such as balloon valving and ballast pour capability. These items and the balloon launch facilities and launch personnel are ably supplied by the Aerospace Instrumentation Division of the Air Force Geophysics Laboratory. The balloon illustrated is typical of those used for our lower altitude flights. A 2,600,000 cu. ft. balloon is generally used for our 30 km flights. Suspended payload weight varies, primarily because of the amount of glass bead ballast carried on a specific flight. A typical gross payload weight is about 800 lbs.

A second gondola exists which is similar to the first but lacks the roll capability and is thus more compact. Fig. 5 shows this gondola suspended from the launch arm just before a balloon release. This gondola is used for flights in areas such as Alaska and Panama where inhospitable surface conditions exist and thus necessitate air recovery of the package. The smaller gondola is required for entry into the C130 snatch aircraft. Other features in the photograph are similar to those used for launch of the ground recovery package. The electronics are all sealed into insulated boxes. A ballast bag is visible on the near side, and the antenna setup at the lower right corner unreels just after launch.

At the termination of every flight, the parachute separates from the balloon upon command and then the package descends for recovery. For ground recovery, a crew is stationed at the predicted impact site to rendezvous with the package. For air recovery, the C130 snatches the parachute at about 15,000 ft. elevation. Fig. 6, a photo by

Capt. Pieri, shows a mock-up package in train behind the C130. For this test the package was dumped from the plane on the cable and then reeled in by the large winch shown at the right. The intent of the test run was to be sure that a package of these strengths, dimensions and weight distribution would trail properly without undue oscillations. The excellent results carried over into snatches of the actual package.

#### 4. The Flight Profile

Between launch and recovery come many critical steps required to obtain 3 good samples at the specified altitudes. Fig. 7 shows a typical profile for a high altitude flight. For the low altitude flight the same sequence applies. Only the actual altitudes are different. Ascent is rapid, about one hour, to ceiling. The maximum altitude is chosen higher than the highest sampling altitude in order to adjust the descent rate. Sampling is accomplished only during descent in order to sample air that has not been exposed to the package. This is probably the most important of the steps taken to sample only uncontaminated air. The desired descent rate is 100 ft/min. In this way, a 1.8 km altitude increment is sampled in one hour. The increments are centered on the specified sampling altitudes, i.e. 30, 25 and 20 km. The descent rate is controlled by valving helium from the balloon. Occasionally, some ballasting is also required. The fan is turned on as soon as descent is initiated and remains on until the final sample has been obtained. No sampling is done during or within 5 minutes subsequent to any ballasting. Termination, i.e. balloon destruct, is initiated as soon after sampling as is possible, the decision being based on recovery area weather and terrain.

#### 5. Sample Handling

The ground recovery crew carry dewars of liquid nitrogen and liquid helium to recharge the cryogens at the impact site. The initial plans for the program were that the samples would remain frozen throughout commercial air transport back to the laboratory; however, after several arguments, etc. en route home following the first two flights, the Airline Pilot's Association indicated in writing that they would no longer carry the cryogenic samplers. As the shipments complied with federal regulations, the decision seems arbitrary and unwarranted. Therefore, except for the two most recent flights from South Dakota where the samples were subsequently trucked to AFGL while frozen, transfer and preliminary analysis have had to be accomplished at the field site. The samples are warmed and allowed to expand into spheres, approximately 22 liter in volume, so that the final pressure is approximately ground level atmospheric pressure. Theoretical studies at AFGL indicated that at these pressures, analysis of nitric oxide and nitrogen dioxide content would have to be performed within 24 hours of warmup to

be considered reliable. Analysis of the remaining species of current interest could be delayed until arrival at the laboratory. The interior surfaces of the spheres must be carefully prepared else absorption of some minor gas species would invalidate subsequent measurements. Currently, the interiors are either gold plated or chemically treated.

## 6. Analysis of Air Samples

A. The sphere containing the air sample is attached successively to two chemiluminescent analyzers to determine the NO and NO<sub>2</sub> content of the sample. A block diagram showing the operating principle of a chemiluminescent analyzer is shown in Fig. 8. Ozone (O<sub>3</sub>) is produced in a stream of compressed air by a generator. This is mixed in a evacuated reactor chamber with a stream of the stratospheric air. The reaction that occurs in the chamber is the same as one which occurs in the stratosphere, i.e. the NO content of the sample reacts with the O<sub>3</sub>. This is a chemiluminescent reaction since part of the energy released by the reaction is released as light. An optical filter allows a specific wavelength from this reaction to pass to a photomultiplier tube where an electric signal is produced which subsequently gets amplified and recorded. The instrument is calibrated so that the amplitude of the output signal is a measure of the NO concentration. NO<sub>x</sub> represents the sum of NO and NO<sub>2</sub>. After the NO content is determined, the stratospheric sample is rerouted through an NO<sub>x</sub> to NO converter, then to the reactor chamber. The new signal amplitude then indicates the NO<sub>x</sub> content and simple subtraction is used to determine the NO<sub>2</sub> content. Two chemiluminescent analyzers are used to confirm the confidence level in the results since the NO and NO<sub>2</sub> content of stratospheric air are only in the low parts per billion range. Instruments from two manufacturers are used and each has been modified in-house to optimize reliability in the very low concentration range.

B. Subsequent to the chemiluminescent analyzer measurements, each sphere is attached to a gas chromatograph where the sample is investigated for all remaining species of interest. A simplified block diagram of such an instrument is shown in Fig. 9. At the heart of the instrument is a so-called "column," actually a coiled section of ¼ inch stainless steel tubing containing one of many available packing materials. Choice of packing material is dictated by the types of gases to be studied. Typically, a packing consists of a hard, beady or granular material with a wax-like coating. To maintain column and detector cleanliness and to provide a medium for transporting the sample gas through the column and detector, a carrier gas, such as nitrogen or helium, is passed through the system on a continual basis. When desired, a small quantity of the stratospheric air is injected upstream of the column. Each gas component in the air has a characteristic transit time through the column, based in part, on column dimensions, temperature and packing material. Therefore, as an example, gas species A exits the column prior to gas species B. Several different detector

types are available, again, depending on what gas species are to be measured. The radioactive source detectors, known as electron capture detectors, are the most sensitive and are used for this experiment. The output signals are weak and require amplification before recording. The detectors are either insensitive to the carrier gas or, if sensitive, the output is constant and can be balanced out electronically. An actual chromatogram is shown at the lower left corner. This was processed by an integrator, a device which both records the signal and provides a printout of peak times and areas. Much of the final processing is still done by hand to provide greater accuracy, especially since some of the peaks represent species concentrations in the low parts per trillion range (i.e. 1 PPT is one part in  $10^{12}$ ). Since the peak height and area are measures of the trace gas concentrations, considerable effort is required to accurately calibrate the instruments for the very low concentrations of interest. Two general approaches are utilized. In the dilution method, a primary standard mixture of each species of interest, at the lowest concentration commercially available (generally one part per million) in a background gas identical to the carrier gas, is passed through a titration tube and then mixed with a much larger stream of the same background gas before injection into the chromatograph. Through successive use of tubes of different diameters, calibration curves are obtained which are applicable down to the low parts per trillion range. A second calibration method employs a tube containing the trace gas. The wall of the tube is permeable, and the rate of flow through the wall is temperature dependent. The emitted gas is mixed with a stream of the carrier gas species for injection into the chromatograph. Calibration curves are obtained by operating at a series of tube temperatures. Both calibration methods are equally applicable to the chemiluminescent analyzers and the gas chromatographs.

## 7. Results

Sixteen flights have been conducted to date and samples have been obtained on all flights. Four flights have been conducted in Alaska ( $64^{\circ}$  N), two in South Dakota ( $45^{\circ}$  N), four in California ( $40^{\circ}$  N), five in New Mexico ( $33^{\circ}$  N) and one in Panama ( $9^{\circ}$  N). All flights have employed cryogenic sampling except the first two in Alaska and the one in Panama. On these three flights, grab sampling (i.e. opening an evacuated sphere at altitude) was employed as a complimentary method. This provides considerably smaller sample quantities, but e.g. was required in Panama where air space restrictions severely limited flight times.

The chemiluminescent analyzers have indicated concentrations of nitric oxide and nitrogen dioxide generally in the 1 to 10 parts per billion (PPB) range, without a strong correlation with altitude and latitude. Sampling always took place of air that had seen sunlight for at least one hour. Values are thus representative of daylight con-



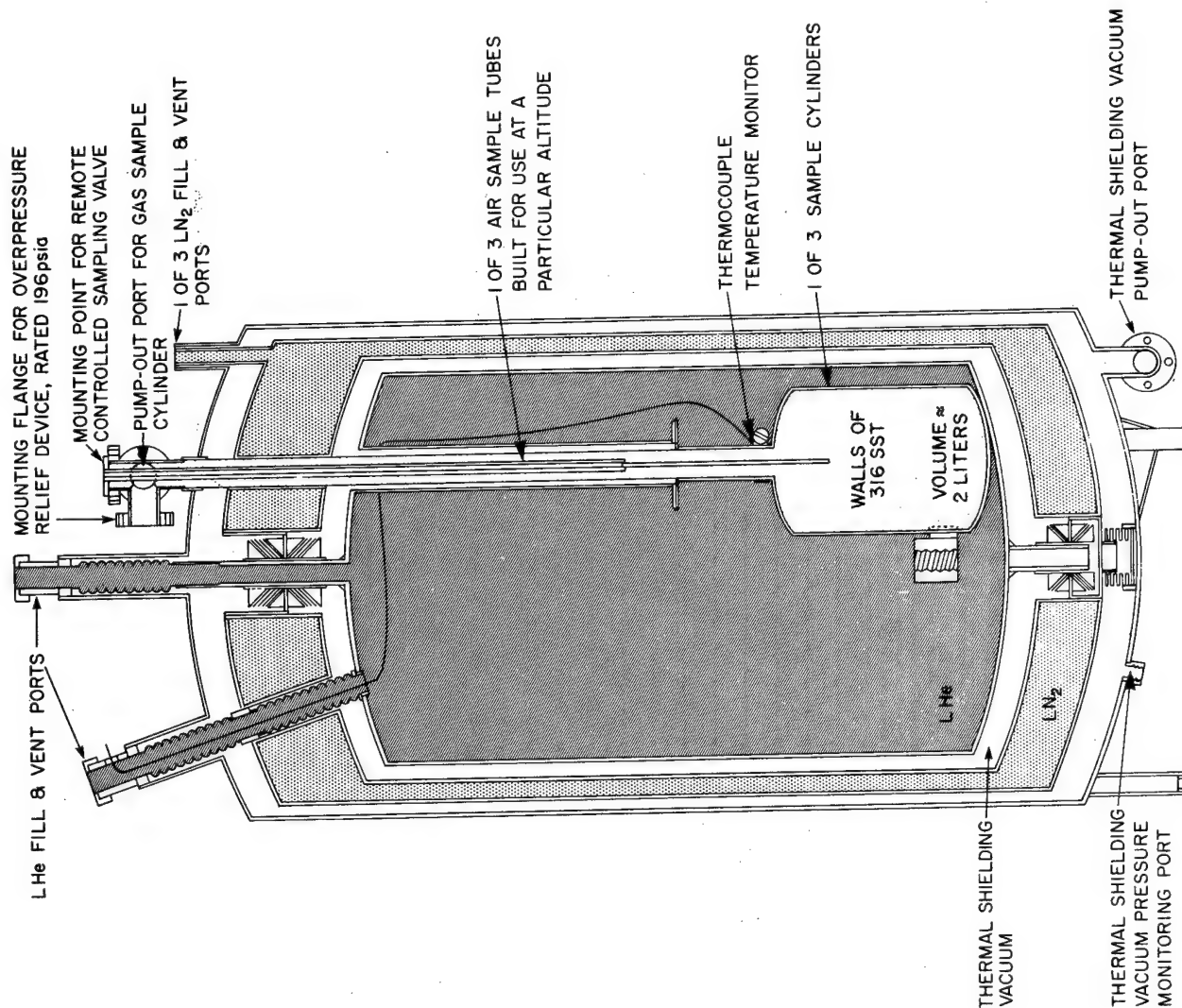
ditions. Nitric oxide content decreases markedly at night.

Values of nitrous oxide exhibit expected variations with altitude and latitude. Figure 10 shows both the decrease in concentration with increasing altitude and the decrease with increasing latitude. The latest Alaska launches, not included here but with data to 30 km, support the conclusions. The South Dakota data is still being processed. The New Mexico and California results were not much different, hence the averaging. Figure 11 shows results from the same flights for CFM12. Again, the more recent Alaska data supports the trends. As a reminder, the typical concentration shown here represents 100 molecules of CFM12 for every trillion ( $10^{12}$ ) molecules of air. The pattern is repeated for CFM11 although the actual concentrations are even lower. The analyses also reveal the absence of CFM113 and CFM114, the two most likely pollutants from the flight package.

## 8. Conclusions

Cryogenic sampling is feasible and substantial quantities of uncontaminated samples are obtainable utilizing a balloon platform. The success of the two recovery methods provides a satisfactory blend between economy and the ability to operate at any location. With the obtaining of a few more flight samples, a substantial data source will be available to establish a baseline value for 5 important trace gas species as a function of altitude and latitude. This occurs at a time when aircraft utilization of the stratosphere is still somewhat limited. The data will assist in the preparation of environmental impact statements, and will serve as a base against which future changes in stratospheric trace gas concentrations, if any, can be compared. Finally, it will serve as a test for theories on trace gas transport to and within the stratosphere.

FIGURE 1. STRATOSPHERIC CRYOGENIC TRIPLE SAMPLER





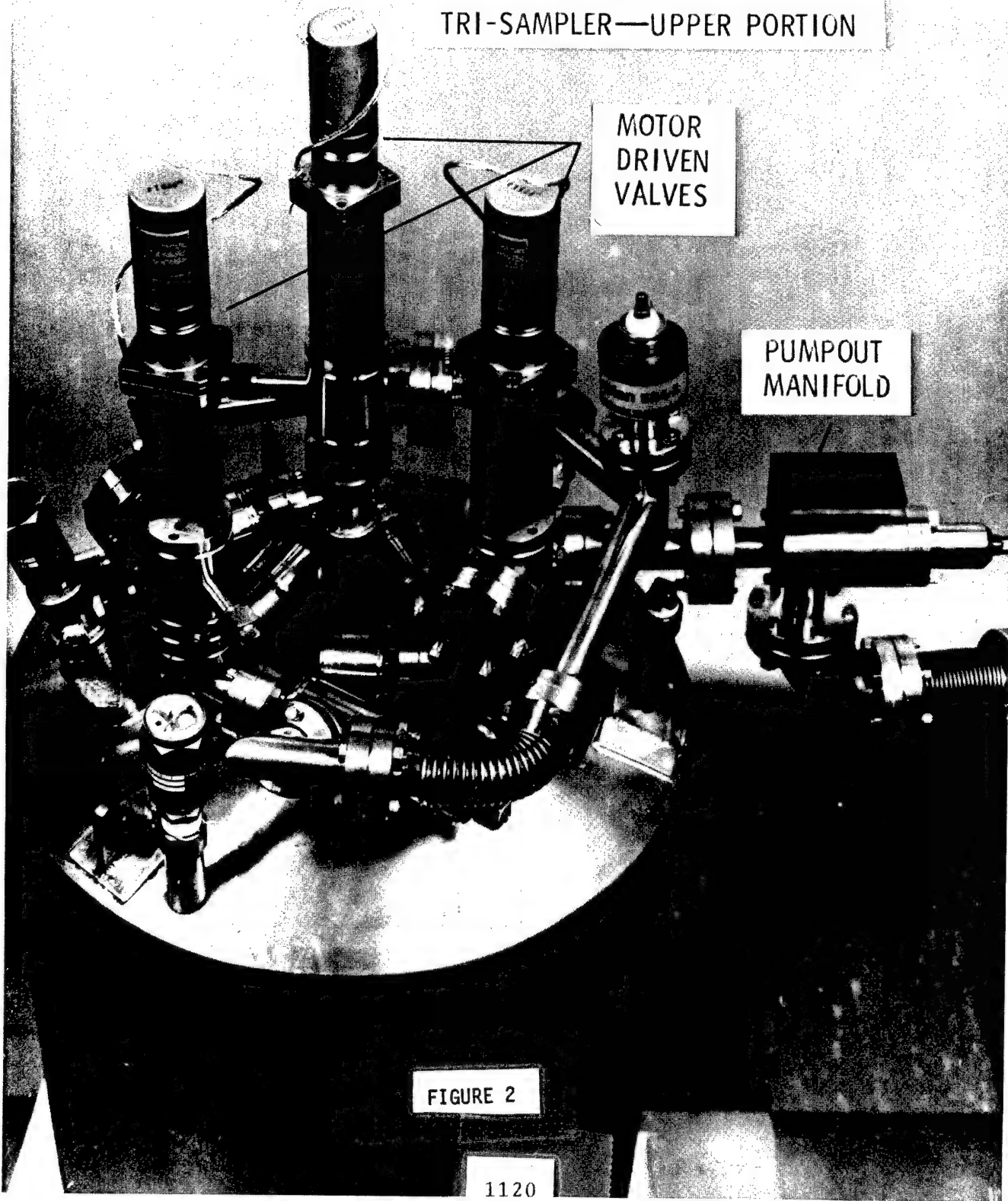
# TRI-SAMPLER—UPPER PORTION

MOTOR  
DRIVEN  
VALVES

PUMPOUT  
MANIFOLD

FIGURE 2

1120



TRI-SAMPLER

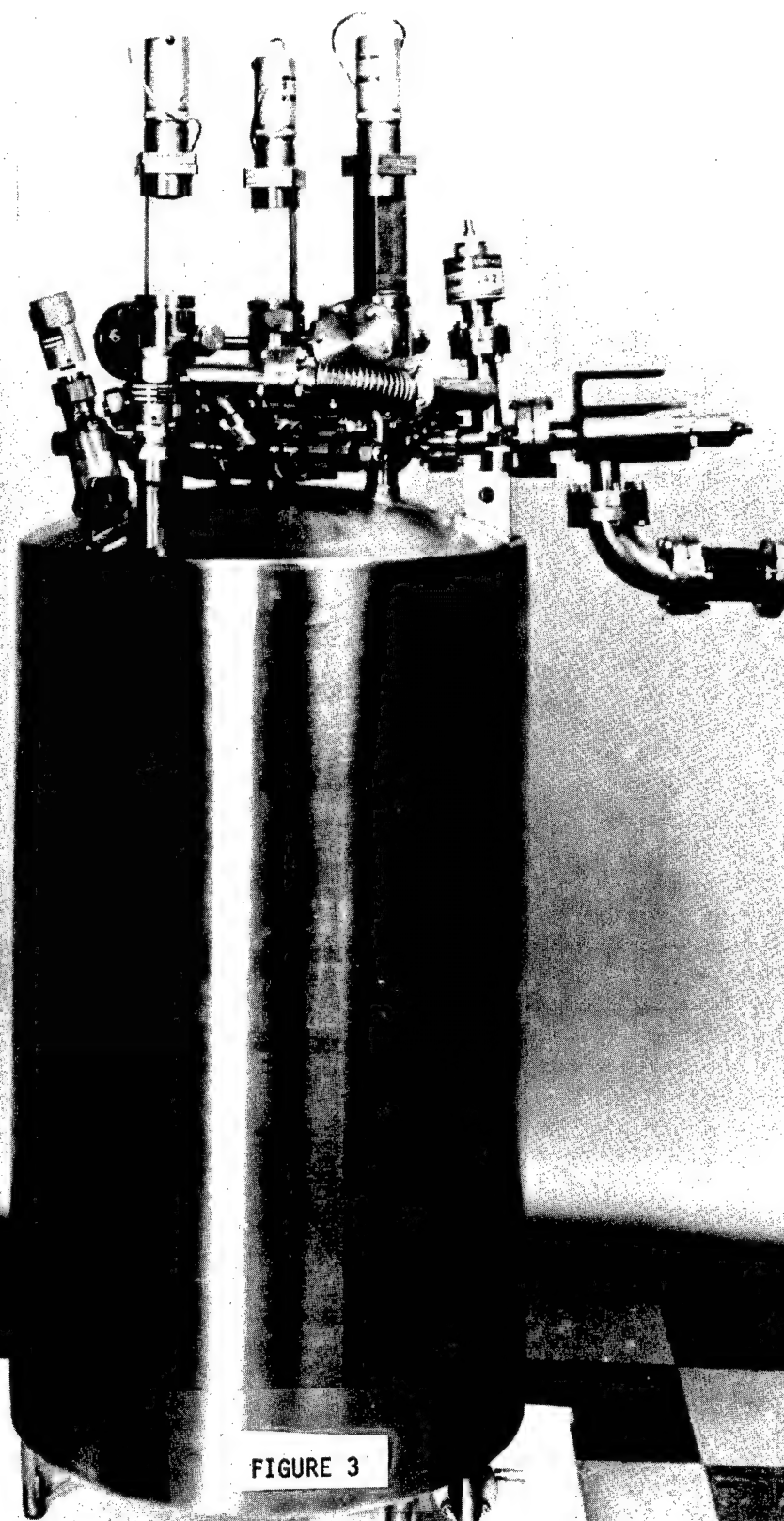


FIGURE 3

1121

FIGURE 4

# TYPICAL BALLOON SYSTEM FOR WHOLE AIR SAMPLING FLIGHT TO 20km ALTITUDE

274,000 cu ft  
BALLOON

48 ft diameter  
PARACHUTE

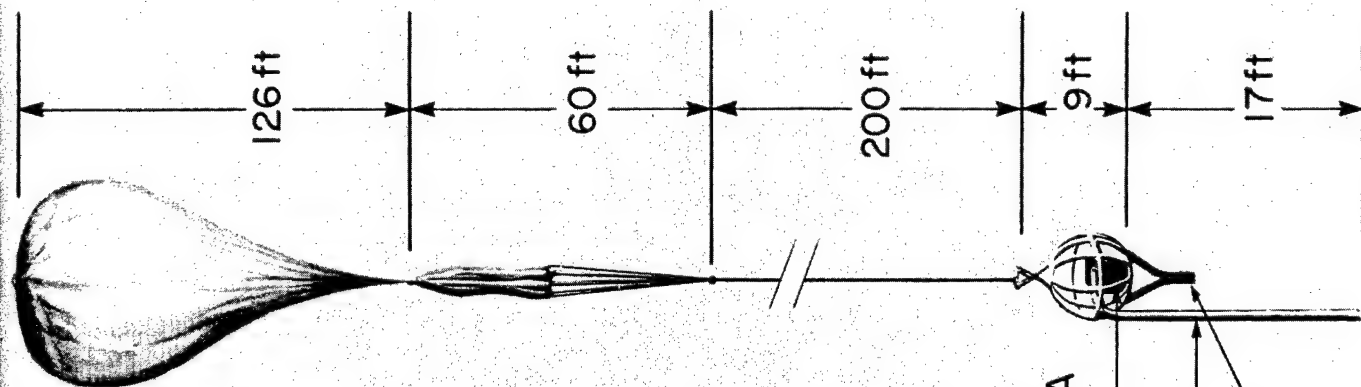
10,000 lb Test  
NYLON LOAD LINE

SELF-RIGHTING GONDOLA

CRYOGENIC SAMPLING  
PACKAGE

BY-PASS AIR IN-LET DUCT  
(3" OD, SST)

BALLAST POUR TUBES  
(3" OD, CANVAS)



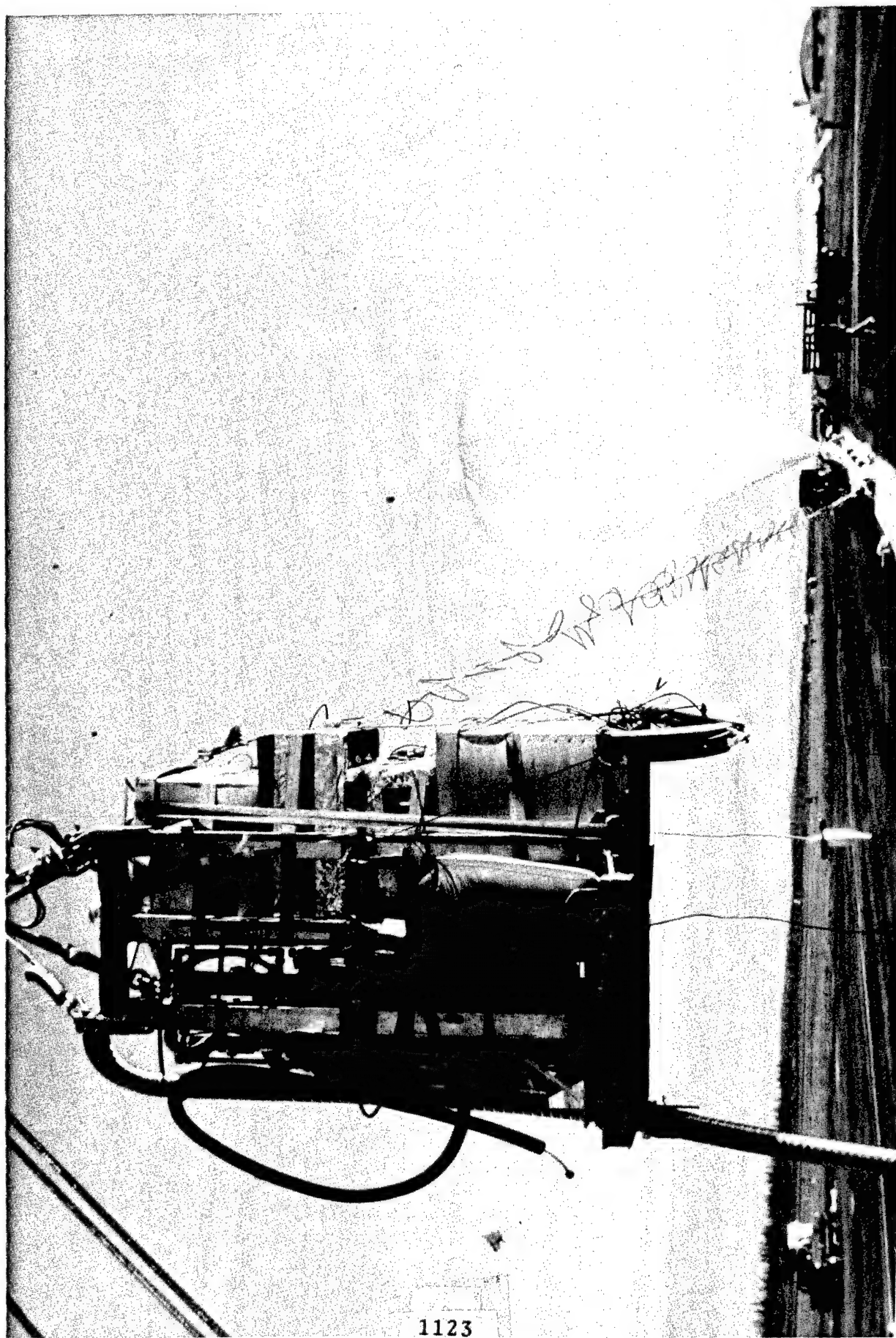


FIGURE 5

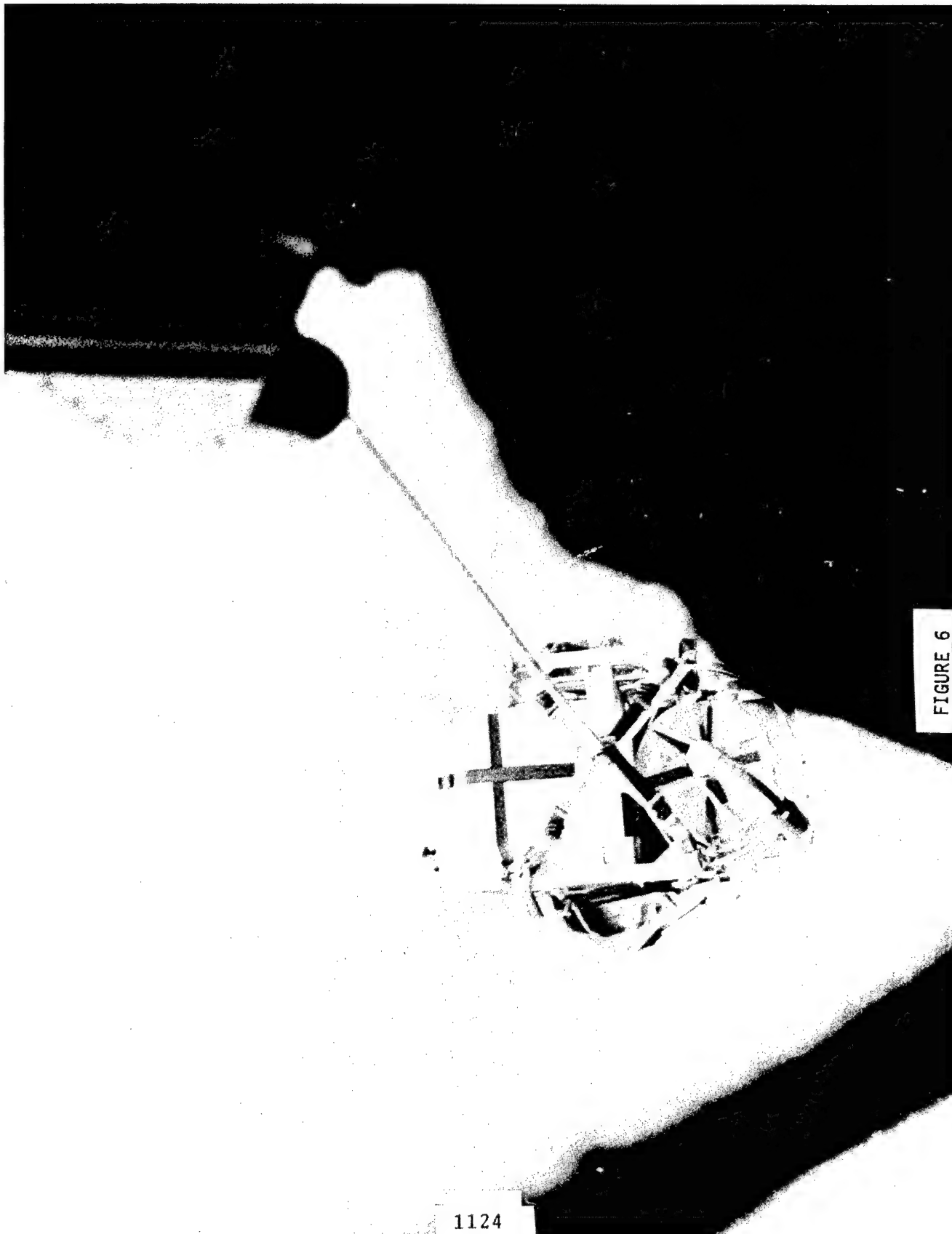
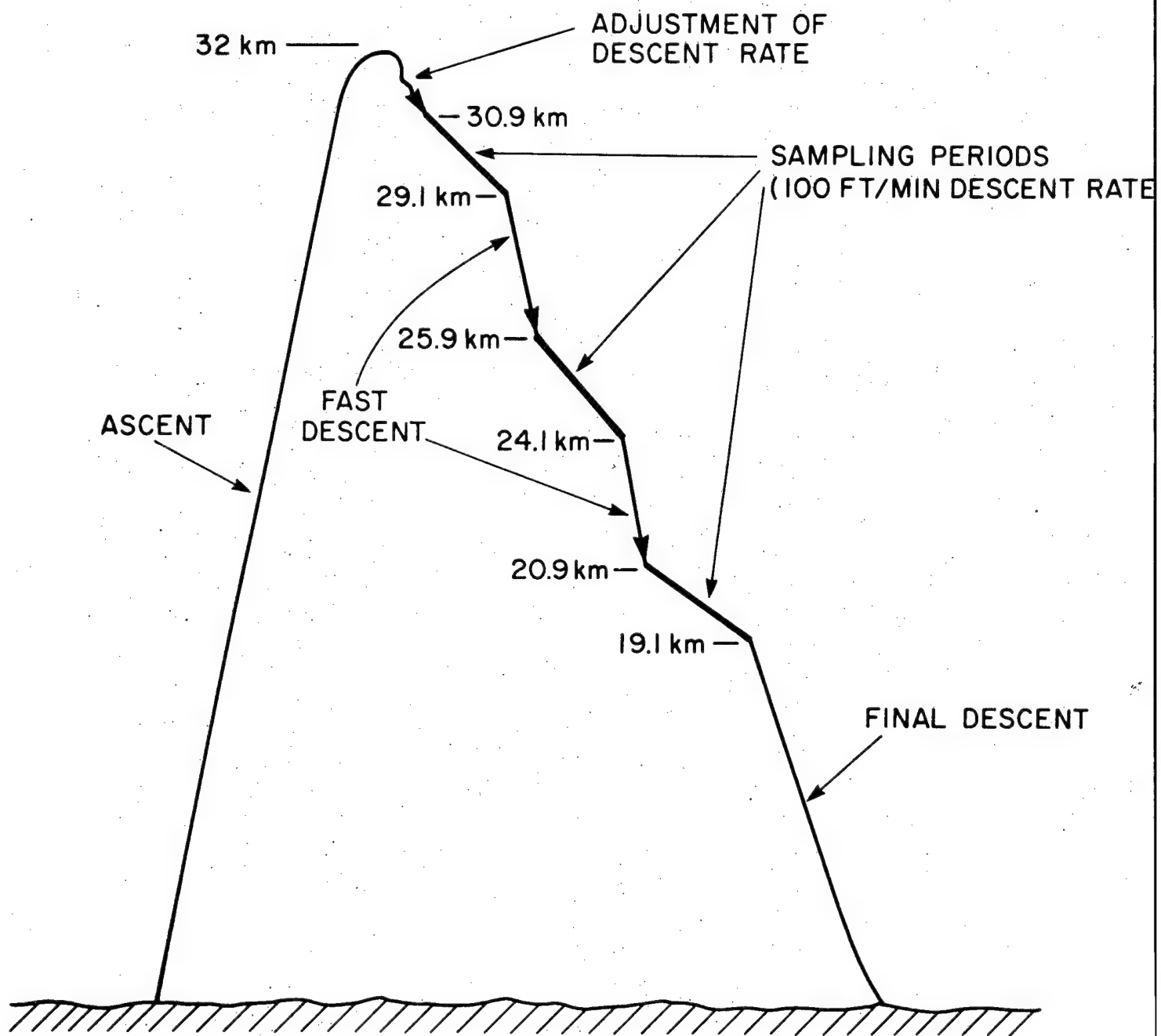


FIGURE 6

## TRI-SAMPLER FLIGHT — HIGH ALTITUDE PROFILE



1125

FIGURE 7

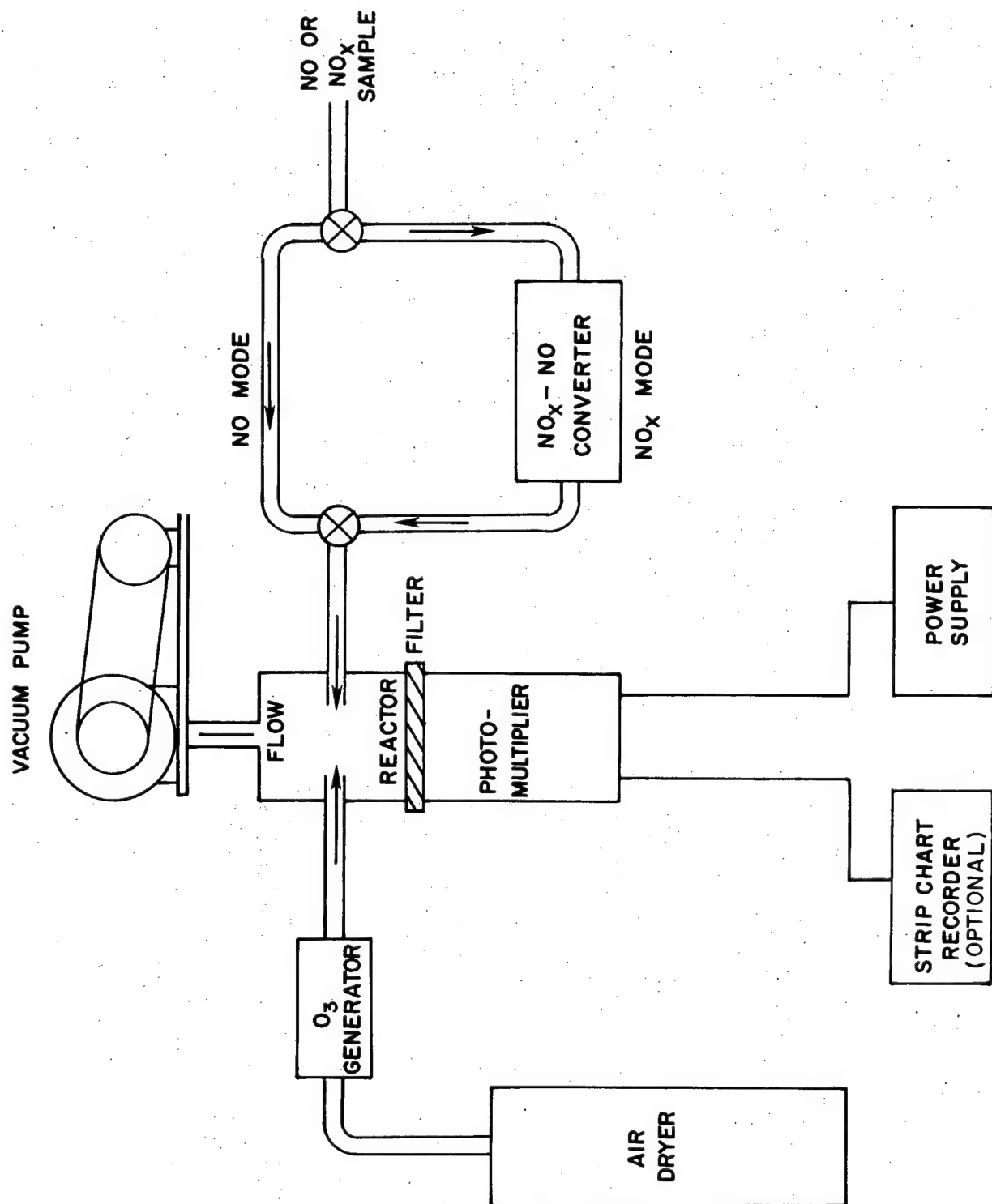
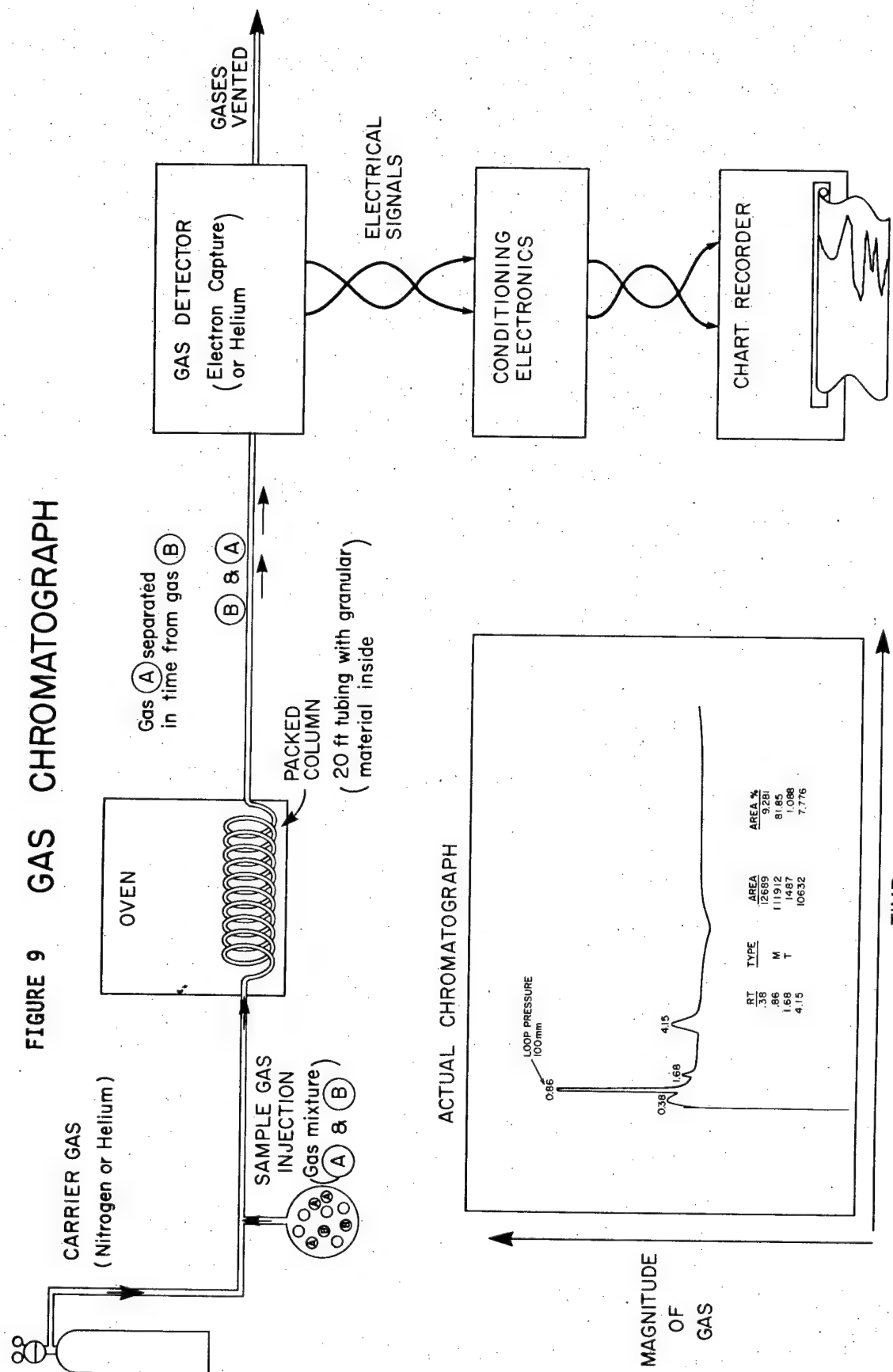


FIGURE 8 CHEMILUMINESCENT NO-NO<sub>x</sub> GAS ANALYZER







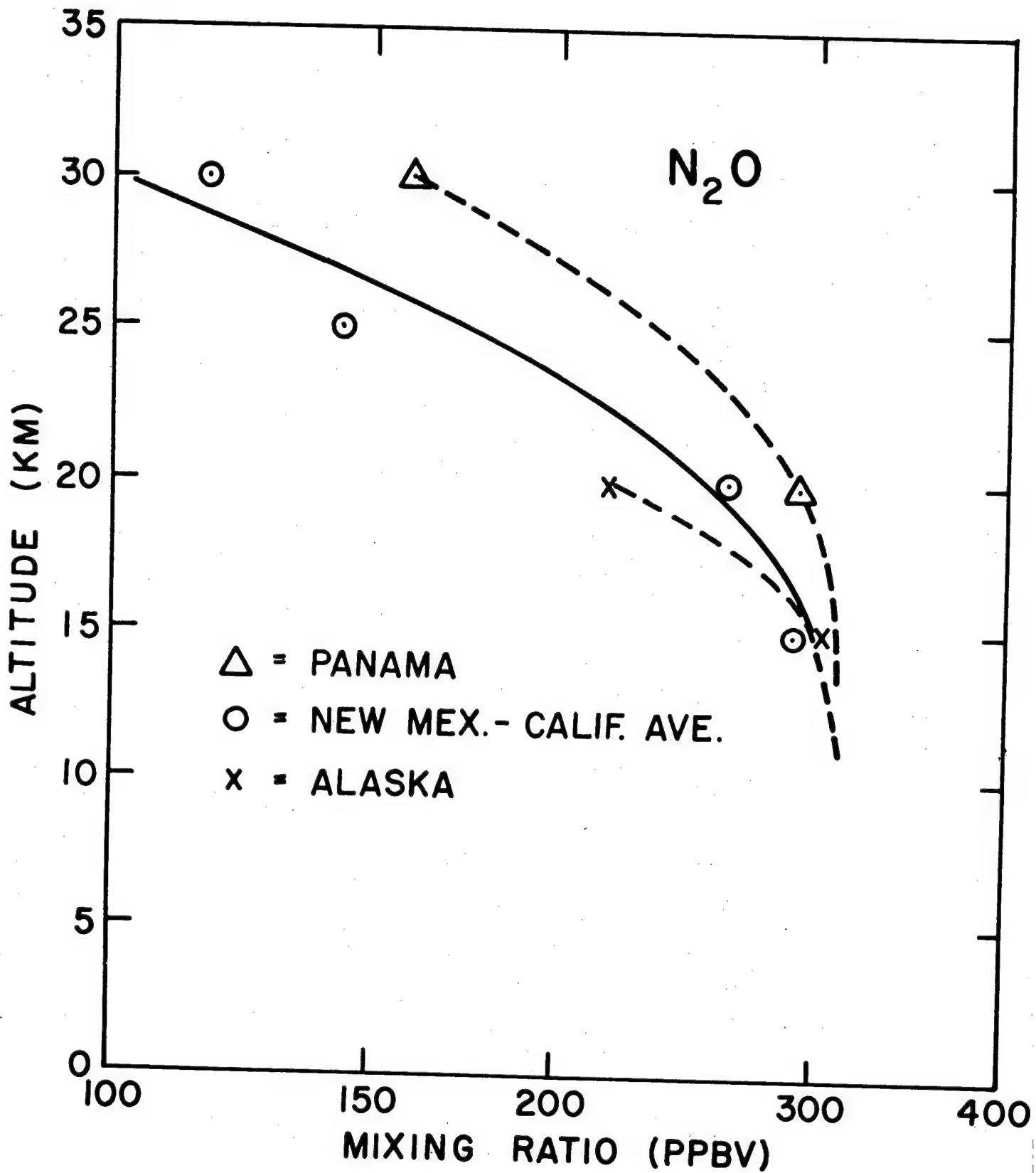


FIGURE 10

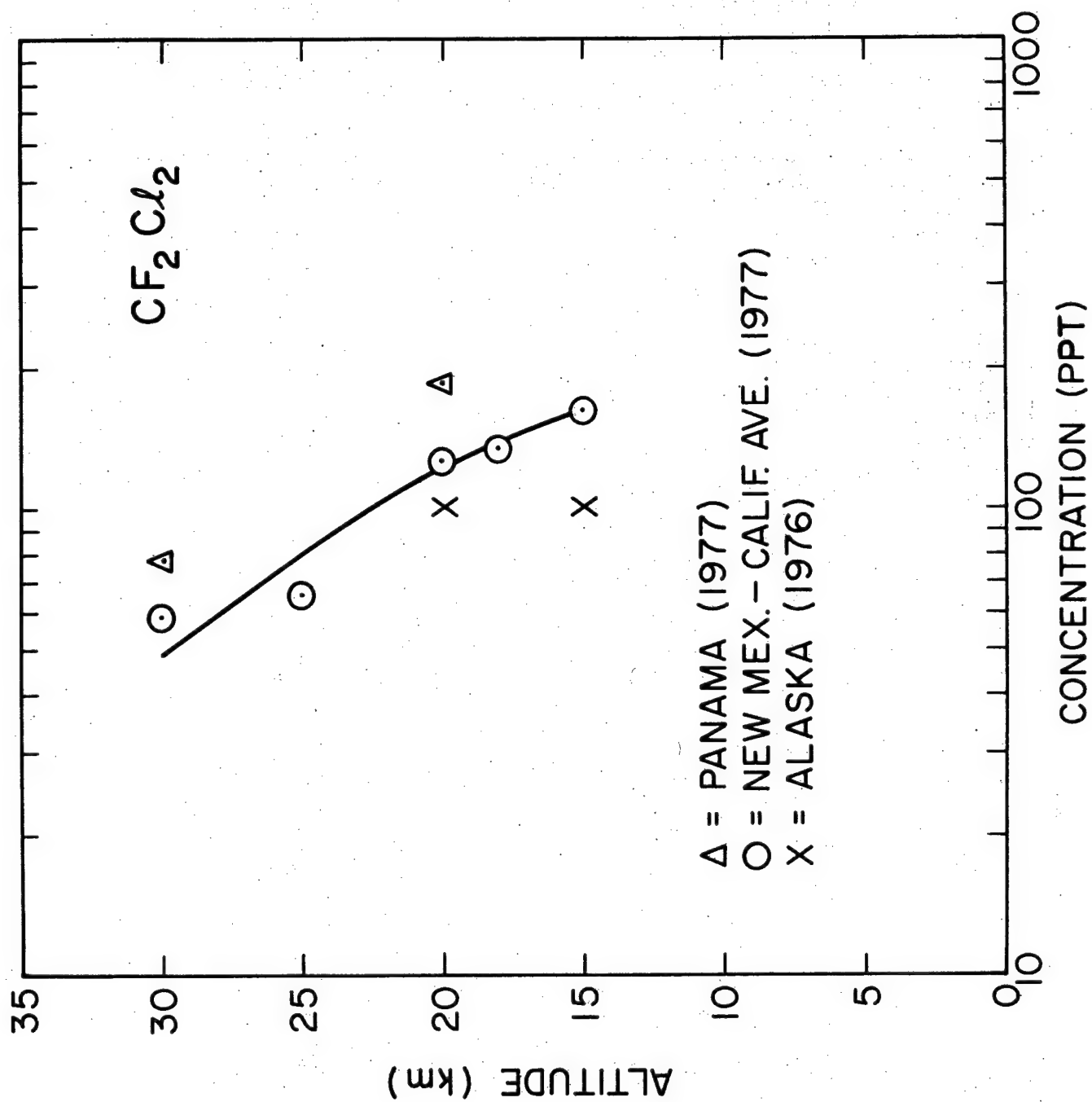


FIGURE 11

### Biographical Sketches

Charles Clifton Gallagher was born in Boston, Massachusetts on February 17, 1937. He graduated from Boston Latin School and received a B.S. degree, cum laude, from Boston College in 1958, with a major in physics. He received M.S. degrees from Boston College in 1960 and from Northeastern University in 1967.

He has been associated with the Air Force Geophysics Laboratory (formerly Air Force Cambridge Research Laboratories) since 1960. From 1960 to 1974 his research was in plasma physics where he published 24 papers, primarily on plasma diagnostics and plasma confinement configurations such as Tormac. Since 1974 he has been associated with the Composition Branch of the Aeronomy Division, studying the trace gas composition of the stratosphere.

As Work Unit Scientist he has coordinated the field sampling and laboratory analyses efforts. Particular attention has been directed towards development of trace gas analytical methods, particularly in the utilization of gas chromatography and chemiluminescent analyzers. Especial problems faced are in the optimization of these techniques for the measurement of extremely low gas concentrations and in establishing calibration methods to make such measurements reliable.

He is a member of the American Physical Society, Sigma Pi Sigma and Sigma Xi.

Captain Robert Victor Pieri, born on 7 April 1949 in Fall River, Massachusetts, graduated cum laude with a Bachelor of Science Mechanical Engineering degree from the University of Massachusetts at Amherst in 1971. Being a Distinguished Graduate of the Air Force ROTC program, he was commissioned in June of that year, but was granted an educational delay before coming on active duty. After marrying the former Patricia Curran, he performed post graduate work at Thayer School on the Dartmouth College campus. After presenting his thesis, based on a computer planning model for sewage treatment on a watershed, he was granted a Master of Engineering degree in 1973.

In September of 1973, Capt. Pieri came on active duty at what is now the Air Force Geophysics Laboratory, working under Dr. Narcisi, developing rocket-borne instrumentation for studying ionospheric phenomenon. At it's inception in 1974, Capt. Pieri was designated to work in the stratospheric gas sampling program. Since that time he has aided in the design and modification of original and commercial equipment to support the sampling program and has been the focal point of all field sampling efforts. He is a member of Tau Beta Pi.

ON THE MODELLING OF TURBULENCE NEAR A SOLID WALL

BY

Kuei-Yuan Chien, Ph.D., USN

Research and Technology Department

Naval Surface Weapons Center  
White Oak Laboratory  
Silver Spring, Maryland

## On the Modelling of Turbulence Near a Solid Wall

### Abstract

A new turbulence model that is valid right down to the solid wall is formulated in the present paper. The  $k-\epsilon$  two-equation model of Launder and Spalding has been adopted to be the high-Reynolds-number limit. Although the general approach is similar to that of Jones and Launder, the detailed proposals are quite different. The Taylor series expansion technique has been used to systematically study the behavior of the turbulent shear stress, kinetic energy and its rate of dissipation near a solid wall. Two new constants are introduced to model the damping effect of the solid wall on the turbulent shear stress and the dissipation. The model is applied to the problem of a fully developed channel flow. Good agreement has been found between the predictions and the measurements of Laufer and that of Clark.

## Introduction

Recently, there has been considerable interest in developing reliable predictive methods for turbulent flowfields. This is undoubtedly because of its significance in many fluid mechanical problems of civil and military applications. It is generally accepted that turbulent flow is governed by the Navier-Stokes equations, and in principle turbulence can be numerically simulated using a digital computer. In the Reynolds number range of technological interest, this is currently beyond our computational capability and may remain so for a long time to come. This is because the number of mesh points required scales like  $Re^{9/4}$  and the number of arithmetic operations scales like  $Re^3 \ln Re$  (Ref. 1), and the Reynolds number  $Re > 10^6$  for most technological applications. Fortunately, the information that is needed by an engineer usually consists of time-averaged data such as lift, drag, etc. Although this information need may expand as the requirements for more advanced technology increase (for example, in the design of sensors, one may need to know more about the structure of turbulence such as the time average of the fluctuating kinetic energy and the length scales involved), it is not clear that one would ever need to know the complete details of a turbulent flowfield. Consequently, the procedure of averaging the Navier-Stokes equations introduced by Reynolds in 1895 has become a very popular approach. The attractiveness of this approach comes from the fact that the averaged dependent variables vary much more gradually in space, and therefore they can be resolved by finite-difference techniques without using excessively fine computational grid.

Because of the nonlinear term in the Navier-Stokes equations, averaging process increases the number of unknowns above the number of equations, and some closure assumptions have to be introduced. This closure problem has been handled with different degrees of sophistication by various research groups (see, e.g. Refs. 2 and 3). The most popular class is the two-equation models in which two partial differential equations are used to describe the development of turbulent kinetic energy and a turbulence length scale (Refs. 4-6). However, the effects of the kinematic viscosity on the turbulence

structure were ignored in these treatments. Consequently, the exact boundary conditions at the wall cannot be satisfied. They avoided the problem by patching to the law of the wall. Such an approach cannot be used when the turbulence Reynolds number is not high as, e.g., in flows with rapid expansions or near transition/turbulence interface.

Turbulence-model equations which provide predictions of the flow within the viscous layer adjacent to the wall have been proposed by several investigators (Refs. 7-9). Among them, only Jones and Launder worked with the more advanced two-equation model. Although the general approach of the present model is the same as that of Jones and Launder, the detailed proposals are substantially different. In fact, it is their ad hoc low-Reynolds-number modification of the equation for the dissipation rate of turbulence energy that has prompted the present study.

In the present study, the Taylor series expansion technique was used to systematically study the proper behavior of the turbulent shear stress, kinetic energy and its rate of dissipation near a solid wall. This will be described in the next section. As an initial attempt to assess the adequacy of the present formulation, the new turbulence model has been applied to the problem of a fully developed channel flow. Some initial results on the distribution of velocity, turbulent shear stress and kinetic energy will be presented and compared with available experimental data.

### The Turbulence Model

The limiting form to which the present model reduces in regions where the direct effect of viscosity on the turbulence structure is negligible is the same as that of Jones and Launder (Ref. 8):

$$\frac{Dk}{Dt} = \frac{\partial}{\partial y} \left( v_t \frac{\partial k}{\partial y} \right) + v_t \left( \frac{\partial u}{\partial y} \right)^2 - \epsilon \quad (1)$$

$$\frac{D\epsilon}{Dt} = \frac{\partial}{\partial y} \left( \frac{v_t}{\sigma} \frac{\partial \epsilon}{\partial y} \right) + c_1 \frac{\epsilon}{k} v_t \left( \frac{\partial u}{\partial y} \right)^2 - c_2 \frac{\epsilon^2}{k} \quad (2)$$

and

$$-\overline{u'v'} = \nu_t \frac{\partial u}{\partial y} \quad (3)$$

where

$$\nu_t = c_\mu \frac{k^2}{\epsilon} \quad (4)$$

The usual boundary-layer approximations have been made in the above equations where  $D/Dt$  is the substantial derivative,  $x$  and  $y$  are, respectively, the coordinates parallel and normal to the solid wall, and  $u$  the velocity in the  $x$ -direction. The quantities  $k$  and  $\epsilon$  are, respectively, the kinetic energy of turbulence and the "isotropic" dissipation (where the summation convention is adopted)

$$\epsilon = \nu \overline{\frac{\partial u_i'}{\partial x_j} \frac{\partial u_i'}{\partial x_j}} \quad (5)$$

which is not the true rate of energy dissipation (Ref. 2)

$$D = \nu \overline{s_{ij}' s_{ij}'} \quad (6)$$

(where  $s_{ij}' = (\frac{\partial u_i'}{\partial x_j} + \frac{\partial u_j'}{\partial x_i})/2$ ). At high Reynolds

numbers,  $D = \epsilon$  because the small-scale turbulence is then isotropic. According to the recommendations of Launder and Spalding (Ref. 10), the following values of the constants are used:  $c_\mu = 0.09$ ,  $c_1 = 1.44$ ,  $c_2 = 1.92$ ,  $\sigma = 1.3$ . The values of  $c_1$  and  $c_2$  employed here differ slightly from those originally adopted in Ref. 8.

To develop a model that will provide predictions of the flow right down to the solid wall, the form of the model described by Eqs. (1) - (4) needs to be modified in several ways. First, the kinematic viscosity must be added in Eqs. (1) and (2) to account for the effect of viscous diffusion of  $k$  and  $\epsilon$ . They are exact in the sense that they appear in the exact form of the transport equations for  $k$  and  $\epsilon$  as derived from the



Navier-Stokes equations. Secondly, since Eq. (4) is the limiting form for  $v_t$  as the direct effect of viscosity is negligible, it is modified only to include the "damping" effect due to the presence of the solid wall

$$v_t = c_\mu \frac{k^2}{\epsilon} [1 - \exp(-c_3 u_* y / \nu)] \quad (7)$$

where  $u_*$  and  $\nu$  are the friction velocity and the viscosity of the fluid, respectively, and  $c_3$  is a constant. Consider a Taylor series expansion for the fluctuating velocity components near  $y = 0$ . Because of the no-slip boundary condition and the continuity equation for an incompressible fluid, one obtains

$$\begin{aligned} u' &= u_1 y + O(y^2) \\ v' &= v_2 y^2 + O(y^3) \\ w' &= w_1 y + O(y^2) \end{aligned} \quad (8)$$

Substituting Eq. (8) into the definition of  $k$ , one obtains

$$k = \frac{1}{2} (u_1^2 + w_1^2) y^2 + O(y^3) \quad (9)$$

A Taylor series expansion of Eq. (2) near  $y = 0$  suggests that  $\epsilon \sim y^2$ . Therefore, Eq. (7) indicates that near  $y = 0$ ,  $v_t \sim y^3$  which is indeed the proper limit as one can deduce from Eqs. (3) and (8). However, substituting Eq. (8) into Eqs. (5) and (6), one obtains

$$D = \epsilon = \nu (u_1^2 + w_1^2) + O(y^2) \quad (10)$$

which indeed reflects the proper physical behavior of the dissipation at a solid wall. From Eqs. (9) and (10), one obtains at  $y = 0$

$$D = \frac{2\nu k}{y^2} \quad (11)$$

To retain the behavior of  $\epsilon \sim y^2$ , it is simply assumed that the dissipation term in the turbulent kinetic energy equation is just the sum of  $\epsilon$  and  $2\nu k/y^2$ . Therefore,

the low-Reynolds-number form of Eq. (1) is written in the following form:

$$\frac{Dk}{Dt} = \frac{\partial}{\partial y}[(\nu + \nu_t) \frac{\partial k}{\partial y}] + \nu_t \left(\frac{\partial u}{\partial y}\right)^2 - \epsilon - \frac{2\nu k}{y} \quad (12)$$

Eq. (2) is similarly modified to read

$$\frac{D\epsilon}{Dt} = \frac{\partial}{\partial y}[(\nu + \frac{\nu_t}{\sigma}) \frac{\partial \epsilon}{\partial y}] + c_1 \frac{\epsilon}{k} \nu_t \left(\frac{\partial u}{\partial y}\right)^2 - c_2 \frac{\epsilon}{k} [\epsilon + \frac{c_4' \nu k}{y^2}] \quad (13)$$

Expanding Eqs. (12) and (13) near  $y = 0$  indicates that, at  $y = 0$ ,

$$c_4' = 2/c_2 \quad (14)$$

if the behavior  $\epsilon \sim y^2$  is preserved. We assume that

$$c_4' = \frac{2}{c_2} \exp(-c_4 u^* y / \nu) \quad (15)$$

In summary, our new model of turbulence is assumed to be governed by Eqs. (7), (12) and (13), with two new constants  $c_3$  and  $c_4$ . Since the "wall" dissipation effect is expected to decrease rapidly,  $c_4 \sim O(1)$ . Unlike Jones and Launder, we have kept all other constants originally appearing in the high-Reynolds-number equations intact. To test the present modelling and to fix the numerical values of  $c_3$  and  $c_4$ , we consider the following problem of a fully developed channel flow.

#### Fully Developed Channel Flow

Eqs. (7), (12) and (13) have been applied to the study of turbulent flow between two parallel plates, driven by a constant pressure gradient. The plates are separated by a distance  $2H$  in the  $y$ -direction and the mean flow is in the  $x$ -direction. Therefore, the continuity equation is automatically satisfied, and the momentum equation reduces to

$$(\nu + \nu_t) \frac{\partial u}{\partial y} = u_*^2 \frac{(H-y)}{H} \quad (16)$$

One may nondimensionalize the equations through the substitutions

$$\tilde{y} = y/H, \quad \tilde{u} = u/u_*, \quad \tilde{k} = k/u_*^2,$$

$$\tilde{\varepsilon} = \varepsilon/(u_*^3/H), \quad \tilde{v}_t = v_t/\nu$$

For convenience, the tilde notation is suppressed and it is understood that, from now on, all variables are dimensionless. Since  $k$  and  $\varepsilon$  depend only on  $y$  for a fully developed flow, the governing equations become

$$\frac{du}{dy} = Re^* \left( \frac{1-y}{1+v_t} \right) \quad (17)$$

$$\frac{d}{dy} \left[ (1+v_t) \frac{dk}{dy} \right] + v_t \left( \frac{du}{dy} \right)^2 - Re^* \varepsilon - \frac{2k}{y^2} = 0 \quad (18)$$

$$\begin{aligned} \frac{d}{dy} \left[ \left( 1 + \frac{v_t}{\sigma} \right) \frac{d\varepsilon}{dy} \right] + c_1 \frac{\varepsilon}{k} v_t \left( \frac{du}{dy} \right)^2 - c_2 Re^* \frac{\varepsilon^2}{k} \\ - \frac{2\varepsilon}{y^2} \exp(-c_4 Re^* y) = 0 \end{aligned} \quad (19)$$

$$v_t = c_\mu Re^* \frac{k^2}{\varepsilon} [1 - \exp(-c_3 Re^* y)] \quad (20)$$

where  $Re^* = u_* H / \nu$ . The boundary conditions are, at  $y = 0$ ,

$$u = k = \varepsilon = 0 \quad (21)$$

and, at  $y = 1$ ,

$$\frac{dk}{dy} = \frac{d\varepsilon}{dy} = 0 \quad (22)$$

Of course, it is also required that  $k/\varepsilon$  is bounded at  $y = 0$ .

The above set of equations was solved by the time-dependent marching technique using the Crank-Nicolson finite difference method, and the results compared with the experimental measurements of Laufer (Ref. 11) and Clark (Ref. 12). A quantity of interest is the (dimensionless) difference between the center velocity and the bulk mean velocity,  $u_c - u_b$ . Clark's data

suggested that this difference is a constant,  $u_c - u_b = 2.32$ . Our calculations at  $Re^* = 650$  and  $1180$  based on  $c_3 = 0.01$  and  $c_4 = 0.5$  also give a constant difference,  $u_c - u_b = 2.22$ , which is within the scatter of the experimental data.

The defect velocity is shown in Fig. 1 for  $Re^* = 1180$ . Also shown are the measurements of Laufer at the same  $Re^*$ , and that of Clark at a slightly higher  $Re^* (= 1280)$ . It is seen that the agreement is good. So is the comparison of the shear stress distribution between the prediction and the measurements of Laufer (Fig. 2).

In Fig. 3, the turbulent kinetic energy distribution at  $Re^* = 1180$  is compared with the measurements of Laufer at the same  $Re^*$  and that of Clark at a slightly lower  $Re^* (= 1110)$ . The agreement is reasonably good although the predicted value is somewhat higher at the center of the channel.

The distribution of the turbulent kinetic energy in the inner layer of the flow ( $y \leq 0.1$ ) is shown in Fig. 4 for  $Re^* = 650$ . Although the measurements show a somewhat sharper distribution, the general trend and the level of the peak are predicted quite well.

#### Concluding Remarks

A turbulence model that is valid right down to a solid wall has been developed and applied to the channel flow problem. Although the comparisons with experiments have not been very extensive, initial results are indeed very encouraging. The model is currently being applied to boundary layer flows with pressure gradients.

## References

1. K. M. Case, et.al., "Numerical Simulation of Turbulence," Stanford Research Institute, Technical Report JSR-73-3, 1973.
2. W. C. Reynolds, "Computation of Turbulent Flows," Ann. Rev. Fluid Mech., Vol. 8, p. 183, 1976.
3. M. Rubesin, "Modeling of the Reynolds Stresses," in NASA Conference Proceedings 2032, Feb. 1978.
4. B. E. Launder and D. B. Spalding, Lectures in Mathematical Models of Turbulence, Academic Press, New York, 1972.
5. K. H. Ng and D. B. Spalding, "Turbulence Model for Boundary Layers near Walls," Physics of Fluids, Vol. 15, p. 20, 1972.
6. H. Vollmers and J. C. Rotta, "Similar Solutions of the Mean Velocity, Turbulent Energy and Length Scale Equation," AIAA Journal, Vol. 15, p. 714, 1977.
7. G. S. Glushko, "Turbulent Boundary Layer on a Flat Plate in an Incompressible Fluid," Izv. Acad. Nauk SSSR Mekh No. 4, p. 13, 1965.
8. W. P. Jones and B. E. Launder, "The Prediction of Laminarization with a 2-Equation Model of Turbulence," Int. J. Heat Mass Transfer, Vol. 15, p. 301, 1972.
9. G. L. Mellor and H. J. Herring, "A Survey of the Mean Turbulent Field Closure Models," AIAA Journal, Vol. 11, p. 590, 1973.
10. B. E. Launder and D. B. Spalding, "The Numerical Calculation of Turbulent Flows," Comp. Math. in Appl. Mech. and Eng., Vol. 3, p. 269, 1974.
11. J. Laufer, "Investigation of Turbulent Flow in a Two-Dimensional Channel," NACA Rept. 1053, 1951.
12. J. A. Clark, "A Study of Incompressible Turbulent Boundary Layers in Channel Flow," J. Basic Eng., Vol. 90, p. 455, 1968.

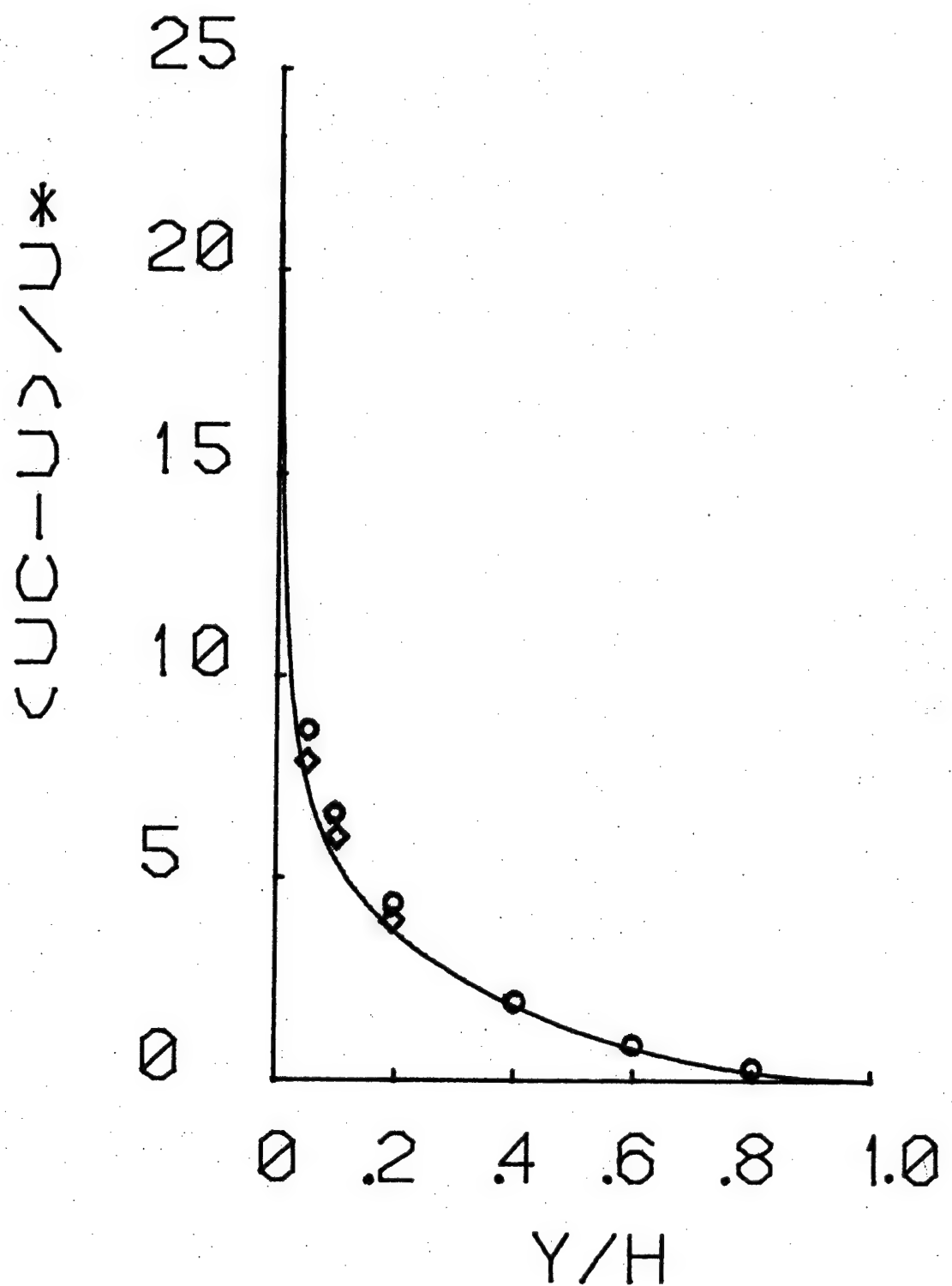


FIG. 1 VELOCITY DISTRIBUTION IN A TWO-DIMENSIONAL CHANNEL.  
THEORY —; DATA: ● (LAUFER), ♦ (CLARK).

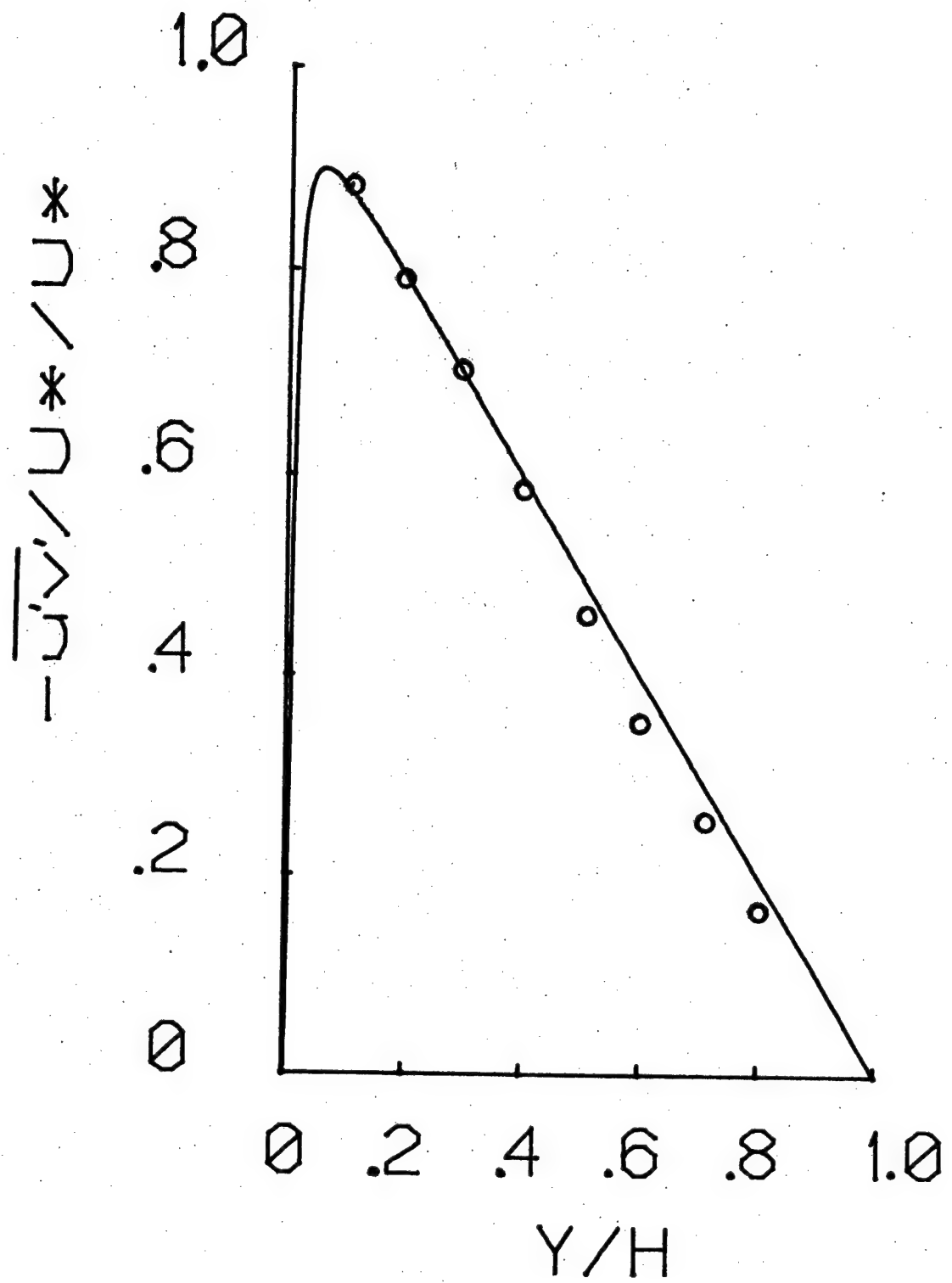


FIG. 2 TURBULENT SHEAR STRESS DISTRIBUTION

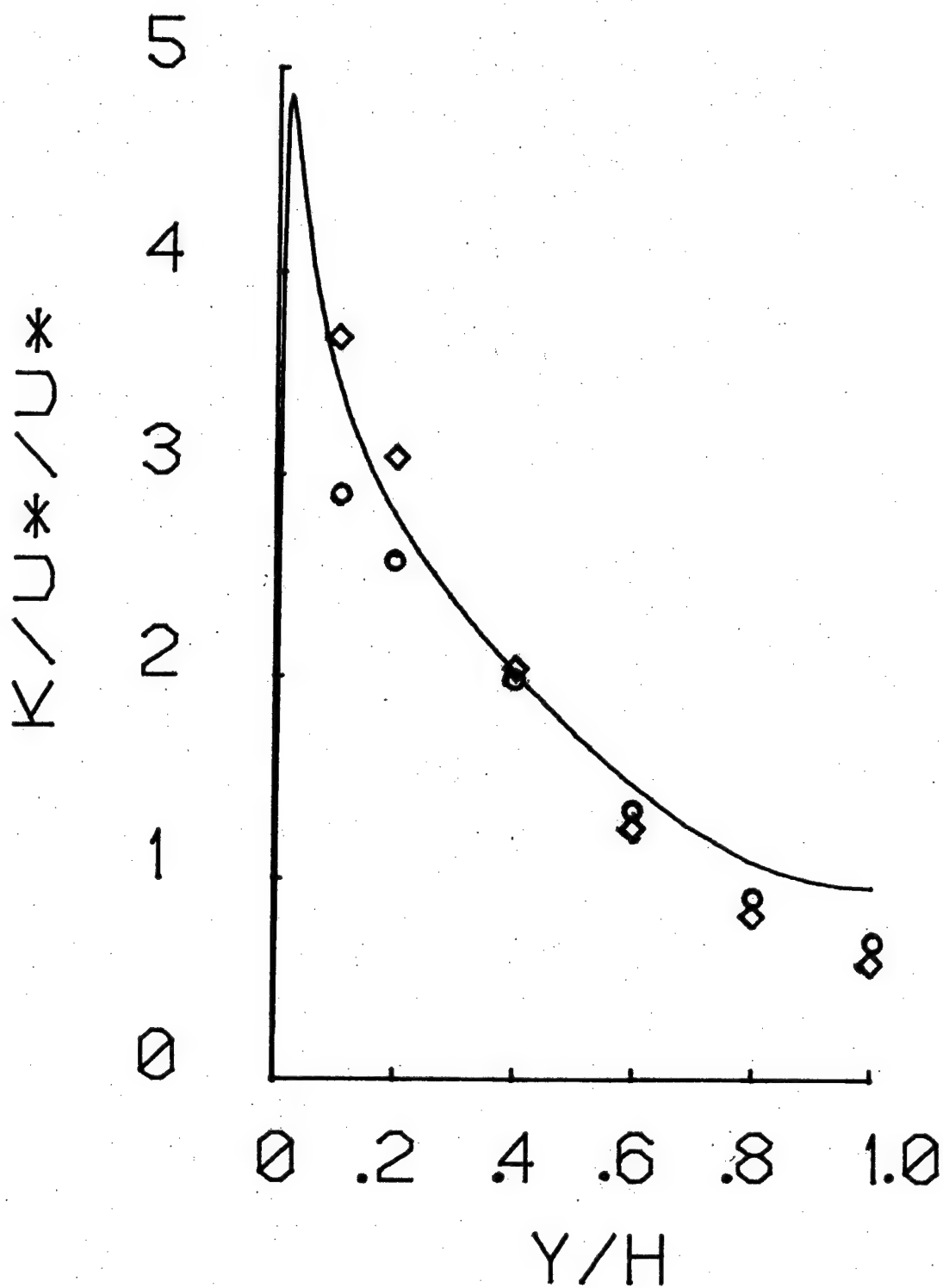


FIG. 3 TURBULENT KINETIC ENERGY DISTRIBUTION



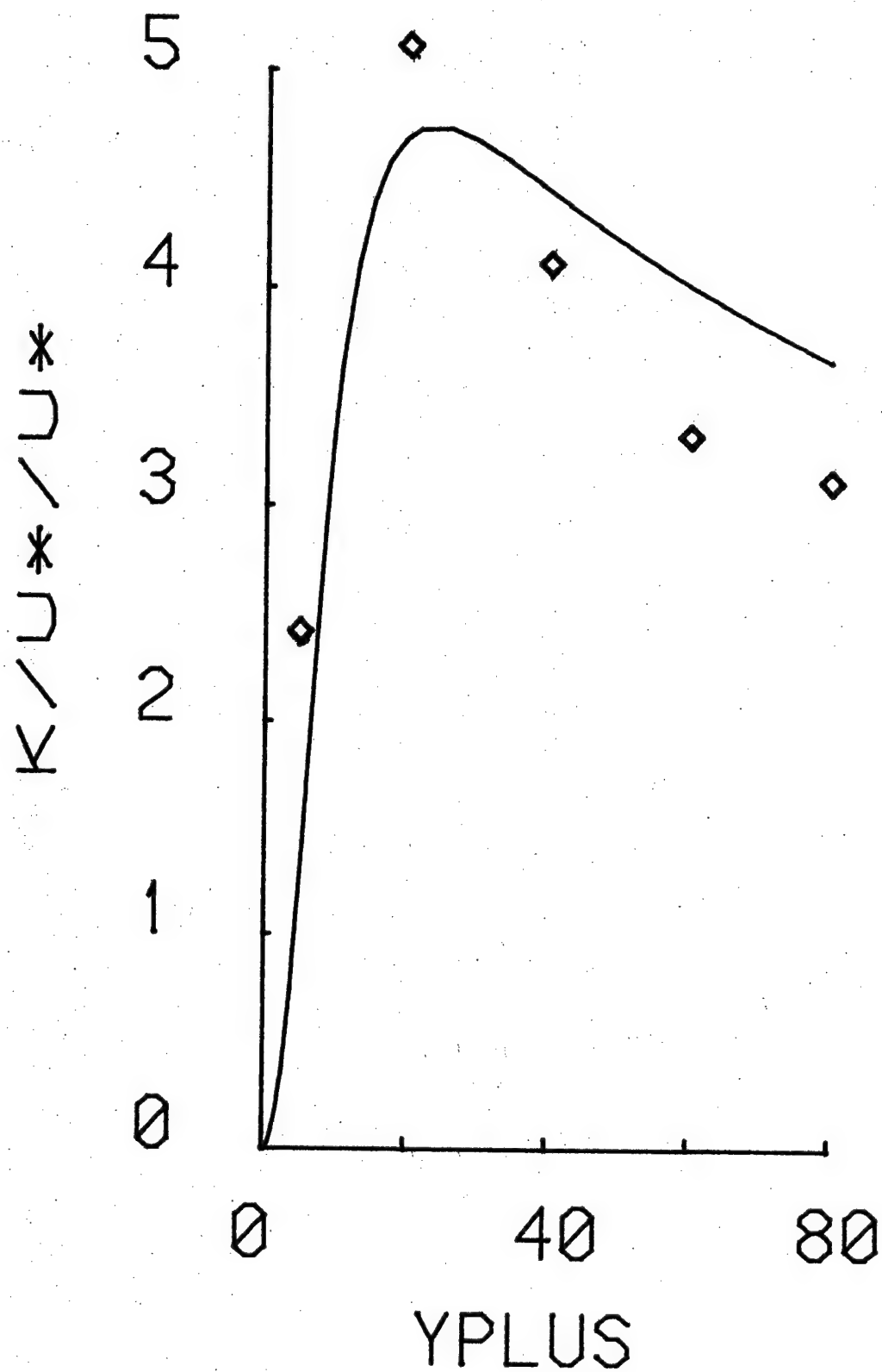


FIG. 4 TURBULENT KINETIC ENERGY DISTRIBUTION  
IN THE INNER LAYER

### Biographical Sketch

Dr. Kuei-Yuan Chien was graduated from the National Taiwan University in 1962 with a B.S. degree in Mechanical Engineering. He came to U.S. in 1963 to enroll into the graduate school of the Massachusetts Institute of Technology where he received a M.S. degree in 1965 and the Ph.D. degree in 1968.

After graduation, he did research in high-temperature gas dynamics and radiative gas dynamics at NASA Ames Research Center as a NRC Research Associate. He has been working at the Naval Surface Weapons Center (formerly the Naval Ordnance Laboratory) as a Research Aerospace Engineer since 1971. His research interests include theoretical and experimental studies of turbulent flows, computational fluid dynamics, rarefied gas dynamics, two-phase flows and numerical modeling of chemical lasers. Dr. Chien is an Associate Fellow of AIAA and a member of its Thermophysics Technical Committee. He is also a member of Sigma Xi and Sigma Gamma Tau.

ATMOSPHERIC ELECTRIC HAZARDS TO AIRCRAFT

BY

L. H. Ruhnke

Naval Research Laboratory

Washington, DC 20375

1146

## ATMOSPHERIC ELECTRIC HAZARDS TO AIRCRAFT

### Abstract

Atmospheric electrical effects associated with clouds, wind, turbulence and precipitation can occur at power levels that are sometimes destructive to electronics and mechanical structures, and often introduce noise to limit operations of computers, communication links and electronic circuits. An analysis of the physical processes which generate electricity reveals that prevention procedures are possible but are not always applied. Airplanes, rockets and helicopters use increasingly sophisticated electronics, new materials like carbon composites, and heavier engines, all of which increase the hazards from atmospheric electric noise. A rapid development of modern avoidance systems has to keep pace with the development of protective procedures or hardware. The influence of heavy helicopter engines on the buildup of dangerous electric charges, the problems of electromagnetic shielding when using carbon composite materials in airplanes, and the effect of lightning radiation on modern electronics is discussed within the context of basic research in atmospheric electricity.

## Introduction

As in many other research areas, funding levels in basic research of atmospheric electricity depends strongly on existing technological problems. One can expect then, that new problems induce increased spending and increased research will lead to technological solutions. Today's aircraft problems with atmospheric electric hazards are largely solved, which explains the relatively low level of research effort in that area. One can foresee, however, a significantly increased hazard of lightning and electrostatics to aircraft and space vehicles presently under development and, therefore, one can speculate on an increased basic research effort in atmospheric electricity. To foresee such tasks one needs to look at the past as well as at a contemporary assessment of problems.

Atmospheric electric hazards to man have always existed. However, only after the discovery by Franklin that lightning is of electrical nature did the idea of a lightning rod develop. For some 30 years thereafter lightning and static electricity was a favorite subject of research and a comparatively large fraction of physical sciences was devoted to it. The technological problem was the protection of buildings and people from lightning strikes. Half of the problem solved with the lightning rod, research proceeded some how, not towards personnel protective device development but went on to design more sensitive electrometers and electrical measurements in fair weather. Finally the personnel protection problems were solved by lightning avoidance rules which were more or less successful. Still today such proverbs as

Eichen sollst du weichen,  
Buchen sollst du suchen

are in Germany well known although not always effective. After this period, atmospheric electricity succumbed as an oddity in research, although its offspring lead directly to radioactivity and cosmic ray research.

The next problem appeared early this century with the development of power transmission lines. These long wires suspended from high towers seemed to attract lightning like a lightning rod and threatened to curtail the electric power industry. By 1920 a surge of research activity dealt with lightning transients and peak currents as well as with the

physics of charge generation within thunderstorms. Much of the lightning statistics came from this time period e.g., that the average lightning current peaks at 10,000 ampere. The solution came by developing proper switching devices and using a grounded conductor above or near power lines. The solution was satisfactory at the time, but as the complexity of power distribution systems increased, failures of hardware or lightning strikes of extreme magnitudes had an increased effect on the well-being of the affected population. The lightning induced black-out in New York on July 13, 1977 is a good example. In this case lightning affected some 8 million people with losses estimated at 310 million dollars.

By 1930 research in atmospheric electricity diminished noticeably until the next technological problem pressed for a solution. This time it came as an avionics problem. Aircraft became dependent on communication by radio, and static charge-up by precipitation and electromagnetic emissions from thunderstorms interfered at times substantially. Research blossomed as never before. A large thunderstorm research program investigated dynamics, cloud physics and electrification of thunderstorms, and over twenty theories for the charge generation processes were discovered. Corona and other electrical breakdown processes were thoroughly investigated and lightning statistics were updated. The average peak current of a lightning was determined to be 20,000 amperes. The solution to the communication problem came by the development of electrostatic dischargers and the use of VHF and UHF radio systems. The menace of thunderstorms was further diminished by the development of weather radar and strict rules to avoid flights into thunderstorms. A general decrease in research funding for atmospheric electricity followed which has not stopped until the present day.

#### Present and Future Technological Problems

In an age of rapid technological developments as in the present, we have to ask the question of what technology trends will be limited or affected by natural atmospheric electric processes and what solutions can be expected through research. Such solutions have to come rapidly to keep pace with the speed of technology development. Otherwise major disasters will occur and demand rapid solutions. The lightning incident of APPOLLO 12 is an example where a considerable hazard was overlooked during a comparatively rapid development

period of large rocket boosters. During launch of APPOLLO 12 weather conditions were marginal but without danger of lightning. The size, shape and electrical capacity of the large boosters was inducive to initiate a lightning in a mild shower cloud where otherwise no lightning would have occurred. Large objects with proper shape can not only enhance electrostatic fields until breakdown occurs but can initiate a spark discharge rather than the normal corona discharge and initiate in this way a lightning. A similar effect is possible if a large object very suddenly appears e.g. a burst of water near an underwater explosion, or when an object travels at very high speed. The problem of aircraft size is significant also for helicopters which charge up readily by engine exhaust and often operate in near surface positions in extremely high electrostatic fields which are generated by surface dust or sea spray. Discharges on ground contact increase in magnitude about with the third power of the helicopter size, which explains some of the recent incidents during tests of the CH53 helicopter.

A second problem of concern is the future use of carbon composites for aircraft. This material has poor shielding properties for lightning frequencies, has bonding problems to metal for P-static elimination and has poor properties to dissipate lightning currents if direct hits are involved.

The last and most severe problem is the trend in microcircuitry. State-of-the-art of component sizes is now about 5 microns. Development of component size of 0.5 microns is a recently announced goal of DOD. As component density increases and component sizes shrink, electrical currents in each component decreases to keep heat dissipation within tolerable limits. But as these currents get smaller, the induced currents by the natural electric and magnetic environment becomes more important. Near-by lightning, corona and spark discharges on airborne vehicles, and transients during grounding procedures or ground contact will induce currents in the frequency range of 10 Hz to 100 KHz, which are difficult to shield with conventional electrostatic shields like aluminum foil. Proper magnetic shielding material will, by its weight, be counterproductive to the trend in microminuturization. It seems therefore, that the limit in microcircuitry will be set by the natural electromagnetic environment. A knowledge and understanding of this environment will therefore be very important for planning and development of microcircuit avionics as well as for operational use. Recent tests by NRL of P and N-MOS type integrated

circuits in a thunderstorm environment demonstrated this concern. Several self-contained components with batteries but without cable connections of any sort were operated one meter away from a simulated lightning path of average amplitude and wave form. All of the components either suffered internal damage or operated incorrectly. These simulated conditions will exist in an aircraft or rocket which is hit by lightning but in which the lightning current is safely guided by good conductors through the length of the aircraft, and in which all lines and cables to microcircuit components which would pick up lightning signals are replaced by non-conductors like optical fibers.

If one imagines an aircraft of the size of a Boeing 747, constructed mainly out of carbon composites and its interior loaded with microcircuits on which the operation has to depend, it seems not possible to use it in other than ideal weather conditions, because the danger of atmospheric electric hazards to it is not yet recognized, not yet understood, and not yet assessable by measurement.

#### Present Basic Research

At present researchers in atmospheric electricity are concerned mainly with lightning and thunderstorms. The basic problem of how electricity is generated in a storm is not yet understood even though about twenty theories offer help. And to eliminate some of these theories is the objective of considerable research. The problem is, that a thunderstorm is very complex in its nature and very unassessable to direct experimentation. It is realized by now that this complexity demands the cooperation of many disciplines and that one needs better means to probe the inside of storms. In a decade of diminishing research funds such tasks seem unrealistic, yet in 1975 the majority of U.S. scientists in atmospheric electricity started a long term cooperative called TRIP (for Thunderstorm Research International Program) in which researchers with varying sources of funding and various research objectives pool their talent and resources to experiment on the same storm, the same lightning signal, the same rain gush to find answers which cannot possibly be obtained by single investigators. Novel measurement methods are involved like doppler radar to determine the velocity field inside a storm, remote sensing of the inside charge distribution by the electric field envelope over the storm, lidar methods to sense air velocities in the near storm environment, and various lightning sensing systems to deduce the structure of lightning inside the storm where eighty



percent of a lightning is hidden by clouds from optical observations. So far this research has not yet eliminated some of the thunderstorm theories but unique insight has been given to the structure of lightning inside a storm. Most significantly it has been found that the centers of charge as well as the initiation levels of lightning coincide much better with temperature than with the convective pattern or the outline of the cloud. Also new data exist on the average peak current of a lightning which is now quoted to be 40,000 amperes. The question which needs to be asked at last is that of relevancy of ongoing basic research to pressing upcoming problems in aviation and rocket operations. Unfortunately the researchers in atmospheric electricity do not know where they are needed although they are always ready to help, and developers of modern technologies do not realize the research potential available nor can they effectively communicate with the research base. That hints with some degree of confidence that solutions to the problem of atmospheric electric hazards will not necessarily come through basic research in atmospheric electricity.

# **ATMOSPHERIC ELECTRIC HAZARDS TO AIRCRAFT**

**LOTHAR H. RUHNKE  
NAVAL RESEARCH LABORATORY**

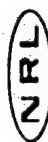
**1750 TO 1780**

| PROBLEM  | BASIC RESEARCH                                     | SOLUTION  |
|--|--|---|
| LIGHTNING PROTECTION<br>OF BUILDINGS<br>AND PEOPLE | STATIC ELECTRICITY<br>FAIR WEATHER<br>MEASUREMENTS | LIGHTNING ROD<br>PROTECTION RULES<br>FOR PEOPLE |

NRL

**1920 TO 1930**

| PROBLEM                               | BASIC RESEARCH  | SOLUTION                              |
|---------------------------------------|---|---------------------------------------|
| POWER TRANSMISSION<br>LINE PROTECTION | LIGHTNING WAVEFORM<br>PEEK CURRENT STATISTICS<br>ELECTRIFICATION THEORIES | AUTOMATIC SWITCHES<br>GROUNDING WIRES |



1940 TO 1950

| PROBLEM                           | BASIC RESEARCH   | SOLUTION  |
|-----------------------------------|--|---|
| AIRCRAFT COMMUNICATION<br>SYSTEMS | ELECTRIFICATION THEORIES<br>THUNDERSTORM DYNAMICS<br>(1ST THUNDERSTORM<br>RESEARCH PROGRAM)<br><br>ELECTRICAL BREAKDOWN<br>PROCESSES | VHF AND UHF<br>COMMUNICATION SYSTEMS<br><br>ELECTROSTATIC DISCHARGERS<br><br>THUNDERSTORM AVOIDANCE<br>RULES<br><br>WEATHER RADAR |

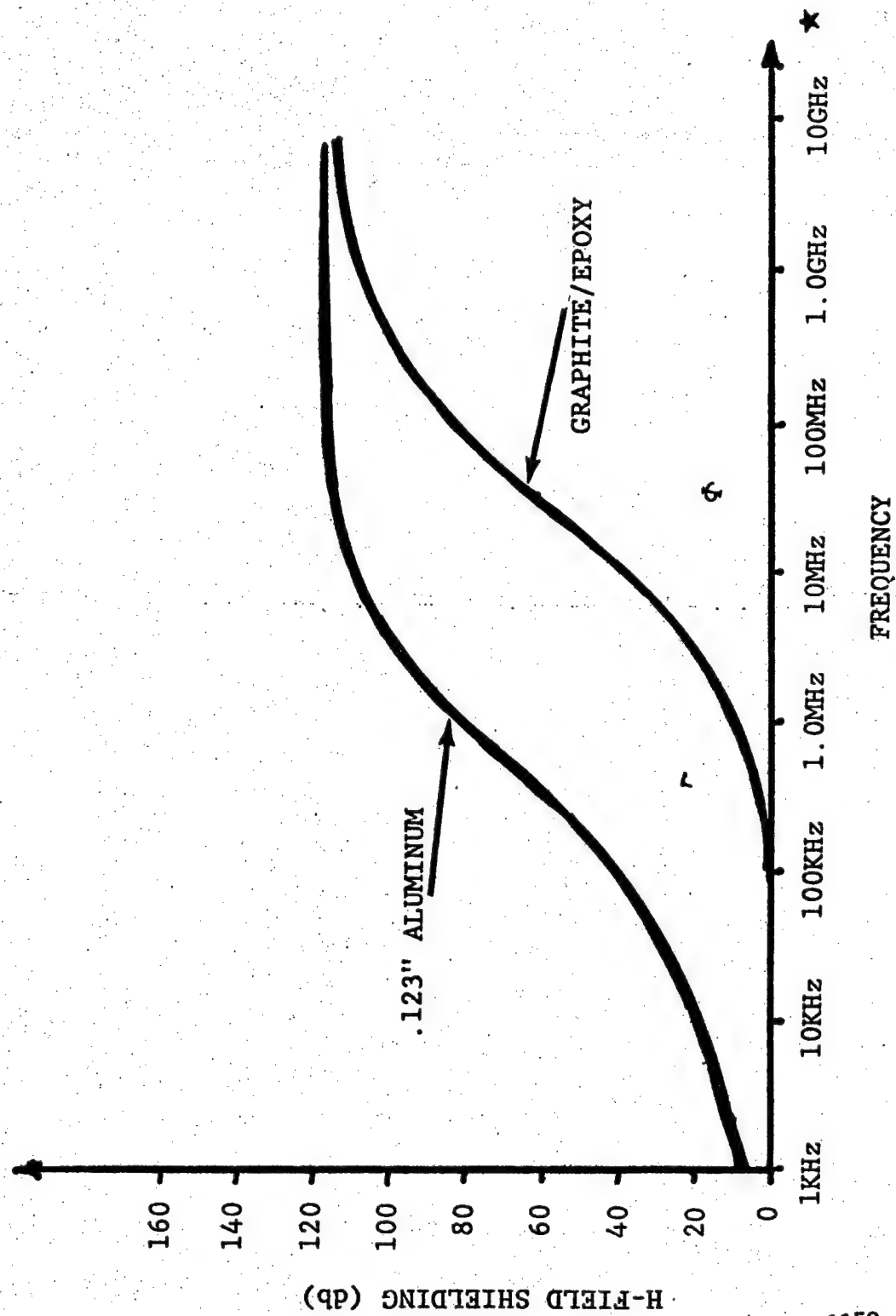
NRL

1975 TO 1985

| PROBLEM           | BASIC RESEARCH  | SOLUTION          |
|-------------------|---|-------------------|
| MICROCIRCUITS     | ELECTRIFICATION THEORIES  | HAZARD ASSESSMENT |
| CARBON COMPOSITES | LIGHTNING STRUCTURE   | WARNING SYSTEMS   |
| VEHICLE SIZE      | THUNDERSTORM MEASUREMENTS<br>(2ND THUNDERSTORM<br>RESEARCH PROGRAM) |                   |

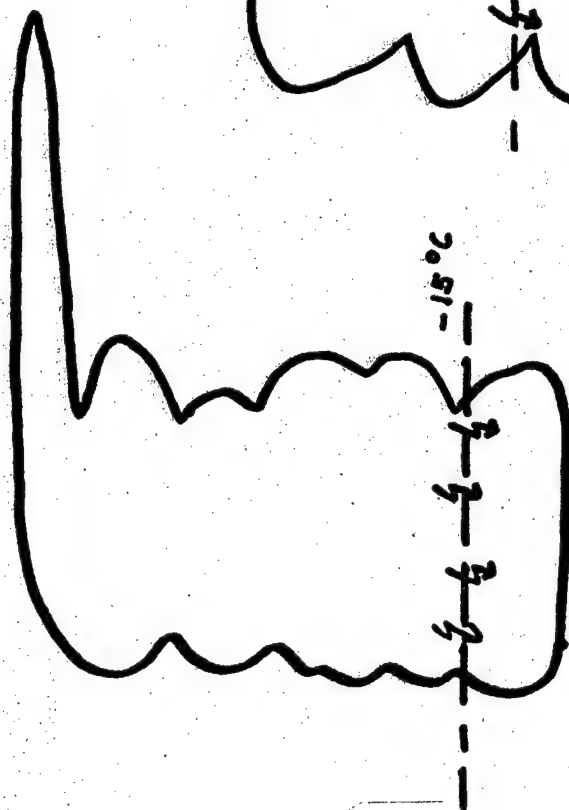
NRL

# MAGNETIC SHIELDING vs. FREQUENCY FOR GRAPHITE/EPOXY AND ALUMINUM

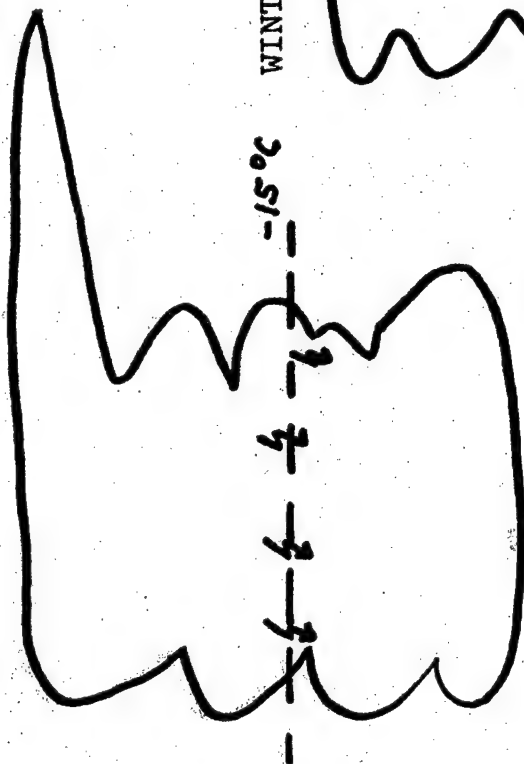


# LIGHTNING INITIATION ALTITUDES

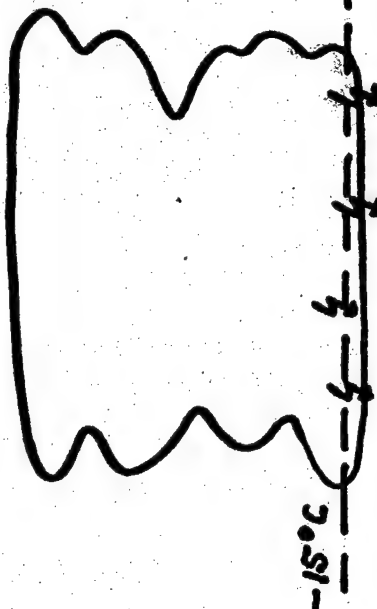
STORMS IN NEW MEXICO



STORMS IN FLORIDA



WINTER STORMS IN JAPAN





## BIOGRAPHICAL SKETCH

Lothar H. Ruhnke was born in Germany on March 2, 1931. He graduated from the Technical University in Munich in 1954 receiving an MS degree in electrical engineering. Subsequently he worked there as Research Assistant at the Institute for Electrophysics on VLF propagation problems. From 1966 to 1969 he studied Meteorology at the University of Hawaii where he received a Ph.D. degree in Geosciences.

He immigrated to the United States in 1957 and researched atmospheric electricity for the U.S. Army Signal Corps in Ft. Monmouth, NY. In 1960 he joined Litton Industries, Inc. as Senior Scientist for atmospheric electricity, cloud physics and electro-dynamics of dielectric liquids. Several patents and numerous scientific publications from this period show a diversified interest in theories, measurements and instrument developments associated with environmental problems. In 1966 the U.S. Department of Commerce appointed him as Scientific Director of the Mauna Loa Observatory in Hawaii where he guided an observational program to monitor global atmospheric pollution and research on tropical rain. From 1969 to 1972 he worked at NOAA's Environmental Research Laboratory in Boulder, Colorado on fog modification and electrostatic hazards in connection with NASA's Appollo program. At present he is Head of the Atmospheric Physics Branch at the Naval Research Laboratory where he guides projects in electrooptics meteorology, aerosol physics and atmospheric electricity. Dr. Ruhnke participates actively in several committees, working groups and international organizations. He is presently the Secretary of the International Commission on Atmospheric Electricity, Secretary of the International Thunderstorm Research Program (TRIP), Chairman of a Working Group on Thunderstorm Research, member of the working group on Atmospheric Optics of the International Radiation Commission and member of Tri-Service and Navy Working Groups on optics and aerosol Physics. He further serves on advisory panels for the Convective Storms Division of NCAR, SEASAT Meteorology and Environmental Observation panels of NASA, and NATO study groups on long term scientific studies. He is a member of the American Geophysical Union and the Scientific Research Society of America.

EFFICIENT OPERATION OF A 100 WATT  
TRANSVERSE FLOW OXYGEN-IODINE CHEMICAL LASER

D. J. Benard, W. E. McDermott,  
N. R. Pchelkin, and R. R. Bousek

Air Force Weapons Laboratory  
Kirtland AFB, New Mexico 87117

ABSTRACT

Efficient extraction of chemically generated  $O_2(^1\Delta_g)$  energy has been obtained in a transverse flow oxygen-iodine laser. The measured power extraction efficiency with off-optimal outcoupling was 15%. Output powers in excess of 100 watts were obtained for periods of up to 5 minutes.

## INTRODUCTION

The oxygen-iodine chemical laser operates on the  $^2P_{1/2} \rightarrow ^2P_{3/2}$  spin-orbit transition of the iodine atom which is pumped by energy transfer from chemically produced  $O_2(^1\Delta)$ . In our previous work<sup>1</sup> lasing was achieved in a longitudinal flow tube and coaxial laser cavity which converted only a small fraction of the available  $O_2(^1\Delta)$  energy into laser output. Most of the  $O_2(^1\Delta)$  energy in the longitudinal flow experiments was catalytically dumped on the walls of the flowtube.

In this paper we report the first example of cw laser action at high power levels and high conversion efficiencies from a chemically pumped oxygen-iodine laser. The results were obtained by improving the chemical  $O_2(^1\Delta)$  generator and by extracting the laser power transverse to the oxygen-iodine flow. The transverse geometry was designed to afford higher gain, more efficient outcoupling, and wall-free operation.

## EXPERIMENTAL

The chemical generator represents a 10X scale up in the oxygen generating capacity of our previous apparatus. Figure 1 shows the generator design. About 5 liters of 90%  $H_2O_2$  and 2 liters of 6N NaOH were admitted to the reactor through the reagent feed lines at the top of the generator. During the loading operation,  $N_2$  was continuously flowed through the bubbler to preclude liquid from entering the bubbler itself and to provide good mixing of the  $H_2O_2$  and NaOH. The mixing of the base and peroxide is an exothermic process that can lead to a run away decomposition of the  $H_2O_2$  if the generator temperature exceeds  $60^\circ C$ . To prevent this, the reagents were mixed in the generator under

vacuum, so that evaporative cooling due to the pumping off of water vapor maintained an operating temperature below 30°C. This mixing process also has the advantage of concentrating the base-peroxide mixture that is used to generate the  $O_2(^1\Delta)$ .

The  $O_2(^1\Delta)$  was generated via the reaction of  $Cl_2$  gas with the basic  $H_2O_2$  solution. The  $Cl_2$  was admitted to the generator through the bubbler structure. Most of the  $Cl_2$  was reacted in the generator and the oxygen production was approximately stoichiometric with the  $Cl_2$  flow rate of 0.03 moles/sec. The effluent from the chemical generator was passed through a liquid nitrogen cold trap of standard reentrant design to remove water vapor and unreacted  $Cl_2$ . The  $O_2(^1\Delta)$  concentration was measured at the exit of the cold trap by monitoring the 1270 nanometer emission ( $a^1\Delta \rightarrow X^3\Sigma$ ) with a narrow bandpass filter and a cooled intrinsic Ge detector. The percent  $O_2(^1\Delta)$  in the flow was measured by scaling the radiative signal to the pressure using a technique we have reported on in a previous paper.<sup>2</sup> Typical results were approximately 35%  $O_2(^1\Delta)$  at pressures of 1 torr in the laser cavity. The distance from the midplane of the generator to the inlet of the laser cavity was approximately 3 meters.

The laser section itself (Figure 2) consisted of a gradual expansion duct from 7.6 cm diameter glass pipe (cross sectional area = 45.6cm<sup>2</sup>) to a 50cm x 2.54 cm (cross sectional area = 127cm<sup>2</sup>) rectangular duct. The rectangular section was terminated into the side of a 15 cm diameter pipe that was connected to a high capacity vacuum pump. The inner surface of the stainless steel laser cavity was coated with halocarbon grease to minimize  $O_2(^1\Delta)$  wall deactivation and iodine atom recombination. The laser mirrors were mounted internally to the vacuum on tubes extending

from either side of the flow region. The mirrors were separated by 1.36 meters. Each mirror tube was purged with a small flow of Argon during operation of the laser.

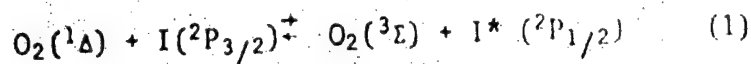
Molecular iodine was injected with a carrier flow of Ar into the oxygen flow via an  $I_2$  bomb heated to approximately  $50^\circ\text{C}$ . The injector itself was a 1 cm OD. stainless steel tube with a thin (0.25 mm) slot 42 cm long milled along its length. The injector tube was centered in the rectangular flow channel approximately 6 cm upstream of the cavity axis with the slot on the downstream side. The injector tube was also resistively heated in order to prevent condensation of  $I_2$  on the interior.

## RESULTS

The limiting apertures in the laser cavity were the walls of the flow tube and the inside diameter of the mirror support tubes. Using a >99.9% maximum reflectance flat back mirror and a 98.3% reflectivity (1.7% transmitting) 5m radius of curvature front mirror the laser output was sufficient to easily burn a mode pattern into a black plastic plate in a few seconds. The mode pattern was equal in size and shape to the area of the limiting aperture (2.5 cm high x 4cm in the flow direction) and an output power of approximately 100 watts was measured using a Scientech disk calorimeter. Operation of the laser was dependent upon generator performance but was easily reproducible.

## DISCUSSION

The extractable  $O_2(^1\Delta)$  energy can be determined from the equilibrium constant,  $K$ , of the pumping reaction:



where 
$$K = \frac{[\text{I}^*(^2\text{P}_{1/2})][\text{O}_2(^3\Sigma)]}{[\text{I}(^2\text{P}_{3/2})][\text{O}_2(^1\Delta)]} = 2.9 \text{ (300}^\circ\text{K)}$$

and the zero gain condition on the inversion density:

$$\frac{\text{I}^*(^2\text{P}_{1/2})}{\text{I}(^2\text{P}_{3/2})} = 0.5 \quad (2)$$

An  $[\text{O}_2(^1\Delta)]/[\text{O}_2(^3\Sigma)]$  ratio of .17 is therefore required to maintain positive gain. Consequently, the extractable energy in the flow corresponds to the  $\text{O}_2(^1\Delta)$  in excess of 17% of the total  $\text{O}_2$ . Thus with 35%  $\text{O}_2(^1\Delta)$ , about 18% of the total  $\text{O}_2$  can contribute to laser output. For our conditions, the extractable energy was 600 watts giving a conversion efficiency in the laser itself of 15%. In these experiments the conversion efficiency was less than 100% because, as will be shown, the laser was overcoupled resulting in inadequate saturation of the lasing medium.

The rate of stimulated emission based on the measured output power aperture size, mirror transmission, and a Doppler broadened stimulated emission cross section was  $1.5 \times 10^4 \text{ sec}^{-1}$ . The rate of loss of excess  $\text{O}_2(^1\Delta)$ , however, is given by the rate of stimulated emission times the ratio of iodine to excess oxygen. At an iodine partial pressure of  $5 \times 10^{-3}$  torr and the optimal lasing conditions, the rate of excess  $\text{O}_2(^1\Delta)$  loss was approximately  $300 \text{ sec}^{-1}$  due to stimulated emission and energy

transfer. The rate of loss of  $O_2(^1\Delta)$  due to the flow through the resonator cavity is  $V/L$  ( $V = 60\text{m/sec}^{-1}$ ,  $L = 4\text{cm}$ ) or  $1500\text{ sec}^{-1}$ . The expected efficiency is therefore approximately  $300/(1500 + 300)$  or 15%. In this analysis the energy transfer rate can be assumed to be very large in comparison to the stimulated emission rate which is then the rate limiting step. Since the forward transfer rate is approximately gas kinetic this assumption is clearly correct.

The optimum mirror outcoupling based on the estimated gain of 5% per round trip and assuming non-productive mirror losses of 0.1% is around 0.5%. Reducing the outcoupling would cause a corresponding increase in the intracavity intensity and therefore accelerate the stimulated emission rate causing greater laser output to occur as the  $O_2/I$  mixture flows through the laser cavity. Alternatively, a longer resonator section would permit greater time for extraction of the  $O_2(^1\Delta)$  energy and thus increase the laser output as well.

In summary, this experiment has demonstrated the feasibility of highly efficient operation of the oxygen-iodine chemical laser. The authors wish to acknowledge the technical assistance of Gary Lee, Pat Timlin, Ken and Don Maier and Charles Fry. The authors are especially indebted to our glass blower Jan Marien, who constructed the large glass traps required for this laser demonstration.

### REFERENCES

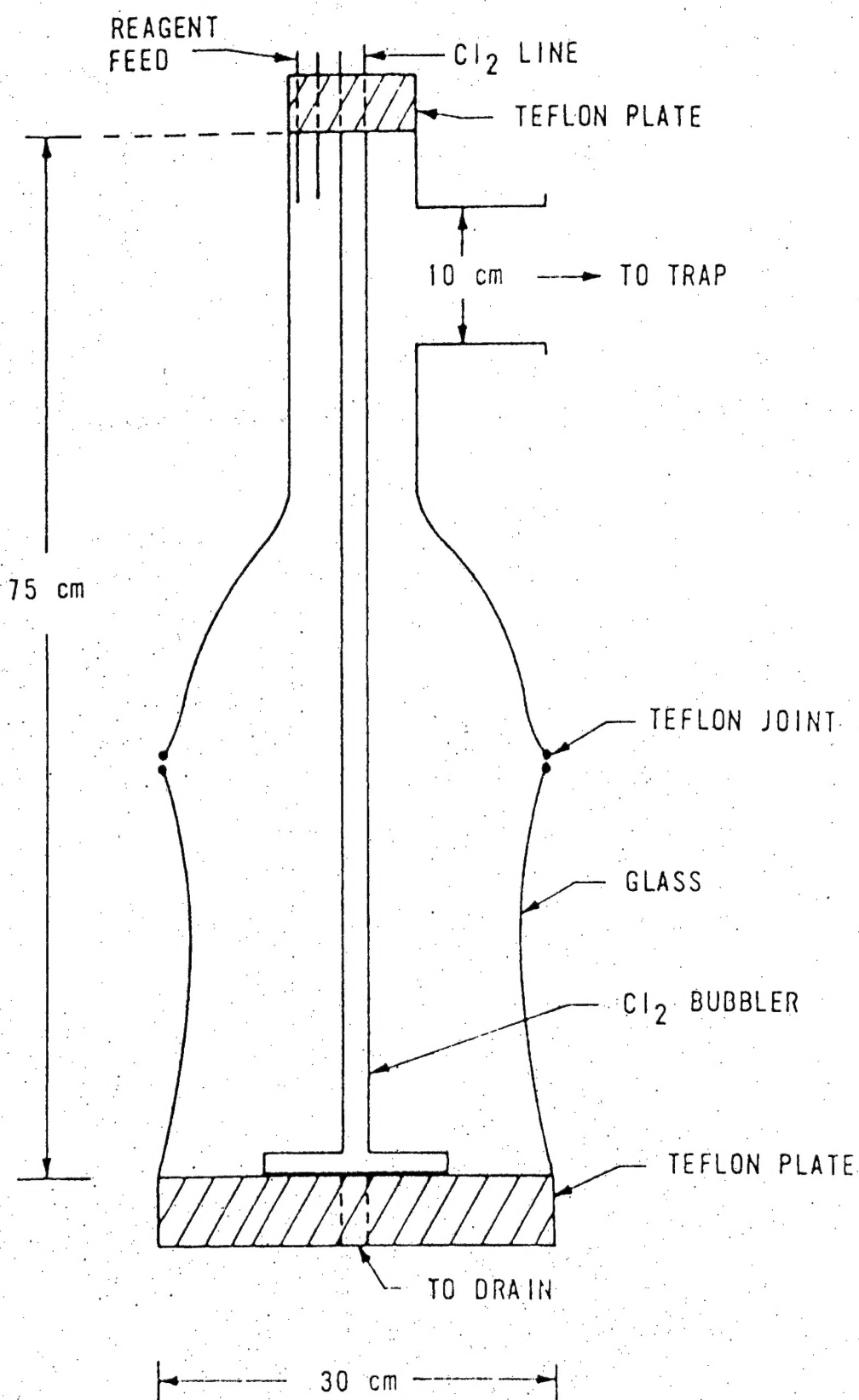
1. W. E. McDermott, N. R. Pchelkin, D. J. Benard, and R. R. Bousek, Appl. Phys. Lett. 32, 469 (1978).
2. D. J. Benard and N. R. Pchelkin, Rev. Sci. Instrum. 49, 794 (1978).

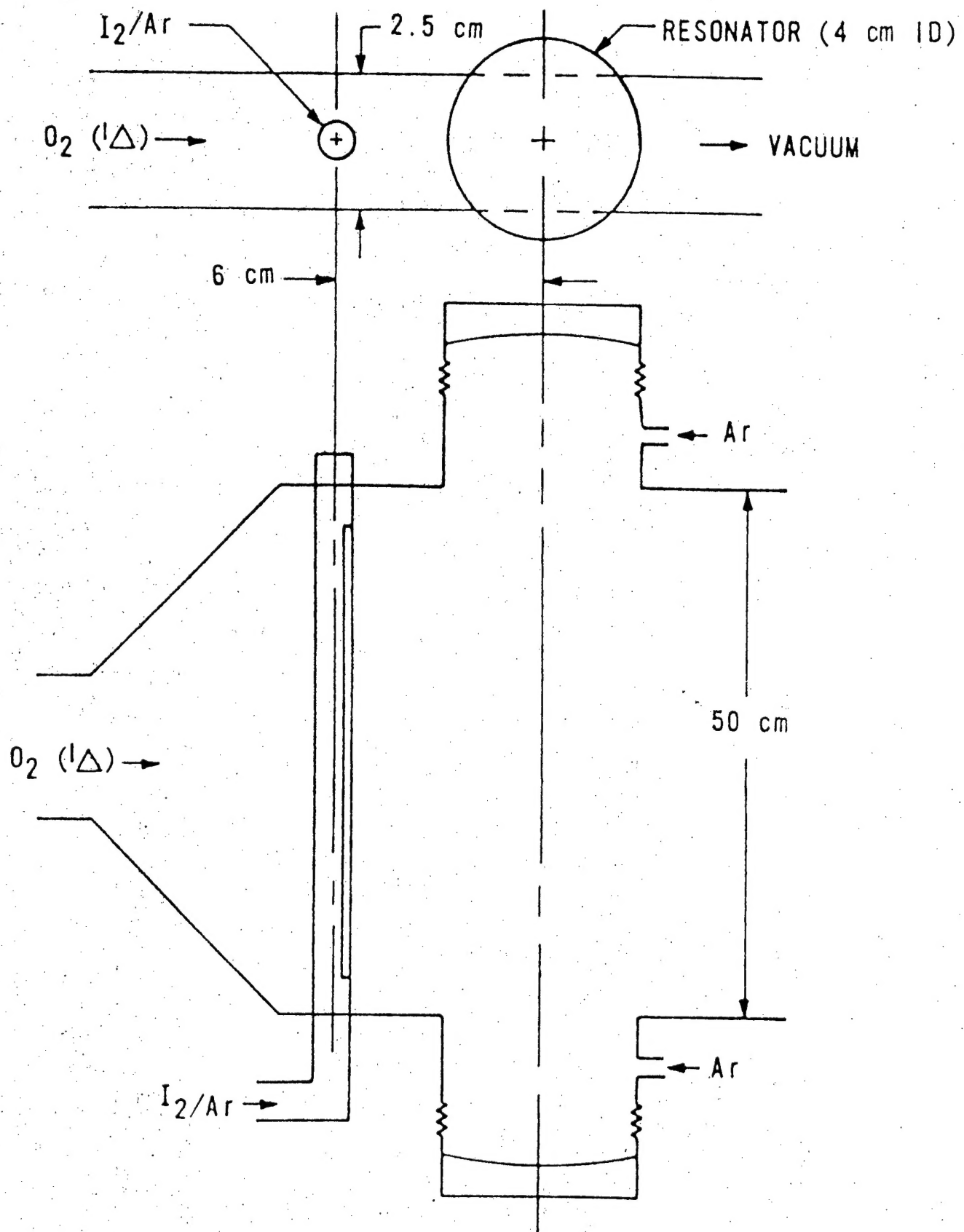


## FIGURE CAPTIONS

Figure 1: Reactor for generation of  $O_2(^1\Delta)$  in 35% concentration at typically 0.30 moles/sec.

Figure 2: Design of transverse-flow laser for extraction of chemical  $O_2(^1\Delta)$  power by energy transfer to iodine atoms.





### Biographical Sketch

Dr. David J. Benard was born in Washington, D.C., in 1946. Dr. Benard attended the University of Illinois from 1964 to 1972, graduating with highest honors in Engineering Physics, followed by graduate work leading to a Ph.D. in Solid State Physics. After graduation, Dr. Benard held positions at the Johns-Hopkins Applied Physics Laboratory, the University of California, Santa Barbara, and most recently, the Air Force Weapons Laboratory. Dr. Benard has been intimately involved with the demonstration of several new chemical lasers and is currently conducting research into potential short wavelength chemical laser systems.

Major McDermott received his Air Force commission in 1965 from the United States Air Force Academy, where he majored in mathematics. He subsequently received MS and PhD degrees in Engineering-Applied Science from the University of California at Davis. His duty assignments have included Nuclear Research Officer with the 1155th Technical Operations Squadron at McClellan AFB, CA, Instructor in Chemistry at the USAF Academy, Research Chemist at the Frank J. Seiler Research Laboratory, and Associate Professor of Chemistry at the USAF Academy. He is presently assigned to the Chemical Laser Branch at the Air Force Weapons Laboratory, where he is project leader for in-house oxygen-iodine chemical laser research. Major McDermott has co-authored several journal articles in chemical physics.

Captain Nicholas R. Pchelkin was commissioned in the USAF under ROTC at San Jose State College, where he received his B.S. degree in chemistry in 1967. Capt Pchelkin completed navigator training in November 1968 and electronic warfare school in July 1969. He has served as an electronic warfare officer on B-52 and A/C 130 Gunships. In July 1976, he attended AFIT at Wright-Patterson AFB. Capt Pcheklin received a M.S. degree in Laser Physics in December 1976 and was subsequently assigned to the Air Force Weapons Laboratory. He is presently continuing research work on chemical lasers and managing several contracts in this area.

Major Ronald R. Bousek was commissioned in the USAF under ROTC at Case Institute of Technology, where he received a B.S. degree in Physics in 1963. After receiving a M.S. degree in Physics from the U.S. Naval Postgraduate School in 1965, he served as Nuclear Research Officer at the 1155 Technical Operations Squadron, McClellan AFB, and at the Air Force Technical Applications Center, Washington, D.C. Major Bousek received a Ph.D. degree in Physics from the University of Arizona in 1976. He is presently managing contractual and in-house R&D efforts to develop new short wavelength high energy chemical lasers at the Air Force Weapons Laboratory, Kirtland AFB.